Design of a static mixer reactor for copper recovery from waste streams

PROEFSCHRIFT

ter verkrijging van de graad van doctor
aan de Technische Universiteit Delft,
op gezag van de Rector Magnificus prof. dr ir J.T. Fokkema,
voorzitter van het College van Promoties,
in het openbaar te verdedigen op
dinsdag 6 september 2005 om 10.30 uur

door

Willem Frederik Cornelis VAN WAGENINGEN

natuurkundig ingenieur
geboren te Westkapelle

Dit proefschrift is goedgekeurd door de promotoren:
Prof.dr.ir. H.E.A. van den Akker en Prof.dr. R.F. Mudde.

Samenstelling promotiecommissie:

Rector Magnificus	voorzitter
Prof.dr.ir. H.E.A. van den Akker	Technische Universiteit Delft (promotor)
Prof.dr. R.F. Mudde	Technische Universiteit Delft (promotor)
Prof.dr. F.J. Muzzio	Rutgers University, USA (NJ)
Prof.dr.ir. J.T.F. Keurentjes	Technische Universiteit Eindhoven
Prof.dr. J.P.M. Sanders	Wageningen Universiteit en Researchcentrum
Prof.dr. J.A. Moulijn	Technische Universiteit Delft
Prof.dr.ir. M.C.M. van Loosdrecht	Technische Universiteit Delft

The project IZW98401: *Development of a plug flow reactor for treating heavy metals containing feeds* was funded by:
Senter, which is an agency of the ministry of economic affairs.
Senter is currently joined with Novem and is now called SenterNovem.

Printed by:
Optima Grafische Communicatie
Pearl Buckplaats 37
3069 BZ Rotterdam
Telefoon: 010-2201149
Fax: 010-4566354
E-mail: account@ogc.nl
ISBN: 90-8559-079-5

Keywords: static mixer, computational fluid dynamics, lattice-Boltzmann, laser Doppler anemometry, mixing, copper reduction, particle

This thesis was created using LaTeX

”Daar men niet zo universeel kan zijn,
dat men alles weet wat van alles te weten is,
moet men weinig weten van alles.
Want het is veel mooier iets van alles te weten dan
alles te weten van een enkel ding”[1].

[1] Blaise Pascal (1623-1662)

Summary

Design of a static mixer reactor for copper recovery from waste streams
W.F.C. van Wageningen

The main goal of the project was the development of a plug flow reactor for the reduction of heavy metals (Cu^{2+}) from industrial waste streams. Potential application of the reduction process inside The Netherlands lies in the IC and galvanic industry, where small waste streams containing aqueous copper exist. Outside The Netherlands, the process could be applicable in the mining industry,e.g. in Chili or South Africa. The copper is reduced in the form of particles by soluble carbohydrates, which provide the electrons for the precipitation. The carbohydrates may originate from another waste stream, which can be found in the food or wood industry. After hydrolysis, these carbohydrates can be applied as reductor. Furthermore, the carbohydrates are degraded, which lowers their carbon oxygen demand and cleans the waste streams biologically. This way, the two waste streams are cleaned simultaneously and a valuable end product in the form of copper particles is recovered.

The main focus of this thesis is on the application of the Kenics™ static mixer in a pipe reactor, in order to achieve plug flow conditions in such a reactor. The static mixer is used to control the residence time of the particles, and to mix the chemical species in the reactor. The key question is under which conditions the application of the static mixer leads to a (more) narrow particle size distribution. A narrow size distribution of the particles is an important aspect, since it enhances the economical value of the end product. To answer this question, the Kenics™ static mixer is studied in detail both numerically and experimentally.

The flow in the Kenics™ static mixer has been investigated both numerically and experimentally in the range of Re=100. . . 1000. It was found that at Re=300 the flow becomes unsteady. Two numerical methods, the Lattice Boltzmann (LB) method and the Finite Volume method (FLUENT) were compared and used to simulate the flow. The LB method proved to be a relatively fast and cheap (in terms of memory) alternative for the simulation of the transient flow in the Kenics™ static mixer at Re>300. Furthermore, the flow field and dynamic behaviour were validated by means of LDA experiments. The transient behaviour observed was explained by studying the dynamics of the vortices in the flow. The transition to unsteady flow takes place, when the vortices start stretching out over an entire mixing element and start creating a disturbance in the flow entering the next mixing element, which subsequently triggers the unsteady behaviour.

To investigate the behaviour of particles in the static mixer, a Particle Tracking (PT) code is developed and linked to and embedded into the LB code. The particle tracking code is based upon the equation of Maxey and Riley (1983) to which the modified lift force (Saffman (1965, 1968)) is added. Furthermore, a growth model for the particles is added to the PT code. The particle growth is based upon the diffusion of Cu^{2+} to the surface of the particle. The Cu^{2+} concentration is solved with a standard finite volume code, which solves the convection-diffusion equation with a sink term. The sink term is directly linked to the growth of the particles present in the finite volume cell. The chemical parameters due to Van der Weijden et al. (2002a) are used as input for the growth model,

where it is assumed that the diffusion of Cu^{2+} is the rate limiting factor.

The results indicate that two important design parameters for the Kenics™ static mixer reactor are the Reynolds number, which is a measure of the flow regime, and the St/Fr ratio, which is a measure of the settling rate of the particles. The two numbers determine to a large extent the mixing, settling and residence time of the particles. Ideally, the particles are uniformly distributed and have an uniform residence time distribution (plug flow). It was found that these conditions were best matched at a low St/Fr ratio (St/Fr$<$1) and at either a low or a high Reynolds number (Re$<$20 or Re$>$200).

In a horizontal reactor, settling of the particles poses a problem that is directly related to the St/Fr ratio. It was found that in order to keep the majority of the particles in suspension the St/Fr ratio should be small and the Reynolds number high (St/Fr$<$0.01 and Re$>$500). Alternatively, the reactor can be placed vertical. If the flow direction is downward in such a reactor, no problems regarding the settling of particles occur, which removes the limit on the St/Fr ratio. However, there remains a limit regarding the mixing of the particles. When the St/Fr ratio is high ($>$1), particles collide with the mixing element, which leads to accumulation of the particles near the mixing elements. It was investigated what the influence of this ill-mixing of the particles was on the particle size distribution. For that purpose, simulations were carried out of growing copper particles in a vertical Kenics™ static mixer reactor. It was found that the particle size distribution is wide, when the particles are not mixed effectively. Therefore, a vertical reactor is also limited by the St/Fr ratio (St/Fr$<$1), when a high quality end product is required, i.e. particles with a narrow size distribution.

The results of the chemical (autoclave) investigations are combined with the numerical results, to propose a design for a continuous (plug flow) reactor. A one-dimensional model is used to predict the reduction of Cu^{2+} in three reactor configurations (batch, horizontal plug flow reactor and vertical plug flow reactor). Experiments in a glass-lined autoclave were used to test the model and to obtain the model parameters. The model is used to predict the (mechanical) energy consumption per kg recovered copper. Furthermore, the total energy demand of the process (heating + pumping/stirring) was evaluated for different reactor types and compared to electro-winning being the conventional method of copper recovery. It was found that heating the liquid towards the set temperature is the main energy consumer.

Based upon its energy demands, the applicability of the reactor is assessed for industrial waste treatment and the mining industry. It was found that the vertical plug flow reactor can be an attractive alternative for electrolysis, when the stream has a high Cu^{2+} concentration or when the stream is contaminated with organic material. It should be noted that the vertical reactor was explicitly designed for the treatment of small waste streams that exist in the Netherlands. For processing the large streams that exist in the mining industry, the throughput of the vertical reactor is too low. This limitation can be overcome by placing different vertical reactors in parallel to accommodate a large throughput. However, the use of another type of static mixer might extend the feasibility of the vertical reactor towards a higher throughput. The design of such a 'large' vertical reactor can be an interesting topic for future investigations.

Samenvatting

Ontwerp van een 'static mixer reactor' voor de terugwinning van koper uit afvalstromen
W.F.C. van Wageningen

Het hoofddoel van het project is de ontwikkeling van een propstroomreactor voor de reductie van zware metalen (Cu^{2+}) uit industriële afvalstromen. Potentiële toepassingen voor het reductieproces binnen Nederland zijn te vinden in de IC industrie en in de galvanische industrie. Buiten Nederland zou het proces toegepast kunnen worden in de kopermijnbouw, bijvoorbeeld in Chili of Zuid Afrika. In de afvalstromen van deze industrieën bevindt zich opgelost koper. Het koper wordt gereduceerd met behulp van koolhydraten, waarbij kleine koperdeeltjes gevormd worden. De koolhydraten verschaffen de elektronen die nodig zijn voor de precipitatie en kunnen gewonnen worden uit afvalstromen van de voedsel- of houtindustrie. Na hydrolyse kunnen deze koolhydraten toegepast worden als reductor. Bovendien worden de koolhydraten afgebroken, hetgeen de 'carbon oxygen demand' (COD) verlaagt bij de biologische zuivering van deze afvalstromen. Op deze manier worden twee afvalstromen gelijktijdig gezuiverd en wordt een waardevol eindproduct in de vorm van koperdeeltjes teruggewonnen.

De focus van dit proefschrift is gericht op de toepassing van de Kenics™ statische menger in een buisreactor om een propstroming te bewerkstelligen. De statische menger wordt gebruikt om de verblijftijd van de deeltjes te beïnvloeden en de chemische stoffen te mengen in de reactor. De hamvraag is onder welke condities het gebruik van de statische menger tot een nauwe deeltjesgrootteverdeling leidt. Een smalle deeltjesgrootteverdeling is belangrijk, omdat het de economische waarde van het eindproduct vergroot. Om deze vraag te beantwoorden is de Kenics™ statische menger in detail bestudeerd, zowel numeriek als experimenteel.

De stroming in de Kenics™ statische menger is zowel numeriek als experimenteel onderzocht in het bereik van Re=100. . . 1000. Het is gebleken dat vanaf Re=300 de stroming tijdsafhankelijk gedrag vertoont. Twee numerieke methoden, de Lattice Boltzmann (LB) methode en de eindige volumen methode (FLUENT), zijn vergeleken en gebruikt om de stroming te simuleren. De LB-methode bleek een relatief snel en goedkoop (met betrekking tot geheugengebruik) alternatief voor de simulatie van de tijdsafhankelijke stroming in de Kenics™ statische menger bij Re$>$300. Bovendien zijn het stromingsveld en dynamisch gedrag gevalideerd d.m.v. LDA experimenten. Het waargenomen tijdsafhankelijke gedrag kon verklaard worden door te kijken naar de dynamica van de wervels in de stroming. De transitie naar een tijdsafhankelijke stroming vindt plaats op het moment dat de wervels zich over de gehele lengte van een mengelement uitstrekken en de stroming bij het volgende element verstoren. Dit veroorzaakt het tijdsafhankelijk gedrag van de stroming in de statische menger.

Om het gedrag van deeltjes in de statische menger te onderzoeken, is er een 'Particle Tracking' (PT) code ontwikkeld en toegevoegd aan de al bestaande LB code. De PT code is gebaseerd op de vergelijking van Maxey and Riley (1983), waaraan de gemodificeerde liftkracht (Saffman (1965, 1968)) is toegevoegd. Bovendien is er een deeltjesgroeimodel toegevoegd aan de PT code. De deeltjesgroei is gebaseerd op de diffusie van Cu^{2+} naar het oppervlak van een deeltje. De Cu^{2+} concentratie

is gesimuleerd met een standaard eindige volumen code. Deze code lost de convectie-diffusie-vergelijking met een bronterm op. De bronterm is direct gerelateerd aan de groei van de deeltjes die zich in een eindige volumen cel bevinden. De chemische parameters uit Van der Weijden et al. (2002a) zijn gebruikt als input voor het groeimodel. Hierbij is er vanuit gegaan dat de diffusie van Cu^{2+} de beperkende factor is voor de reactiesnelheid.

De resultaten laten zien dat er twee belangrijke ontwerpparameters voor de Kenics™ statische menger zijn: het Reynolds getal, hetgeen een maat is voor het stromingsregime, en de verhouding tussen het Stokes en het Froude getal (St/Fr), hetgeen een maat is voor de uitzaksnelheid van de deeltjes. Deze twee getallen bepalen voor een groot deel het mengen, het uitzakken en de verblijftijd van de deeltjes. In het ideale geval zijn de deeltjes uniform verdeeld over de menger en hebben ze een uniforme verblijftijdsspreiding (propstroom). Het bleek dat deze condities het best benaderd werden bij een lage St/Fr verhouding (St/Fr$<$1) en ofwel een laag dan wel een hoog Reynoldsgetal (Re$<$20 of Re$>$200).

Bij een horizontale reactor, vormt het uitzakgedrag van de deeltjes een probleem wat direct gerelateerd is aan de St/Fr verhouding. Het bleek dat om het merendeel van de deeltjes in suspensie te houden een lage St/Fr verhouding en een hoog Reynolds getal nodig is (St/Fr$<$0.01 en Re$>$500). Een alternatief is een verticale reactor. Als de stromingsrichting naar beneden is in zo'n reactor, doen er zich geen problemen voor met betrekking tot het uitzakken van deeltjes. Hetgeen de limiet aan de St/Fr verhouding opheft. Er blijft echter een beperking voor wat het mengen van de deeltjes betreft. Als de St/Fr verhouding groot is ($>$1), botsen de deeltjes met de mengelementen, wat leidt tot een opeenhoping van deeltjes bij de mengelementen. Er is onderzocht wat de invloed van deze slecht gemengde deeltjes is op de deeltjesgrootteverdeling. Hiervoor zijn simulaties uitgevoerd van groeiende koperdeeltjes in een verticale reactor met een statische menger. Het bleek dat de deeltjesgrootteverdeling breed is, wanneer de deeltjes niet effectief gemengd zijn. Daarom is er ook bij een verticale reactor een beperking voor de St/Fr verhouding (St/Fr$<$1), wanneer er een eindproduct van hoge kwaliteit (nauwe deeltjesgrootteverdeling) gewenst is.

Om tot een nieuw ontwerp voor een propstroomreactor te komen zijn de numerieke resultaten gecombineerd met chemische experimenten uitgevoerd in een autoclaaf. Er is een 1-dimensionaal model gebruikt om de reductie van Cu^{2+} in drie verschillende reactorconfiguraties te voorspellen (batch reactor, horizontale propstroomreactor en verticale propstroomreactor). Experimenten in een autoclaaf met glazen binnenbehuizing zijn gebruikt om het model te testen en de modelparameters te bepalen. Het model is vervolgens gebruikt om het (mechanische) energieverbruik per kg teruggewonnen koper te voorspellen. Bovendien is de totale energiebehoefte van het proces (verwarmen + pompen) geëvalueerd en vergeleken met elektrowinning (EW), hetgeen de conventionele methode is voor terugwinning van opgelost koper. Het verwarmen van de vloeistof tot de reactietemperatuur bleek de grootste energieverbruiker te zijn.

De toepasbaarheid van de reactor voor industriële afvalwaterbehandeling en kopermijnbouw is onderzocht gebaseerd op het energieverbruik. Het bleek dat een verticale reactor een aantrekkelijk alternatief kan zijn voor elektrolyse, als de afvalstroom een hoge Cu^{2+} concentratie bevat of als de afvalstroom vervuild is met organisch materiaal. Het dient opgemerkt te worden dat de verticale reactor expliciet ontworpen is voor behandeling van kleine afvalstromen binnen Nederland. Voor het verwerken van grote stromen (bijvoorbeeld bij de kopermijnbouw) is de doorzet van de verticale reactor te laag. Deze limitatie kan overwonnen worden door meerdere reactoren parallel te plaatsen. Echter, het gebruik van bijvoorbeeld een ander type statische menger kan mogelijk de doorzet van de verticale reactor vergroten en de toepasbaarheid uitbreiden. Het ontwerp van zo'n grote verticale reactor vormt een interessant onderwerp voor toekomstig onderzoek.

Nomenclature

Acronyms

BBO	Boussinesq-Basset-Oseen
BGK	Bhatnagar-Gross-Krook
CDS	Central Difference Scheme
CFD	Computational Fluid Dynamics
CSTR	Continuous Stirred Tank Reactor
CV	Control Volume
FE	Finite Element
FFT	Fast Fourier Transform
FHP	Frisch-Hasslacher-Pomeau
FL	FLUENT
FV	Finite Volume
IA	Interrogation Area
IC	Integrated Circuit
LB	Lattice Boltzmann
LDA	Laser Doppler Anemometry
LES	Large Eddy Simulation
LG	Lattice Gas
NS	Navier-Stokes
PFR	Plug Flow Reactor
PISO	Pressure-Implicit with Splitting of Operators
PIV	Particle Image Velocimetry
PRESTO	PREssure STaggering Option
PT	Particle Tracking
RANS	Reynolds Averaged Navier Stokes
RIM	Refractive Index Matching
SIMPLE(C)	Semi-Implicit Method for Pressure-Linked Equations (Consistent)
TVD	Total Variation Diminishing

Roman symbols

A	area	[m^2]
A_0	constant growth constant	[m/s]
B_0	linear growth constant	[1/s]
$\mathbb{D}$	diffusion coefficient	[m^2/s]
C	coefficient	
c	concentration	[-/m^3]
$\vec{c}_i$	lattice velocity at link i	
D	element or tube diameter	[m]
D_I	length of an IA	[m]
d	diameter	[m]
e	(direction) vector	

Roman symbols (continued)

F	Force	[N]
f	frequency	[Hz]
$f_\mathrm{i}(\vec{r},t)$	particle density at link i	
G	gradient (velocity)	[1/s]
G	growth rate	[m/s]
G_0	reciprocal growth constant	[m^2/s]
g	gravitational acceleration	[m/s^2]
$H()$	Heaviside function or unit step function	[m]
h	height	[m]
J	coefficient	
J	nucleation	[particles/(m^2 s)]
K	normalised pressure drop	
k	wave number	[1/m]
k_a	area shape factor	
k_r	reaction rate constant	[1/s]
k_v	volume shape factor	
L	element length	[m]
l	(specific particle) size	[m]
l	axial position	[m]
l_p	distance of particle to wall	[m]
m	mass	[kg]
m_j	moments of PSD	[particles·m^{j-2}]
N_I	number of particles in an IA	
n	refractive index	
n	number	
$n_\mathrm{i}(\vec{r},t)$	discrete (Boolean) velocity direction of (LG) particle	
$n(l,\vec{x},t)$	population density	[particles/m^3]
p	pressure	[Pa]
$\mathbf{R}$	rotation matrix	
r	radial coordinate	[m]
r	radius	[m]
$\vec{r}$	lattice point	
S	power of spectra	
S	source or sink term	
S	surface	[m^2]
s	distance	[m]
s	standard deviation	
$\vec{s}$	displacement vector	[m]
T	temperature	[K]
t	element (blade) thickness	[m]
t	time	[s]
t	lattice time-step	
$\vec{U}$	velocity vector (PIV)	[m/s]
u	velocity (related to flow)	[m/s]
V	volume	[m^3]
v	velocity (related to particle)	[m/s]
w	width	[m]
x	axial coordinate	[m]
y	spatial coordinate	[m]
z	spatial coordinate	[m]

Greek symbols

α	twist angle of mixing element	[rad]
β	angle between two consecutive elements	[rad]
Δt	time step	[s]
δ	gap width between particle and wall	[m]
ϵ	$\frac{\sqrt{\mathrm{Re_G}}}{\mathrm{Re_p}}$	
ϵ	particle fraction: number of particles relative to injected number of particles	
θ	angle	[rad]
λ	bulk viscosity coefficient	[Pa s]
λ	wavelength	[nm]
μ	dynamic viscosity	[Pa s]
ν	kinematic viscosity	[m^2/s]
ρ	density	[kg/m^3]
σ	standard deviation	
$\vec{\vec{\sigma}}$	stress tensor	[kg/(m s^2]
τ	shear stress	[Pa]
τ	BGK relaxation parameter	
τ	relaxation time	[s]
τ	residence time	[s]
Φ_m	mass-flow rate	[kg/s]
Φ_l	flow rate	[m^3/s]
ϕ	angle	[rad]
ϕ	scalar	
Ω_i	collision operator at link i (LG)	

Dimensionless numbers

Da I	First Damköhler number
Fr	Froude number
Pe	Peclet number
Re	Reynolds number based on D
St	Stokes number

Subscripts

$\perp$	perpendicular
0	initial or reference
a	added mass
ax	axial
b	body
bd	between data
beam	laser beam
burst	LDA burst
C	cell
c	control (volume)
cycles	cycles of burst
D	drag
E or e	east
f	face
G	Gradient
i	lattice link
l	liquid

Subscripts (continued)

$_{lift}$	lift of particle
$_{McL}$	McLaughlin
$_{m}$	mass
$_{med}$	median
$_{mixer}$	tube with static mixer
$_{n}$	normal
$_{nodes}$	grid nodes
$_{out}$	out of plane
$_{p}$	particle
$_{proc}$	processor
$_{r}$	reaction
$_{rad}$	radial
$_{res}$	residence
$_{sheet}$	laser sheet
$_{s}$	slip
$_{s}$	specific
$_{sample}$	sample point (PFR)
$_{tan}$ or $_{t}$	tangential
$_{tot}$	total (time)
$_{tube}$	tube without static mixer
$_{v}$	volume
$_{W}$ or $_{w}$	west
$_{w}$ or $_{wall}$	wall

Superscripts

*	dimensionless
$^{+}$	dimensionless wall units
^{eq}	equilibrium

Contents

1

Introduction

1.1 Background: Waste-to-waste-to-product technology

Heavy metals such as copper are of utmost importance to mankind. They are used in electronic devices, heat exchange devices, electric wires and so on. Unfortunately, heavy metals are harmful to the environment. Therefore, waste water that contains heavy metals needs to be treated prior to discharge. A conventional method to treat waste-water containing heavy metals is via electrolysis or cementation. The use of scrap iron for the cementation of copper was already used in the 1500s in Spanish copper mines, but the quality of the copper was low due to impurities. Currently, electrolysis or electro-winning is widely used for copper recovery. It has the advantage that copper of high quality is formed, but it has the disadvantage that it requires a large amount of electrical power. Furthermore, an expensive solvent extraction step is necessary. Recently, Hage et al. (1999) showed that an alternative for electrolysis can be a reduction process based on oxidation of carbohydrates. Hage et al. performed their experiments in an autoclave. The advantage of this method is that it only requires power for heating and pumping. Furthermore, this novel reduction process can be used to process two waste streams simultaneously and recover a valuable end product. A process that works along this principle is an example of a waste-to-waste-to-product technology.

Waste-to-waste-to-product technology is a promising new field in environmental engineering. If used effectively, it has the potential of making profit out of waste. This forms an economic incentive for the cleaning of environmentally hazardous waste streams, which fits the concept of the triple P's (People, Planet and Profit) that more and more companies adopt nowadays. This philosophy puts equal weight on the well being of people, the care for the environment and the need for a healthy economy. In this study, a waste stream containing heavy metals (e.g. copper, silver or gold) is combined with a waste stream containing carbohydrates (e.g. starch, wood dust, sugar) in order to recover the metal in the form of metal powder. Here, the carbohydrates provide the electrons, which are necessary for the precipitation of the aqueous metal. The heavy metals are recovered and the carbohydrates are degraded. The waste stream containing heavy metals can originate from various industries such as the electronic, galvanic or mining industry. The waste stream containing carbohydrates can originate from organic waste streams, which can be found in the food or wood industry, and can be applied as reductors after hydrolysis. In this process, the negative impact of both streams on the environment is reduced. Figure 1.1 shows a schematic overview of the reduction of aqueous copper with the novel process.

One of the advantages that this novel reduction process has over electrolysis is that the heavy metals are reduced into particles and that it has the potential of being more energy efficient. In electrolysis, the end product consists of copper formed at the cathodes, whereas the autoclave reduction process delivers copper powder. Especially, when the particle size distribution is narrow, the copper powder

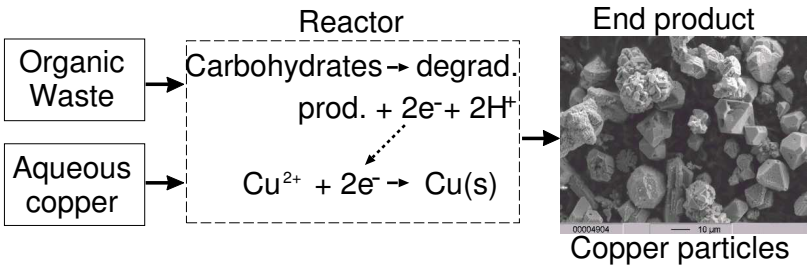

Figure 1.1: Cu^{2+} reduction with carbohydrates: solid particles are formed

is potentially more valuable. Furthermore, it is possible to treat waste streams that contain more than one heavy metal and recover these metals with a single reactor (Van der Weijden et al. (2001)).

In The Netherlands, the novel reduction process can be applied to the IC and galvanic industry. A typical IC company in The Netherlands produces a waste stream of the order of 2 m^3/day (23 mL/s), while the Cu^{2+} concentration of the stream is in the range of 1.2. . . 40 g/L. The original design of a plug flow reactor was based upon this stream. Recently, Bergsma (2003) showed that the waste streams in these companies are too small to justify the investment costs of a novel reactor. He proposed that central waste collectors/processors would be more interested in the novel reduction process. Several of these waste processing companies showed interest in the novel process such as Interchemic B.V., VECOM B.V., SITA Ecoservice B.V., Stokkermans Chroomindustrie B.V., BREDOX B.V. and Verstraeten Verbruggen Groep. Bergsma (2003) points out the following advantages that this process has over electrolysis:

- The process has a selectivity for copper (and silver).
- Organic contamination of the waste stream does not pose problems.
- Organic waste streams can (partly) be processed at the same time.
- Low concentrations can be treated.

He also mentions an important drawback of the novel reduction process: for application in The Netherlands, the entire national production of copper containing waste water is necessary to make a novel reactor economically feasible. However, the process has the potential to be successful in The Netherlands, when waste streams containing other heavy metals can be processed with the same reactor.

Outside The Netherlands, the reduction process could be applicable in the mining industry, e.g. in Chile or South Africa. In the mining industry, large streams of aqueous copper exist. The total amount of copper that is recovered by means of electrolysis is of the order of 1 Mton/year and the size of the streams that contain the aqueous copper is of the order of 1 m^3/s. Because of these enormous streams, the energy efficiency of the process plays an important role. If the novel process can be more energy efficient than electrolysis, a significant reduction in energy consumption can be achieved. Furthermore, the copper mining industry is responsible for a large fraction (10%) of the total amount of green house gases (CO_2) emitted by Chile (Maldonado et al. (2001)). The novel reduction process could help to reduce the emission levels.

It should be noted that the project sponsor, IOP Senter, demands an application inside The Netherlands. The main focus of the project was therefore on the treatment of small copper containing waste streams and not on the large streams that can be found in the copper mining industry.

1.1.1 IOP heavy metals: project partners and sponsors

At TU Delft, a joint project between the Kramers Laboratorium and Resources Engineering Group (formerly known as Raw Materials Processing) was started to render this novel reduction process economically feasible and to develop a suitable reactor environment, i.e. a plug flow reactor (PFR). The Resources Engineering Group, which is part of the Faculty of Civil Engineering and Geosciences, is specialised in the following three subjects: the design and the development of equipment for physical and chemical separation processes, the improvement of the processing of primary ores and secondary raw materials (metals), and environmental technology such as recycling and waste treatment. The expertise of the Kramers Laboratorium, which is part of the Faculty of Applied Sciences, is in the field of fluid mechanics and transport phenomena with a focus on the process industry.

The project was sponsored by Senter, which is an agency of the Ministry of Economic Affairs and is responsible for the subsidies, credit and fiscal arrangements in the area of technology, energy and environment. The goal of Senter is to strengthen the position of the industry and the knowledge infrastructure in The Netherlands in a sustainable fashion. One should note that Senter has been currently joined with Novem and is now called Senternovem. Senter has sponsored several innovative research programs (IOPs) one of them being the IOP heavy metals, from which this project was funded. Several companies have participated in the project such as CES B.V., RAMAER B.V., PRIMIX B.V., Corus N.V., Biofuel B.V., Ceramic Oxides International B.V., Philips Galvanotechniek Eindhoven and Ondeo Industrial Solutions.

1.2 Continuous reactor

The ultimate goal of the project is to develop a continuous plug flow reactor for the process. The process conditions, the feasibility of the novel reduction process and the chemical parameters were determined by Dr. R.D. van der Weijden from the Resources Engineering Group. Publications about this study have appeared in various journals and conference proceedings: Aurich and Koene (2001) and Van der Weijden et al. (1999, 2001, 2002a,b, 2003). Van der Weijden showed that the process can be an alternative for electrolysis and that it is applicable to various industrial waste treatment or mining processes. Most of her work was based on autoclave experiments, which provided vital data about the chemical process. This data were used as input for the development and numerical simulations of a continuous reactor.

The two types of continuous reactors that are often used in the process industry are the continuous stirred tank reactor (CSTR) and the plug flow reactor (PFR). Despite the fact that a CSTR has drawbacks, it is often used because of the large amount of knowledge and experience that exists about stirred tank reactors. At the Kramers Laboratorium the stirred tank reactor has been the subject of several numerical investigations for the past years. Derksen and Van den Akker (1999) showed that the Lattice Boltzmann (LB) method in combination with the Smagorinsky model for sub-grid scale turbulence is a powerful tool to simulate the turbulent flow in a stirred vessel. This work was extended to multiphase (liquid-solid) flow by Derksen (2003). Furthermore, the LB method was used by Hollander et al. (2003) to study agglomeration in stirred vessels. Recently, Hartmann et al. (2004) continued on this work and studied the hydrodynamics in a Rushton turbine stirred vessel. In his work, a large eddy simulation (LES) carried out with LB, was compared to the Reynolds averaged Navier Stokes (RANS) model in the commercial package CFX; the numerical results were compared to LDA measurements. All in all, the scientific work at the Kramers laboratorium has led to an increase in understanding of the dynamic (multiphase) flow in a Rushton stirred vessel and shows the importance of stirred vessels and mixing for the process industry. However, a plug

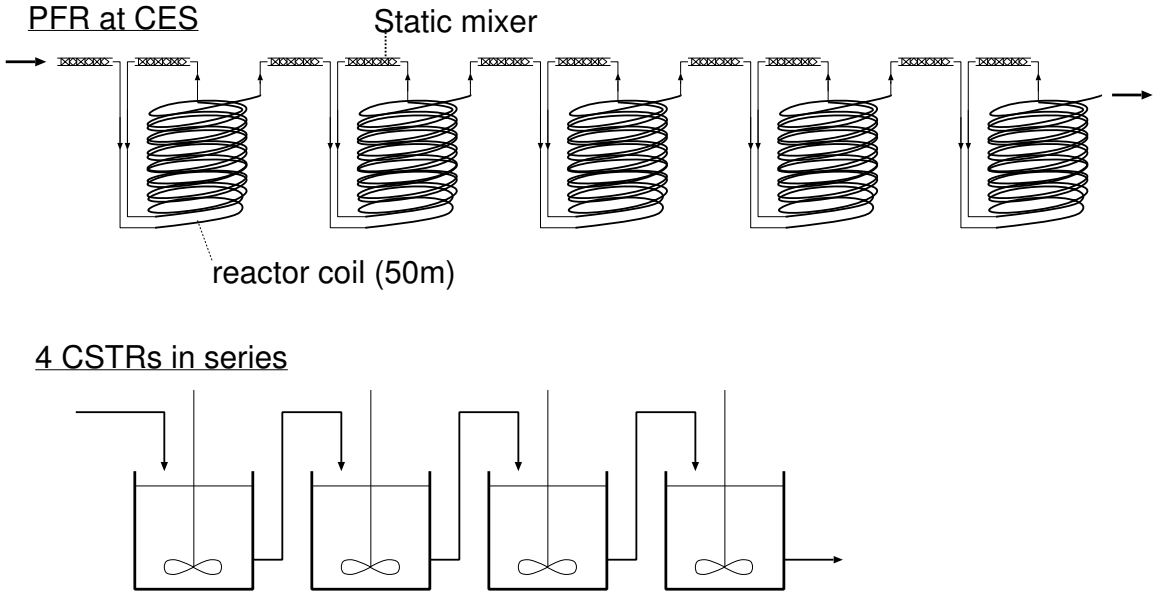

Figure 1.2: Schematic overview of the 'plug flow' reactor used at CES and 4 CSTRs in series.

flow reactor can be used as an alternative for continuous stirred tank reactors and batch reactors. An example of the use of a plug flow reactor in an environmental or 'green' context is the study of Gerdemann and Penner (2003), in which a plug flow reactor is used for carbon sequestration.

A CSTR is the conventional reactor, which is mostly used for continuous processing. At the former company CES B.V., a system of 4 CSTRs in series was compared to a PFR (figure 1.2). Preliminary results indicated that the 'plug flow' reactor was more efficient than four CSTRs in series, when processing gold ore. These results formed the starting point for further research of the PFR and eventually led to this project. This result is not surprising, because in general a CSTR has a lower yield than a PFR. Furthermore, the residence time distribution of a CSTR is far from ideal. Even if we assume that the CSTR is an ideally stirred vessel, the residence time distribution deviates significantly from plug flow, (figure 1.3). Since a narrow residence time distribution is necessary to obtain a narrow particle size distribution, a PFR is preferred over a CSTR.

The original configuration of the PFR (figure 1.2) consisted of 10 coiled tubes (5 pairs) interconnected with static mixers. In the laminar flow regime, a helically coiled tube has an axial dispersion coefficient, which is smaller than in a comparable straight pipe. However, to keep the particles formed in suspension a high axial velocity is necessary. Since the density ratio of the metallic particles and fluid is high ($\rho_p/\rho_l \approx 9$), the particles will be pushed towards the outer wall of the coil due to the centrifugal force. Furthermore, secondary flow in the form of Dean (1927) vortices (see also Schlichting (1968)) is present in a coiled tube. Small particles follow the flow better and may be more uniformly distributed along the coiled tube, because they may be transported back towards the centre of the pipe by the Dean vortices. Large particles, on the other hand, may experience a centrifugal force, which is large compared to the hydrodynamical forces. As a result, large particles may eventually be located near the outer wall of the coiled tube. This difference of location between large and small particles may enhance the difference in size, because large particles may slow down near the wall and as a results have a longer residence time, which gives them more time to grow. For this reason, a straight reactor seems preferable. In this case, the settling of large particles needs to be prevented, which can be achieved by a high axial velocity.

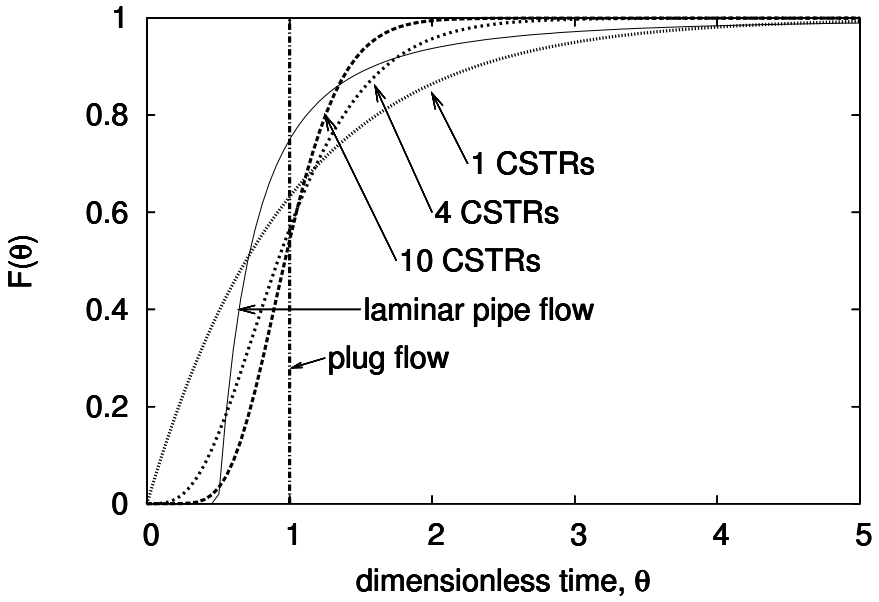

Figure 1.3: Distribution function of the residence time in PFR, CSTR and (laminar) pipe.

Static mixers can be added to the reactor to enhance mixing by helping to keep particles in suspension and to minimise the axial dispersion. However, the static mixers were also a cause for clogging of the PFR at CES. Therefore, the Kenics™ static mixer is the main topic of investigation of this thesis. The focus is on the flow and behaviour of growing particles inside the Kenics™ static mixer.

1.3 The Kenics™ static mixer

Basically, a static mixer is a stationary obstacle placed in a tubular reactor in order to promote mixing and can be seen as the equivalent of the stirrer in a stirred tank reactor. It has the advantage that it has no moving parts and it extracts the energy required for mixing from the flow in the form of an increase in pressure drop. Furthermore, the maintenance cost and operating cost of static mixers are lower than conventional stirrers and a static mixer requires less space. In this dissertation, the Kenics™ static mixer (figure 1.4) is investigated and assessed for its applicability in the novel reduction process. The Kenics™ static mixer is manufactured by one of the companies involved in the project, PRIMIX B.V. It should be noted that PRIMIX used the term PRIMIX™ static mixer rather than Kenics™ static mixer, which is a brand name of Chemineer Inc. In this work, however, the mixer will be referred to as the Kenics™ static mixer, since in literature this term is used for this type of mixer for the passed decades.

In this context, it is mentioned that at the Kramers Laboratorium a special case of the Kenics™ static mixer manufactured by PRIMIX is investigated. This (PRIMIX™) static mixer is welded to the tube by a sophisticated welding technique. Numerical as well as experimental research has confirmed that this novel static mixer has a significantly higher heat transfer than a non-welded mixer, (Van der Kleij (2004); Mudde et al. (2004)). Furthermore, the mixing properties and pressure drop of the PRIMIX static mixing in the laminar regime were investigated with the commercial package FLUENT and experiments were conducted, (Van Pijpen (2002); Mudde et al. (2002)). These results showed good agreement with existing models and data of the static mixer.

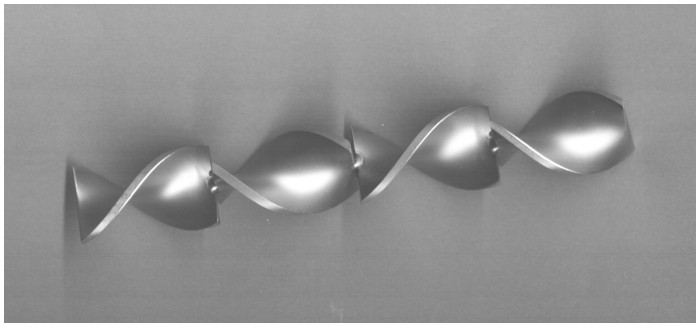

Figure 1.4: A four element Kenics™ static mixer

It has been mentioned previously that the particle size distribution of the copper powder should be narrow to obtain a high quality end product. One way of achieving this is by controlling both the residence time of the copper particles formed in the process and the mixing of the aqueous copper. The residence time and mixing can be controlled by adding static mixers to the tubular reactor. Ideally, the flow in the reactor should approach plug flow. Hobbs and Muzzio (1997b) show that the Kenics™ static mixer approaches plug flow, when the number of mixing elements is increased. This property of the mixer and the fact that one of the companies involved in the project is a manufacturer of this static mixer is the main reason to investigate the suitability of the static mixer for the novel reduction process.

1.4 Numerical techniques

Computational Fluid Dynamics (CFD) is used to study the flow and behaviour of growing particles in the Kenics™ static mixer. First, the commercial CFD package FLUENT was used to calculate the flow in the Kenics™ static mixer. FLUENT is a generic multi-purpose code, which can be applied with success to various applications. At the Kramers Laboratorium, FLUENT has been used routinely in the past decade to investigate single-phase and multi-phase flows, mixing properties and flow of complex media. The flow in a stirred vessel was investigated numerically by Bakker (1992). Venneker (1999) extended this work in order to predict the turbulent flow and gas dispersion in stirred vessels with population balance equations. Furthermore, the flow and collection efficiency of a cyclone were assessed with FLUENT by Hoekstra (2000). Recently, FLUENT was used to predict the heat and mass transfer to a cylinder sheeted by a porous layer, Sobera et al. (2003). The aim of this research was to improve protective clothing, which is used for example by the military to protect against biological or chemical attacks. Kritzinger et al. (2001) used FLUENT to investigate the flow and mixing properties of a novel monolithic stirrer. The monolithic stirrer can be used to replace a conventional stirrer in an existing reactor (called retro-fitting). The flow through the channels of the monolith as well as the flow in the stirred vessels were simulated with FLUENT.

FLUENT has the advantage that it has a user friendly graphical interface and that the complex computational meshes can easily be built with GAMBIT, which is a CAD-like mesh generator. An important drawback of FLUENT is the relatively high memory requirements per computational cell. Furthermore, FLUENT becomes slow when a transient flow is simulated on a dense mesh, which is necessary to simulate the transitional flow in the Kenics™ static mixer. Therefore, an alternative method was explored as well, the Lattice Boltzmann (LB) method. More details on these issues can be found in chapter 4 and in Van Wageningen et al. (2004a).

Kandhai et al. (1999) showed that LB can be used to simulate the flow in a SMRX static mixer and can be an alternative for standard (FV) or (FE) codes. The same code was used in this study to investigate the flow in the Kenics™ static mixer. The advantage that the LB method has over conventional methods, is that it is easy to parallelise and can be used to simulate complex geometries. Furthermore, the LB method is specifically designed and optimised for the standard computer architecture. A drawback of the LB method is the fact that the boundaries at the wall in LB are stair-cased. Therefore, a relatively dense grid is required in order to accurately resolve the flow in complex geometries. More sophisticated methods to deal with the wall are currently being developed, Chen et al. (1998); Bouzidi et al. (2001); Verberg and Ladd (2002); Rohde et al. (2002).

At the Kramers Laboratorium, improved wall methods and local grid refining have been developed by Rohde et al. (2002, 2004). These improvements remove the major drawbacks of the LB method. Furthermore, the LB method has been used to study turbulence and particle dynamics in crystallisers (Ten Cate (2002)) and to investigate shear induced agglomeration (Hollander (2002)). The parallel computations in the Kramers Laboratorium are performed on an in-house Linux cluster, which is currently comprised out of 80 nodes. Each node consists of two dual Pentium processors. Two to four nodes were used for the numerical simulation of the flow in the Kenics™ static mixer with the LB method.

To investigate the behaviour of particles in the static mixer, a particle tracking (PT) code was developed and linked to and embedded into the LB code. The PT code was based upon the equation of Maxey and Riley (1983) to which the Saffman (1965, 1968) lift force was added. Furthermore, a growth model for the particles was added to the PT code. The particle growth was based upon the diffusion of Cu^{2+} to the surface of the particle. The Cu^{2+} concentration was solved with a standard finite volume code, which solves the convection diffusion equation with a sink term. This sink term is directly linked to the particles that are present in the finite volume cell. The chemical parameters of Van der Weijden et al. (2002a) were used as input for the growth model, where it is assumed that the diffusion of Cu^{2+} is the rate limiting factor. With this novel code, the particle size distribution can be estimated under different reactor conditions. Validation is an important aspect of CFD. The CFD results of LB and FLUENT were compared with one an other and the results were compared to experimental data. Two experimental techniques were used: Particle Image Velocimetry (PIV) and Laser Doppler Anemometry (LDA).

1.5 Experimental techniques

Particle Image Velocimetry (PIV) was used to measure the flow in a two-element glass mixer. The mixer was made optically transparent with the Refractive Index Matching (RIM) technique. The PIV setup was based upon the setup that was used by Ten Cate et al. (2002) to measure the flow around a settling sphere and the RIM technique was based upon the work of Muguercia et al. (1993) and Cui and Adrian (1997). A setup was built for gravity driven flow. An accurate temperature control was necessary to maintain the index matching at the measurement section. The PIV/RIM technique allowed accurate measurements of the flow field in a cross-sectional plane of the Kenics™ static mixer. However, the geometry of the glass mixer deviated too much from the standard Kenics™ static mixer. Although, the CFD geometry was modified to closer resemble the glass mixer, only qualitative agreement was obtained. A one to one comparison was not possible due to the small geometrical differences that were still present.

To obtain a quantitative comparison between CFD and experiment a more accurate mixer was desired. Therefore, it was decided to perform point measurements with LDA in a steel Kenics™ static

mixer, which has a far more consistent geometry. With these experiments a quantitative agreement between LB and LDA could be obtained. The work of Harteveld et al. (2004) and Van Maanen (1999) should be mentioned in this context. Van Maanen (1999) performed an extensive research into noise sources of LDA and the retrieval of turbulence properties out of LDA data. Harteveld et al. (2004) used LDA to investigate the complex multiphase flow in a bubble column, for which he developed a novel dual burst wavelet processor, which was partly based upon the work of Van Maanen (1999).

1.6 Scope of this study

The novel reduction process is the starting point of this project, which focuses on the treatment of waste streams containing copper. The goal of the project is to develop an advanced 'multi-phase' plug flow reactor (PFR) for the novel reduction process, where the main focus of investigation was on the suitability of the Kenics™ static mixer for this reactor. To render the process economically feasible, a high quality end-product is necessary. A narrow particle size distribution is potentially more valuable. Therefore, the aim is to develop the right reactor conditions (in both chemical and physical respect), which may lead to high-quality copper particles with a narrow particle size distribution. The key question is whether it is possible to get a close to uniform particle size distribution in Kenics™ static mixer reactor. Therefore, it is investigated whether it's possible to achieve good mixing of species in the reactor as well as to provide plug flow conditions for the copper particles formed in the reactor. The physical parameters such as the flow conditions and the behaviour of growing particles inside the Kenics™ static mixer are studied numerically. The flow field is validated by means of LDA and PIV measurements and the size distribution of particles is studied by using discrete particle simulations of the growing particles. The results and findings are discussed in this dissertation.

In figure 1.5, a schematic overview is given of the project. The chemical parameters obtained from autoclave experiments are used as input parameters for the CFD simulations. In the end, the CFD results together with the autoclave data are used to make an optimum reactor design. The dashed box indicates the main focus of this thesis. The two main issues of this study are the growth of the copper particles and the hydrodynamics inside the Kenics™ static mixer.

1.7 Outline

This thesis is structured as follows. First, in chapter 2, the basic principles of the Kenics™ static mixer are explained and an overview of the numerical model, theory and methods is given. Next, the experimental techniques are described and discussed in chapter 3, which include Particle Image Velocimetry (PIV), Refractive Index Matching (RIM) and Laser Doppler Anemometry (LDA). In chapter 4, the dynamic and time dependent flow in the Kenics™ static mixer is discussed as well as the numerical techniques that are used to calculate the flow field. Both FLUENT and LB are introduced. This chapter has appeared in the AIChE Journal (Van Wageningen et al. (2004a)). In chapter 5, the mixing of particles in the Kenics™ static mixer is studied under different flow conditions. This chapter is an extension of the paper presented at the 11th European Mixing Conference in Bamberg (Van Wageningen et al. (2003)). In chapter 6, the growth of particles and reduction of copper ions is investigated numerically in a four element Kenics™ static mixer reactor. Furthermore, the particle size distributions obtained under different operating conditions are compared and the suitability of the Kenics™ static mixer is assessed. This chapter will appear in Chemical Engineering Science and was presented at the 18th International Symposium on Chemical Reactor Engineering (ISCRE 18) in Chicago (Van Wageningen et al. (2004b)). In chapter 7, a design

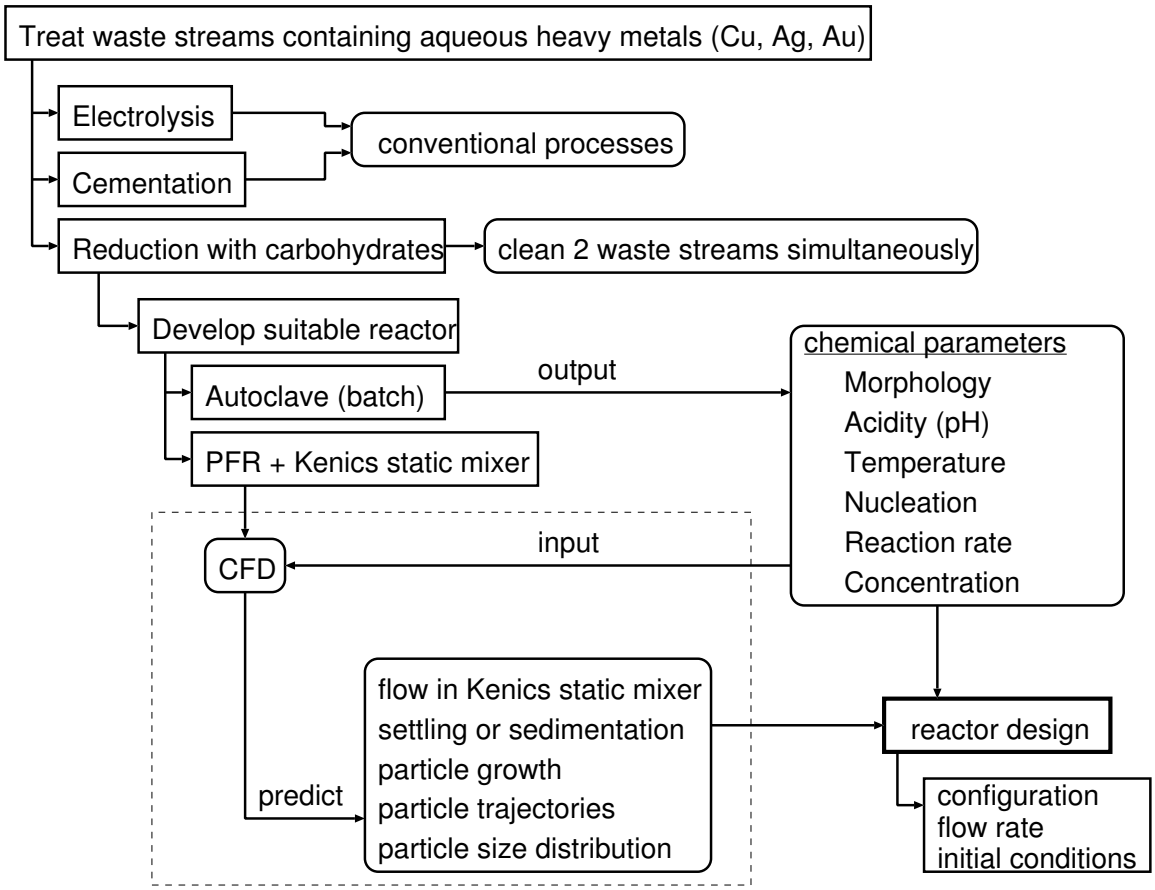

Figure 1.5: Schematic overview of the Senter project.

proposal for a continuous 'plug' flow reactor (in both a vertical and a horizontal setup) and for a batch reactor are given, where the main focus is on the energy efficiency of the process. Parts of this chapter will be submitted to Mineral Engineering. Finally, the conclusions regarding this work are given in chapter 8.

2

Theoretical models and numerical methods

In this chapter, the basic working principles of the Kenics™ static mixer are described and the different flow regimes that occur in the Kenics™ static mixer are evaluated. Furthermore, the physical and chemical aspects that are important for the reduction process and particle growth are presented. Various models are necessary to correctly predict the particle growth and Cu^{2+} reduction by means of Computational Fluid Dynamics (CFD). The simulations are carried out in a tubular reactor, which is equipped with a Kenics™ static mixer. The Kenics™ static mixer is added to promote plug flow conditions and to increase the mixing performance of the reactor. The flow in the mixer is numerically solved with two methods: the finite volume method, which is implemented in the commercial package FLUENT, and the lattice Boltzmann method. The principles of both methods are explained in this chapter. Furthermore, a particle tracking code, which solves the Boussinesq-Basset-Oseen (BBO) equation, has been developed. as well as a finite volume solver, which solves the convection-diffusion equation with sink-term. The numerical models of these codes are discussed and the relevant dimensionless groups are given, which can be used for scaling.

2.1 Static mixers

Mixing is important for the process industry. Conventional chemical reactors make use of mechanical stirrers. They are used to mix or blend different fluids, bring reacting species into contact, suspend discrete particles or bubbles, etc. In general, such a stirred tank reactor consists of a vessel that is usually equipped with baffles on the sides, in which an impeller brings the fluid in motion. The baffles are used to prevent the fluid from rotating along with the impeller. This configuration is used for centuries for mixing. The main innovations lie in the baffle/impeller configuration and impeller type.

An alternative for the stirred tank reactor can be a continuous pipe reactor. To enhance mixing, control the residence time, promote heat exchange and/or suspend particles, static mixers are added to such a reactor. Here, the static mixer can be compared to the impeller in a stirred tank reactor. A static mixer has the advantage that is doesn't have moving parts, which leads to lower maintainance and operating costs. In principle, a static mixer is nothing more than a stationary object, which is placed inside the tube. Ideally, it disturbs the flow in such a manner that desired flow conditions are obtained. The most commonly used static mixers are the SMX and Kenics static mixer, see figure 2.1. The basic principle of these mixers is to split, stretch and recombine the fluid, in order to achieve mixing.

Rauline et al. (2000) compare the Kenics static mixer and SMRX mixer under different circumstances. The SMX static mixer has the advantages that a relatively short length is necessary to obtained full mixing. Rauline et al. (2000) show that the SMX mixer can be about 3.3 time shorter

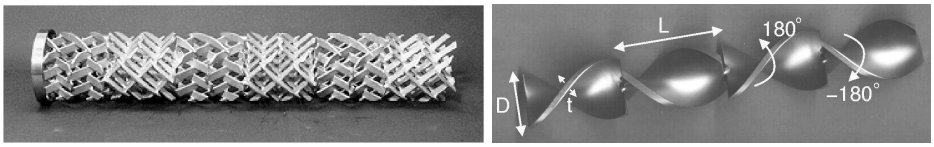

Figure 2.1: Example of the SMX (left) and Kenics (right) static mixer.

then the Kenics static mixer to obtain the same amount of distributive mixing. Under these conditions both mixers have similar pressure drops. If length is an issue the SMX mixer is favourable. The disadvantage of the SMX mixer is that it is more expensive then the Kenics static mixer. Since space is not an issue, the Kenics static mixer seems favourable for this project due to its lower costs. Therefore, this study focusses on the Kenics static mixer. The geometry of the Kenics static mixer consists of a series of mixing elements, each consisting of a short helix of length L, which is equal to 1.5 times the tube diameter D (i.e. the aspect ratio L/D=1.5). The helices are rotated clockwise and counterclockwise at an angle of 180° and are placed at an angle of 90° with respect to each other.

2.1.1 Mixing mechanism and hydrodynamics of Kenics static mixer

The mixing mechanism of the Kenics static mixer is different at low and high Reynolds numbers, where the Reynolds number is based upon the tube diameter. At a low Reynolds number the flow is alligned with the mixing elements, while at a high Reynolds number vortical structures start to play a role in the mixing process. These vortical structures cause an early transistion to unsteady (time dependent) flow, which makes the flow in the Kenics static mixer interesting from a hydrodynamical point of view.

Low Reynolds mixing

The Kenics static mixer was orginally designed to operate at a low Reynolds number. In this regime, mixing takes place via cutting, stretching and recombining of the flow. First, the mixing element cuts the flow into two pieces. Second, the pieces are stretched along the mixing element and at the intersection with next element, they are recombined and cut again, after which the process repeats itself. The mixing process is illustrated in figure 2.2.

In the low Reynolds range, the flow is alligned with the mixing element and no vortical structures

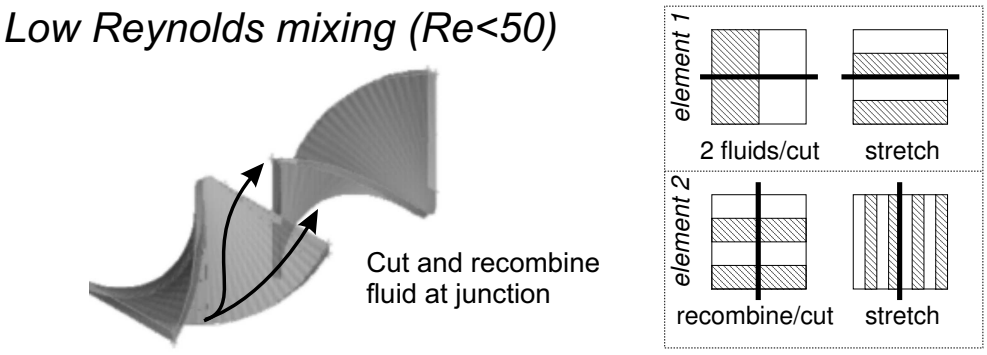

Figure 2.2: Working principle of Kenics static mixer at low Reynolds numbers

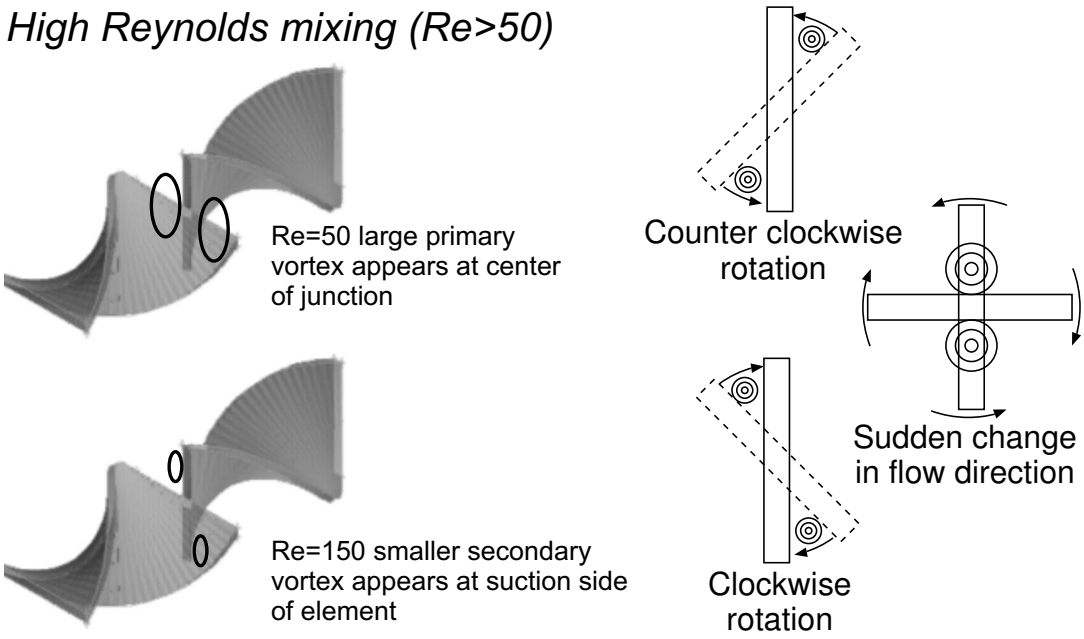

Figure 2.3: Working principle of Kenics static mixer at a high Reynold number

are present in the flow. The cutting of the flow takes place because the mixing elements are at an angle of 90° and the fluid is stretched because of the rotation of the mixing elements. This way even the most viscous flows can be mixed.

High Reynolds mixing

At higher Reynolds numbers the static mixer is comparable to a rotating plate that suddenly changes its rotation direction. At the suction side of the mixing element vortices appear, which are similar to vortices that appear when a plate is rotated. Furthermore, due to the sudden change in flow direction at the junction of two mixing elements, a large vortical structure appears at the center of the mixing element. These vortical structures can contribute to the mixing. Their location is illustrated in figure 2.3.

If the Reynolds number is increased even further, the flow becomes unsteady. The vortices start to oscillate and eventually, move and merge together. This oscillatory behaviour of the vortices contributes to the mixing process. More details on the mixing characteristics of the Kenics static mixer can be found in Van Wageningen et al. (2003) and in chapter 5 of this thesis. In these studies, the mixing efficiency and residence time distribution are evaluated under different flow conditions by means of tracer particles.

2.2 Models needed for simulation of reduction and growth process

To predict the correct particle size distribution in the Kenics™ static mixer, a good understanding of the growth mechanism and transport of the particles in the flow is important. Ideally, all particles grow in a similar manner. If all particles have the same initial size, growth rate and residence time, it is obvious that their final sizes will be equal. The question is whether we can get as close as

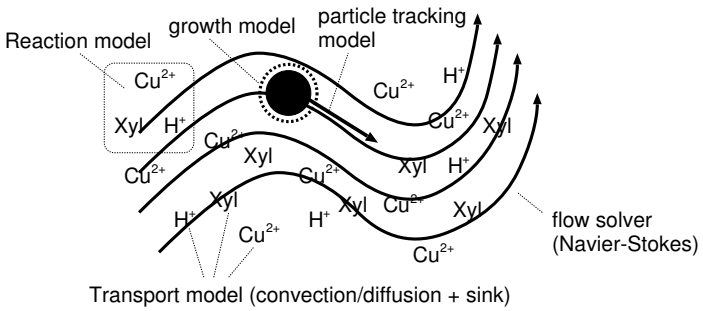

Figure 2.4: Schematic overview of the models needed to describe the reduction process.

possible to this ideal situation. For this purpose the Kenics™ static mixer is added to the tubular reactor. CFD is used as a tool to simulate the transport and growth of the particles inside this mixer.

In order to use CFD, various aspects need to be modelled. Figure 2.4 provides an impression of the different models that are needed to describe the process, which include:

- The chemical reaction, in which the copper ions (Cu^{2+}) and carbohydrates (xylose) are involved. Its rate is determined by the acidity, i.e.the H^+ concentration, and temperature, which are normally kept constant during the process.
- The transport of the species (xylose, Cu^{2+}, H^+) involved in the reaction
- The growth and transport of the particles
- The flow inside the Kenics™ static mixer reactor

Some assumptions are made, which simplify the problem. A uniform temperature over the reactor is assumed. The Kenics™ static mixer promotes heat exchange and in practise, the reactor is kept at constant temperature. Both aspects support this assumption. In reality, the acidity increases during the process. However, in practise the acidity is controlled by addition of NaOH. Therefore, a constant acidity is assumed. Furthermore, an excess doses of carbohydrates (xylose) is assumed. In that case the influence of the carbohydrate concentration is minimal.

Two approaches are used to solve this problem numerically: a three step approach and a simultaneous approach. In the three step approach the different models are simulated sequential. First, the 3-dimensional laminar-velocity field and pressure are computed by solving the full Navier-Stokes equations. The velocity field is used as input for the second step, which consists of the calculation of the transport of the chemical species involved in the process and their reactions. The obtained Cu^{2+} concentration is used as input for the third step, which consists of the calculation of the trajectory and growth of the individual particles. This method will be explored in more detail in section 2.4 and is also described in Van Wageningen et al. (2002). The drawback of this method is that it is only applicable for steady state problems and that the chemical reaction does not take place at the surface of the particles. Here, the chemical reaction is modelled as a first order reaction, which only depends on the local species concentrations and not on the presence of a particle. Therefore, the three-step approach is only valid, when the particles are uniformly distributed over the reactor.

Since the reaction takes place at the surface of the particles, an improvement to the three-step method would be the inclusion of the location and surface of the particles into the reaction model. An other improvement is to make the flow solver time dependent. These improvement are implemented in the simultaneous approach. In this case the flow, the particle trajectories, Cu^{2+} concentration and

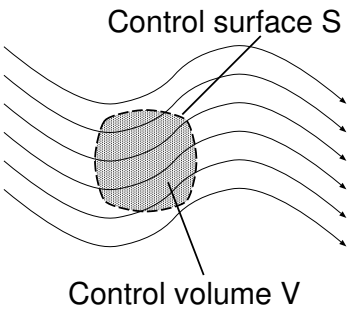

Figure 2.5: Finite control volume fixed in space (conservative form).

particle growth are solved simultaneously. Furthermore, the particle growth is directly linked to the decrease of the Cu^{2+} concentration. This method will be explored in more detail in section 2.5 and is also described in chapter 6, which is based upon Van Wageningen et al. (2004b).

2.3 Modelling of the flow

Traditionally, the flow of a fluid is modelled with the continuity and Navier-Stokes equations, which are based on the conservation mass and Newton's second law. In the finite volume approach, a finite control volume, which is fixed in space, is considered (figure 2.5). When mass is conserved, the change of mass in time is equal to the amount of mass that flows in the control volume through the surface S. This leads to the continuity equation in integral and conservative form:

$$\frac{\partial}{\partial t}\int\int\int_V \rho \mathrm{d}V + \int\int_S \rho\vec{u}\cdot\mathrm{d}\vec{S} = 0 \tag{2.1}$$

where ρ is the density of the fluid, $\vec{u}$ is the local velocity vector, V and S are the volume and surface, respectively. With the Gauss-divergence theorem, the continuity equation in conservative form can be derived from equation 2.1:

$$\frac{\partial \rho}{\partial t} + \nabla\cdot(\rho\vec{u}) = 0 \tag{2.2}$$

and for incompressible flow (constant density) this equation is reduced to

$$\nabla\cdot\vec{u} = 0. \tag{2.3}$$

The Navier-Stokes equation based upon a fixed control volume and Newton's seconds law can be written as:

$$\frac{\partial}{\partial t}\int\int\int_V \rho\vec{u}\mathrm{d}V = -\int\int_S \rho\vec{u}\vec{u}\cdot\mathrm{d}\vec{S} + \int\int\int_V \vec{F}_{\mathrm{body}}\mathrm{d}V + \int\int_S \vec{\vec{\sigma}}\cdot\mathrm{d}\vec{S} \tag{2.4}$$

where F_{body} are the body forces (e.g. gravity) and $\vec{\vec{\sigma}}$ is the stress tensor, which yields:

$$\vec{\vec{\sigma}} = -\begin{pmatrix} 1 & 0 & 0 \\ 0 & 1 & 0 \\ 0 & 0 & 1 \end{pmatrix} p + \begin{pmatrix} \tau_{xx} & \tau_{yx} & \tau_{zx} \\ \tau_{xy} & \tau_{yy} & \tau_{zy} \\ \tau_{xz} & \tau_{yz} & \tau_{zz} \end{pmatrix} \tag{2.5}$$

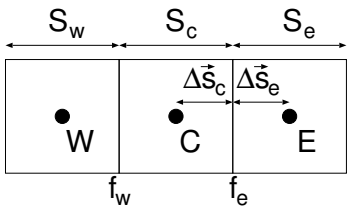

Figure 2.6: Interpolation of cell centred value towards faces.

where p is the pressure and τ is the shear stress. For a Newtonian flow the shear stress tensor is equal to

$$\vec{\vec{\tau}} = \begin{pmatrix} \lambda\nabla\cdot\vec{u} + 2\mu\frac{\partial u_x}{\partial x} & \mu\left(\frac{\partial u_y}{\partial x} + \frac{\partial u_x}{\partial y}\right) & \mu\left(\frac{\partial u_z}{\partial x} + \frac{\partial u_x}{\partial z}\right) \\ \mu\left(\frac{\partial u_y}{\partial x} + \frac{\partial u_x}{\partial y}\right) & \lambda\nabla\cdot\vec{u} + 2\mu\frac{\partial u_y}{\partial y} & \mu\left(\frac{\partial u_z}{\partial y} + \frac{\partial u_y}{\partial z}\right) \\ \mu\left(\frac{\partial u_z}{\partial x} + \frac{\partial u_x}{\partial z}\right) & \mu\left(\frac{\partial u_z}{\partial y} + \frac{\partial u_y}{\partial z}\right) & \lambda\nabla\cdot\vec{u} + 2\mu\frac{\partial u_z}{\partial z} \end{pmatrix} \tag{2.6}$$

where μ is the dynamic viscosity and λ is the bulk viscosity coefficient, which is frequently set to $\lambda = \frac{2}{3}\mu$. It should be noted that for incompressible flow ($\nabla\cdot\vec{u} = 0$) the terms with λ disappear. Again with the Gauss-divergence theorem, equation 2.4 can be re-written as

$$\frac{\partial}{\partial t}\rho\vec{u} + \nabla\cdot(\rho\vec{u}\vec{u}) = \vec{F}_{\text{body}} + \nabla\cdot\vec{\vec{\sigma}}, \tag{2.7}$$

which is the Navier-Stokes equation.

2.3.1 Discretization - Finite Volume

If the flow is Newtonian and incompressible the equations 2.3 and 2.7 form a closed system and can be solved numerically. In this work, only Newtonian and incompressible fluids are considered and the commercial package FLUENT is used to solve the flow. FLUENT is a generic multi-purpose code for modelling fluid flow and heat transfer in complex geometries. It numerically solves the Navier-Stokes equations on unstructured meshes and uses a control-volume-based technique, which is also referred to as finite-volume. The governing equations (2.3 and 2.7) are integrated on the individual control volumes. This way an algebraic set of equations is constructed. The equations are linearised to numerically solve the unknowns (velocities and pressure). Furthermore, the domain is divided into discrete control volumes using a computational grid, which is created with the grid-generator Gambit and consists of hex-wedged cells, twisted along the helical elements of the mixer.

In FLUENT the pressure and velocity are both stored at the cell centre (co-located). Therefore, interpolation of these value towards the faces of the cell is necessary. The following schemes for the velocity interpolation can be selected in FLUENT (Fluent Inc. (2003b)):

- First order upwind interpolation: the value at the cell centre ϕ_C, is used at the downstream faces of the cell.
- Second order upwind interpolation: the value at the (upwind) cell centre and its gradient are used to calculate value at the face f, $\phi_f = \phi_C + \nabla\phi_C\cdot\Delta\vec{s}_C$, where $\Delta\vec{s}_C$ is the distance vector between the face centre and cell centre (figure 2.6). It should be noted that ϕ_C are the values of the upstream cell with respect to the face.

- Central difference scheme: the values and gradients from the two cells that share the same face are used to obtain the face value. The east face value $\phi_{f,e}$ of cell C becomes with CDS: $\phi_{f,e} = \frac{1}{2}\left(\phi_C + \nabla\phi_C \cdot \Delta\vec{s}_C + \phi_E + \nabla\phi_E \cdot \Delta\vec{s}_E\right)$ (figure 2.6).
- Power-law scheme: it uses the analytical solution of the one-dimensional convection/diffusion equation to interpolate values towards the cell face.
- QUICK scheme: a combination of CDS and upwind is used for the interpolation,

$$\phi_{f,e} = \theta\left[\frac{S_w}{S_c + S_w}\phi_P + \frac{S_c}{S_c + S_w}\phi_E\right] + (1-\theta)\left[\frac{S_e + 2S_c}{S_e + S_c}\phi_P - \frac{S_c}{S_e + S_c}\phi_W\right] \quad (2.8)$$

  where the distances S are illustrated in figure 2.6. It should be noted that in FLUENT the value of θ is solution dependent.

In this work the central difference scheme of FLUENT was selected, since this scheme is most transparent and it is second order accurate.

For the interpolation of the pressure the following schemes are available in FLUENT:

- The linear scheme, which computes the face pressure as the average of the pressure values in the adjacent cells.
- The second order pressure scheme, which reconstructs the face pressure similar to the second order accurate convection schemes.
- The PRESTO! (PREssure STaggering Option) scheme, which uses the discrete continuity balance for a staggered control volume about the face to compute the pressure at the face.

The second order pressure scheme was selected in this work.

In the segregated solver of FLUENT, which is used in this study, the momentum and continuity equations are solved sequentially. In this sequential procedure, the continuity equation is used as an equation for pressure. The pressure does not appear explicitly in the continuity equation for incompressible flows. In FLUENT three schemes can be used to introduce the pressure into the continuity equation: the SIMPLE (Semi-Implicit Method for Pressure-Linked Equations), SIMPLEC (SIMPLE-Consistent) and PISO (Pressure-Implicit with Splitting of Operators) scheme. The SIMPLE and SIMPLEC scheme both correct the predicted pressure, by evaluating the mass flow rate through the faces, where the sum of the mass-flow rate through all faces has to be zero to satisfy the continuity equation. The PISO scheme applies, some corrections to the SIMPLE scheme, such as skewness correction. The equations were interpolated until convergence was reached within one time-step (10^{-3} for continuity, 10^{-4} for velocities).

It should be noted that FLUENT is a generic multi-purpose code, which is designed for steady-state flow problems. FLUENT can also solve transient problems, but solves them as a sequence of steady state problems, which makes the code slow compared to a non steady CFD solver. Therefore, for the transient simulations an alternative flow solver was used.

2.3.2 Lattice Boltzmann method

Conventional flow modelling is based on macroscopic continuum equations (e.g. Navier-Stokes as is described above). The macroscopic behaviour of the flow is the result of the interaction of small individual molecules. In theory, it is possible to obtain the macroscopic behaviour of the flow via simulation of the interaction of all individual molecules, but due to the large number of molecules

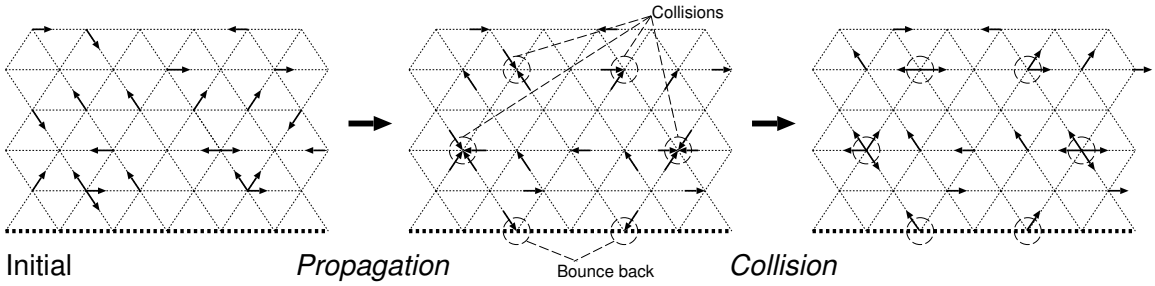

Figure 2.7: Propagation and collision phase of the 2D FHP-model.

in fluid flows this approach is impossible in reality. It is, however, possible to simulate fictitious particles, whose behaviour on a macroscopic level mimics the Navier-Stokes equation. The lattice gas method follows this approach.

In this method, fictitious particles reside on the nodes of a regular lattice, which is fixed in space. The nodes are interconnected and the particles can only move along the lattice links. First, the particles are propagated over the lattice according to their (discrete) velocity direction. In one discrete time step, the particles move towards the next node. This phase is called the propagation phase. Second, the particles, which have arrived at the next node, interact with one another and change their velocity direction accordingly to certain collision rules. This phase is called the collision phase. The propagation and collision phase of the 2D FHP-model are illustrated in figure 2.7, where FHP are the first letter of the names from the developers of the model, Frisch, Hasslacher and Pomeau. They were the first, who obtained the correct Navier-Stokes equation from the lattice gas automata on a hexagonal lattice (Frisch et al. (1986)).

In the collision phase, mass and moment are conserved. Most collisions are trivial, which means that there is only one possibility to conserve mass and momentum and there is no change in direction of the particles. Some head on collisions can have multiple outcomes and are called non-trivial. In this case the particles change their direction. Figure 2.8 shows examples of some trivial collision and the non-trivial collisions of the 2D FHP model. With these simple rules the Navier-Stokes equation is obtained on a macro-scale. The particles and particle interactions on the nodes act as cellular automata, which on a macro-scale mimic the Navier-Stokes equation.

In the lattice gas method the particle occupation is described by a set of Boolean variables $n_\mathrm{i}(\vec{r},t)$, where the index i indicates the discrete velocity directions of the particles and $\vec{r}$ indicates the position of the node. The time evolution equation of the lattice gas is equal to:

$$n_\mathrm{i}(\vec{r}+\vec{c}_\mathrm{i},t+1) = n_\mathrm{i}(\vec{r},t) + \Omega_\mathrm{i}\left(n_\mathrm{i}(\vec{r},t)\right) \qquad (\mathrm{i}=0,1,\ldots,M) \tag{2.9}$$

where $\vec{c}_\mathrm{i}$ are the local particle velocities and Ω_i are the collision operators. Only one particle is allowed in each velocity direction at a certain node, which is similar to the Pauli exclusion principle and leads to a Fermi-Dirac local equilibrium distribution (Frisch et al. (1987)).

In the lattice gas method the particle occupation is described by a set of Boolean variables. In the lattice Boltzmann (LB) method these set of variables are replaced by (real) particle distribution functions, which are mesoscopic variables. The advantage of the LB method is that statistical noise is eliminated, while the locality of the kinetic approach is retained. An extensive review of the Lattice Boltzmann method is given by Chen and Doolen (1998).

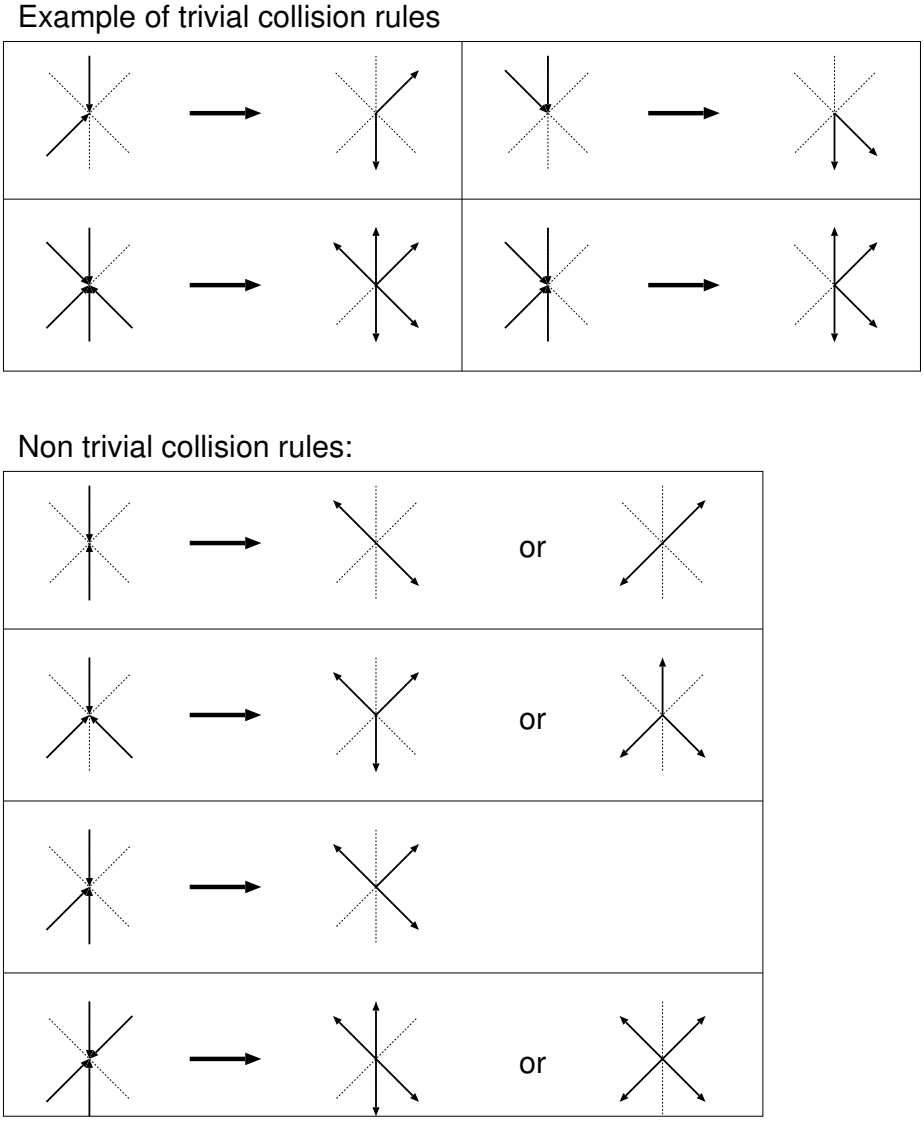

Figure 2.8: Collision rules of the 2D FHP-model.

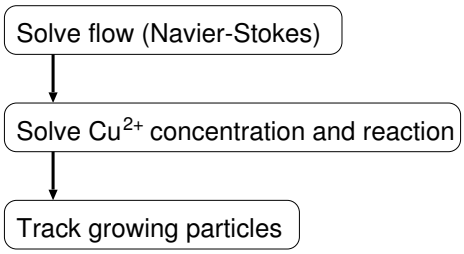

Figure 2.9: Three step method: sequential simulation.

In the study presented here, the BGK (Bhatnagar-Gross-Krook) collision operator is used. The BGK collision operator makes use of a single time relaxation. The BGK evolution equation is as follows:

$$f_{\mathrm{i}}(\vec{r}+\vec{c}_{\mathrm{i}},t+1) = f_{\mathrm{i}}(\vec{r},t) + \frac{1}{\tau}(f_{\mathrm{i}}^{\mathrm{eq}}(\vec{r},t) - f_{\mathrm{i}}(\vec{r},t)), \tag{2.10}$$

where $f_{\mathrm{i}}(\vec{r},t)$ denotes the particle density which resides on lattice point $\vec{r}$ at time-step t, and is moving along link i with local particle velocity $\vec{c}_{\mathrm{i}}$, τ is the so-called BGK relaxation parameter. The BGK evolution equation 2.10 is similar to the lattice gas (LG) evolution equation 2.9, where the term $\frac{1}{\tau}(f_{\mathrm{i}}^{\mathrm{eq}}(\vec{r},t) - f_{\mathrm{i}}(\vec{r},t))$ is the BGK collision operator.

A detailed comparison between FLUENT and the Lattice Boltzmann method is made in chapter 4. Furthermore, in that chapter a comparison of LB with experiments is made.

2.4 Three step method: a preliminary estimation

The three-step-method is only used for steady (Re<200) flow in the Kenics™ static mixer. In these simulations it is assumed that the particle distribution is uniform and that gravity plays a minor role, which is only the case when the particles are extremely small (<5 μm). Figure 2.9 shows the three sequential steps, which were used to predict the particle size distribution in Van Wageningen et al. (2002). In the first step, the 3-dimensional laminar-velocity field and pressure is computed by solving the full Navier-Stokes equations. The outcome is used as input for the second step, which consists of the calculation of the transport of the chemical species and their chemical reactions. After the Cu^{2+} concentration is solved, discrete particles are tracked through the concentration field.

Calculation of Cu^{2+} concentration

Van der Weijden et al. (2002a) describe in detail the hydrolysis and degradation reactions of several carbohydrates and their influence on the reduction of Cu^{2+}. For xylose, the reaction can be described by the following equation:

$$\mathrm{Cu}^{2+} + \mathrm{C_5H_{10}O_5} + \mathrm{H_2O} \rightarrow \mathrm{Cu(s)} + \mathrm{C_5H_{10}O_6} + 2\mathrm{H}^{+} \tag{2.11}$$

It is assumed that there is an excess doses of xylose so the xylose concentration does not influence the reaction rate. The reduction process stops, when the pH drops below 1.3. A low pH forms a barrier for further carbohydrate oxidation. Since the acidity increases during the process, pH control is necessary. In this study, it is assumed that the pH remains constant during the process, which can be achieved by a continuous injection with NaOH.

The Cu^{2+} concentration is solved as a passive scalar with a sink term and was incorporated into FLUENT using a user defined function (UDF). For the scalar interpolation the second-order upwind scheme was selected and the following mass balance was used for the Cu^{2+} concentration:

$$\frac{\partial}{\partial x_\mathrm{i}}\Big(u_\mathrm{i}\,[\mathrm{Cu}^{2+}]\Big) = \frac{\partial}{\partial x_\mathrm{i}}\Big(\,\mathbb{D}\,\frac{\partial}{\partial x_\mathrm{i}}\,[\mathrm{Cu}^{2+}]\Big) - k_\mathrm{r}\,[\mathrm{Cu}^{2+}] \tag{2.12}$$

where $\mathbb{D}$ is the diffusion coefficient of Cu^{2+} and k_r is the reaction rate constant. The surface of the particles did not influence the reaction rate constant, because the surface of the titanium wall was dominant over the surface of the particles. The rate constant proved to be independent of Cu^{2+} concentration and it depended solely on the pH.

It was assumed that all the reduced Cu^{2+} ends up as metallic copper particles. The Cu(s) formed on one particle becomes: $\frac{k_\mathrm{r}[\mathrm{Cu}^{2+}]}{c_\mathrm{p}}$, where c_p is the local particle concentration. The growth is based upon the local Cu^{2+} and particle concentration in the reactor and can be modelled as follows:

$$\frac{\mathrm{d}V_\mathrm{p}}{\mathrm{d}t} = \frac{k_\mathrm{r}[\mathrm{Cu}^{2+}]}{c_\mathrm{p}\,\rho_\mathrm{p}} \tag{2.13}$$

where V_p and ρ_p are the volume and the density of a particle, respectively.

An important drawback of this method, is the fact that the surface is not included in the reaction model. The reaction depends only on the Cu^{2+} concentration. Inclusion of the surface into the reaction would make the model more realistic. One way to achieve this is via population balance modelling. In appendix A the applicability of the population balance for different growth models is discussed.

With the population balance method a more realistic model for the chemical reaction can be obtained, because the surface of the particles can be modelled. Furthermore, the population balance method has the advantage that the statistical properties of the particles can be solved as passive scalars with a source term, which makes the calculation less computational demanding than a simultaneous simulation of discrete particles and the Cu^{2+} concentration. A drawback of this method is that the exact location of the particles is not taken into account. The particles exist in the form of concentrations of their statistical properties and behave as flow followers. Moreover, gravity is not included into the model. Since the density ratio between the particles and fluid is rather large ($\frac{\rho_p}{\rho}$=9), settling of particles has a big influence on the location of the particles, which ultimately determines the location and rate of the reaction. Because of these limitations, the population balance method (like the first order reaction model) is only suitable for small (tracer-like) particles.

2.4.1 Discrete Particle Models

After the Cu^{2+} concentration field is solved, particles that grow during their residence in the reactor are tracked. It is assumed that the particles behave more or less as flow followers. Gravity is neglected and only drag is considered, which makes this approach only valid for very small particles. For the three-step-approach, FLUENT was used to calculate the velocity field, concentrations and to track the growing particles. The following force balance (without gravity) was used for the small particles:

$$m_\mathrm{p}\frac{\mathrm{d}v_\mathrm{p}}{\mathrm{d}t} = F_\mathrm{D} \tag{2.14}$$

where m_p and v_p are the mass and the velocity of the particle, respectively and F_D is the drag force on a spherical particle. The drag force is given by:

$$F_\mathrm{D} = C_\mathrm{D}\cdot\frac{\pi}{4}\,d_\mathrm{p}^2\cdot\frac{1}{2}\,\rho\,(u-v_\mathrm{p})^2 \tag{2.15}$$

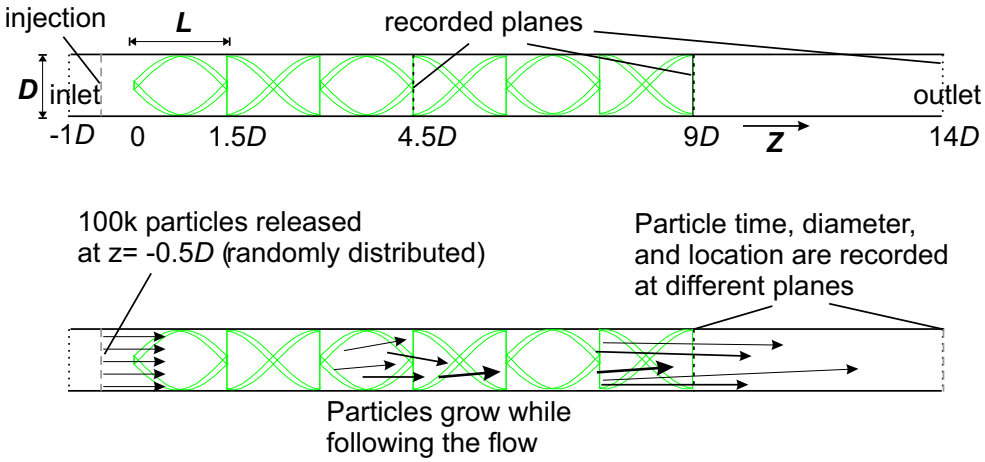

Figure 2.10: Numerical setup and particle record planes.

where ρ is the density of the liquid, C_{D} the drag coefficient and $(u - v_{\mathrm{p}})$ the slip velocity. The drag coefficient is modelled as follows:

$$C_{\mathrm{D}} = a_1 + \frac{a_2}{\mathrm{Re_p}} + \frac{a_3}{\mathrm{Re_p^2}} \tag{2.16}$$

where $\mathrm{Re_p}$ is the Reynolds number of the particle (based upon the particle diameter and slip velocity) and the a's are constants that apply for smooth spherical particles over a range of $\mathrm{Re_p}$ given by Morsi and Alexander Morsi and Alexander (1972).

Integration in time of equation 2.14 yields the velocity of the particle along its trajectory, which is predicted by $\frac{\mathrm{d}\,x}{\mathrm{d}\,t} = v_{\mathrm{p}}$. In FLUENT (Fluent Inc. (2003b)) a length scale controls the size of the integration time-step. The integration time-step Δt is computed by FLUENT based on a specified length scale l, and the velocity of the particle v_{p} and of the liquid phase u:

$$\Delta t = \frac{l}{v_{\mathrm{p}} + u} \tag{2.17}$$

If the first order reaction model is applied the growth is based on equation 2.13. The growth equation is implemented in FLUENT via a user defined function that modifies the diameter of the particle based upon the local Cu^{2+} concentration.

The size of the particles is determined by the Cu^{2+} concentration the particles encounter and by their residence time inside the reactor. The properties of the particles are recorded at certain planes inside the reactor. The following particles variables are recorded when passing the different recording planes: residence time, diameter and location. Figure 2.10 shows where the different planes are located (at $x = 4.5D$ which is half way the mixer, at $x = 9D$ which is at the exit of the mixer and at $x = 14D$ which is the outlet plane). All the particles that have passed the recording planes are used to determine the particle size distribution.

Figure 2.10 also shows the numerical setup, which consists of a 6 element Kenics™ static mixer with an L/D ratio of 1.5. A developed laminar velocity profile is used for the inlet boundary condition (at $x = -D$). The mixer starts at 1 diameter from the inlet ($x = 0$) and ends at 10 diameters from the inlet ($x = 9D$). The outlet is located at 4 diameters from the exit of the mixer ($x = 14D$). An outflow boundary is chosen, which sets the derivatives in the flow direction of all flow variables

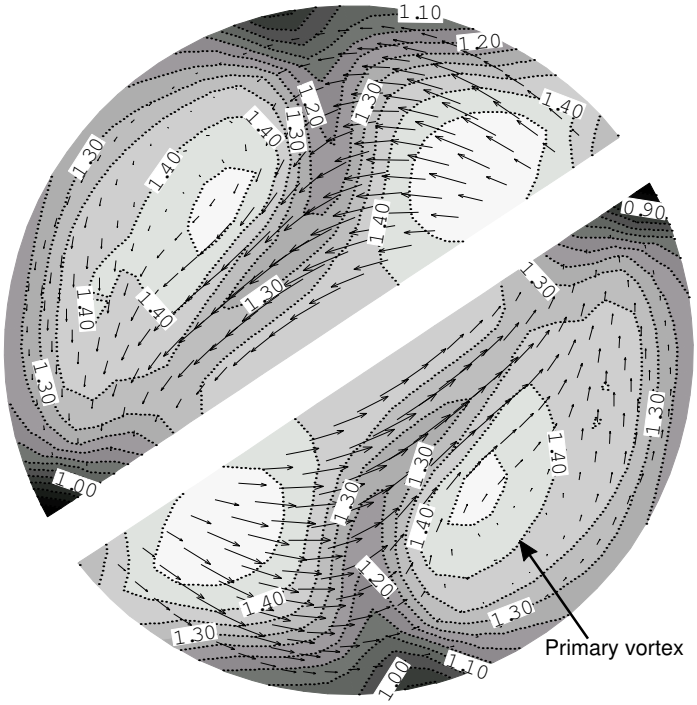

Figure 2.11: Re=50 (5$^{\text{th}}$ element), the large vortex ends at $0.3D$ from a cross-section, contours show the Cu^{2+} concentration in g/L.

(except pressure) to zero at the outlet face. No-slip boundaries are applied at the walls. The Cu^{2+} concentration is constant at the inflow boundary $(0.002*\rho)$[g/L] and the precipitation process is described as a source term in equation 2.12. Discrete particles that grow are tracked through the Kenics™ static mixer reactor and their statistical properties were recorded at the outlet. In the next section, some of the results are shown.

2.4.2 Preliminary results

In Van Wageningen et al. (2002), the three step method was used and the velocity field and corresponding Cu^{2+} concentrations at some cross-sections in the mixer were evaluated at different Reynolds numbers. Furthermore, the particle size distributions at the outlet were given for the corresponding Reynolds numbers and they were linked to the prevailing flow conditions inside the mixer. This section briefly discusses the results for Re=50 and Re=200.

Flow structures and Cu^{2+} concentration

Two large (primary) vortices form directly downstream the junction of two mixing elements, because of the sudden change (180°) in twist direction. The primary vortex is found at all the simulated Reynolds numbers (50,100 and 200). Furthermore, the flow structures that form near the junction of two elements are similar for all the simulated Reynolds numbers (50, 100, 200), but the Cu^{2+} concentration differs for each Reynolds number. At Re=50, the Cu^{2+} concentration is far from uniform (figure 2.11). While, at Reynolds 200, a far more uniform Cu^{2+} concentrations is observed (figure 2.12).

The more uniform Cu^{2+} concentrations at higher Reynolds numbers can be explained by the appearance of a secondary vortex at the suction side of an element and the fact that the primary vortical

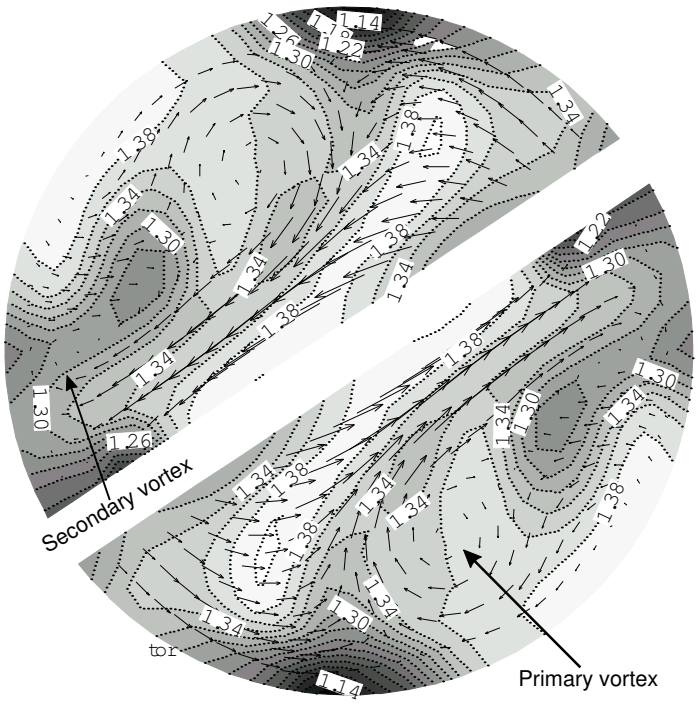

Figure 2.12: Re=200 (5th element), two vortices at $0.3D$ from a cross-section, contours show the Cu^{2+} concentration in g/L.

structure is longer. The interplay of two vortices enhances the mixing of the flow. The secondary vortex does not appear at Re=50 and Re=100, which means that vortex mixing does not occur under these conditions. At Re=50 the primary vortex has a short length in the axial direction and the laminar velocity profile develops fast, which leads to differences in the residence time. Near the wall the residence time is long, which results in a longer reaction time and as a consequence the Cu^{2+} concentration is lower near the wall.

The Poiseuille profile, which is dominant at low Reynolds numbers, causes variations in the Cu^{2+} concentration. At the junction of two mixing elements the Poiseuille profile splits in two parts and mixing takes place at a large scale due to the splitting. The primary vortex breaks the Poiseuille profile, but large differences in the axial velocity are still present, which leads to a non-uniform Cu^{2+} concentration. At Re=200, the Poiseuille profile is replaced by the interplay of the two vortices, which leads to a more uniform axial velocity distribution. Due to the low axial velocity inside the secondary vortex, the Cu^{2+} concentration drops in that region. However, the most uniform concentration was still found at Re=200.

Particle size distribution

100k particles with an initial size of 0.05 μm were tracked and the particles that escaped at the outlet were used for statistics. The figure 2.13 shows the recorded particle size distributions at the outlet. An almost Gaussian distribution is found at Re=200. At Re=50, the particle size distribution deviates from the Gaussian distribution.

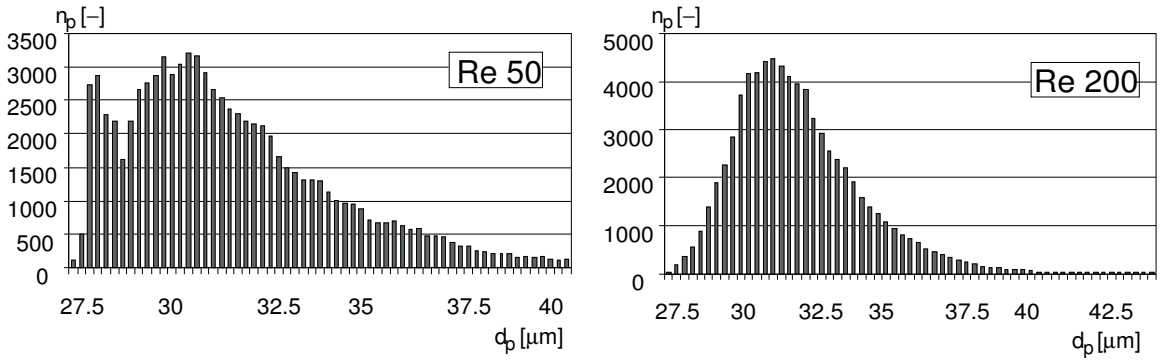

Figure 2.13: the particle size distributions of Re=50 (left) and Re=200 (right) at the outlet of the reactor (D=0.05 cm).

Concluding remarks

Industry seeks a uniform distribution for the end product, which is the copper particles formed. In this study the Kenics™ static mixer was chosen as a reactor environment. The 'best' distribution was found at Re=200. The results show that the hydrodynamics influence the end product and that flow structures can have a large effect on the concentration and particle size distribution even under laminar conditions.

One should notice that the chemical process is approximated with a simple first order reaction. This hypothesis holds only under certain conditions. Furthermore, gravity was neglected and a simple force balance was used to track the particles. In reality these assumption do not hold. The particles become quite large and have the tendency to settle down at the bottom of the reactor. Therefore, gravity should be included into the force balance. Furthermore, the surface of the particles, which is the source of the reaction should be included into the reaction equation, because a non uniform distribution of the particles over the reactor, makes the first order reaction model, which does not include the surface and position of the particles, invalid. These shortcomings have been overcome in the simultaneous approach, which is discussed in the next section.

2.5 Simultaneous simulation

Because of the limitations that the three-step-method has, a different method is explored. In this novel method, the velocity field, particles and Cu^{2+} concentration are updated within one time-step. Van Wageningen et al. (2004a) show that the flow becomes unsteady, when Re>300. Therefore, the velocity field is solved with a lattice Boltzmann (LB) code, which is a parallel transient solver developed by Drona Kandhai. FLUENT also has a transient option, but the calculation of transient flows is very slow, because FLUENT is a steady state solver, which solves transient flows as a sequence of steady state problems. Furthermore, the coupling between the particle growth and sink term of the Cu^{2+} concentration lead to instabilities in FLUENT. Since the source code of FLUENT was not available, it was not possible to solve these problems. Therefore, a particle tracking code was developed based upon the equation of Maxey and Riley (1983) and included into the LB code. To the particle tracking code, a finite volume (FV) code was added, which solves the convection/diffusion equation of the Cu^{2+} concentration. The sink term of this equation was linked to the particle growth.

Figure 2.14 shows the scheme that was used for the simultaneous simulations. First, the particles,

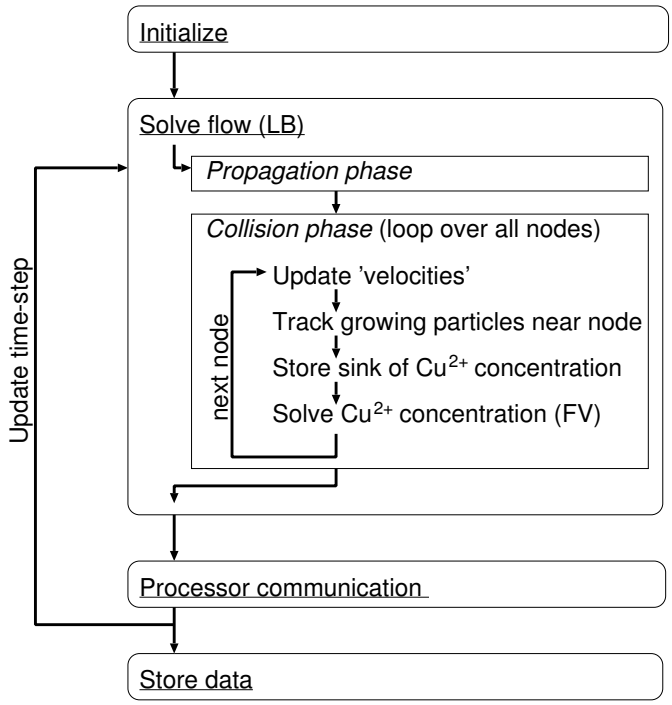

Figure 2.14: Scheme of simultaneous simulation

flow properties, Cu^{2+} concentration are initialised. Second, the flow is solved with the lattice Boltzmann flow solver, which consist of two phases: the propagation phase and the collision phase. The particle tracking code, was included into the collision phase of the LB code, because at this stage the velocities at the nodes are known. Furthermore, a particle growth model is added, which depends on the local Cu^{2+} concentration. Next, the Cu^{2+} concentration is solved with a convection/diffusion equation with sink term. The sink term of the Cu^{2+} concentration is directly linked to the particle growth, which was stored in the previous step. Third, communication takes place between the different processors, because the code is parallel. After the communication, the time step is updated and the process repeats itself. Finally, when the desired number of time steps is reached, the data is stored.

2.5.1 Particle tracking

The growing particles move through the reactor. Their trajectory are influenced by the surrounding flow field and body forces (gravity). The particle motion is modelled with the BBO equation to which the lift force is added. The velocities and velocity gradients, which are obtained from the LB code are used as input for the particle tracking. Since the velocities are only directly known in the collision phase of the (BGK) LB code, the particle code is included into this phase to minimise the number of calculations. More details on the numerical scheme, particle tracking model and behaviour of particles in the mixer will be given in chapter 5.

This study focuses on dilute Cu^{2+} concentrations. As a result the mass loading of the copper particles is low. Therefore, the exchange of momentum of the particles to the flow is neglected (one way coupling). In other words, the particles do not influence the flow. Furthermore, a particle growth model is included, which is based upon the diffusion of Cu^{2+} towards the surface of the particles.

Particle growth model

The growth of the particles is determined by their residence time and the concentration of aqueous copper the particles encounter. If the particles are small compared to the grid spacing, the diffusion process can be described as follows. The diffusion equation in spherical coordinates for the Cu^{2+} concentration yields

$$\frac{\mathrm{d}Cu^{2+}}{\mathrm{d}t} = \mathbb{D}(T)\frac{\mathrm{d}}{\mathrm{d}r}(r^2\frac{\mathrm{d}Cu^{2+}}{\mathrm{d}r}) = 0 \tag{2.18}$$

where $\mathbb{D}(T)$ is the diffusion coefficient, which is a function of the temperature. The boundary conditions for this problem are:

$$\begin{aligned} r = r_p &\rightarrow Cu^{2+} = Cu^{2+}_{\text{surface}} \\ r = \infty &\rightarrow Cu^{2+} = Cu^{2+}_{0} \end{aligned}$$

where r_p is the radius of the copper particle, Cu^{2+}_0 is the bulk concentration and Cu^{2+}_{surface} is the concentration at the surface of the particle The analytical solution of this problem is given by

$$Cu^{2+}(r) = (Cu^{2+}_{\text{surface}} - Cu^{2+}_0)\frac{r_p}{r} + Cu^{2+}_0 \tag{2.19}$$

The mass flow Φ_m is equal to

$$\Phi_m(r) = 4\pi r^2(\mathbb{D}(T)\frac{\mathrm{d}Cu^{2+}}{\mathrm{d}r}) \tag{2.20}$$

From equations 2.19 and 2.20 the mass-flow to the surface of the particle, $\Phi_m(r_p)$ can be obtained:

$$\Phi_m(r_p) = 4\pi r_p\mathbb{D}(T)(Cu^{2+}_0 - Cu^{2+}_{\text{surface}}) \tag{2.21}$$

The mass-flow determines the volumetric and radial growth of a single spherical particle, which are equal to:

$$\frac{\mathrm{d}V_p}{\mathrm{d}t} = \frac{\Phi_m}{\rho_p} \quad \text{and} \quad \frac{\mathrm{d}r_p}{\mathrm{d}t} = \frac{\Phi_m}{4\pi r_p^2\rho_p} = \frac{\mathbb{D}(T)[Cu^{2+}](t)}{r_p\rho_p} \tag{2.22}$$

where V_p and ρ_p are the volume and density of the particle, respectively. It is assumed that the reaction is much faster then the diffusion towards the surface, which implies that the surface concentration is equal to zero and it is assumed that the Cu^{2+} concentration in a computational cell is equal to the bulk Cu^{2+} concentration. The sink term of the Cu^{2+} concentration can be obtained from the mass transfer to all the particles:

$$\frac{\mathrm{d}}{\mathrm{d}t}[Cu^{2+}](t) = -\frac{\sum_{i=1}^{n_p}\Phi_{m,i}}{V_{\text{control}}} = S_{Cu^{2+}} \quad \text{where} \quad \Phi_{m,i} = 4\pi r_{p,i}\mathbb{D}(T)[Cu^{2+}] \tag{2.23}$$

where n_p is total number of particles in the control volume V_{control}.

2.5.2 Convection/Diffusion equation

If a finite control volume fixed in space is considered (figure 2.15), the time rate of change of the Cu^{2+} concentration can be obtained from a simple mass balance over the control volume.

$$\frac{\partial}{\partial t}\oint_V [Cu^{2+}]\mathrm{d}V = \underbrace{\oint_S [Cu^{2+}]\vec{u}\cdot\mathrm{d}\vec{S}}_{convection} - \underbrace{\oint_S \mathbb{D}\nabla[Cu^{2+}]\cdot\mathrm{d}\vec{S}}_{diffusion} + \underbrace{\oint_V S_{Cu^{2+}}\mathrm{d}V}_{source} \tag{2.24}$$

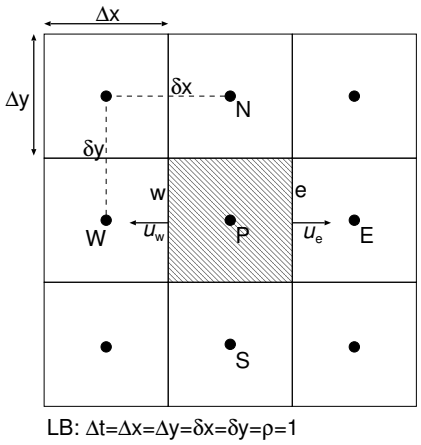

Figure 2.15: Control volume for convection/diffusion equation (2D)

With the Gauss-divergence theorem, the convection/diffusion equation in conservative form can be derived from equation 2.24:

$$\frac{\partial}{\partial t}[\mathrm{Cu}^{2+}] = \nabla \cdot ([\mathrm{Cu}^{2+}]\vec{u}) - \nabla \cdot \mathbb{D}\nabla[\mathrm{Cu}^{2+}] + S_{\mathrm{Cu}^{2+}} \tag{2.25}$$

where the source term is linked to the particle growth as described previously. Based upon equation 2.24 the discretization of a cubic control volume is straight forward. In the lattice Boltzmann code, the density, the dimension of the cube and the time step are all equal to one:

$$\Delta t = \Delta x = \Delta y = \Delta z = \rho = 1 \tag{2.26}$$

which simplifies the calculations. Figure 2.15 shows the control volume around a LB grid node in 2D. The diffusive terms are interpolated using a central difference scheme. The east face of the control volume around node P has the following diffusive terms:

$$\left(\mathbb{D}\frac{\partial[\mathrm{Cu}^{2+}]}{\partial x}\right)_{\mathrm{e}} \Delta y \Delta z \;=\; \left(\mathbb{D}\frac{[\mathrm{Cu}^{2+}]_{\mathrm{E}} - [\mathrm{Cu}^{2+}]_{\mathrm{P}}}{\Delta x}\right)_{\mathrm{e}} \Delta y \Delta z \overset{(LB)}{=} \mathbb{D}\left([\mathrm{Cu}^{2+}]_{\mathrm{E}} - [\mathrm{Cu}^{2+}]_{\mathrm{P}}\right) \tag{2.27}$$

where E and e denote the east node and east face, respectively. The diffusive term of the west face is equal to

$$\left(\mathbb{D}\frac{\partial[\mathrm{Cu}^{2+}]}{\partial x}\right)_{\mathrm{w}} \Delta y \Delta z \;=\; \left(\mathbb{D}\frac{[\mathrm{Cu}^{2+}]_{\mathrm{P}} - [\mathrm{Cu}^{2+}]_{\mathrm{W}}}{\Delta x}\right)_{\mathrm{w}} \Delta y \Delta z \overset{(LB)}{=} \mathbb{D}\left([\mathrm{Cu}^{2+}]_{\mathrm{P}} - [\mathrm{Cu}^{2+}]_{\mathrm{W}}\right) \tag{2.28}$$

where W and w denote the west node and west face, respectively. The convective terms are calculated with a first order upwind scheme. The convection through the east face is equal to

$$u_{\mathrm{e}}[\mathrm{Cu}^{2+}]_{\mathrm{E}}\, \Delta y \Delta z \overset{(LB)}{=} u_{\mathrm{e}}[\mathrm{Cu}^{2+}]_{\mathrm{E}} \qquad (u_{\mathrm{e}} > 0) \tag{2.29}$$

$$u_{\mathrm{e}}[\mathrm{Cu}^{2+}]_{\mathrm{P}}\, \Delta y \Delta z \overset{(LB)}{=} u_{\mathrm{e}}[\mathrm{Cu}^{2+}]_{\mathrm{P}} \qquad (u_{\mathrm{e}} < 0) \tag{2.30}$$

$$\tag{2.31}$$

and the convection through the west face is equal to

$$u_{\mathrm{w}}[\mathrm{Cu}^{2+}]_{\mathrm{W}}\, \Delta y \Delta z \overset{(LB)}{=} u_{\mathrm{w}}[\mathrm{Cu}^{2+}]_{\mathrm{W}} \qquad (u_w > 0) \tag{2.32}$$

$$u_{\mathrm{w}}[\mathrm{Cu}^{2+}]_{\mathrm{P}}\, \Delta y \Delta z \overset{(LB)}{=} u_{\mathrm{w}}[\mathrm{Cu}^{2+}]_{\mathrm{P}} \qquad (u_w < 0) \tag{2.33}$$

where the velocities u_{e} and u_{w} are positive when they point outward the control volume. The terms of the north, south, top and bottom phase are similar to the ones of the east and west face.

An upwind scheme can cause numerical or false diffusion. When the flow is not aligned with the cells, the false diffusion can be important. In the case of the Kenics™ static mixer, the flow is not aligned with the structured grid. Therefore, there can be an overprediction of the diffusion of the copper ions. An estimation of the false diffusion is made with the approximate expression of De Vahl Davis and Mallinson (1972) for a two dimensional situation, which is given by:

$$\mathbb{D}_{\mathrm{false}} = \frac{\rho u \Delta x \Delta y \sin 2\theta}{4(\Delta y \sin^3 + \Delta x \cos^3 \theta)} \tag{2.34}$$

where θ is the angle made by the velocity vector with the x direction. It can be observed that, when the angle θ is 45 degrees and when the flow rate is highest (high Peclet number), the false or numerical diffusion is maximal. When the grid is 'dense', the numerical diffusion becomes smaller. The LB solver uses a relatively dense grid so the numerical diffusion is expected to be small. It was found that in the worsts case (at Re=1000), the false diffusion coefficient is equal to $\mathbb{D}_{\mathrm{false}}$=8·10^{-11} m^2/s. The 'real' diffusion coefficient of the copper ions is of the order of $\mathbb{D}$=3·10^{-9} m^2/s, which is much larger than the 'false' diffusion coefficient. It should be noted that there are more accurate schemes for the convective terms such as the TVD scheme (Lathouwers (1999)). The TVD scheme is not applied, because the numerical diffusion is much smaller than the 'real' diffusion. In this case, a simple upwind scheme is sufficient.

2.6 Scaling

Since the grid-spacing of the LB solver is always equal to one, scaling of the numerical problem is necessary to translate the results towards 'real life' dimensions. A convenient way to find the right scaling rules is to make the governing equations dimensionless. This way the dimensionless numbers, which can be used to scale, are identified. The following equations are solved numerically and made dimensionless:

- The Navier-Stokes equation (fluid flow)
- The BBO-equation (particle motion)
- The convection-diffusion equation with sink term (copper ion concentration)
- Mass balance (particle growth)

The dimensionless form of the Navier-Stokes equation is equal to:

$$\frac{\mathrm{d}\vec{u}^*}{\mathrm{d}t^*} + \vec{u}^* \cdot \nabla \vec{u}^* = \frac{1}{\mathrm{Re}} \nabla^2 \vec{u}^* - \nabla p^* \tag{2.35}$$

where

$$\mathrm{Re} = \frac{u_0 \, D}{\nu} \tag{2.36}$$

is the Reynolds number, which is based on the tube diameter D and mean axial velocity u_0. The motion of the particles is given by the BBO-equation. In dimensionless form, this equation can be described in the following way:

$$\frac{\mathrm{d}\vec{v}_{\mathrm{p}}^*}{\mathrm{d}t^*} = \frac{\vec{v}_{\mathrm{s}}^*}{\mathrm{St}} + \frac{\vec{1}}{\mathrm{Fr}} + \frac{3}{2}\rho^* (\nabla^* \vec{u^*}) \cdot \vec{u^*} + \vec{F}_{\mathrm{lift}}^* \tag{2.37}$$

where

$$\mathrm{St} = \frac{\rho_\mathrm{a} d_\mathrm{p}^2}{18\mu}\frac{\overline{u}_0}{\mathrm{D}}, \quad \mathrm{Fr} = \frac{\rho_\mathrm{a}}{\rho_\mathrm{p}-\rho_\mathrm{l}}\frac{\overline{u}_0^2}{\mathrm{D}g} \quad \text{and} \quad \rho^* = \frac{\rho_\mathrm{l}}{\rho_\mathrm{a}} \tag{2.38}$$

are the Stokes number, Froude number and the density ratio, respectively. The gravity force (Fr) and drag force (St) are the dominant forces. If the problem is stationary the terminal velocity of a particle is equal to the ratio between the Stokes and the Froude number, which can be used to scale. The convection-diffusion equation in dimensionless form is equal to

$$\frac{\mathrm{d}c^*}{\mathrm{d}t^*} = \frac{1}{\mathrm{Pe}}\nabla^{*2}c^* - \nabla^*(\vec{u}^*\, c^*) - \mathrm{Da\,I}\, c^* \tag{2.39}$$

where

$$\mathrm{Pe} = \frac{u_0\,\mathrm{D}}{\mathbb{D}} \quad \text{and} \quad \mathrm{Da\,I} = \frac{k_\mathrm{r}\mathrm{D}}{u_0} \tag{2.40}$$

are the Peclet and Damköhler I number, respectively. Here, a first order reaction (Da I) determines the sink of the equation. When the sink term is linked to the particle growth the reaction rate k_r is equal to $k_\mathrm{r} = 4\pi\mathbb{D}\, l_\mathrm{s}$, where

$$l_\mathrm{s} = \frac{1}{V_\mathrm{control}}\sum_{i=0}^{n_\mathrm{p}} r_{\mathrm{p,i}} \tag{2.41}$$

is the specific length of the particles.

2.6.1 Scaling rules

Since the grid spacing is per definition one, the length scale is equal to the number of grid nodes in that direction. For example if the characteristic length scale is determined by the tube diameter, the 'LB' diameter is equal to the number of grid nodes in the radial direction. The viscosity in LB is equal to $\mu = \frac{2\tau-1}{6}$, where τ is a relaxation parameter. The Reynolds number, which is used to scale, can be written in LB quantities:

$$\mathrm{Re} = \frac{u_0\, D}{\nu} \overset{(LB)}{=} \frac{6 n_\mathrm{cells} u_{0,\mathrm{LB}}}{2\tau - 1} \tag{2.42}$$

where n_cells is the number of cells of the characteristic length, which is the tube diameter. The table 2.1 shows the scaling of the liquid and particle velocity towards dimensionless quantities.

Table 2.1: Scaling rules

Quantity	*Symbol*	*Dimensionless*	*Scaling rule*
Particle velocity relative to liquid velocity	v_s	$v_\mathrm{s}^* = v_\mathrm{s}/\overline{u}_0$=St/Fr	St/Fr
Liquid velocity	u	$u^* = u/\overline{u}_0$	Re
Time	t	$t^* = t\overline{u}_0/D$	
Diffusion coefficient	$\mathbb{D}$	$\mathrm{Pe} = u_0\, D/\mathbb{D}$	Pe
Reaction rate	k_r	$\mathrm{Da\,I} = k_\mathrm{r}\mathrm{D}/u_0$	Da I

3

Experimental study into the Kenics™ static mixer

This chapter gives an overview of the experimental techniques. Two non-intrusive techniques, Particle Image Velocimetry (PIV) and Laser Doppler Anemometry (LDA), are used to investigate the flow in the Kenics™ static mixer. For both methods the flow is measured via small tracer particles, which are suspended and distributed uniformly in the flow. The main purpose of the experiments is to validate the CFD results. The outline of this chapter is as follows. First, a brief introduction about the Kenics™ static mixer and experiments that are reported in literature is given. Second, the properties of the tracer particles that are used to measure the flow are discussed. Third, the experimental setup, method and results of PIV are explained and discussed, respectively. Fourth, the setup, method and results of LDA are dealt with and finally, some concluding remarks are made.

3.1 Introduction

The Kenics™ static mixer has a large range of applications such as blending, heat transfer, mass transfer and residence time control. A static mixer takes the energy that is needed for the mixing out of the fluid, which translates into a pressure loss. Most early experimental work was focused on the pressure drop e.g.Wilkinson and Cliff (1977); Sir and Lecjacks (1982); Shah and Kale (1991); Heywood et al. (1984); Grace (1971) and on the residence time distribution e.g. Nigam et al. (1980); Kemblowski and Pustelnik (1988). This work resulted in useful correlations to predict the pressure drop in the Kenics™ static mixer. However, for validation of numerical work detailed information about the velocity field is necessary. Visualisation is another tool that is used in literature for validating CFD data. Already in 1971, Grace (1971) showed in detail the mixing properties of the Kenics™ static mixer at low Reynolds numbers. Two fluids were mixed in the Kenics™ static mixer. When steady state was reached, the fluid was hardened after which the mixer was cut into pieces. This way the mixing of two fluids in the Kenics™ static mixer could be studied. Pahl and Muschelknautz (1982) extended this work to other types of static mixers. Recently, more fancy techniques such as Laser Induced Fluorescence (LIF) were used to study the effect of striation thinning e.g. Jaffer and Wood (1998); Fourcade et al. (2001). Fourcade et al. (2001) showed that CFD together with the tracking of tracer particles could be used to calculate the average value of the rate of striation thinning. Their work was based on the micro-mixing theory of Ottino (1989). Their numerical results were validated qualitatively with the LIF technique. Good agreement was reported between the CFD and experimental results.

Most experimental studies that were found in literature were performed at low Reynolds numbers ($Re < 10$, steady state). Furthermore, detailed information about the flow field is lacking in literature, while this is essential for a thorough validation of CFD results. Therefore, instead of focusing on the mixing performance via dye or fluorescence, the work presented in this chapter aims to provide detailed information about the velocity field inside the Kenics™ static mixer. Moreover, the higher

Table 3.1: Properties of liquids used for PIV and LDA, respectively

	$\rho_\mathrm{l}\,[10^3\,\mathrm{kg/m^3}]$	$\mu\,[10^{-3}\,\mathrm{kg/m^3}]$	$\overline{u}_\mathrm{ax}\,[10^{-3}\,\mathrm{m/s}]$	$\mathrm{St}[10^{-6}]$	$v^*_{\mathrm{s},0}$
LDA	1.2	$35\cdots76$	$10\cdots350$	<2	$<3\,10^{-5}$
PIV	0.95	3.1	$5\cdots60$	<3	$<5\,10^{-4}$

Reynolds numbers in the 'transitional' regime (Re>300) are investigated as well. One should note that the Reynolds number is based upon the tube diameter D.

Two non-intrusive measurement techniques were used to obtain detailed velocity information inside the Kenics™ static mixer. First, Particle Image Velocimetry (PIV) was used in combination with Refractive Index Matching (RIM) in a two element static mixer, which was made of glass (Dorsman (2001)). Unfortunately the glass mixer had some geometrical inconsistencies, which made the experiments unsuitable for quantitative validation. Therefore, in addition Laser Doppler Anemometry (LDA) was used to perform point measurements in a 12 element metal static mixer. Velocity profiles at different Reynolds numbers up to Re=500 could accurately be measured with this technique. Furthermore, the transition from steady to unsteady flow could be measured and studied with LDA.

3.2 Measurement of velocity flow via seeding particles

Both PIV and LDA measure the flow via particles suspended in the flow, where it is assumed that the particles follow the flow. A particle follows the flow when the relaxation time of the particle τ_p is small compared to the relaxation time of the flow τ_l, which is at low Stokes number, St, defined as

$$\mathrm{St} = \frac{\tau_\mathrm{p}}{\tau_\mathrm{l}} = \frac{\rho_\mathrm{p} d_\mathrm{p}^2}{18\mu}\frac{\overline{u}_0}{\mathrm{D}} \tag{3.1}$$

where ρ_p and d_p are the density and diameter of the particle respectively, μ is the dynamic viscosity, $\overline{u}_0$ is the mean axial velocity and D is the tube diameter. An other issue is the settling of the particles due to gravity. In dimensionless form gravity appears as a Froude number (Fr):

$$\mathrm{Fr} = \frac{\rho_\mathrm{p}}{\rho_\mathrm{p}-\rho_\mathrm{l}}\frac{\overline{u}_0^2}{\mathrm{D}g} \tag{3.2}$$

where ρ_l is the density of the liquid and g is the gravitational acceleration. When only the gravitational and drag forces are considered, the terminal velocity of the seeding particles in dimensionless form $v^*_{\mathrm{s},0}$ is equal to the St/Fr number, which can be derived from the dimensionless particle force balance (chapter 5).

$$v^*_{\mathrm{s},0} = \frac{\mathrm{St}}{\mathrm{Fr}} = \frac{(\rho_\mathrm{p}-\rho_\mathrm{l})g}{18\mu}\frac{d_\mathrm{p}^2}{\overline{u}_\mathrm{ax}} \tag{3.3}$$

For both PIV and LDA hollow glass spherical particles were used, which had a density of ρ_p=1055 kg/m^3 and an average diameter of d_p=11.2 μm with a standard deviation of σ_p=6.6 μm The diameter of the tube was 5 cm for both the LDA and PIV experiment. For PIV a mixture of benzyl alcohol and ethanol (96% pure) was used and for LDA a mixture of glycerol and water was used. The properties of the liquids, which were used for LDA and PIV respectively, are listed in table 3.1.

One can observe that the Stokes number for both PIV and LDA is of the order of 10^{-6}, which means that the relaxation time of the particle is six orders smaller than the relaxation time of the fluid. Hence, the particles are good flow followers. The terminal velocity relative to the average axial velocity is at most $5 \cdot 10^{-4}$ for PIV and $3 \cdot 10^{-5}$ for LDA, which means that the settling of the particles does not pose a problem. Therefore, the seeding particles are suitable to measure the flow.

3.3 PIV Measurements

3.3.1 Setup

The setup consists of a 2 element Kenics™ static mixer, which is made of glass. The glass elements were made by twisting a heated glass plate and they were carved to fit into a glass tube after which they were welded to the wall of the tube. The aspect ratio of the glass mixer are L/D=1.9 and t/D=0.08 and the length and diameter of the mixing elements are L_0=95 mm and D_0=50 mm, respectively. The twist angles of the two elements were -170 and 205 degrees, respectively. It should be noted that this deviates from the standard Kenics™ static mixer, which has an L/D ratio of 1.5 and twist angles of -180 and 180 degrees, respectively.

To make the glass mixer optical transparent, the refractive index of the fluid was matched to the refractive index of the glass elements and tube. Furthermore, the tube and mixing element were placed in a glass square box, which was filled with the same fluid. This way both the tube and mixing elements became 'invisible' to the laser light and no laser light was reflected. Furthermore, the direction of the light did not change, when passing through the glass elements. A schematic overview of the flow system that was used for PIV is shown in figure 3.1. The flow is gravity driven via an overflow vessel. The flow rate is set by adjustment of the pressure drop over the setup, which is visualised by the difference in height (Δh). The 'exact' flow rate was determined after the experiment by means of the correlation between the temperature fluctuations, which were measured by the probes (2) and (3). The probes are located before and after the mixer, respectively and the distance between the probes is 1.3 m. A membrane pump pumps the liquid from the buffer vessel (50 L) into an overflow vessel, which is placed 1.5 m above the setup. One part of the liquid flows back into the buffer vessel and the other part flows through the setup. This way a constant flow rate is obtained in the setup. The flow rate is controlled by a valve at the end of the flow system and is measured with the two PT100 probes. The liquid was indexed matched to the glass setup. In the next section, more details about the refractive index matching technique are given.

3.3.2 Refractive Index Matching

The fluid consisted of a mixture of ethanol (96% pure) and benzyl alcohol. The ratio between the two fluids and the temperature determines the refractive index of the mixture. Muguercia et al. (1993) shows that the refractive index matching of the mixture is equal to the refractive index of glass at a temperature of approximately 293K and a benzyl alcohol fraction of 58%. Since the refractive index depends on the wavelength, slight variations to this value are necessary to match the index for the wavelength (λ=514.5 μm) of the Argon-ion laser (3.6 W, single line 1.2 W) that was used for the PIV experiment. One should note that the dependence on the wavelength makes this technique less suitable for a dual beam technique such as 2D LDA. Furthermore, the refractive index depends strongly on the temperature. Cui and Adrian (1997) showed that the temperature fluctuations should be smaller than 0.1 K in order to maintain the index matching. Therefore, a feedback system was installed, which kept the temperature fluctuation within 0.05 K. Figure 3.2 shows an example of the temperature measurements at the 3 probes.

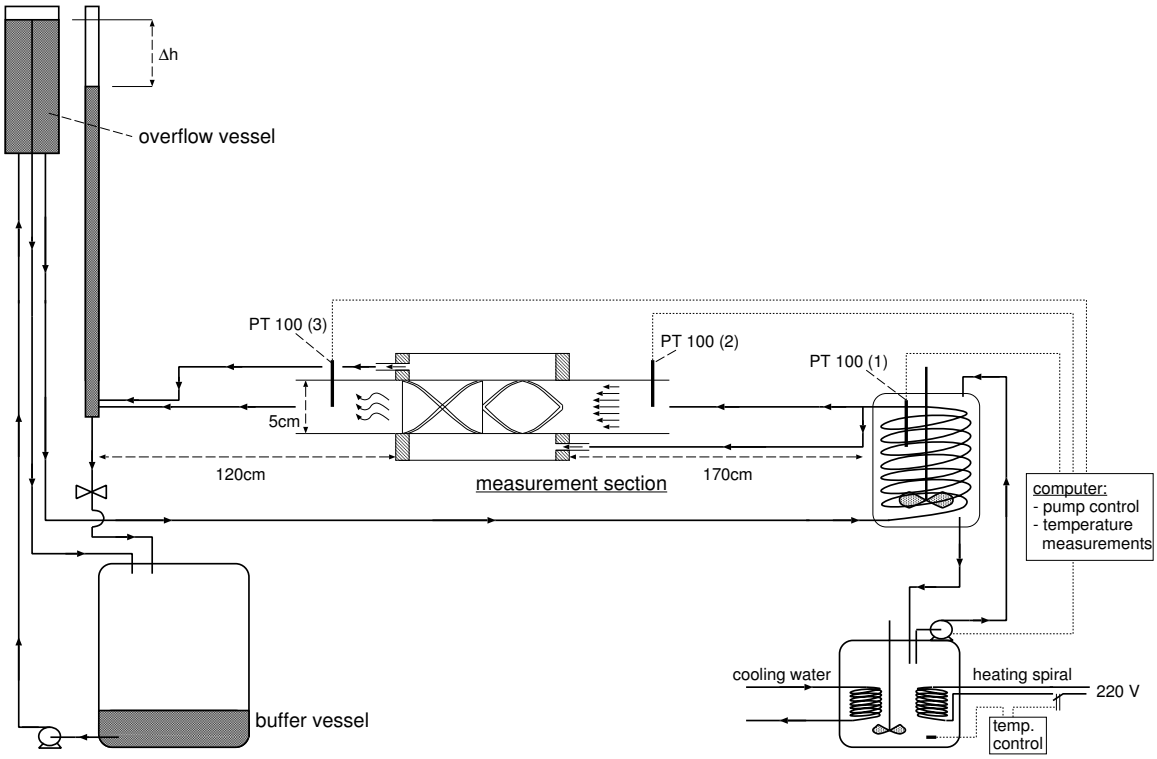

Figure 3.1: Schematic overview of PIV setup.

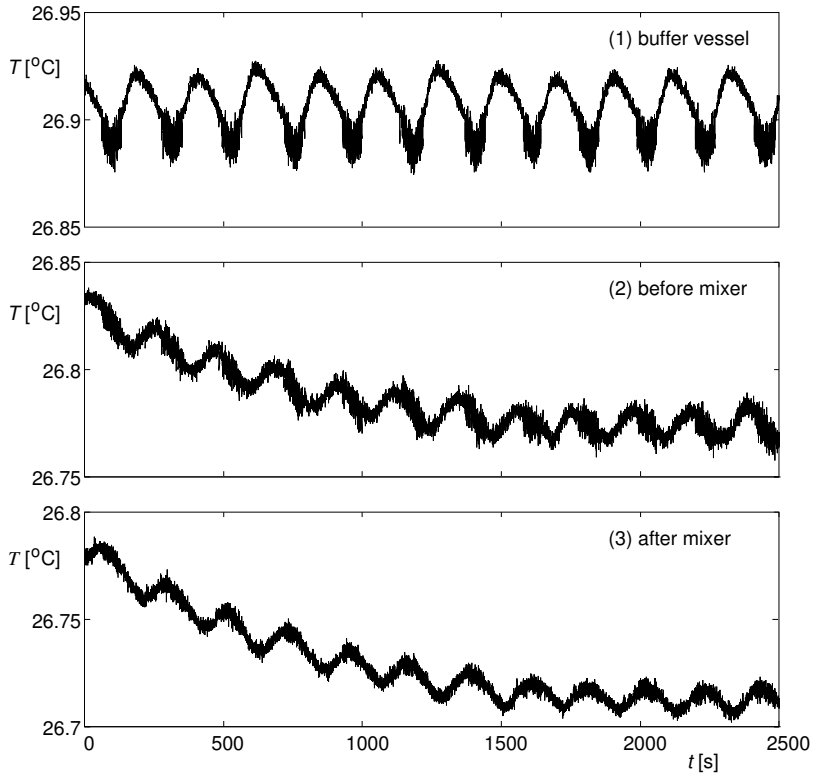

Figure 3.2: Temperature characteristics of temperature control system

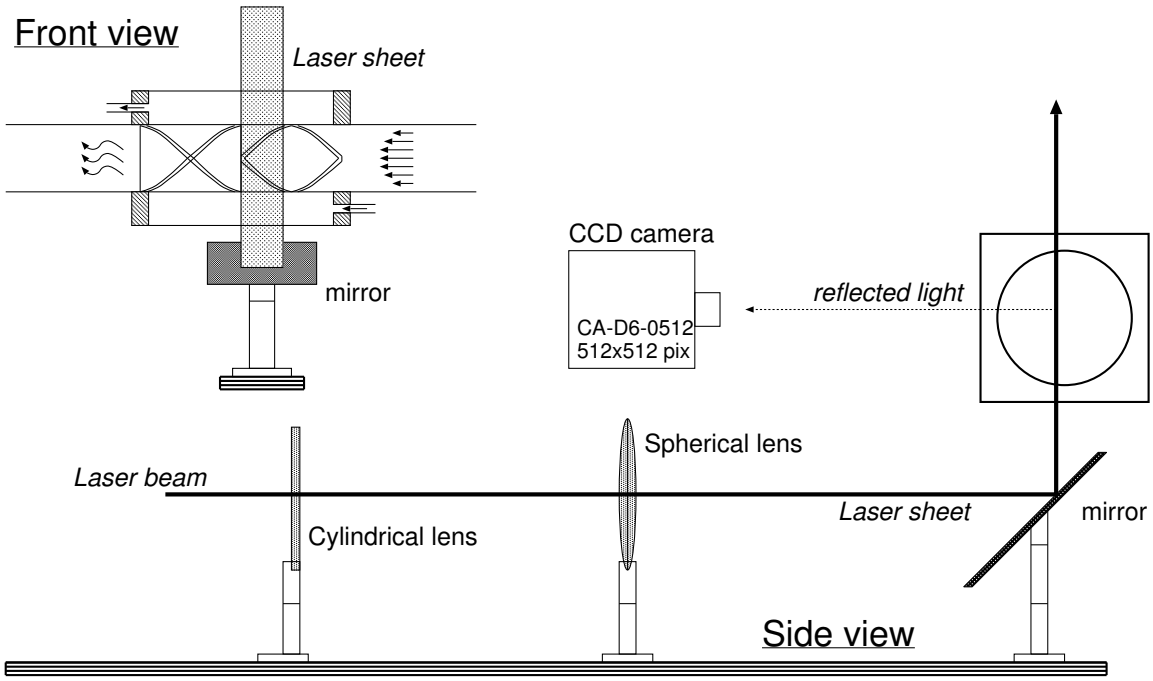

Figure 3.3: Optical setup of PIV.

The temperature control system was comprised of a stirred buffer vessel which exchanges its heat to the fluid via a heating coil. This vessel is kept at constant temperature via a thermostat, which can heat the stirred buffer vessel by inserting hot water. A computer controls the flow of hot water to the buffer vessel. Because of the large size of the buffer vessel (50 L) the temperature fluctuations were small (figure 3.2). The small drop in temperature after some time, which can be observed in the bottom two graphs in figure 3.2, is caused by a decreasing room temperature. One should note that the temperature of the fluid drops, when the fluid flows through the system. However, the drop between temperature over the measurement section (between probe (2) and (3)) was less then 0.05 K and the PIV measurements only took about 10 seconds. Hence the index matching was maintained at the measurement section. An overview of the entire setup, which includes the temperature control system is shown in figure 3.1. The refractive index was matched by adjusting the temperature of the buffer vessel such that the matching was perfect at the measurement section. The matching was evaluated by looking at refraction of the light sheet, which was also used for the PIV experiment (figure 3.3). The light sheet was placed at a curved part of the mixing element (maximum distortion), after which the temperature was adjusted such that the distortion of the light sheet was minimal (no refraction).

3.3.3 Principe of PIV and optical setup

In PIV the velocity is determined by measuring the displacement of tracer particles at certain time intervals. In digital PIV the tracer particles, which are illuminated by a laser sheet, are recorded with a CCD camera at different times separated by small time intervals. The laser sheet was formed by a cylindrical lens, which had a focal length of 6 mm, and a positive spherical lens, which had a focal length of 250 mm. The sheet had a width of 70 mm and thickness of approximately 2 mm in the measurement plane. The CCD camera (Dalsa Dalstar CA-D6) had a resolution of 512x512 (8bit) and a maximum frame rate of 250 frames per second. Furthermore, a 26 mm lens was attached to the camera. An overview of the optical setup can be found in figure 3.3.

After the PIV images are recorded, the background noise of the raw image is subtracted. Furthermore, the digital PIV recordings are divided into subareas, which are called interrogation areas (IA) (figure 3.4). The size of an IA was equal to 32x32 pixels and a 50% overlap of the IAs was used. It is assumed that within one IA the tracer particles move homogeneously between two recordings. The displacement of the particles is determined by cross correlation between the corresponding IA's of two subsequent PIV recordings and a Gaussian peak fit estimator is applied to obtain sub-pixel accuracy. The maximum relative error was found at the lowest velocities and was about 7%. The relative error of the highest velocity was much lower and was about 1%. With the displacement of the particles, $\vec{s}$, and the time interval Δt between two recordings the (2D) velocity vector $\vec{U}$ can be obtained in the plane of the laser sheet.

Keane and Adrian (1990) give four optimisation rules for a good PIV recording.

1. the number of particles in an IA, N_{I}, should be bigger than 15 ($N_{\mathrm{I}} > 15$).
2. the (in-plane) displacement of the particles should be smaller than 1/4 of the length of an IA, D_{I}, ($|\vec{s}| < 0.25 D_{\mathrm{I}}$).
3. the out of plane displacement of the particles, $\vec{s}_{\mathrm{out}}$, should be smaller than 1/4 of the thickness of the laser sheet, t_{sheet}, ($|\vec{s}_{\mathrm{out}}| < 0.25 t_{\mathrm{sheet}}$).
4. the relative variation of the in-plane velocity should be smaller than 4 times the particle image diameter, d_τ divided by the length of an IA. ($\frac{|\Delta \vec{U}|}{\vec{U}} < 4 \frac{d_\tau}{D_{\mathrm{I}}}$).

These optimisation rules are derived to maximise the signal to noise ratio of the correlation peak, which makes the correlation peak easier to detect. By adding sufficient amount of seeding the first rule is obeyed. The second and third rule are obeyed by adjusting the frame rate of the camera, such that the in-plane displacement was less then 1/4 of length of an IA. Furthermore, the size of the IA was equal to 2 mm x 2 mm, which is equal to the laser sheet thickness. Hence, the IA has a cubic form. Furthermore, the out of plane motion is smaller than the in-plane motion. Therefore, when condition two is satisfied, condition three will automatically be satisfied. The variation of the velocity within an IA cannot be controlled, but was found to be small. Only near the wall the last rule will not be satisfied. Less then 2% of the vectors were spurious. It was decided not to remove the spurious vectors, because there were very few spurious vectors. More details of this technique can be found in Raffel et al. (1998).

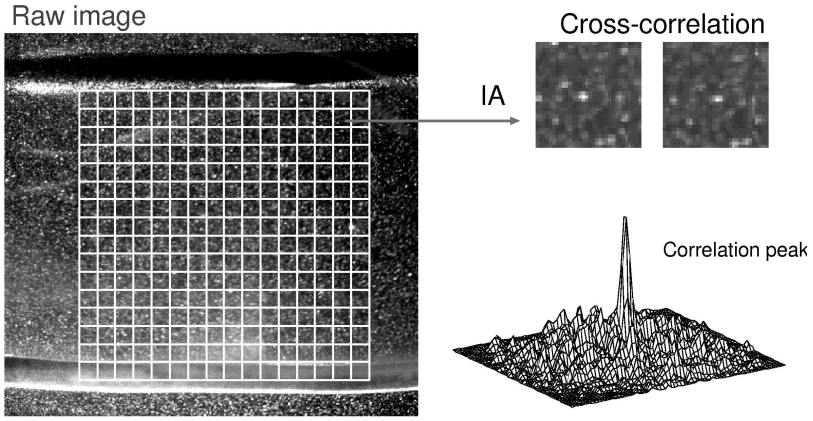

Figure 3.4: Data processing of PIV.

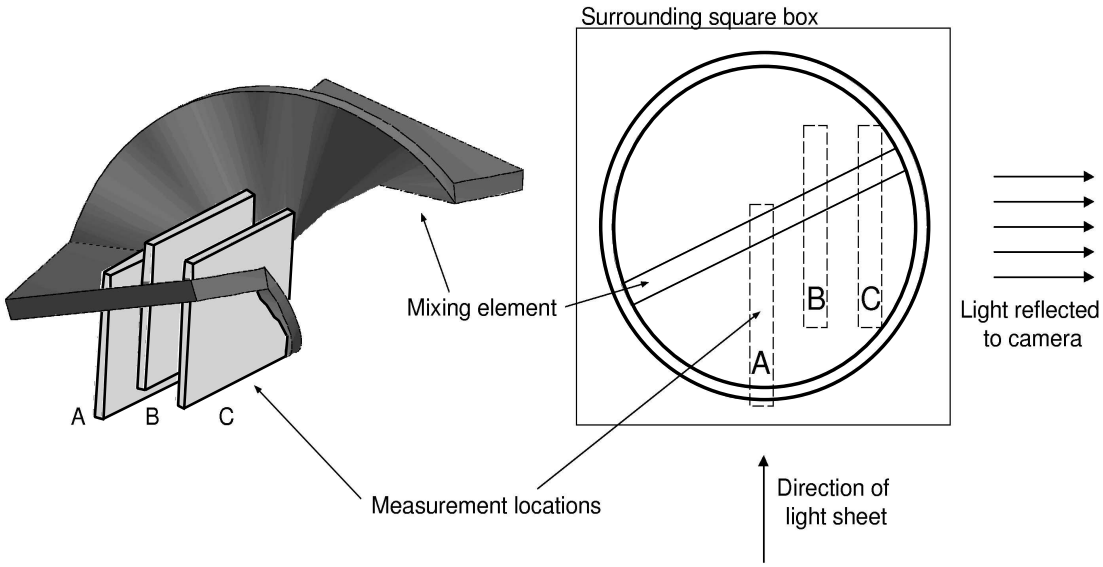

Figure 3.5: Measurement location of PIV.

3.3.4 Results

The PIV results that were obtained in the glass mixer are compared to numerical results, which were obtained with the commercial package FLUENT v5.3. Grid independent results were obtained in a two element mixer. An inflow and outflow boundary were used. The inflow boundary consisted of a parabolic velocity profile and is located 1.5 D before the start of the first element. The outflow boundary consisted of a constant gradient and was located 6 D behind the end of the second element. One should note that since the glass elements were hand made, they were not perfect. The elements start with a straight section after which the twist begins. This geometry was mimicked and created with commercial package Gambit v1.3. This way a comparison between the PIV and numerical results was possible. An overview of the measurement locations and the geometry of the mixer can be found in figure 3.5.

Measurements were taken at two Reynolds numbers, Re=80 and Re=430. It should be noted that only half of the total number of vectors is shown and that spurious vectors are not removed. Figure 3.6 shows the velocity vectors of the PIV (top) and CFD (bottom) results for Re=80 and the contours indicate the velocity magnitude. It can be observed that there are discrepancies between the PIV and CFD results. Especially, at location B the direction of the vectors differs significantly. Also the velocity magnitude shows differences. These differences between the CFD and PIV are likely caused by geometrical inconsistencies.

At Re=430 the differences are smaller and qualitative agreement is found at all three measurement locations (figure 3.7). Small differences still arise due to the geometrical differences between the CFD and PIV geometry. Despite of these small differences the direction of the velocity vectors is similar for both PIV and CFD.

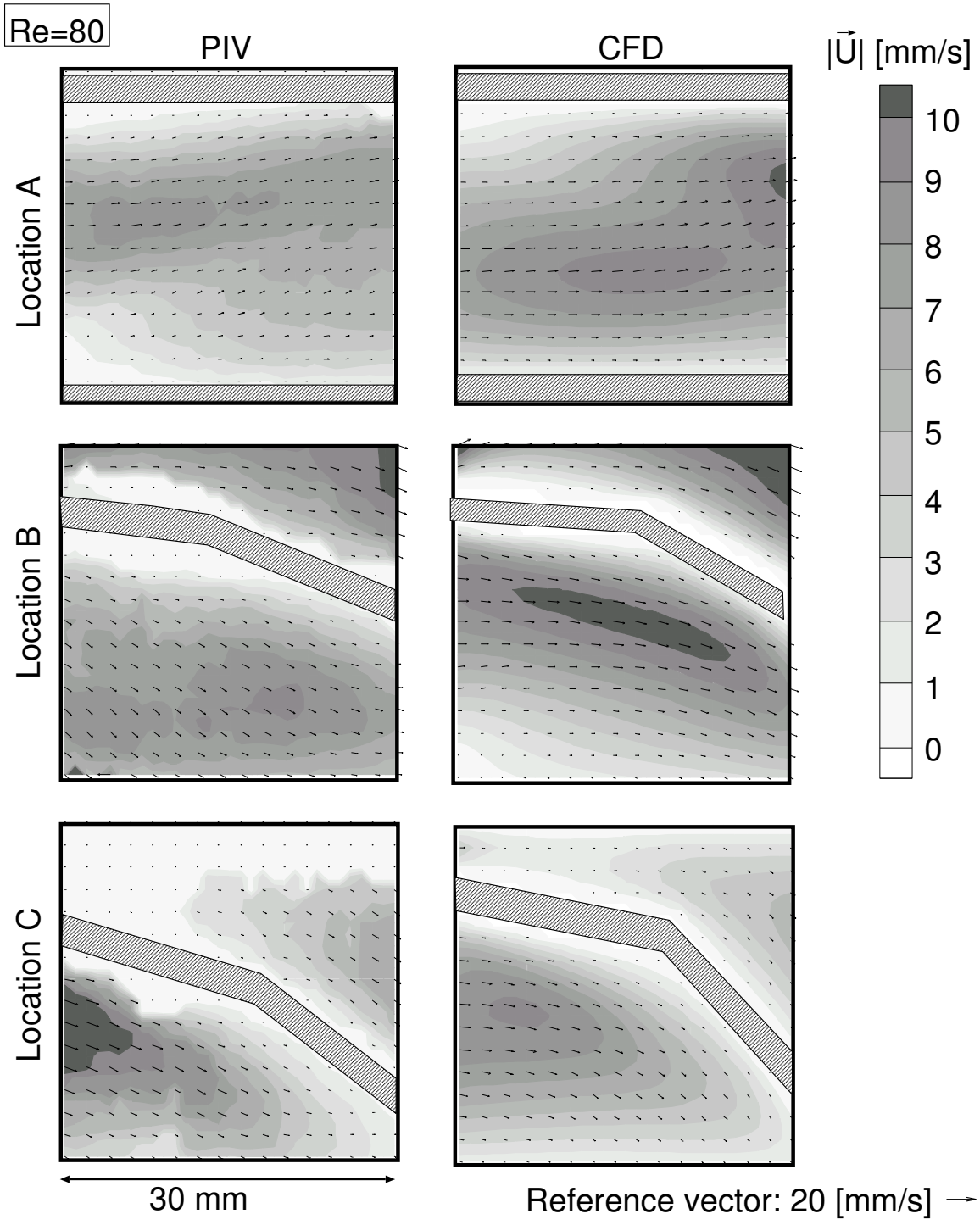

Figure 3.6: Comparison of PIV and CFD at Re=80

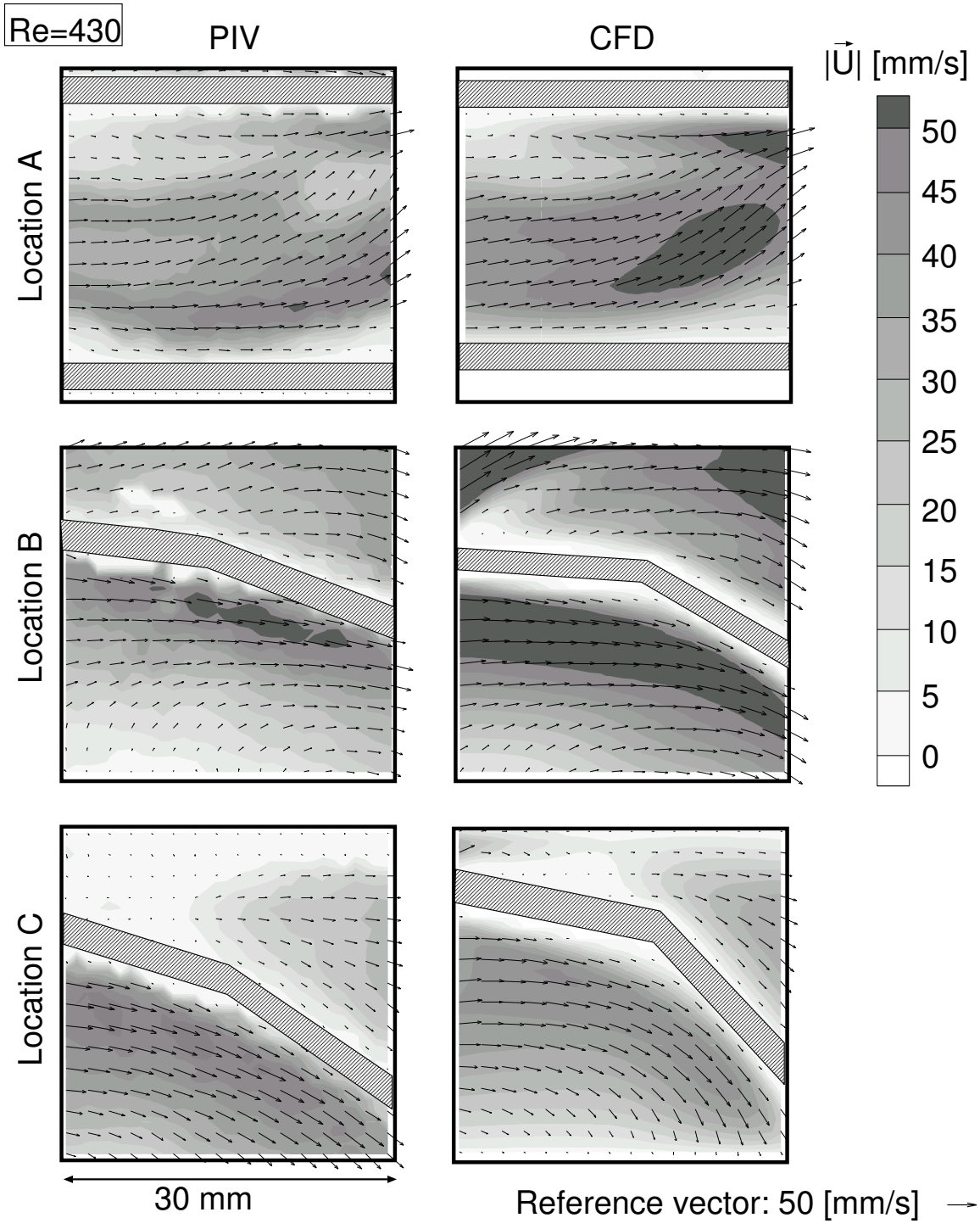

Figure 3.7: Comparison of PIV and CFD Re=430

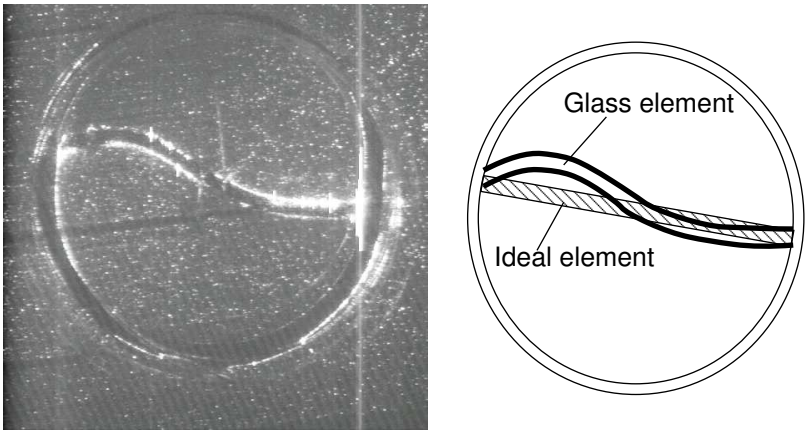

Figure 3.8: Imperfect shape of glass mixing element (should be straight line)

Non ideal geometry of PIV-experiments

The cross section of a mixing element was illuminated with the laser sheet to investigate in detail the shape of a mixing element. Figure 3.8 shows the cross section, which is located roughly half way a mixing element. It can be observed that the mixing element is 'wavy', while it should be straight.

Apparently this difference in geometry has more influence at low Reynolds numbers, since the PIV and CFD results deviate more at Re=80. At the higher Reynolds number qualitative agreement could be found between CFD and PIV. However, a quantitative comparison was desired. An alternative mixer had to be found, since the hand made glass mixer proved to be inconsistent. A possible improvement in the production of the glass mixer is pouring glass in a mold, but this proved to be too expensive. It was decided to use a steel mixer, because a steel mixer has a far more consistent geometry. In a steel mixer it was no longer possible to use the PIV/RIM measurement technique. Instead, point measurement with LDA were performed.

3.4 LDA Measurements

3.4.1 Setup

The setup consists of a 12 element Kenics™ static mixer, which is comprised of stainless steel and is coated black in order to reduce reflections. The aspect ratios of the 'experimental' static mixer are L/D=1.6 and t/D=0.083 and the length and diameter of the mixing elements are L_0=76.5 $\pm$ 1 mm and D_0=48.0 $\pm$ 0.1 mm, respectively. The measurement section is made optical accessible by a perspex tube and is surrounded by a square box with glass windows in it in order to reduce refraction. A schematic overview of the experimental setup is given in figure 3.9. The flow in the 9^{th} element is measured. Fluent simulations had indicated that the flow in the Kenics™ mixer is fully developed after about three or four mixing elements. The LDA measurements were compared to lattice Boltzmann (LB) simulations. A 4 element periodic mixer was simulated with LB. As was expected, the developed flow is comparable to the flow in a periodic mixer, which is in fact an infinitely long mixer.

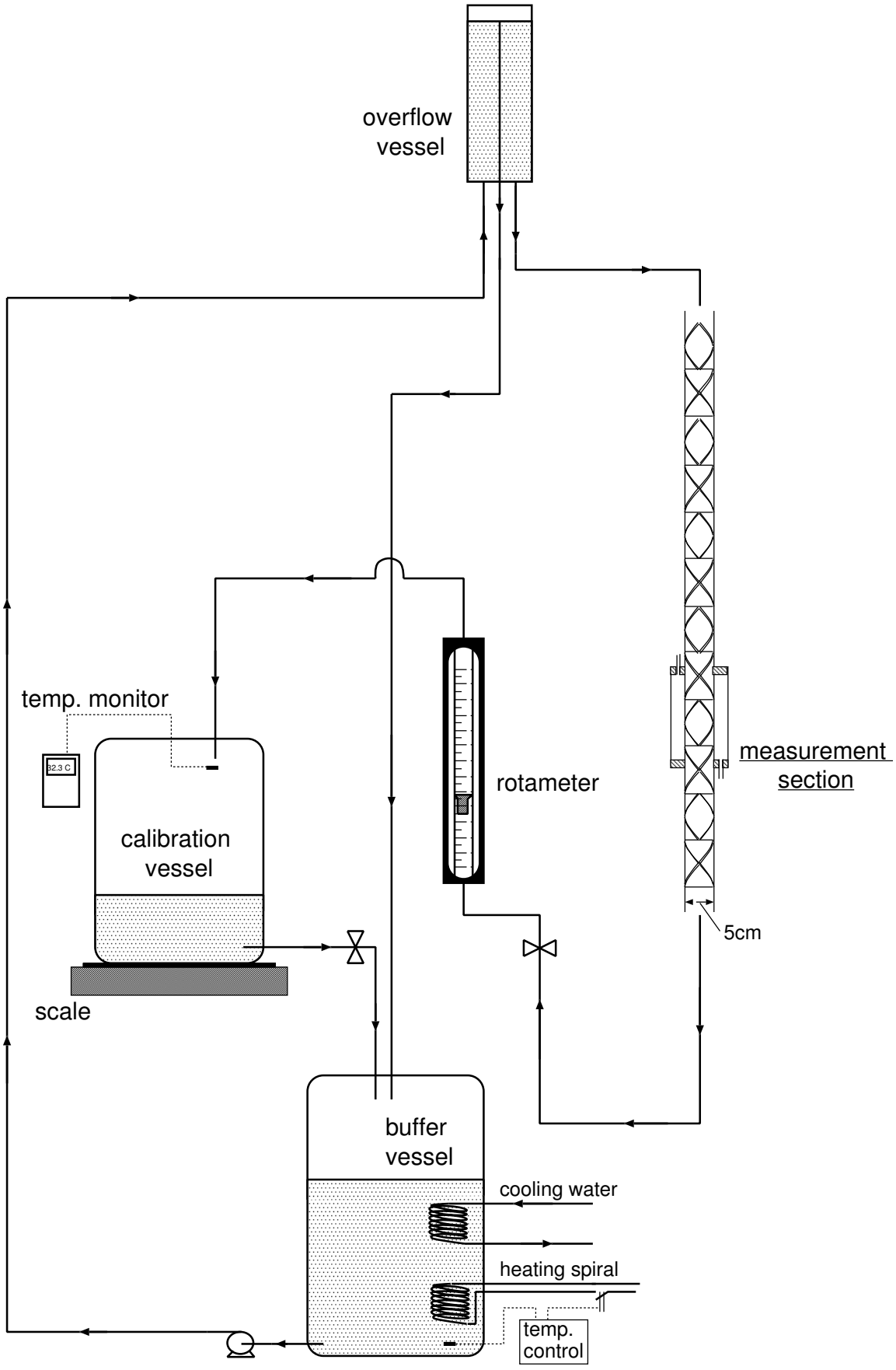

Figure 3.9: Schematic overview of LDA setup.

3.4.2 Viscosity modification

The accuracy of LDA measurements is better at higher velocities. Therefore, a glycerol/water (mass fraction glycerol≈80%) solution is used to increase the viscosity in order to be able to increase the velocity (while keeping the Reynolds number constant). This results in a smaller uncertainty in the LDA measurements at the relatively low Reynolds numbers. The flow is gravity driven in order to ensure a constant flow-rate. Furthermore, a feedback system is used to control the temperature via a heating and cooling unit (figure 3.9). The temperature is kept constant with an accuracy of 0.1°C and the Reynolds number is set by varying the viscosity and velocity (Re=20,50,100,. . . ,450,500). The flow-rate is measured with a rotameter, which is calibrated for each viscosity with an integrated mass-flow calibration system. The calibration method was tested with LDA measurements in an empty tube and proved to be reliable. One of the disadvantages of the use of a rotameter, is the fact that it needed calibration for each new viscosity that was used.

3.4.3 Principle of LDA

LDA uses the principle that the frequency of laser light scattered of a moving particle is Doppler shifted. The LDA measurement technique is used from some decades and has been extensively described by Drain (1980); Absil (1995); Van Maanen (1999). The frequency or Doppler shift is proportional to the velocity of the particle. One should note that there is a Doppler shift from laser towards particle and from particle towards detector, which can be considered a double Doppler shift. To measure the frequency shift, a second beam is used and the principle of optical beating or heterodyning of two frequencies is used to determine the frequency difference between the two beams. In the differential or dual beam technique, which is used in this work, the optical beating takes place because of the difference in angle of the two beams. Absil (1995) shows that the difference frequency f, which is observed by the detector is equal to

$$f = f_{\text{pre}} + \frac{v_{\perp} 2 \sin(\alpha/2)}{\lambda} \tag{3.4}$$

where f_{pre} is the pre-shift frequency and $v_{\perp}$ is the velocity of the particle perpendicular to the direction of observation and in the plane of the beam pair. α is the angle between the two beams or beam pair and λ is the wavelength of the laser beam.

A convenient way to look at the Laser Doppler technique is in terms of the fringe pattern, which is formed by the two intersecting beams. The spacing between the interference fringes, s_{fringe}, is equal to

$$s_{\text{fringe}} = \frac{\lambda}{2 \sin(\alpha/2)} \tag{3.5}$$

A particle that passes the fringe pattern will experience a modulation of light intensity of frequency f, which is equal to the differential Doppler frequency (equation 3.4). One should note that a frequency pre-shift of one of the beams can be interpreted as a moving fringe pattern. Once the frequency f is known, the velocity can readily be obtained:

$$v_{\perp} = s_{\text{fringe}}(f - f_{\text{pre}}) \tag{3.6}$$

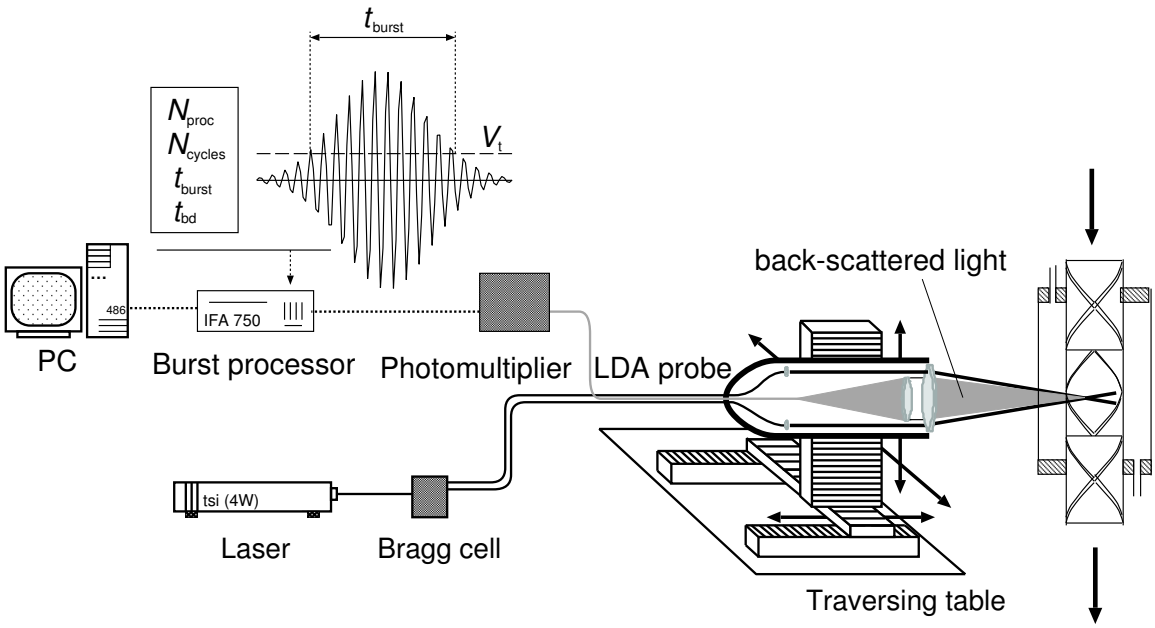

Figure 3.10: Optical setup of LDA.

3.4.4 Optical setup

An overview of the optical setup is given in figure 3.10. The light source consists of a 4W Ar^+ laser (λ=488 and 514.5 nm). Both lines of the laser are used and one of the beams of each beam pair is given a frequency pre-shift (200kHz). The two beam pairs are transmitted via a (2D) probe in back-scatter mode, which was equipped with a 250 mm lens and was traversed with a traversing table (steps of 0.1 mm). Two-component LDA allows the simultaneous measurement of both the axial and tangential velocity component in the measurement volume. The measurement volume is formed by the intersection of the beams. The velocity components are measured indirectly by detecting the back-scattered light of seeding particles, which are added to the flow and consist of glass hollow spheres (section 3.2). The scattered light, which is (two times) Doppler shifted, is detected and transformed to an electrical signal by a photomultiplier detector. The electrical signal or burst is processed by the IFA 750 processor. The IFA removes the pedestal (low frequency component) of the burst and counts the number of cycles of each burst N_{cycles}, which is determined by the number of half cycles or zero passes. One should note that the zero level was lifted above the noise level by applying a threshold voltage (V_{t}=200mV). Before processing the data, the signal is passed through a band pass filter (30kHz...300kHz). Furthermore, the IFA records the burst duration t_{burst}, time between two consecutive burst (time between data) t_{bd}, and processor number (N_{proc}=1,2), which indicates from which beam pair the burst originated. The number of cycles (i.e. 2 times the number of half cycles or zero passes), burst duration (i.e. the number of coefficients between the first and last zero passes divided by the sampling rate), time between data and processor are stored on a standard PC and processed afterwards. The Doppler frequency can be obtained from the number of cycles and burst duration:

$$f = \frac{N_{\mathrm{cycles}}}{t_{\mathrm{burst}}} \tag{3.7}$$

The data-rate, which is the number of bursts per second, was about 50-300 Hz.

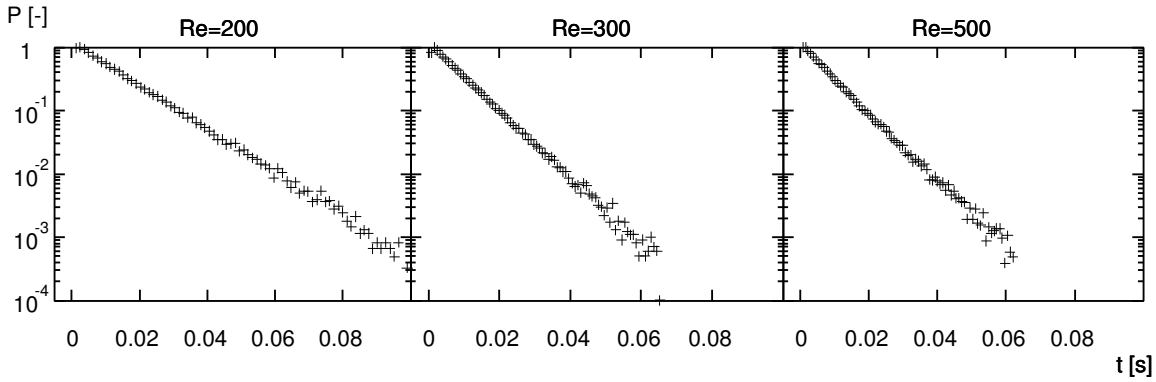

Figure 3.11: Time between data distribution at different Reynolds numbers (axial component).

After processing the raw data, two velocity time series are obtained of respectively the axial and tangential velocity component. Figure 3.11 shows that the time between data distribution was Poisson distributed, which is normal for single-phase LDA data. A deviation from the Poisson distribution usually is an indication of an error source, (Van Maanen (1999)). The data was re-sampled using sample and hold in order to calculate the spectra with the FFT. For the re-sample frequency the average data-rate was used.

3.4.5 Measurement location and volume

Velocity profiles are measured halfway a mixing element in a developed flow and power spectra are calculated from a monitor point that was located in the middle of the profile. Figure 3.12 shows the location of the velocity profile and monitor point. It can be observed that the beams are refracted when passing from air to the measurement section. One should note that the refraction, which is caused by the glass wall and perspex tube are neglected. Since the refractive index of both perspex and glass ($n \approx$1.5) are very close to the refractive index of the glycerol/water solution ($n \approx$1.44) and since the angles at which the laser beams pass the glass and perspex surfaces are small, this will not introduce a large error. Here, for the entire medium a refractive index of n=1.44 is assumed in order to calculate the position of the measurement volume with Snell's law. In practise, the position of the wall is determined by traversing the measurement volume towards the wall. When the measurement volume touches the wall a high data rate will be detected. The measured frequency at the wall is in fact the pre-shift frequency that is scattered from dirt particles or impurities of the glass wall. Since the particles are not moving a more or less continuous burst will be formed, which yields a high data-rate.

The resolution of the LDA measurements is determined to a large extend by the size of the measurement volume. When assuming a Gaussian laser beam (d_{beam}=2.1 mm) and taking into account refraction, the dimensions (length, height, width) of the measurement volumes are equal to l=1.1 mm, and $h = w$=0.07 mm, (Absil (1995); Drain (1980)). The blue beam pair (λ=514.5 nm) is located perpendicular to the green beam pair (λ=488 nm). As a result the measurement volume of the blue beam pair is turned 90 degrees around the radial axis. Furthermore, the refractive index is dependent on the wavelength, which could lead to a dislocation of the measurement volumes. The empirical relation of Cauchy is used to estimate, the difference in refraction:

$$n = \mathrm{A} + \frac{\mathrm{B}}{\lambda^2} \tag{3.8}$$

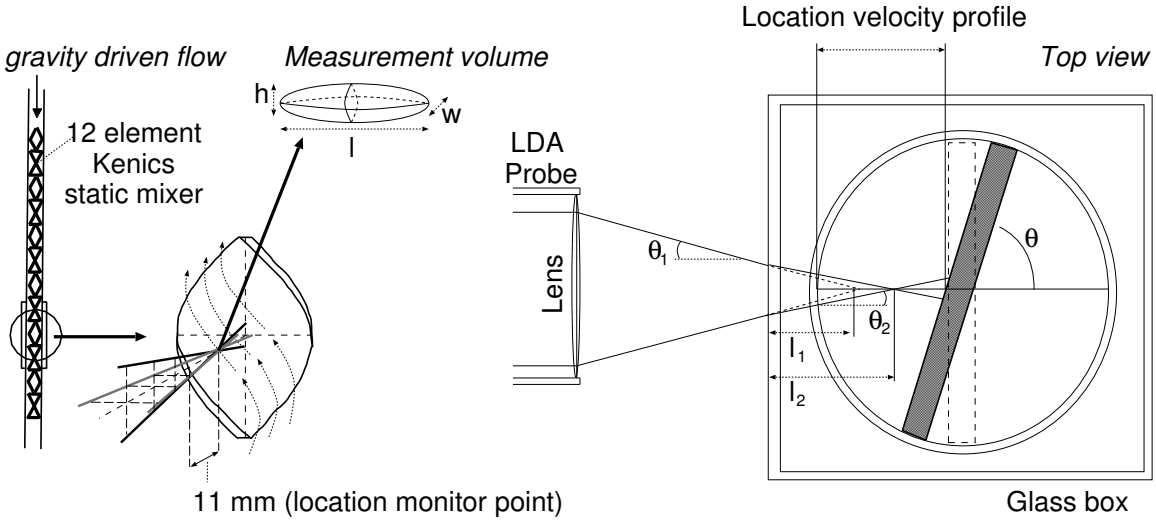

Figure 3.12: Measurement location of monitor point and velocity profiles.

where A≈1.4 and B≈3092 nm^2. It was found that the dislocation in the radial is at most 0.1 mm (near the mixing element), which is of the same order as the accuracy of the position of the measurement volume and small compared to the length of the measurement volume. Therefore, the difference in refraction will not distort the measurements.

3.4.6 Results

The velocity profiles are measured with LDA and compared to velocity profiles that are obtained with Lattice Boltzmann (LB) simulations. The LB method and numerical setup are described extensively in chapter 4. The static mixer is at an angle of θ=65° with respect to the centre line of the laser beams (figure 3.12). When this angle is taken into account, the LB and LDA velocity profiles match for all Reynolds numbers which are measured (figures 3.13 and 3.14). In these figures, the bottom axis indicates the radial position relative to the tube diameter ($r^* = \frac{r}{D}$) and the left and right axis both indicate the velocity relative to the mean velocity ($u^* = \frac{u}{u_0}$). The alignment error in the radial position is in the order of 1.5 mm, which is about 3% of the tube diameter. The error in the dimensionless velocity was at most 0.01. At Re=500 (figure 3.14) the dimensionless mean velocity and standard deviation are plotted. The mean velocity of the LB simulation was obtained by averaging between time step 18000 and 20000. The relatively large standard deviation at Re=500 is mainly caused by the unsteady flow in the form of the oscillation of vortices and compares quite well to the LB simulations. However, near the wall a deviation is found in the tangential component. This deviation is absent in the axial component. Unfortunately, a satisfactory explanation for this deviation could not be found.

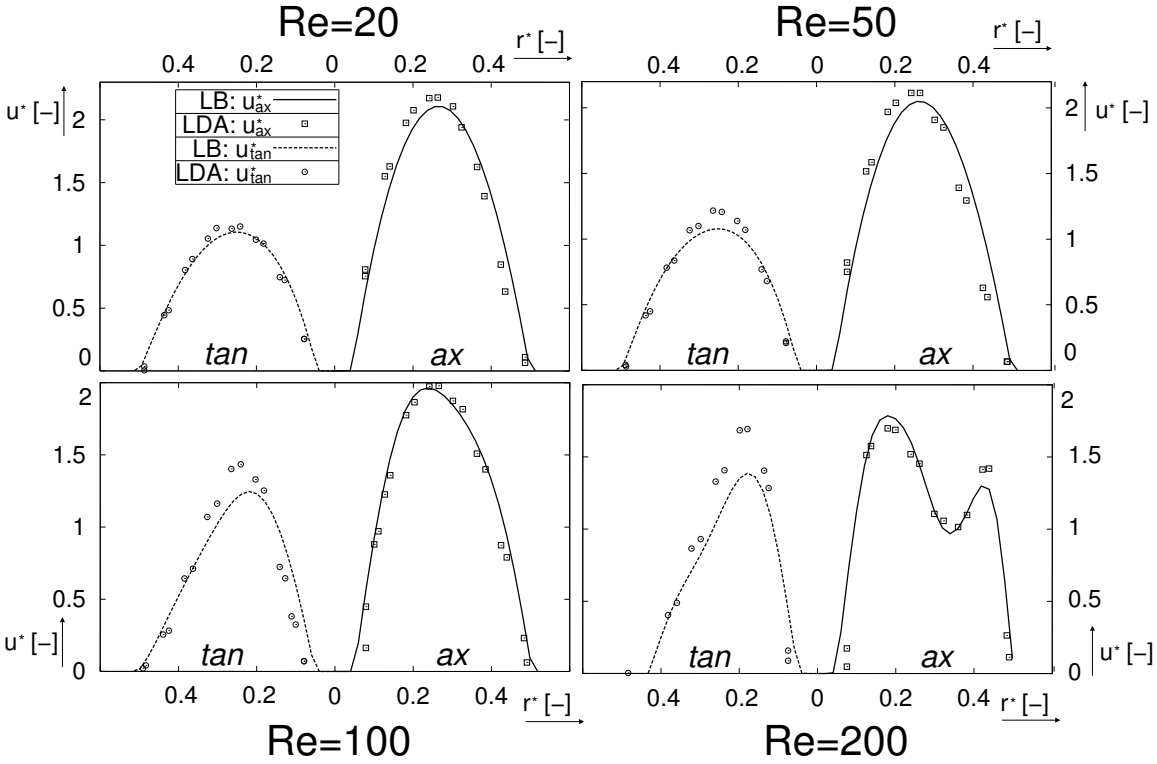

Figure 3.13: Comparison of the tangential (left-side) and axial (right-side) velocity profiles obtained with LDA and LB at Re=20,50,100,200.
(Re=20. . . 100: μ_0=0.070 Pa s, ρ_0=1212 kg/m^3 Re=200: μ_0=0.0385 Pa s, ρ_0=1208 kg/m^3)

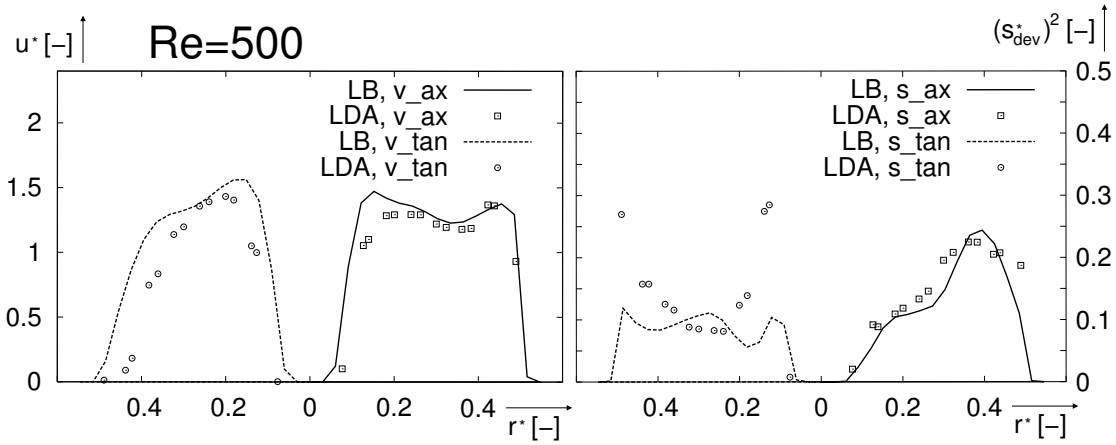

Figure 3.14: Comparison of the tangential and axial velocity profiles (left figure) and standard deviation (right figure) obtained with LDA and LB at Re=500. (μ_0=0.0275 Pa s, ρ_0=1194 kg/m^3)

3.4.7 Dynamic behaviour of the flow

Simulations have indicated that the flow has an early transition to unsteady flow. This transition was studied by recording time series of the velocity in the middle of the velocity profile. The exact location of the monitoring point is shown in figure 3.12. The transition to unsteady flow can clearly be observed in the time series. Figure 3.15 shows the time series at the monitor point of Re=200,300,500. It can be observed that oscillations appear in the flow. At Re=200 the fluctuations are caused by small uncertainties in the velocity. When the Reynolds number increases significant fluctuations appear (Re=300) and they become more irregular at higher Reynolds numbers (Re=500). These strong fluctuations are an indication for the transient behaviour of the flow.

The unsteady behaviour of the flow is explored in more detail by looking at the frequency spectra. Figure 3.16 shows the power spectra of Re=300 and Re=500, which are the average of55 spectra. The spectra are normalized with the highest power, which was found at Re=500. At Re=300 two peaks are observed. The small peak at $f \approx 7$ s^{-1} could be linked to the oscillation of the vortical structures that arises in the mixer and was also observed in the LB simulations, In chapter 4 more details on the oscillatory behaviour of the vortices is given and comparison of experimental and numerical data is made. The low frequency peak (f=1 s^{-1}), which can also observed in the time series, was absent in the simulations. It is assumed that this low frequency is caused by vibration or resonance of the setup, since this low frequency peak was not observed at other Reynolds numbers and was absent in the simulation. At Re=500 the oscillatory behaviour becomes more irregular, which translates into a broader spectrum. The time series also indicates a more violent and irregular fluctuation of the velocity. A similar trend was also observed in the simulations (chapter 4).

3.5 Concluding remarks

In this chapter, it was shown that the PIV technique together with the RIM technique is a powerful technique to study the flow inside complex media. However, due to imperfections in the geometry of the glass mixer, it was not possible to obtain data suitable for a quantitative comparison. Improvements can easily be made by improving the shape of the mixer for example by molding the mixer. Unfortunately, such technique is expensive and the manufacturing time was uncertain. Despite the geometrical inconsistencies of the static mixer, a qualitative agreement was found at Re=430. Since the experiments were not detailed enough for a quantitative comparison of numerical and experimental results, it was decided to abandon the PIV technique and continue with LDA.

Point measurements in a steel static mixer were performed with LDA. A good agreement between the CFD results and LDA measurements was found. Furthermore, the measurements demonstrated that an early transition to unsteady flow takes place in the Kenics™ static mixer. A more detailed description of the CFD methods will be provided in the next chapter. In this chapter also a more detailed analysis of the transition will be given.

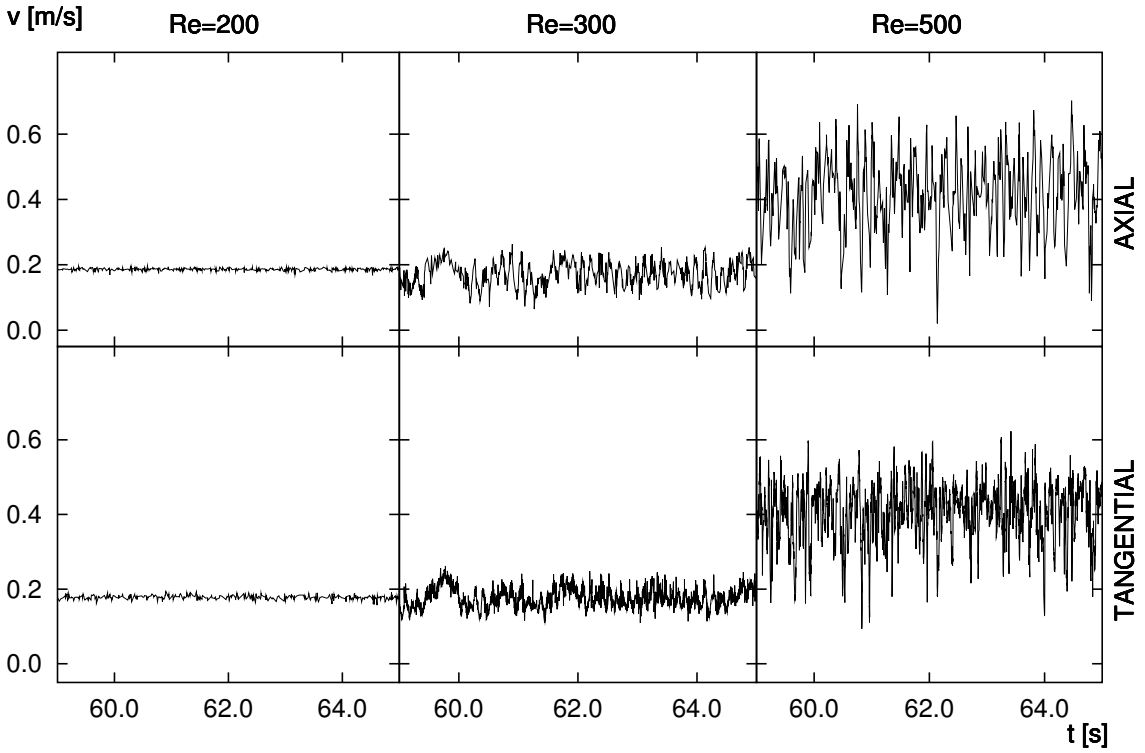

Figure 3.15: Time series of axial (top) and tangential (bottom) velocity at monitor point.

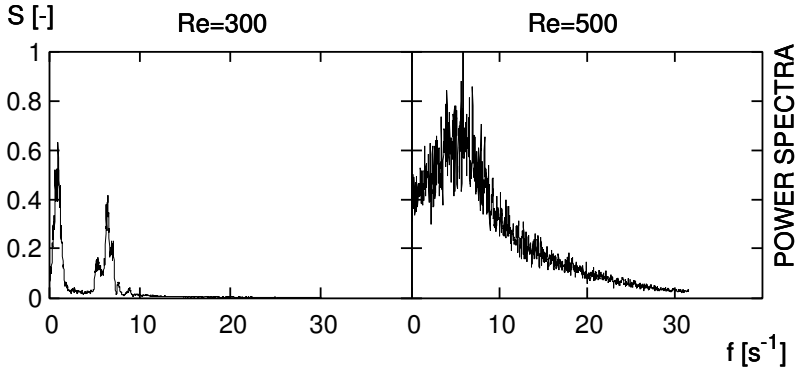

Figure 3.16: Power spectra (obtained with LDA) at Re=300 and Re=500, respectively.

4

Dynamic Flow in Kenics™ static mixer: An Assessment of various CFD methods

The flow in the Kenics static mixer is investigated in detail both numerically and experimentally in the range of $\mathrm{Re} = 100 \ldots 1000$. It was found that at $\mathrm{Re} = 300$ the flow becomes unsteady. Two numerical methods, the lattice Boltzmann (LB) method and the finite volume method (FLUENT), were compared and used to simulate the flow. The LB method proved to be a relatively fast and cheap (in terms of memory) alternative for the simulation of the transient flow in the Kenics static mixer at $\mathrm{Re} > 300$. Furthermore, the flow field and dynamic behaviour were validated by means of LDA experiments. The transient behaviour observed could be explained by studying the dynamics of the vortices in the flow. The transition to unsteady flow takes place, when the vortices start to stretch out over an entire mixing element and create a disturbance in the flow, which subsequently triggers the unsteady behaviour. [1]

4.1 Introduction

The Kenics static mixer, which is designed already in the 60s, is mainly used for in-line blending of liquid, heat exchange and to promote plug flow (i.e. uniform residence time). A large number of studies, which have been conducted over the past decades, focus on one or more of these three research topics.
(1) The publications that focus on mixing are Grace (1971); Wilkinson and Cliff (1977); Sir and Lecjacks (1982); Pahl and Muschelknautz (1982); Heywood et al. (1984); Arimond and Erwin (1985); Bakker and LaRoche (1995); Rauline et al. (1995); Hobbs and Muzzio (1997a, 1998); Hobbs et al. (1998); Rauline et al. (2000); Mudde et al. (2002). (2) The publications that focus on heat exchange are Grace (1971); Chen and MacDonald (1973); Genetti (1982); Cybulski and Werner (1986)); Lecjacks et al. (1987); Joshi et al. (1995); Mudde et al. (2004). (3) the publications that focus on the residence time distribution are Grace (1971); Nigam et al. (1980); Kemblowski and Pustelnik (1988); Hobbs and Muzzio (1997b).

There are several advantages which a static mixer has over a mechanical mixer (e.g. a stirred tank reactor): the low maintenance and operating costs, low space requirements and the fact that there are no moving parts in a static mixer. A static mixer is in principle nothing more than a stationary obstacle placed in a tubular reactor in order to promote mixing. In the case of the Kenics static mixer the obstacle consists of twisted metal plates, which are welded together. The twisted plates or mixing elements are designed in such a way that a mixing element splits the liquid into two streams and recombines the two streams formed by the previous element. This is achieved by placing the

[1] This chapter is published as Van Wageningen et al. (2004a)

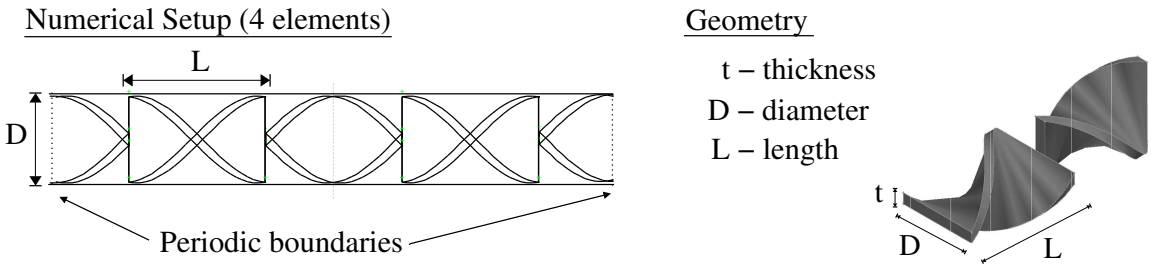

Figure 4.1: Numerical setup and geometry of Kenics static mixer.

elements at an angle of $90°$. The twist angle of a mixing element is $180°$ and two consecutive elements alternate in rotation direction, see figure 4.1. This way the liquid is not only split at each element, but also forced to change its rotation which also contributes to the mixing via the formation of vortices and 'stretching' of the fluid. More information about static mixers can be found in Harnby et al. (1992).

Here, the Kenics static mixer is investigated as part of a project which concerns the recovery of copper from waste streams by means of waste to waste technology, Hage et al. (1999). Waste to waste technology is based on cleaning waste streams by combining two different waste streams. In this project waste streams containing copper ions are combined with waste streams containing carbohydrates in order to recover copper particles, which are the end product. The copper particles formed grow during their residence in the reactor and their size determines their economic value. A more uniform size has a higher economic value. Therefore, in order to improve the economic value of the end product, it is important to control the residence time of the copper particles. One way to achieve this is to place Kenics static mixers along the reactor.

One of the problems that can occur in the Kenics static mixer reactor is the entrapment of particles. In order to keep all particles in suspension a high velocity –and as a result a high Reynolds number ($\mathrm{Re} \approx 10^5$)– is necessary. However, the growth of the particles is a slow process, which leads together with the high axial velocity to an extremely long reactor. Therefore, as an alternative, a vertical reactor is investigated. The vertical reactor avoids problems with sedimentation and can operate at much lower velocities. The only restrictions are the residence time distribution and the mixing of the particles, which both have to be virtually uniform. The Reynolds number at which such a reactor should operate, varies from $\mathrm{Re} = 100$ up to $\mathrm{Re} = 1000$. For this range little is known about the laminar structures that occur in the flow of a Kenics static mixer, since most studies only present reliable data on low Reynolds number flows ($\mathrm{Re} < 10$), e.g. Hobbs et al. (1998); Bakker and LaRoche (1995), who both used FLUENT to simulate the flow in the Kenics static mixer.

Unfortunately, validation is often lacking in literature, while a good grid independence study or comparison with experiments is a vital part of CFD. Therefore, CFD results which were obtained at a relatively high Reynolds number ($\mathrm{Re} > 200$) and on a relatively coarse grid e.g. Hobbs and Muzzio (1998), should be interpreted with care and it can be questioned whether all the results are valid. So, the aim of this study is to obtain accurate results up to at least $\mathrm{Re} = 500$ and to validate these results with LDA measurements for the flow in a Kenics static mixer.

In literature several numerical studies on the flow in a Kenics static mixer have been published. The focus was either on the pressure drop, Rauline et al. (1995) or the mixing characteristics, Arimond and Erwin (1985); Hobbs and Muzzio (1997b,a), which are to a large extend based upon the work of Ottino (1989). Arimond and Erwin (1985) were among the first to study the mixing properties

of the Kenics static mixer with Computational Fluid Dynamics (CFD). They simulated the mixing of two similar fluids, which differed only in color (black and white), and they showed that their results are in good agreement with a comparable experiment. Hobbs and Muzzio (1997b,a) used the commercial finite volume (FV) code FLUENT to calculate the flow field and developed software to track tracer particles through the static mixer in order to characterize the mixing. This approach was also followed by Fourcade et al. (2001), who used a finite element (FE) code, POLY3D to calculate the flow field and an in-house code to track the tracer particles. Fourcade et al. (2001) validated the mixing characteristics of the static mixers by means of Laser Induced Fluorescence (LIF).

In order to track small particles in the static mixer, Mudde et al. (2002) solved the particle force balance, in which only the drag force was considered. They showed that the end location of a particle is very sensitive to small errors in its trajectory. Their explanation is that a particle has to chose either 'left' or 'right', when it approaches a new mixing element. Therefore, small errors in the particle trajectory can cause a different 'choice' at one of the elements, which will lead to a totally different end position of the particle. A similar argument can be made for the flow field. Small errors in the flow field might, therefore, also lead to different trajectories of the particles, which stresses the importance of an accurate flow field and the need for validation. One should note that this argumentation is valid for a single particle realization and that despite of the large errors, which can be made in a single realization, the statistical information obtained with multiple particle realizations can still be correct.

In this investigation the commercial package FLUENT was used to calculate the flow in the Kenics static mixer. FLUENT is a generic multi-purpose code, which can be applied with success to various applications, Fluent Inc. (2003a). However, in an attempt to refine the computational grid used in the Kenics static mixer, FLUENT appeared to have very high memory requirements for the refined mesh, which was ultimately needed for the grid independence tests at relatively high Reynolds numbers ($\mathrm{Re} = 500$). Therefore, an alternative approach was used, namely the lattice Boltzmann (LB) method. Kandhai et al. (1999) showed that LB could be used to simulate the flow in a SMRX static mixer and can be an alternative for standard (FV) or (FE) codes. However, in their work a detailed validation with an experimentally measured flow field was not reported. Furthermore, the geometry of the SMRX static mixer is very different from the Kenics static mixer which is considered in this work.

This chapter will describe the comparison of the performance of the commercial package FLUENT V6 (FV) to the LB code with respect to CPU time and memory requirements, and will give an overview of the grid independent CFD results of different flow regimes, which occur in the Kenics static mixer. The CFD results are validated by means of Laser Doppler Anemometry (LDA) measurements. Furthermore, the transition from steady to unsteady flow at $\mathrm{Re} \approx 300$ is investigated in detail both experimentally and numerically. In the next section, the numerical methods (LB and FLUENT) are described and a validation of both methods is shown. In the third section, the LDA setup is described and the LDA results are compared with the LB results. Finally, the dynamic behaviour in the Kenics static mixer is discussed in more detail and the conclusions are presented.

4.2 Computation of Flow Field

4.2.1 Numerical Setup

The commercial package FLUENT V6 and an in-house lattice Boltzmann code (LB) are used to simulate the flow in a 4 element Kenics static mixer. The aspect ratios of the mixing elements are ($\mathrm{t/D} = 0.08$) and ($\mathrm{L/D} = 1.5$), see figure 4.1. Periodic boundary conditions and a constant body

Grid	Size
FL: very coarse	15k
FL: coarse	90k
FL: default	0.7M
LB : coarse (D=80)	2.4M
LB : default (D=120)	7.8M
LB : dense (D=160)	19.3M
LB : denser (D=180)	27.5M
LB : densest (D=200)	37.7M

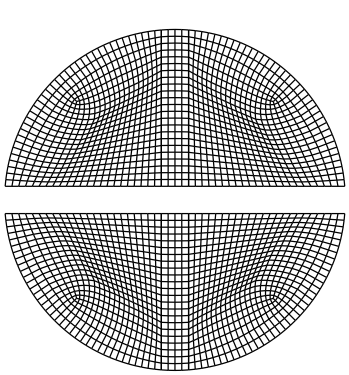

FLUENT default mesh

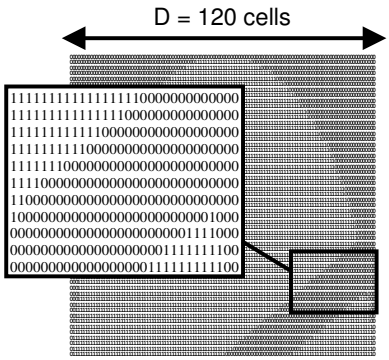

LB default grid

Figure 4.2: Overview of cross sections of grids used.

force are applied in the axial direction and no slip boundaries are used at the wall. This way an 'infinitely' long mixer is simulated. The FLUENT grid is created with GAMBIT 2.0 and consists of 700k hexahedral cells twisted along the elements. The (structured and stair-cased) LB grid consists of 10M grid nodes, which boils down to 7.8M nodes in the flow domain. The other nodes are wall nodes. The different grids are illustrated in figure 4.2. Different cases are solved on a Linux (Redhat 7.1) cluster with multiple nodes. Each node has a dual Intel Pentium processor (2 times 1.6 GHz) and 1 GB of memory. All simulations are carried out on 2 nodes (4 CPUs, 2 GB). An overview of the interpolation schemes and solver options used in FLUENT and a more detailed description of the LB method are given in section 4.2.2.

Different Reynolds numbers ($\mathrm{Re} = 10 \ldots 1000$), which are based on the tube diameter D and mean axial velocity $\overline{u}_{\mathrm{ax}}$ are investigated. The Reynolds number is adjusted by varying the viscosity η of the liquid. The initial condition of the simulated flow in the mixer is a zero velocity field, on which a constant body force, F_{b}, is applied (similar to gravity). Eventually the flow converges to a certain pressure drop and mean axial velocity, which determines the Reynolds number. For $\mathrm{Re} < 200$ the flow converges to a steady state solution, while for $\mathrm{Re} > 300$ the flow remains unsteady. Figure

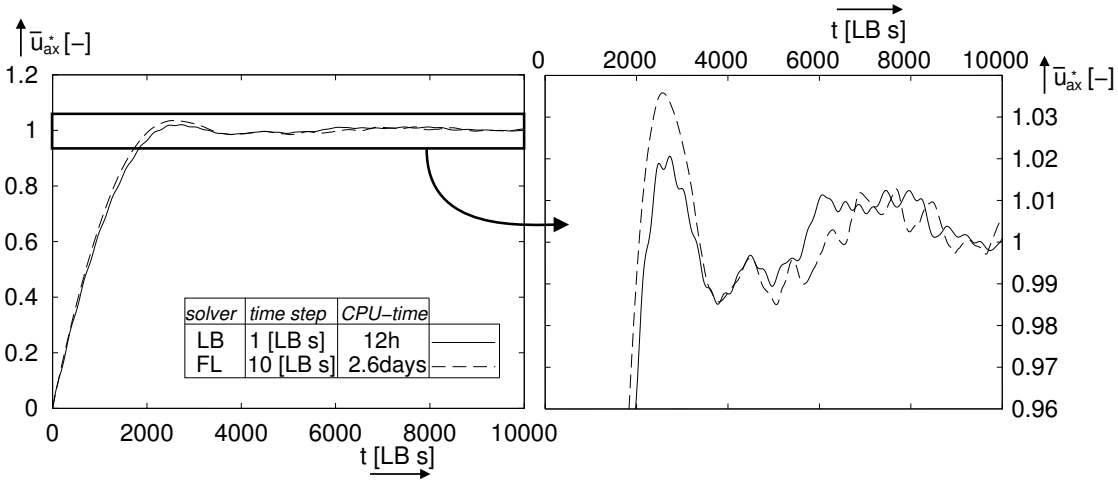

Figure 4.3: Development of mean axial velocity at $\mathrm{Re} = 500$ from start-up ($t = 0$, $\vec{u} = 0$) on the default grids.

4.3 shows the mean axial velocity, which is developing from start-up at $\mathrm{Re} = 500$. The mean axial velocity is made dimensionless by its average value in the time interval $9000 - 10000$ [LB s]. ([LB s] indicates the time in lattice Boltzmann units.) The small fluctuations in the mean axial velocity indicate the unsteady behaviour and are observed in both the FLUENT and LB simulations. A small time-step is necessary to capture these oscillations, which is by definition 1 [LB s] for the LB simulation and is set to 10[LB s] for the FLUENT simulation.

4.2.2 LB Solver

In contrast to conventional numerical schemes, which are based on discretizations of the macroscopic continuum equations, the lattice Boltzmann method is a mesoscopic approach for simulating fluid flow. In this method a fluid is modeled by the dynamics of the population of fictitious particles, which reside on a discrete lattice. The lattice nodes are linked with a number of their neighbours. In the case of the D3Q19 BGK model, Qian et al. (1992), which is used in this study, each node has 18 links to neighbouring nodes ('rest' particles are also included at each node). The particles move along these links during the propagation phase and interact with each other during the so-called collision phase, in which the particles exchange momentum via a specific collision operator. In the BGK model the collision operator is based on a single time relaxation.

The time evolution of the BGK model is given by the following equation:

$$f_{\mathrm{i}}(\mathbf{r} + \mathbf{c}_{\mathrm{i}}, t+1) = f_{\mathrm{i}}(\mathbf{r}, t) + \frac{1}{\tau}(f_{\mathrm{i}}^{\mathrm{eq}}(\mathbf{r}, t) - f_{\mathrm{i}}(\mathbf{r}, t)), \tag{4.1}$$

where $f_{\mathrm{i}}(\mathbf{r}, t)$ denotes the particle density which resides on lattice point $\mathbf{r}$ at time-step t, and is moving along link i with local particle velocity $\mathbf{c}_{\mathrm{i}}$, τ is the so-called BGK relaxation parameter. The equilibrium distribution function, $f_{\mathrm{i}}^{\mathrm{eq}}$, (valid for small Mach numbers) can be written up to $O(\mathbf{u^2})$, Qian et al. (1992):

$$f_{\mathrm{i}}^{\mathrm{eq}} = \rho w_{\mathrm{i}}\left[1 + 3\mathbf{c}_{\mathrm{i}} \cdot \mathbf{u} + \frac{9}{2}(\mathbf{c}_{\mathrm{i}} \cdot \mathbf{u})^2 - \frac{3}{2}\mathbf{u}^2\right] \tag{4.2}$$

where ρ is the density, w_{i} are the weight-factors and $\mathbf{u}$ is the macroscopic velocity (in LB units). The density and macroscopic velocity can be obtained at each lattice point from the moments of the distribution function $f_{\mathrm{i}}(\mathbf{r}, t)$:

$$\rho(\mathbf{r}, t) = \sum_{i=0}^{18} f_{\mathrm{i}}(\mathbf{r}, t) \tag{4.3}$$

$$\mathbf{u}(\mathbf{r}, t) = \frac{\sum_{i=0}^{18} f_{\mathrm{i}}(\mathbf{r}, t)\mathbf{c}_{\mathrm{i}}}{\rho(\mathbf{r}, t)} \tag{4.4}$$

The pressure is linked to the density and is equal to $p = \rho/3$. Qian and Orszag (1993) showed that if the density variation $\delta\rho$ is small, the corresponding momentum equation is the same as the Navier-Stokes equation (in LB units). A detailed overview of the lattice Boltzmann method can be found in, Chen and Doolen (1998).

The LB method uses a staircase, structured grid and as a result a large number of grid points are necessary. The grid spacing determines the time-step size. Therefore, a dense grid will lead to a small time-step. The tube diameter in LB units, D_{LB} is equal to the number of nodes in the radial direction, $n_{\mathrm{nodes,rad}}$ and the viscosity is equal to $\eta = \frac{2\tau - 1}{6}$. The body force was equal to $F_{\mathrm{b}} = 10^{-4}$ and τ was used to set the viscosity. The Reynolds number can be used to scale and is given by:

$$\mathrm{Re} = \frac{6\rho\, D_{\mathrm{LB}}\, \overline{u}_{\mathrm{ax}}}{2\tau - 1} \tag{4.5}$$

The LB units can be transformed to dimensionless units in the following way:

$$\rho^* = 1 \qquad \mathrm{D}^* = 1 \qquad \overline{u^*}_{\mathrm{ax}} = 1 \qquad \eta^* = \frac{1}{\mathrm{Re}}$$

$$l^* = \frac{l}{D_{\mathrm{LB}}} \qquad u^* = \frac{u}{\overline{u}_{\mathrm{ax}}} \qquad t^* = \frac{t\, D_{\mathrm{LB}}}{\overline{u}_{\mathrm{ax}}} \qquad p^* = \frac{\frac{p}{3} - F_{\mathrm{b}} x}{\rho \cdot {\overline{u}_{\mathrm{ax}}}^2}$$

where the symbol $*$ is used to denote the dimensionless units. The 'LDA' or 'real world' units can be transformed to dimensionless units in a similar manner:

$$\mathrm{Re} = \frac{\rho_0\, \mathrm{D}_0\, \overline{u}_{0,\mathrm{ax}}}{\eta_0}$$

$$\rho^* = 1 \qquad \mathrm{D}^* = 1 \qquad \overline{u^*}_{\mathrm{ax}} = 1 \qquad \eta^* = \frac{1}{\mathrm{Re}}$$

$$l^* = \frac{l}{\mathrm{D}_0} \qquad u^* = \frac{u}{\overline{u}_{0,\mathrm{ax}}} \qquad t^* = \frac{t\, \mathrm{D}_0}{\overline{u}_{0,\mathrm{ax}}} \qquad p^* = \frac{p_0}{\rho_0 \cdot {\overline{u}_{0,\mathrm{ax}}}^2}$$

where the subscript 0 denotes the values used in the LDA experiment.

4.2.3 FLUENT Solver

FLUENT is a generic multi-purpose code for modeling fluid flow and heat transfer in complex geometries. It numerically solves the Navier-Stokes equations on unstructured meshes. The Navier-Stokes equation for a Newtonian fluid yields:

$$\frac{\partial \mathbf{u}}{\partial t} + \mathbf{u} \cdot \nabla \mathbf{u} = -\frac{1}{\rho} \nabla p + \frac{\eta}{\rho} \nabla^2 \mathbf{u}. \tag{4.6}$$

A detailed description of the solver and interpolation schemes that are used by FLUENT can be found in Fluent Inc. (2003b).

For the sake of simplicity the FLUENT parameters are matched to the LB parameters and the solution was obtained in LB units. The LB units are translated to dimensionless units afterward. For this specific application the following solver options were selected in FLUENT:

- the segregated solver with second order implicit temporal discretization,
- the central-differencing discretization scheme (CDS),
- the second order pressure scheme.

The equations were interpolated until convergence was reached within one time-step (10^{-3} for continuity, 10^{-4} for velocities).

4.2.4 Grid Independence and Pressure Drop

Results obtained on different grid sizes are compared, which have a size of $15\mathrm{k}, 90\mathrm{k}, 700\mathrm{k}$ for the FLUENT solver and $2.4\mathrm{M}, 7.8\mathrm{M}, 19.3\mathrm{M}, 27.5\mathrm{M}, 37.7\mathrm{M}$ for the LB solver, respectively. The results corresponding to $\mathrm{Re} = 200$ and $\mathrm{Re} = 500$, respectively, are compared with respect to the pressure drop, velocity and vorticity. The LB results are used as a reference point for the FLUENT results.

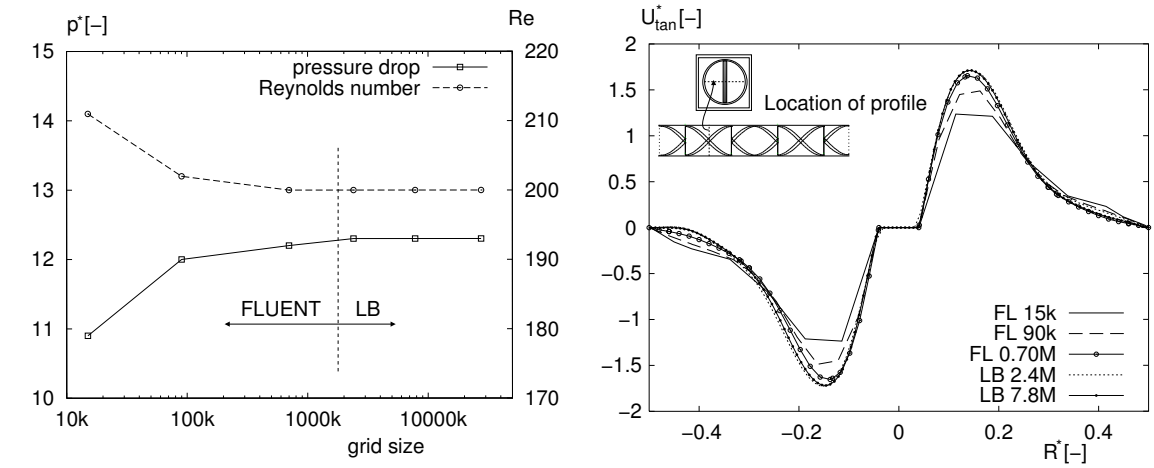

Figure 4.4: Grid independence check of pressure drop, Reynolds number and tangential velocity profiles around $\mathrm{Re} = 200$ at $t = 10000$ [LB s].

The left hand side of figure 4.4 shows the pressure drop and Reynolds number at different grid sizes and at $t = 10000$ [LB s]. The Reynolds number is determined by the average axial velocity, to which the solution eventually converges. The viscosity and body force are set in such a way that a Reynolds number of $\mathrm{Re} = 200$ is obtained. The points to the right of the vertical dashed line. are calculated with the LB method, while the others are calculated with FLUENT. It should be noted that since all the simulations have the same initial conditions, they should converge to the same Reynolds number and pressure drop. The right hand side of figure 4.4 shows the corresponding velocity profiles which are located along a line half way a mixing element.

It can be observed that the pressure drop and Reynolds number can already be predicted with reasonable accuracy at a relatively coarse (90k) FLUENT mesh. However, the corresponding velocity profile obtained on this mesh still shows some differences with the ones obtained on the more dense meshes. On the other hand the velocity profile obtained on the default FLUENT mesh compares reasonably well to the velocity profiles obtained on the $2.4\mathrm{M}$ and $7.8\mathrm{M}$ LB grids. So, in order to

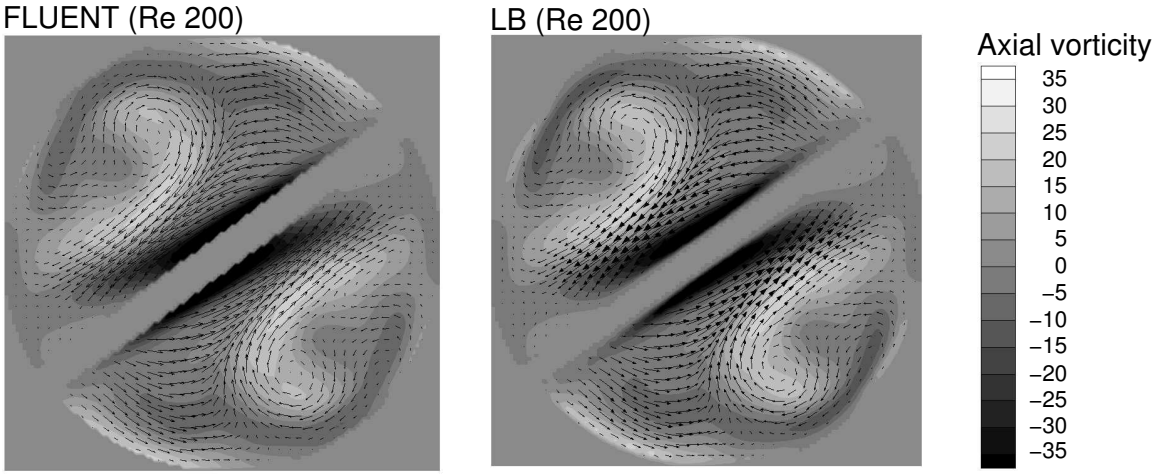

Figure 4.5: Flow structures and vorticity at $\mathrm{Re} = 200$ on the default FLUENT and LB grids (located at 0.3 D from the start of a mixing element and at $t = 10000$ [LB s]).

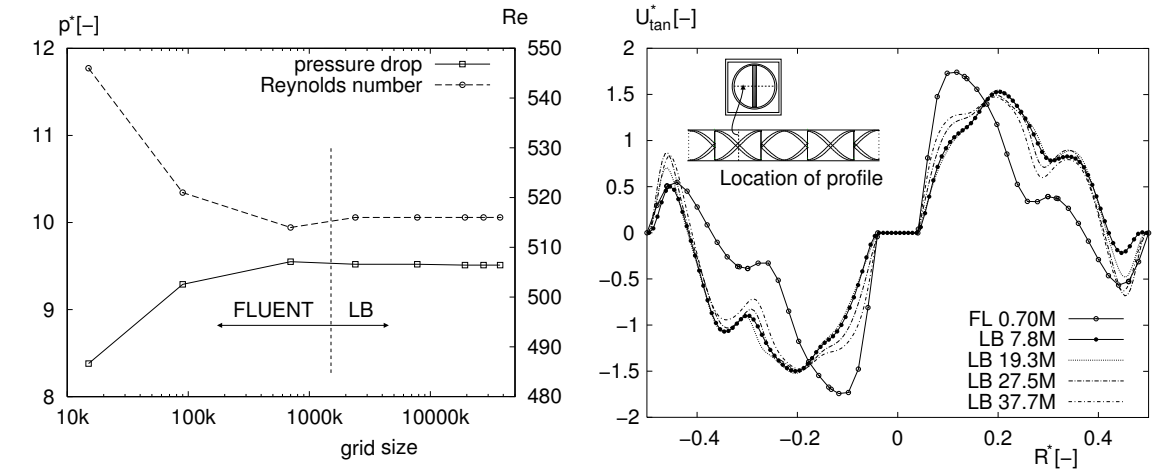

Figure 4.6: Grid independence check of pressure drop, Reynolds number and tangential velocity profiles around $\mathrm{Re} = 500$ at $t = 10000$ [LB s].

get accurate results for $\mathrm{Re} = 200$, the minimal requirements are the $(0.7\mathrm{M})$ mesh for FLUENT and the $(2.4\mathrm{M})$ grid for LB, respectively. Furthermore, figure 4.5 shows that the overall flow structures and axial vorticity, which are obtained on the default grids, match almost perfectly.

Figure 4.6 shows the pressure drop and Reynolds number at different grid sizes (left hand side) as well as velocity profiles along a line half way a mixing element (right hand side) at $t = 10000\,\mathrm{LB\ s}$. The viscosity and body force are set such that a Reynolds number of $\mathrm{Re} = 500$ is obtained. The points to the right are calculated with the LB method, while the others are calculated with FLUENT. The pressure drop and Reynolds number can be predicted on the default FLUENT $(0.7\mathrm{M})$ mesh. However, the corresponding velocity profiles show significant differences. It seems, that the FLUENT mesh is still not 'dense' enough to capture all features of the flow. However, when looking at the overall flow structures and vorticity, which are shown in figure 4.7, one can see that the differences are not too large. The velocities obtained on the LB default $(7.8\mathrm{M})$ grid also shows some small differences with the ones obtained on the more dense grids, but in general they agree

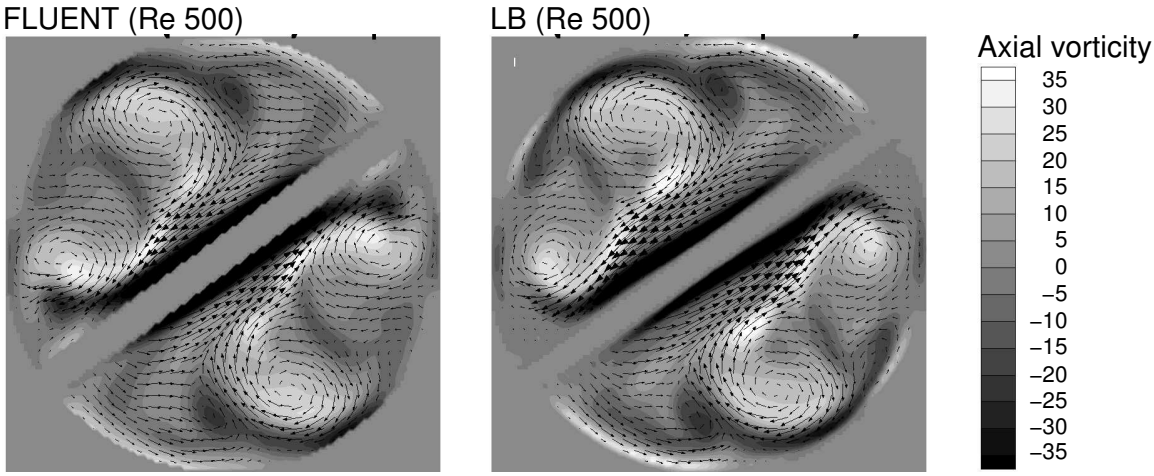

Figure 4.7: Flow structures and vorticity at $\mathrm{Re} = 500$ on the default FLUENT and LB grids (located at 0.3 D from the start of a mixing element and at $t = 10000$ [LB s]).

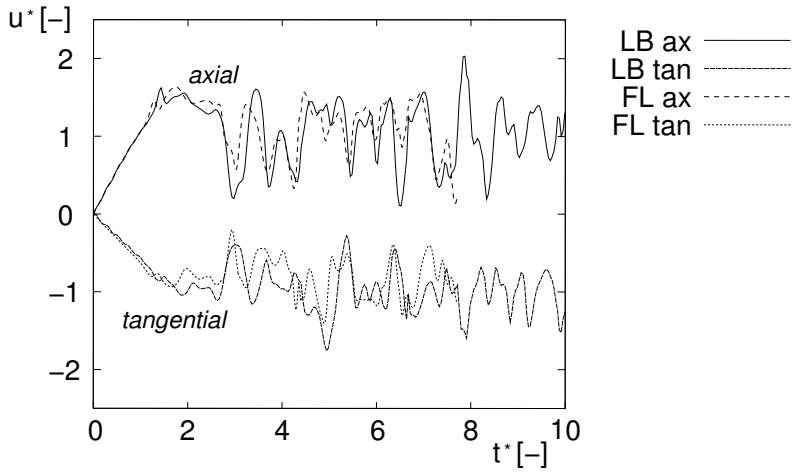

Figure 4.8: Axial and tangential velocity in monitor point close to the center of a vortex at $\mathrm{Re} = 500$.

well. It should be noted that although the global geometries match, there can be small differences in the location and time of the LB profiles due to the different lattice spacing of the grids and discrete time-step size. Furthermore, LB used far less CPU-time than FLUENT. The computational demands of both methods will be discussed in more detail in section 4.2.5.

Figure 4.8 shows the time characteristics of the velocity at a monitoring point which is located close to the center of one of the vortices. In spite of the differences observed in the velocity profiles, there is a good agreement between the LB and FLUENT time series, which are both obtained on the default grids. Even for the longer times we see that the flow oscillations correspond reasonably well. This time-dependent behaviour will be explored in more detail in section 4.4.

In figure 4.9, the normalized pressure drop K as a function of the Reynolds number is plotted for the

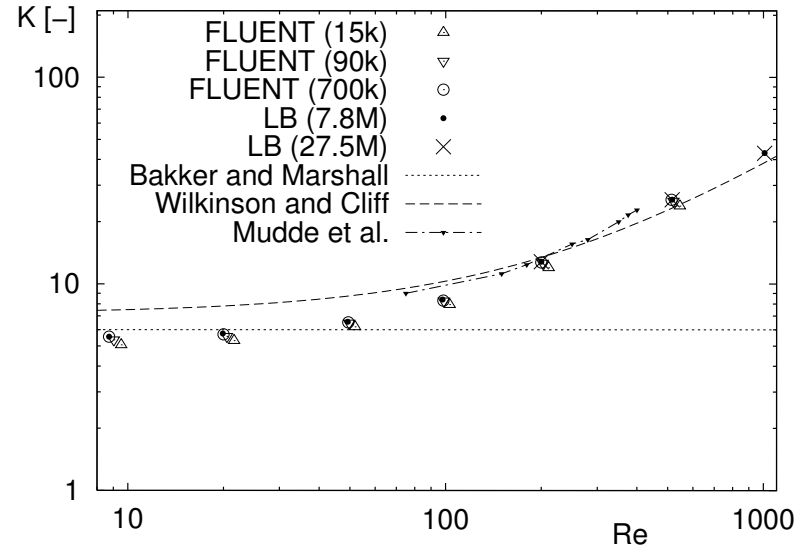

Figure 4.9: Normalized pressure drop as a function of Reynolds number at different grid sizes.

different grid sizes and is also compared with correlations used in literature, Bakker and Marshall (1992); Wilkinson and Cliff (1977) and experimental data, Mudde et al. (2002). In literature the normalized pressure drop is usually presented as the ratio between the pressure drop over a static mixer and over an empty tube of equal length, respectively:

$$K = \frac{\Delta\, p_{\mathrm{mixer}}}{\Delta\, p_{\mathrm{tube}}} \tag{4.7}$$

For low Reynolds numbers the results correspond to the correlation from Chemineer, Bakker and Marshall (1992) and for high Reynolds numbers the results correspond to the correlation from Wilkinson and Cliff (1977). The results are also in good agreement with the experimental data from Mudde et al. (2002). It should be noted, that the $\mathrm{L/D}$ ratio of the mixer used by Mudde et al. (2002) was 1.6 instead of 1.5. However, this small difference doesn't seem to have much influence on the pressure drop. Furthermore, the FLUENT results compare well to the LB results except for the results obtained on the very coarse $(15\mathrm{k})$ mesh, which are slightly of. However, the $(15\mathrm{k})$ results could still be good enough for some engineering purposes, which concern only the pressure drop.

4.2.5 Computational demands of LB and FLUENT

Table 4.1 shows the comparison of the computational demands of FLUENT and LB, respectively. One should note that the steady results are calculated with both the steady and transient solver of FLUENT and that all values related to time are presented in default LB units. For the steady flow at $\mathrm{Re} = 200$, FLUENT can use the steady solver and is roughly two times faster than LB (coarse). When the transient start-up ($\vec{u} = 0$ at $t = 0$) is simulated at $\mathrm{Re} = 200$, FLUENT can use a bigger time-step than LB, but still is roughly two times slower than LB (coarse). Since FLUENT has the option to select the steady state solver, it out performs LB for the low (steady) Reynolds numbers. It should be noted, however, that the LB method intrinsically solves a time-dependent flow and that the time-step is directly linked to the grid-spacing.

At $\mathrm{Re} = 500$, the flow is unsteady and FLUENT needs a smaller time-step than at $\mathrm{Re} = 200$, in order to capture the oscillations that occur in the flow. As a result the computational time that FLUENT needs at $\mathrm{Re} = 500$ increases dramatically. FLUENT now is about five times slower than LB, which makes the LB method especially for this range a good alternative.

Table 4.1: Comparison LB and FLUENT with respect to CPU-time and memory at $t = 10000[\mathrm{LB\ s}]$ (in default LB units) .

Solver	*grid-size* [M]	*time-step size* [LBs]	*number of time-steps*	*CPUs*	*Memory* [MB]	*CPU-time* [h]
$\mathrm{Re} = 200$ **(steady)**						
FLUENT (unsteady)	0.7	100	100	4	660	4.5
FLUENT (steady)*	0.7	∞	1	4	660	1.3
LB (coarse)**	2.4	1.5	6667	4	490	2.3
LB (default)	7.8	1	10000	4	1600	12
$\mathrm{Re} = 500$ **(unsteady)**						
FLUENT (unsteady)	0.7	10	1000	4	660	62
LB	7.8	1	10000	4	1600	12

* The steady state solver of FLUENT was selected.

** Since the grid spacing is bigger, the time-step is larger.

The memory usages of both methods are of a different order. FLUENT uses roughly about 4 times more memory per grid cell than LB uses per grid node. LB uses about 165 bytes per grid node, but about 22% of the nodes are unused wall nodes, which also consume memory. Taking this into account, LB uses effectively about 215 bytes per used grid node, while FLUENT uses about 990 bytes per grid cell. Another disadvantage of an iterative solver like FLUENT is the dramatic increase of CPU-time, when the grid is refined, which makes FLUENT slow at dense grids. However, the LB method also has one drawback. Because of the stair case grid, LB minimally needs about $2.4\mathrm{M}$ grid nodes in order to correctly describe the walls of the Kenics static mixer. Therefore, the LB method is most effective, when a dense mesh is required for the flow structures as well.

4.3 Laser Doppler Anemometry

4.3.1 Experimental Setup

The setup consists of a 12 element Kenics static mixer, which is comprised of stainless steel and is coated black in order to reduce reflections. The flow in the Kenics mixer is fully developed after about three or four mixing elements and the developed flow is comparable to the flow in the 4 element periodic mixer, which is in fact an infinitely long mixer. The aspect ratios of the 'experimental' static mixer are $\mathrm{L/D} = 1.6$ and $\mathrm{t/D} = 0.083$ and the length and diameter of the mixing elements are $\mathrm{L}_0 = 76.5 \pm 1\ \mathrm{mm}$ and $\mathrm{D}_0 = 48.0 \pm 0.1\ \mathrm{mm}$, respectively. The LB simulations are adjusted to match this geometry. Furthermore, the measurement section is made optical accessible by a perspex tube and is surrounded by a square box with glass windows in it in order to reduce refraction.

The accuracy of LDA measurements is better at higher velocities. Therefore, a glycerol/water solution is used to increase the viscosity in order to be able to increase the velocity (while keeping the Reynolds number constant). This results in a smaller uncertainty in the LDA measurements at the relatively low Reynolds numbers. The flow is gravity driven in order to ensure a constant flow-rate. Furthermore, a feedback system is used to control the temperature via a heating and cooling unit. The temperature is kept constant with an accuracy of $0.1^\circ\mathrm{C}$ and the Reynolds number is set by varying the viscosity and velocity ($\mathrm{Re} = 20, 50, 100, \ldots, 450, 500$). The flow-rate is measured with a rotameter, which is calibrated for each viscosity with an integrated mass-flow calibration system. The calibration method was tested with LDA measurements in an empty tube.

A dual beam 4W (Ar^+) laser is used and the light is transmitted via a (2D) probe in back-scatter mode, which allows simultaneous measurement of both the axial and tangential velocity component in a measurement volume. The measurement volume is formed by the intersection of the beams. The velocity components are measured by detecting the back-scattered light of seeding particles, which are added to the flow and consist of glass hollow spheres. These particles are neutrally buoyant and have a diameter in the order of $10\mu\mathrm{m}$. The data is pre-processed by the IFA 750 processor and stored on a normal desktop PC. The data-rate was about $50 - 300\ \mathrm{Hz}$. In figure 4.10 an overview of the setup and measurement location is given.

After processing the raw data two velocity time series are obtained of respectively the axial and tangential velocity component. The time between data (time between two data points) distribution was Poisson distributed, which is normal for LDA data. (A deviation from the Poisson distribution usually is an indication of an error source, Van Maanen (1999).) The data was re-sampled using sample and hold in order to calculate the spectra with the FFT. For the re-sample frequency the average data-rate was used. Profiles are measured halfway a mixing element in a developed flow.

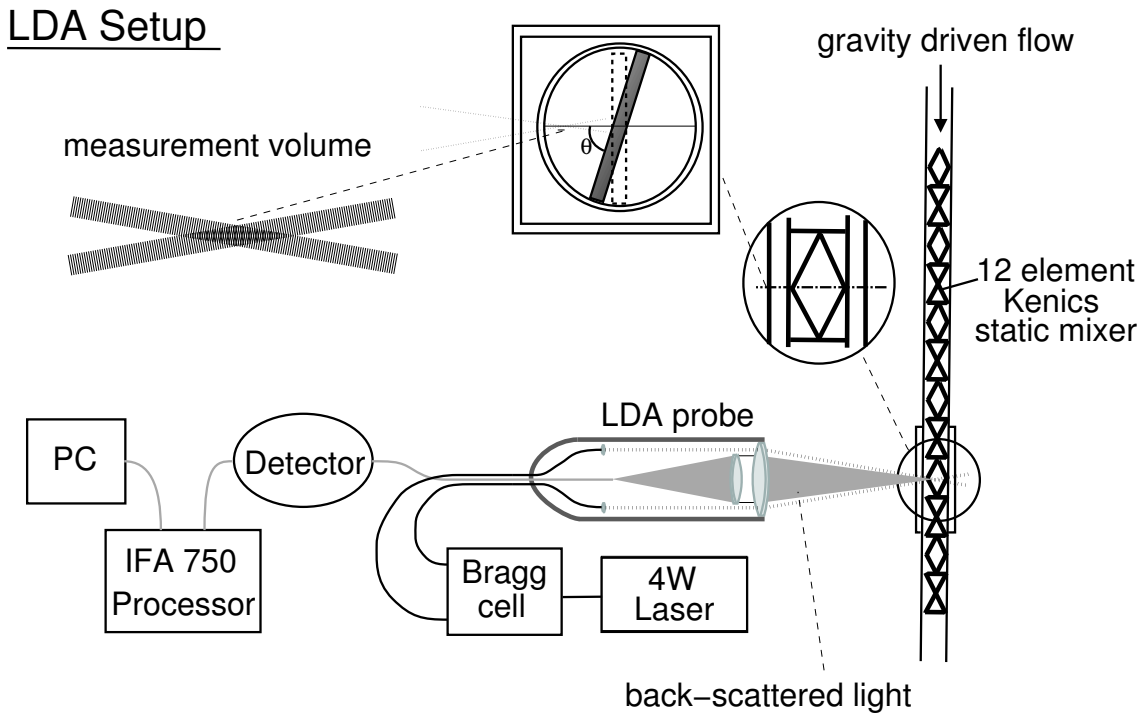

Figure 4.10: LDA setup and location of measurement volume.

4.3.2 Velocity profiles

The static mixer is at an angle of $\theta = 65^\circ$ with respect to the center line of the laser beams (see figure 4.10). When this angle is taken into account, the LB and LDA velocity profiles match for all Reynolds numbers which are measured, see figures 4.11 and 4.12. The alignment error in the radial position is in the order of $1.5\ \mathrm{mm}$, which is about 3% of the tube diameter. The error in the dimensionless velocity was at most 0.01. At $\mathrm{Re} = 500$ (figure 4.12) the dimensionless mean velocity and standard deviation are plotted. The mean velocity of the LB simulation was obtained between $t = 18000[\mathrm{LB\ s}]$ and $t = 20000[\mathrm{LB\ s}]$. The relatively large standard deviation at $\mathrm{Re} = 500$ is mainly caused by the unsteady flow in the form of the oscillation of vortices and compares quite well to the LB simulations. However, near the wall a deviation is found in the tangential component. This deviation is absent in the axial component. Unfortunately, a satisfactory explanation for this deviation could not be found.

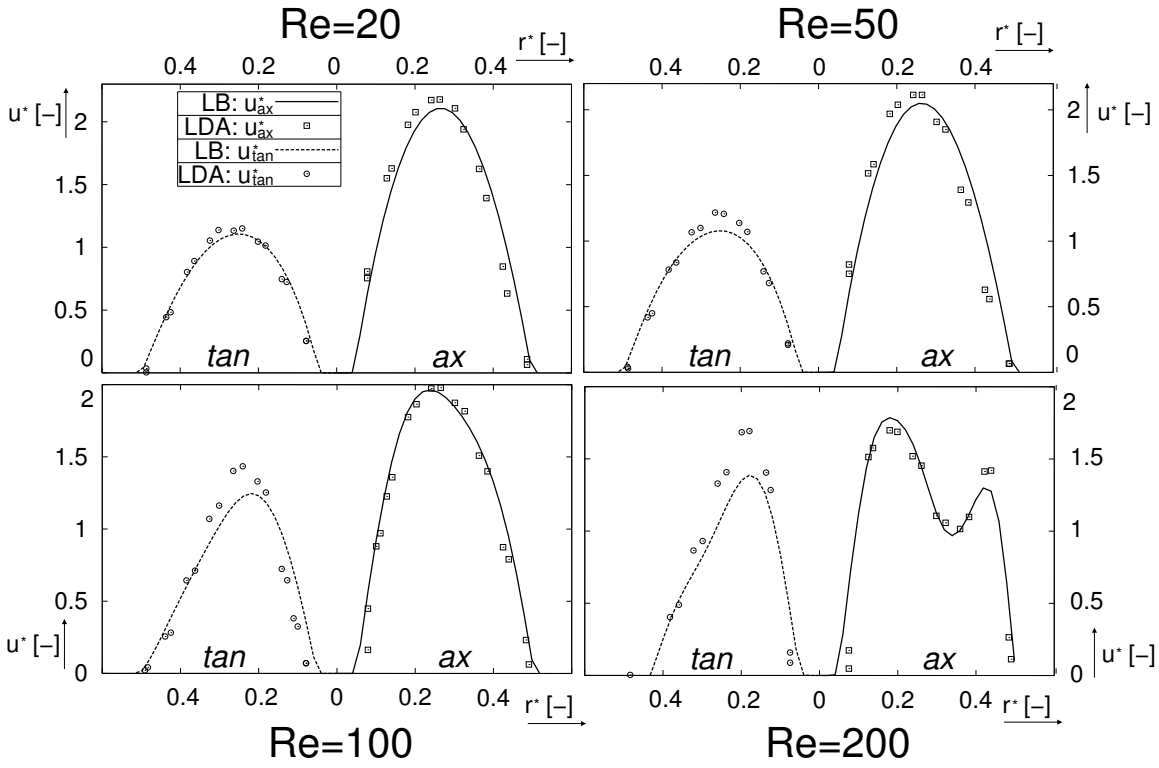

Figure 4.11: Comparison of velocity profiles obtained with LDA and LB at $\mathrm{Re} = 20, 50, 100, 200$. ($\mathrm{Re} = 20 \ldots 100 : \eta_0 = 0.070\ \mathrm{Pa\,s},\ \rho_0 = 1212\ \mathrm{kg/m^3}$ $\mathrm{Re} = 200 : \eta_0 = 0.0385\ \mathrm{Pa\,s},\ \rho_0 = 1208\ \mathrm{kg/m^3}$)

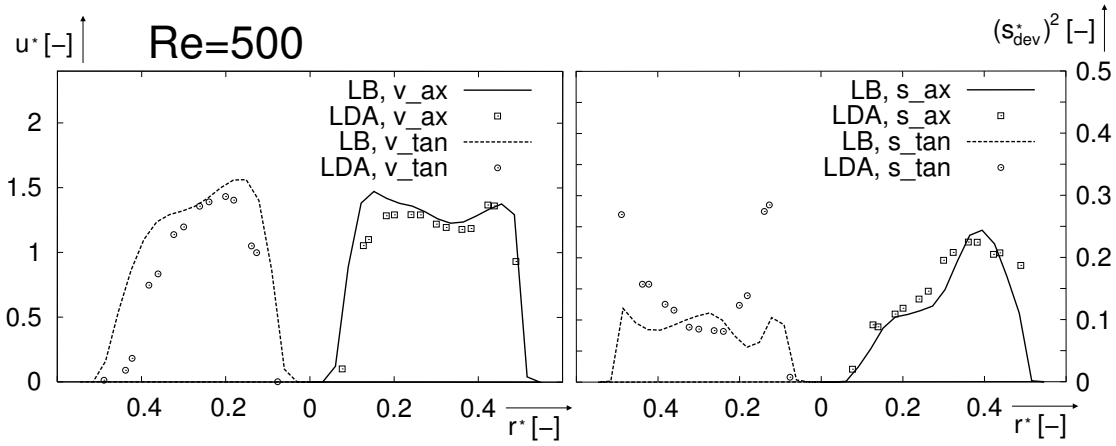

Figure 4.12: Comparison of velocity profiles (left figure) and standard deviation (right figure) obtained with LDA and LB at $\mathrm{Re} = 500$. ($\eta_0 = 0.0275\ \mathrm{Pa\,s},\ \rho_0 = 1194\ \mathrm{kg/m^3}$)

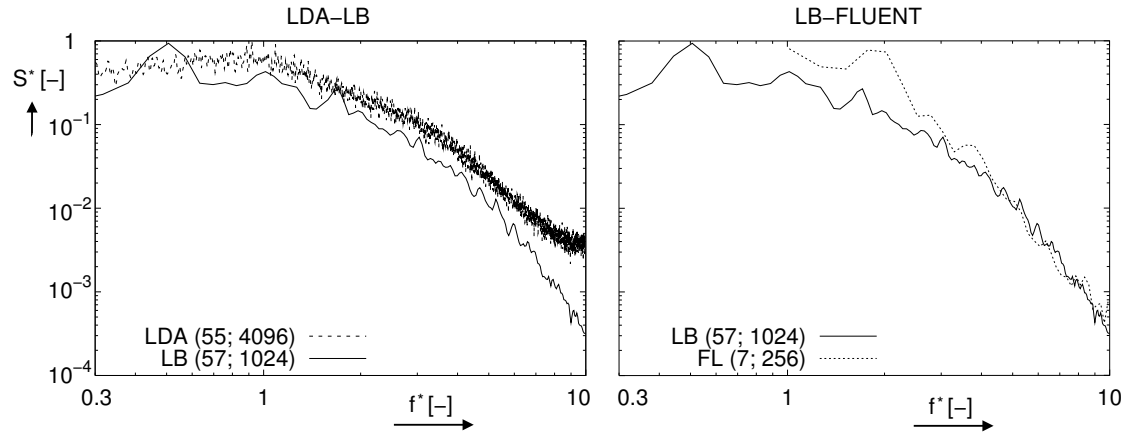

Figure 4.13: $\mathrm{Re} = 500$: Comparison (normalized) power-spectra of LDA to LB and LB to FLUENT, numbers between brackets indicate: (number of blocks; block size).

4.4 Oscillations in Kenics static Mixer

4.4.1 Dynamic behavior

The dynamic behaviour of the flow in the Kenics static mixer is investigated by looking at the power-spectra. The power-spectra are obtained from the times series, which are measured (LDA) or simulated (LB) in a monitor point. The monitor point is located at the middle of the velocity profiles, which were measured with LDA. At this location the noise, which is caused by scattering light, was minimal and the fluctuations in the velocity were significant. The time series, which were obtained at this point, are made dimensionless with respect to the time $t^* = t\,\overline{u}_{\mathrm{ax}}/\mathrm{D}$ and velocity $u^* = u/\overline{u}_{\mathrm{ax}}$. The dimensionless time-series are split into a number of blocks (55 for LDA, 57 for LB and 7 blocks for FLUENT). The blocks have a 50% overlap and each block is multiplied by a Gaussian window. For each block the FFT is taken and the spectra are summed and averaged. It should be noted that the LDA and LB results were more accurate than the FLUENT results, since more blocks are used to obtain the spectra.

The power-spectra of LDA, LB and FLUENT, which are normalized by the highest power, are compared at $\mathrm{Re} = 500$ (axial component), see figure 4.13. The spectra of LDA and LB show good agreement for the low frequencies and also the slope, which starts around $f^* = 1$ is predicted well. However, there is a deviation at the high frequencies, which is caused by the fact that high frequencies are not fully resolved by LDA, because of noise and the re-sampling of the data, Van Maanen (1999). The spectra of LB and FLUENT show good agreement for the high frequencies at which the slopes match. However, there is a small deviation at lower frequencies, which is probably caused by the low accuracy of the FLUENT spectrum. The FLUENT time series ($t_{tot} = 20\mathrm{k}$ LB s) are much shorter than the LB time series ($t_{tot} = 300\mathrm{k}$ LB s). And as a result the FLUENT time series can only be divided into 7 blocks, which causes a low accuracy of the FLUENT spectrum. The reason for the short FLUENT time series is the long computational time. A simulation of (300k LB s) would take 10 weeks with FLUENT and takes only 2 weeks with LB (on 4 CPUs). Therefore, a shorter time series was used for FLUENT.

The transition from steady to unsteady is investigated experimentally with LDA. The transition is found around $\mathrm{Re} = 300$, see figure 4.14. The spectra, which are obtained at $\mathrm{Re} \leq 250$, consist only of noise, because the flow is steady at this range. When the Reynolds number is increased to $\mathrm{Re} = 300$, an oscillation starts to appear, which proves to have a frequency peak around $f^* = 2$.

This frequency is observed in both the axial and tangential component and corresponds to a length-scale ($1/k$) of roughly half a diameter ($1/k = \mathrm{D}/f^*$), which is the largest length-scale in the radial direction (the mixer cuts the tube in half). When the Reynolds number is increased further to $\mathrm{Re} = 350$, the oscillation becomes irregular, which results in an uniform spectrum up to $f^* = 1$ after which the spectrum drops. The uniform part of the spectrum corresponds to scales larger than the length of a mixing element ($f^* < 0.67$) and are likely a results of the periodicity of the 'Kenics static mixer'. The non-uniform part of the spectrum corresponds to the scales smaller than the tube diameter, which are caused by the irregular oscillation of the vortices. This behaviour is also observed at higher Reynolds numbers up to $\mathrm{Re} = 500$, see figure 4.15. Furthermore, the relative power of the small scales (i.e. smaller than the tube diameter) increases as the Reynolds number increases.

Figure 4.16 shows the auto-correlation function at $\mathrm{Re} = 300$ and $\mathrm{Re} = 500$ of the LB and LDA dimensionless time series, respectively. At $\mathrm{Re} = 300$ both LB and LDA show a periodic signal, but the frequency differs (LB: $f^* = 1$ and LDA: $f^* = 1.75$). One should note that the correlation of the LDA time series is lower due to uncorrelated noise, which affects the LDA data. The difference in frequency might be caused by the periodicity of the LB geometry. The static mixer used in the LDA setup consists of 12 elements, while the one used in the LB simulation is periodic over 4 elements. Therefore, the frequency, which is found in the LDA time series, might be influenced by the entrance and exit effects of the static mixer. A longer mixer might be necessary to capture the right transition with the LDA experiments. At $\mathrm{Re} = 500$ the auto-correlation functions of LDA and LB both show that there is almost no correlation. Again, the lower correlation of the LDA time series is caused by the uncorrelated noise, which is absent in the LB simulation. Taking this into account, the auto-correlation functions of LDA and LB agree reasonably well. So, it seems that for the irregular fluctuations in the velocity at $\mathrm{Re} = 500$ the periodicity of the mixer is less important.

4.4.2 Flow in Kenics static mixer at different Re

The early transition to unsteady flow at $\mathrm{Re} = 300$ can be explained by looking at the vortical structures, which are formed in a mixing element of the Kenics static mixer, see figure 4.18. At the low Reynolds numbers $\mathrm{Re} \leq 200$ the vortical structures end within one mixing element and the flow aligns with the twist of the element before it reaches the next mixing element, which results in a steady flow. At higher Reynolds numbers $\mathrm{Re} > 300$ the vortical structures stretch out along the entire length of a mixing element and the flow no longer has time to align with the mixing element. As a result the vortical structures create a disturbance at the intersection of two mixing elements, which triggers the unsteady behavior.

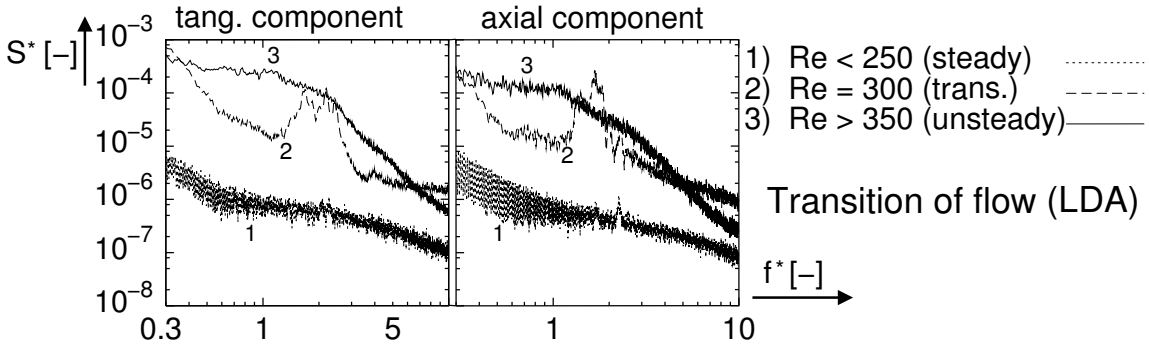

Figure 4.14: Power-spectra indicate transition from steady to unsteady (LDA).

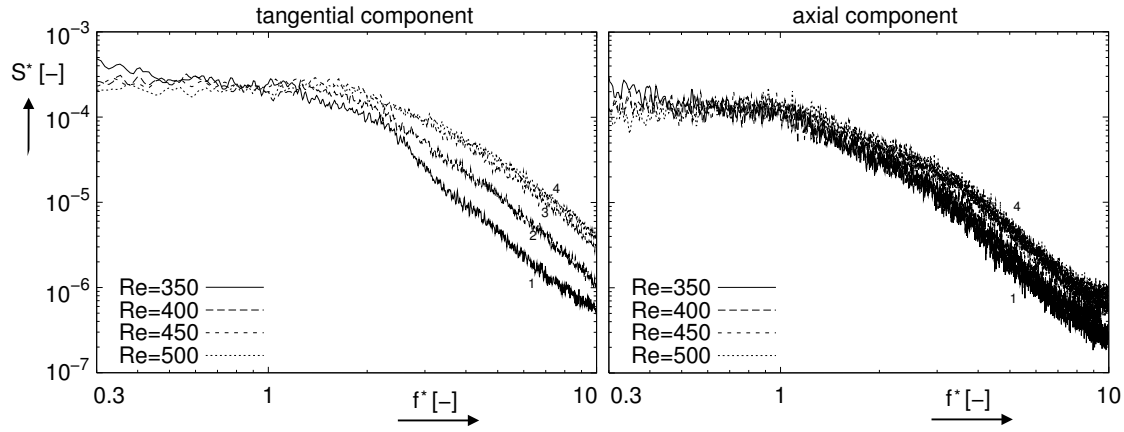

Figure 4.15: Power-spectra of unsteady flow in Kenics static mixer at $\mathrm{Re} > 350$ (LDA).

This unsteady behaviour is visualized for $\mathrm{Re} = 500$ and $\mathrm{Re} = 1000$ as a functions of time (in [LB s]), see figure 4.17. Five snapshots are shown. The first snapshot shows a developed flow ($t = 0$ LB s) and the others the progression of the flow in time (up to $t = 100$ LB s). Although, the fluctuations in a point can be significant, they don't seem to influence the overall structures of the flow. The vortices oscillate a bit, but they are stable at $\mathrm{Re} = 500$ and the flow is still symmetric. At $\mathrm{Re} = 1000$, however, the flow becomes more unsteady and is no longer symmetric. Vortices merge with one another and the overall flow pattern seems to constantly change. Although, large structures remain dominant, smaller structures appear and disappear over time. The flow seems to become turbulent at $\mathrm{Re} = 1000$, but no cascade process of vortices, which break up into smaller vortices, can be observed.

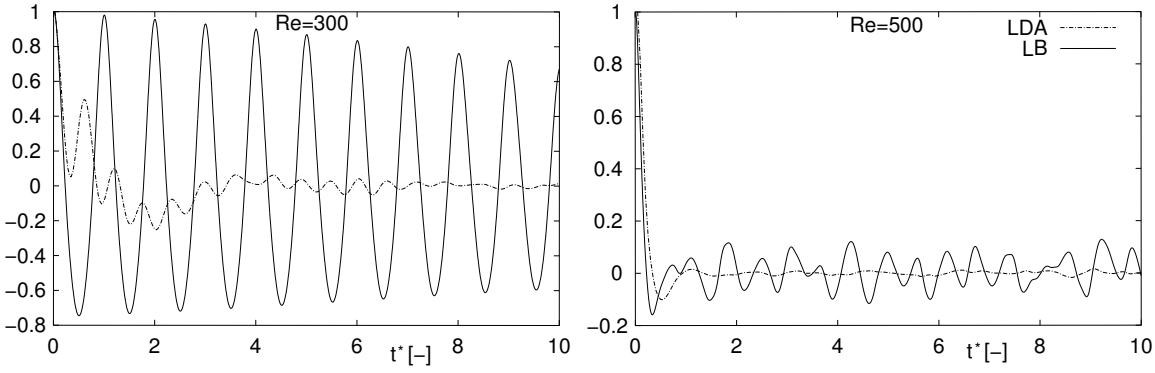

Figure 4.16: Auto-correlation function of LB and LDA time series at $\mathrm{Re} = 300$ and $\mathrm{Re} = 500$.

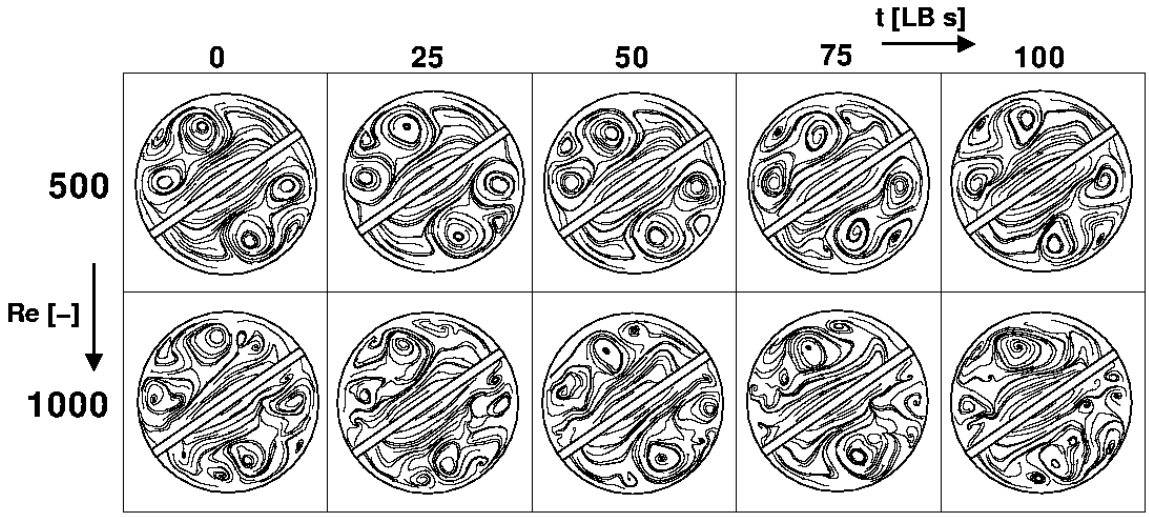

Figure 4.17: Small oscillations of vortex core at $\mathrm{Re} = 500$ and $\mathrm{Re} = 1000$ visualized by 2D stream-traces located at 0.3D from start of mixing element.

4.5 Discussion and Conclusions

A good agreement between the results obtained with LB, FLUENT and LDA measurements, regarding the velocity field and its time characteristics, was obtained.

At low Reynolds numbers the flow is steady and FLUENT was more efficient than LB. At $\mathrm{Re} = 200$ FLUENT is about two times faster than LB. This is mainly because FLUENT can use the steady state solver together with a coarser grid. The time-step in LB is connected to the lattice spacing. As the boundaries at the wall in LB are stair-cased, a relatively dense grid is required in order to accurately resolve the flow in complex geometries. More sophisticated methods to deal with the wall are currently being studied, Chen et al. (1998); Bouzidi et al. (2001); Verberg and Ladd (2002); Rohde et al. (2002). Besides that, LB is intrinsically an unsteady solver, which has to converge to the steady solution. Formulation of steady LB solvers is currently still a research topic, Bernaschi and Succi (2003).

At the higher (transient) Reynolds numbers the picture changes. Small scale structures (vortices) appear in the flow, which require a more dense grid and the use of a smaller time step. FLUENT then also needs a small time step to capture the oscillations, which leads to a rather long computational time. In this case, FLUENT is about five times slower than LB. LB has a high spatial resolution and small time step at low computational cost, which makes it a promising tool to study the dynamic behaviour in transitional flows. It should be noted that FLUENT is a generic purpose code, while the LB code was specifically designed and optimized for this range.

The CFD results were validated by LDA experiments. The velocity profiles as well as the power spectra agreed quite well. It seems that both the flow and time scales are predicted well by the simulations. Furthermore, the (LDA) power-spectra provide us with information about the transition of the flow from steady state to transient flow. The transition takes place around $\mathrm{Re} = 300$ and is also found in the simulations at almost the same Reynolds number.

Although, good agreement was found between the CFD results and the LDA data, one should note that the comparison with LDA was made along a single line, which is located half way a mixing

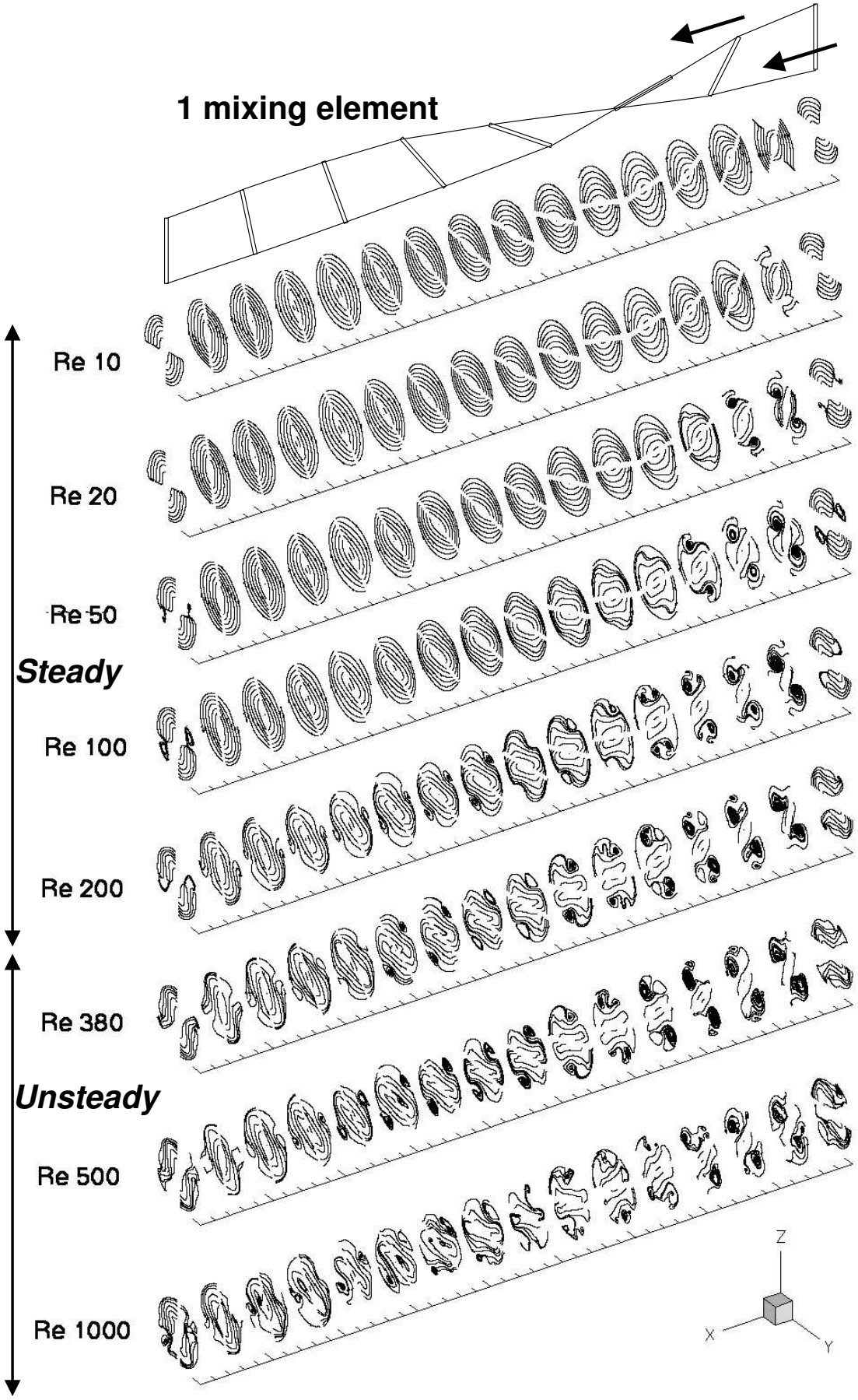

Figure 4.18: Flow structures in mixing element of Kenics static mixer at different Reynolds numbers visualized by 2D stream-traces at various planes in mixing element.

element (figure 4.10). The results of the simulations indicate that the most critical part of the flow might be located at the intersection of two elements. Experimental data in this area would be helpful to provide us with a more rigorous test as to validate the CFD results. Therefore, a more detailed LDA or other experimental study into the flow of the Kenics static mixer can be an interesting topic for future research.

The onset of the transient behaviour could be explained by the length of the vortices, which stretch out along a mixing element. It seems that when the flow doesn't have enough time to align with the mixing elements, the vortical structures create a disturbance at the intersection of two mixing elements. This disturbance triggers the transient and chaotic behavior, which occurs already at a relative low Reynolds number. If the Reynolds number is increased the flow gets more and more chaotic and more small vortical structures appear and at $\mathrm{Re} = 1000$ the flow seems to have become turbulent.

The insight, which is gained about the flow in the Kenics static mixer, can be valuable for other studies such as the mixing process of the liquids or solids (particles). A particle tracking code can be implemented into LB code enabling to study mixing of particles or tracers, Van Wageningen et al. (2003). It is also possible to study higher Reynolds number, when LES is incorporated in the Lattice Boltzmann solver, **?**. Furthermore, multi-phase models for LB seem to be ready in the near future, Chen and Doolen (1998), which opens up the possibility to simulate industrial multi-phase flows in static mixers.

5

Numerical study on suspending small particles in a Kenics™ static mixer

In this chapter the mixing of particles in the Kenics™ static mixer is evaluated. For this purpose, a particle tracking code was developed and added to the existing LB code. The particle tracking code was based upon the equation of Maxey and Riley (1983) to which the modified (Saffman (1965, 1968)) lift force was added. As mentioned before, the Kenics™ static mixer was investigated as part of a project which concerns the recovery of copper from waste streams by means of waste to waste technology, Hage et al. (1999). The copper particles formed grow during their residence in the reactor and their size distribution determines their economic value. A more uniform size has a higher economic value. In order to improve the economic value of the end product, it is therefore important to control the residence time of the copper particles. Problems that can occur in this type of reactor are for example clogging due to sedimentation or entrapment of particles. It is important to understand under which flow conditions these problems may occur. Therefore, the aim of this work is to obtain a quantitative description of the mixing process of the dispersed particles in the Kenics™ static mixer and to find the optimal conditions under which the Kenics™ static mixer reactor should operate[1].

5.1 Introduction

In the literature, several numerical studies on the flow in a Kenics™ static mixer have been published. The focus was either on the pressure drop, e.g. Rauline et al. (1995) and Hobbs et al. (1998), or on the mixing characteristics, which are to a large extend based upon the work of Ottino (1989). Nowadays, mixing is usually studied numerically by means of tracking tracer particles, e.g. Hobbs and Muzzio (1997b), and Fourcade et al. (2001). A similar approach is used in this study. But instead of tracking tracers, which follow streamlines, the particle force balance is solved. The forces considered are the drag, the gravity, the surrounding-fluid stress, the added mass force and the lift force. The Basset force is neglected and Stokes drag is assumed. Using this approach the particle trajectories are calculated and their position, and properties are recorded at different planes along the Kenics™ static mixer reactor. For this purpose, a particle tracking code was developed and assessed. The particle tracking code was added to an in-house LB code. Both codes are written in the c programming language.

Part of this work was published in Van Wageningen et al. (2003). However, in that work, the staircased boundary condition, which is used for the LB solver, was also used for the particles. This

[1] This chapter is an extension of the work that has appeared in Van Wageningen et al. (2003)

approach introduced an error in the trajectories of particles close to the wall and caused particles to get trapped at the staircase wall. Furthermore, the particle tracking code was limited to steady state, because it was run separate from the LB code. In the work presented here, these limitations have been removed. A smooth boundary is used for the particles, which consists of an analytical function of the mixing elements, and the particle tracking code is linked and embedded into the LB code. Both codes are solved simultaneously.

The outline of this chapter is as follows: First, the equation of motion of the particles and forces that are involved in that equation are described in detail. Second, a short description of the numerical techniques is given. Third, the numerical setup is explained. Finally, the results are presented and discussed, after which some concluding remarks are made.

5.2 Equation of motion of particles

Because of the contributions of Boussinesq, Basset and Oseen the equation of particle motion under constant forcing is often referred to as the BBO equation. The basic idea behind the BBO equation can be described in the following way. The motion of the particle disturbs the flow, which is in the far field at rest. This disturbance of the flow is assumed to be at such a low Reynolds number that the liquid force, which acts on the particle, can be calculated from the results of an unsteady Stokes flow.

The original BBO equation is only valid if the far field of the flow is steady and uniform. Tchen (1947) extended the original BBO equation first to a case where the far field of the flow is unsteady but uniform and second to a case where the far field of the flow is unsteady and nonuniform. However, Tchen's derivations contained some inconsistencies. Maxey and Riley (1983) pointed out and resolved these inconsistencies in Tchen's equation and the subsequent versions of Tchen's equation. They came up with a consistent approximation for the equation of motion for a small rigid spherical particle. One should note that the approximations made by Maxey and Riley (1983) are valid, when

$$\mathrm{Re_p} = \frac{d_\mathrm{p}|\vec{v}_\mathrm{s}|}{\nu} << 1 \quad \text{and} \quad \frac{d_\mathrm{p}^2}{\nu}\frac{u_0}{D} << 1 \tag{5.1}$$

where $\mathrm{Re_p}$ is the Reynolds number of the particle, d_p is the diameter of the particle, $\vec{v}_\mathrm{s} = \vec{u} - \vec{v}_\mathrm{p}$ is the slip velocity, ν is the kinematic viscosity and u_0 and D denote the characteristic velocity and length scale of the flow, respectively. Keeping in mind these conditions, the 'full' equation of motion for a small rigid spherical particle with diameter d_p and mass m_p, which is moving with velocity v_p, yields:

$$\begin{aligned} m_\mathrm{p}\frac{\mathrm{d}\vec{v}_\mathrm{p}}{\mathrm{d}t} = &\underbrace{(m_\mathrm{p}-m_\mathrm{l})\vec{g}}_{\text{gravity}} + \underbrace{m_\mathrm{l}\frac{\mathrm{D}\vec{u}}{\mathrm{D}t}}_{\text{acceleration}} + \underbrace{\frac{1}{2}m_\mathrm{l}\Big[\frac{\mathrm{D}\vec{u}}{\mathrm{D}t} - \frac{\mathrm{d}\vec{v}_\mathrm{p}}{\mathrm{d}t} + \overbrace{\frac{\mathrm{d}}{\mathrm{d}t}\big(\frac{1}{40}d_\mathrm{p}^2\nabla^2\vec{u}\big)}^{\text{correction}}\Big]}_{\text{added mass}} - \underbrace{3\pi d_\mathrm{p}\mu(\vec{v}_\mathrm{p}-\vec{u})}_{\text{drag}} \\ &- \underbrace{\frac{\pi}{8}d_\mathrm{p}^3\mu\nabla^2\vec{u}}_{\text{Faxen}} - \underbrace{\frac{3\pi}{2}d_\mathrm{p}^2\mu\int_0^t \Big(\frac{\frac{\mathrm{d}}{\mathrm{d}\tau}\{\vec{v}_\mathrm{p}(\tau) - \vec{u}[\vec{x}_\mathrm{p}(\tau),\tau] - \overbrace{\frac{1}{24}d_\mathrm{p}^2\nabla^2\vec{u}}^{\text{correction}}\}}{[\pi\nu(t-\tau)]^{\frac{1}{2}}}\Big)\mathrm{d}\tau}_{\text{history}} + \vec{F}_\mathrm{lift} \end{aligned} \tag{5.2}$$

where m_l is the mass of the liquid that is displaced by the particle, $\vec{u}$ is the velocity of the liquid at the position of the particle and μ is the dynamic viscosity. The lift force $\vec{F}_\mathrm{lift}$ is added to the equation of Maxey and Riley (1983), because it usually acts in a plane perpendicular to the drag force. Therefore, although the lift force is small compared to the drag force, it can have some influence

on the particle trajectories. For example, when gravity acts in the axial flow direction and the flow direction is downward (vertical case), the lift force can force particles that are in the near wall region towards the wall.

Before implementing the equation of Maxey and Riley (1983) some simplification are made. First, a constant gradient of the liquid velocity around the particle is assumed. In that case the Faxen drag force as well as the correction terms for the added mass and history force can be neglected. Second, the history force itself is neglected. The history force can be significant in the following cases: (1) when a particle starts to move from standstill, (2) when the density of the liquid is large compared to the density of the particle, and/or (3) when the particles are large. In this work the initial velocity of the particle is set to the liquid velocity. The density of the liquid is 9 times smaller than density of the particles and the particles are small. Therefore, the history force will likely be small compared to drag force. To check this assumption, the importance of the history force is investigated after the particle tracking has been performed. It was found that the history force is indeed small for most cases (section 5.2.3). When these simplifications are taken into account and the terms are rearranged, the equation of motion for particles, which is used in the particle tracking code, becomes:

$$\frac{\mathrm{d}\vec{v}_\mathrm{p}}{\mathrm{d}t} = \underbrace{\frac{18\mu\ \vec{v}_\mathrm{s}}{d_\mathrm{p}^2\rho_\mathrm{a}}}_{\text{drag}} + \underbrace{\frac{\rho_\mathrm{p}-\rho}{\rho_\mathrm{a}}\vec{g}}_{\text{gravitation}} + \underbrace{\frac{3}{2}\frac{\rho}{\rho_\mathrm{a}}\frac{\mathrm{D}\vec{u}}{\mathrm{D}t}}_{\text{acceleration}} + \underbrace{\frac{\vec{F}_\mathrm{lift}}{m_\mathrm{p}+\frac{1}{2}m_\mathrm{l}}}_{\text{lift}} \tag{5.3}$$

where ρ is the density of the liquid and ρ_a is defined as

$$\rho_\mathrm{a} = \rho_\mathrm{p} + 0.5\rho \tag{5.4}$$

The forces that are considered can be divided into the *drag* force, *lift* force, *gravitational* force, which includes buoyancy and gravity, and the force related to the *acceleration* of the surrounding liquid. The lift force is treated in section 5.2.2. Furthermore, in section 5.2.3, an overview is given of the magnitude and significance of the different forces.

The dimensionless form of equation 5.3 is obtained by multiplication with $D/\overline{u}_0^2$ and yields:

$$\frac{\mathrm{d}\vec{v}_\mathrm{p}^*}{\mathrm{d}t^*} = \frac{\vec{v}_\mathrm{s}^*}{\mathrm{St}} + \frac{\vec{1}}{\mathrm{Fr}} + \frac{3}{2}\rho^*\frac{\mathrm{D}\vec{u}^*}{\mathrm{D}t^*} + \vec{F}^*_{\mathrm{lift,m}} \tag{5.5}$$

where

$$\mathrm{St} = \frac{\tau_\mathrm{p}}{\tau_\mathrm{l}} = \frac{\rho_\mathrm{a} d_\mathrm{p}^2}{18\mu}\frac{\overline{u}_0}{D}, \qquad \mathrm{Fr} = \frac{\rho_\mathrm{a}}{\rho_\mathrm{p}-\rho}\frac{\overline{u}_0^2}{Dg}, \qquad \rho^* = \frac{\rho}{\rho_\mathrm{a}} \qquad \text{and} \qquad F^*_{\mathrm{lift,m}}$$

are the Stokes number, the Froude number, the dimensionless liquid density and the dimensionless lift force per unit mass, respectively. The relaxation time of the particle and liquid are indicated by τ_p and τ_l, respectively. Because the acceleration force and lift force are small, the principal forces are the drag force and the gravitational force. Therefore, the dimensionless slip velocity will be roughly equal to the ratio between the Stokes and the Froude number (St/Fr) in a stationary case. For small particles this ratio determines to a large extend the movement of the particles and can be used as a scaling parameter.

As mentioned before, Stokes drag is used. In that case the Reynolds number of the particle should be much smaller than one. However, in some cases the Reynolds number of the particle is close to one ($0.1<\mathrm{Re}<1.0$), which introduces an error. Therefore, in this range a different relation for the drag force is used, which is described in the next section.

5.2.1 Drag force

A general expression for the 'steady state' drag force is given by

$$\vec{F}_{\mathrm{drag}} = \mathrm{C_D}(\mathrm{Re_p}) A_{\perp} \frac{1}{2} \rho |\vec{v}_{\mathrm{s}}| \vec{v}_{\mathrm{s}} \tag{5.6}$$

where $\mathrm{C_D}(\mathrm{Re_p})$ is the drag coefficient and $A_{\perp} = \frac{\pi}{4} d_{\mathrm{p}}^2$ is the frontal area of the particle in the direction of the flow. When $\mathrm{Re_p}$ <0.1, Stokes drag is used ($\mathrm{C_D} = \frac{24}{\mathrm{Re_p}}$). In that case equation 5.6 becomes:

$$\vec{F}_{\mathrm{drag}} = 3\pi\mu d_{\mathrm{p}} \vec{v}_{\mathrm{s}} \tag{5.7}$$

where d_{p} denotes the diameter of the particle.

In case that $\mathrm{Re_p}$¿0.1, the model of Morsi and Alexander (1972) is used to determine the drag coefficient. The expression for the drag coefficient yields

$$C_{\mathrm{D}} = a_1 + \frac{a_2}{\mathrm{Re_p}} + \frac{a_3}{\mathrm{Re_p^2}} \tag{5.8}$$

where a_1, a_2 and a_3 are constants, which are given in table 5.1. Near the wall the drag force needs to be modified. In this study, modifications are made to the drag force based upon the work of Chen and McLaughlin (1995).

Modification of drag force near a wall

Since the particles and their relative distance to the wall are small compared to the curvature of the wall, a 'flat' wall is assumed. Figure 5.1 shows the drag force on a small spherical particle near a 3D wall. To correctly modify the drag force, the drag force is first transformed to the coordinate system of the vector normal to the wall, which consists of the normal vector of the wall e_{n} and the two tangential vectors of the wall $e_{\mathrm{t}1}$ and $e_{\mathrm{t}2}$, which are perpendicular to e_{n}. Second the drag force is multiplied by the correct corrections factors (Chen and McLaughlin (1995)) and third it is transformed back to Cartesian coordinates:

$$\vec{F}_{\mathrm{drag,wall}} = C_{\mathrm{wall,t1}}(\vec{F}_{\mathrm{drag}} \cdot \vec{e}_{\mathrm{t}1})\vec{e}_{\mathrm{t}1} + C_{\mathrm{wall,n}}(\vec{F}_{\mathrm{drag}} \cdot \vec{e}_{\mathrm{n}})\vec{e}_{\mathrm{n}} + C_{\mathrm{wall,t2}}(\vec{F}_{\mathrm{drag}} \cdot \vec{e}_{\mathrm{t}2})\vec{e}_{\mathrm{t}2} \tag{5.9}$$

The expression that is used to calculate the normal vector of the wall can be found in section 5.3.2.

The correction factors of Chen and McLaughlin (1995) give a best fit to the exact solution of O'Neill (1964) (table 5.2) for the correction factors $C_{\mathrm{wall,t1}}$ and $C_{\mathrm{wall,t2}}$:

$$\begin{aligned} C_{\mathrm{wall,t1}} = C_{\mathrm{wall,t2}} = \quad & \exp\left[1.465 \exp\left\{ -0.03176\left(\ln \tfrac{\delta^+}{r_{\mathrm{p}}^+} + 6.150\right)^2\right\} - 0.1\right] \\ & \text{when} \quad 0.01 < \tfrac{\delta^+}{r_{\mathrm{p}}^+} \leq 10 \\ C_{\mathrm{wall,t1}} = C_{\mathrm{wall,t2}} = \quad & 1 \\ & \text{when} \quad \tfrac{\delta^+}{r_{\mathrm{p}}^+} > 10 \end{aligned} \tag{5.10}$$

where $\delta^+ = y^+ - r_{\mathrm{p}}^+$ is the dimensionless gap width between the particle and the wall. For the correction factor $C_{\mathrm{wall,n}}$ Chen and McLaughlin (1995) present a simplification of Brenner (1961)'s

Table 5.1: Constants for the determination of C_{D}, Morsi and Alexander (1972)

$\mathrm{Re}_{\mathrm{p,d}}$	a_1	a_2	a_3
$0.1 \cdots 1$	3.69	22.73	0.0903
$1 \cdots 10$	1.222	29.1667	-3.8889
$10 \cdots 100$	0.6167	46.5	-116.67
$100 \cdots 1000$	0.3644	98.33	-2778
$1000 \cdots 5000$	0.357	148.62	$-47.5 \cdot 10^3$
$5000 \cdots 10000$	0.46	-490.546	$578.7 \cdot 10^3$
$10000 \cdots 50000$	0.5191	-1662.5	$5.4167 \cdot 10^6$

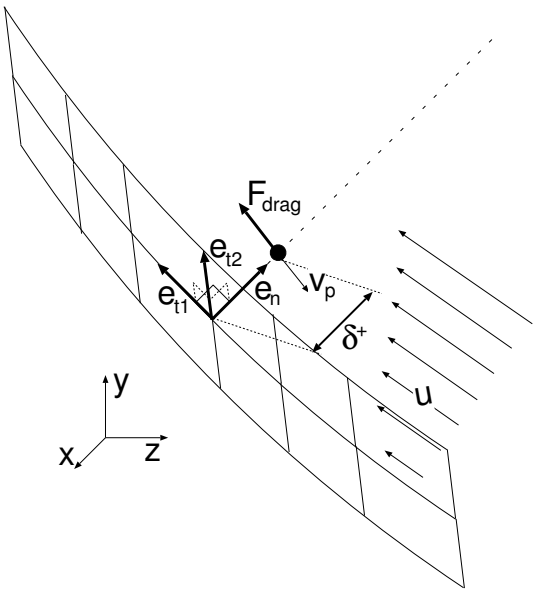

Figure 5.1: Drag force and normal vector e_{n} of a particle close to the wall.

exact solution (table 5.2):

$$C_{\text{wall,n}} = \frac{2}{\alpha^2} + 0.4 \ln \frac{1}{\alpha} + 1.04 \quad \text{when} \quad 0.01 < \frac{\delta^+}{r_\text{p}^+} \leq 0.5$$
$$\text{with} \quad \alpha = \ln \left[\frac{\delta^+ + r_\text{p}^+}{r_\text{p}^+} + \sqrt{\left(\frac{\delta^+}{r_\text{p}^+}\right)^2 + 2\frac{\delta^+}{r_\text{p}^+}} \right] \tag{5.11}$$

$$C_{\text{wall,n}} = \exp\left[4.526 \exp\left\{ -0.0662 \left(\ln \frac{\delta^+}{r_\text{p}^+} + 5.217 \right)^2 \right\}\right] \quad \text{when} \quad 0.5 < \frac{\delta^+}{r_\text{p}^+} \leq 10 \tag{5.12}$$

$$C_{\text{wall,n}} = 1 \quad \text{when} \quad \frac{\delta^+}{r_\text{p}^+} > 10 \tag{5.13}$$

It should be noted that if $\frac{\delta^+}{r_\text{p}^+} < 0.01$, the value at $\frac{\delta^+}{r_\text{p}^+} = 0.01$ is taken. A more accurate description would be the lubrication theory of Goldman et al. (1967). This effect is neglected in this study, since other errors e.g. the accuracy of the flow field are relatively large close to the wall and make a more accurate wall model redundant. Furthermore, the correction factor $C_{\text{wall,n}}$ is very large close to the wall, which will result in no slip of the particle in the direction normal to the wall ($v_{\text{p,n}} = u_\text{n}$). Hence, a particle will slow down when moving towards the walls, which makes the bouncing of a particle at the wall very unlikely. Instead a particle will gently touch the wall.

5.2.2 Lift force

The lift force on a small spherical particle in an unbounded linear shear flow was analysed by Saffman (1965, 1968). The expression for the Saffman lift force yields:

$$F_{\text{lift,Saffman}} = 1.615\, \rho\, \nu^{\frac{1}{2}}\, d_\text{p}^2\, (u - v_\text{p})\, |G|^{\frac{1}{2}}\, \text{sgn}(G) \tag{5.14}$$

where $G = \frac{\text{d}u}{\text{d}y}$ is the liquid velocity gradient. In figure 5.2 the direction of the lift force is illustrated for different particle velocities. The lift force can be expressed in its dimensionless form in the following way:

$$F^*_{\text{lift,m}} = \frac{F_\text{lift}}{m_\text{p} + \frac{1}{2} m_\text{l}} \frac{\text{D}}{\overline{u}_0^2} = 3.084 \frac{\rho\, \nu^{\frac{1}{2}}}{\rho_\text{a}} \frac{\text{D}}{\overline{u}_0^2} \frac{|u - v_\text{p}|\, |G|^{\frac{1}{2}}\, \text{sgn}(G)}{d_\text{p}} \tag{5.15}$$

It should be noted that Saffman's expression is valid under the assumptions that both the Reynolds number of the particle and Reynolds number of the velocity gradient are small compared to unity and that the Reynolds number of the particle is much smaller than the square root of the Reynolds number of the velocity gradient:

$$\text{Re}_\text{G} = \frac{G d_\text{p}^2}{\nu} << 1 \tag{5.16}$$

$$\text{Re}_\text{p} = \frac{|\vec{v}_\text{s}| d_\text{p}}{\nu} << 1 \tag{5.17}$$

$$\text{Re}_\text{p} << \sqrt{\text{Re}_\text{G}} \tag{5.18}$$

Table 5.2: Wall correction factors based on O'Neill's and Brenner's exact solution

$\frac{\delta^+}{r_p^+}$	$C_{\mathrm{wall,x'}}, C_{\mathrm{wall,z'}}$		$C_{\mathrm{wall,y'}}$		
	O'Neill	Eq. 5.10	Brenner	Eq. 5.11	Eq. 5.13
0.010	3.496	3.517	101.9	102.0	
0.080	2.344	2.370	14.00	14.08	
0.270	1.802	1.810	4.997	5.038	
0.500	1.589	1.593	3.205	3.215	3.214
0.640	1.513	1.519	2.737		2.726
1.250	1.322	1.350	1.905		1.892
2.160	1.218	1.243	1.527		1.525
3.430	1.148	1.170	1.333		1.334
5.120	1.103	1.118	1.223		1.224
7.290	1.068	1.080	1.156		1.157
10.0	1.053	1.051	1.114		1.113

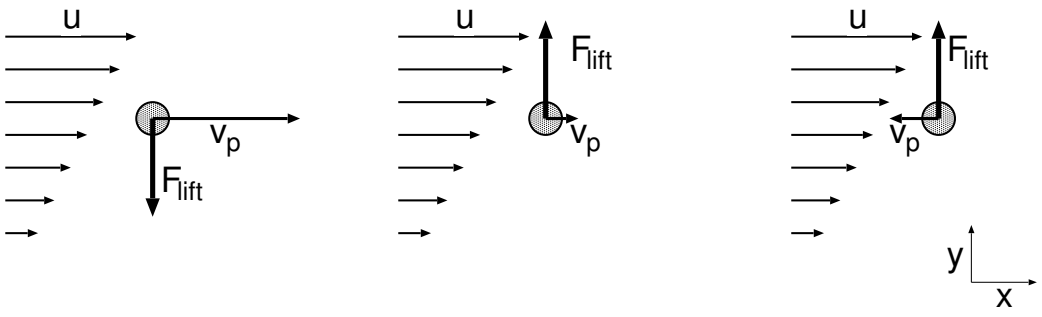

Figure 5.2: Lift force of a particle moving in shear flow.

McLaughlin (1991) extended the analytical expression of Saffman (1965, 1968) to situations in which $\mathrm{Re_p}$ is not small compared to $\sqrt{\mathrm{Re_G}}$. He proposed a modification of the Saffman lift force that yields:

$$\vec{F}_{\mathrm{lift,McL}} = \frac{J(\epsilon)}{2.255}\vec{F}_{\mathrm{lift,Saffman}} \tag{5.19}$$

where the coefficient J is a function of $\epsilon = \frac{\sqrt{\mathrm{Re_G}}}{\mathrm{Re_p}}$. The values of J are listed in table 5.3. Mei (1992) compared the analytical values of McLaughlin (1991) and Saffman (1965, 1968) to a fit, which is based on the numerical results of Dandy and Dwyer (1990) and on the analytical work of Saffman. The correlation that was used by Mei (1992) for the shear lift force yields:

$$\begin{aligned}
\vec{F}_{\mathrm{lift,Mei}} &= S_{\mathrm{Mei}}\ \vec{F}_{\mathrm{lift,Saffman}} \\
S_{\mathrm{Mei}} &= \left(1 - 0.3314\sqrt{\alpha}\right)\exp\left[-\frac{\mathrm{Re_p}}{10}\right] + 0.3313\sqrt{\alpha} \quad (\text{when} \quad \mathrm{Re_p} \leq 40) \\
S_{\mathrm{Mei}} &= 0.0524\sqrt{\alpha\ \mathrm{Re_p}} = 0.0524\sqrt{0.5\ \mathrm{Re_G}} \quad (\text{when} \quad \mathrm{Re_p} > 40)
\end{aligned} \tag{5.20}$$

where $\alpha = \frac{1}{2}\mathrm{Re_p}\epsilon^2 = \frac{1}{2}\frac{\mathrm{Re_G}}{\mathrm{Re_p}}$.

In figure 5.3 the shear lift force based upon the correlation of Mei (1992) is compared to the values given by McLaughlin (1991) for different values of $\mathrm{Re_{G,d}}$ and $\mathrm{Re_{p,d}}$. The results are normalised by the Saffman lift force. There is a big discrepancy between the values of McLaughlin and the correlation of Mei at low $\mathrm{Re_G}$. Mei (1992) claims that this discrepancy is caused by the fact that the values of McLaughlin (1991) are only valid for low $\mathrm{Re_{p,d}}$. However, at low $\mathrm{Re_{p,d}}$ and low $\mathrm{Re_{G,d}}$ the discrepancy is worst. The only agreement between the two is found, when they both approach the Saffman value. Therefore, one can state that the two do not agree at all. The question arises which model is correct.

In literature Mei's correlation is often cited due to its simplicity. For particles that have a Reynolds number smaller than one, the Mei correlation is equal to the Saffman lift force. Since for all cases that are investigated in this work the particle Reynolds number was smaller than one, it is not necessary to use Mei's correlation. For this range, Mei's correlation is equal to Saffman's value. Therefore, it was decided not to use Mei's correlation.

Correction to the lift force is necessary when $!(\mathrm{Re_p} << \sqrt{\mathrm{Re_G}})$ or $!(\mathrm{Re_p^2} << \mathrm{Re_G})$. Since the Reynolds number of the particles is much smaller than one, correction is only necessary, when the Reynolds number of the gradient is very small. This is the case, when the term $d_\mathrm{p}^2 G$ is small, but in that event also the lift force is very small, see equation 5.14. Since a small lift force will have a little effect on the particle trajectory, the correction is neglected and it was decided to use the Saffman lift force in the bulk flow (far from the wall). Near the wall the lift force needs to be modified, which is explained in the next section.

Modification of lift force near a wall

In the work presented here, modifications are made to the lift force based upon the work of Chen and McLaughlin (1995). Since the particles and their relative distance to the wall are small compared to the curvature of the wall, a 'flat' wall is assumed. To modify the lift force near the wall, three expressions are used, which are illustrated in figure 5.4. If a particle is touching the wall the correlation of Leighton and Acrivos (1985) is used:

$$F_{\mathrm{lift,n}} = 9.22\ G\ \mu\ r_\mathrm{p}^2 \frac{G\ r_\mathrm{p}^2}{\nu} \tag{5.21}$$

Table 5.3: Values of J for several values of ϵ, McLaughlin (1991).

ϵ	J	ϵ	J
0.025	$-13.3\cdot10^{-6}$	0.7	1.2554
0.05	$-284.5\cdot10^{-6}$	0.8	1.436
0.1	$-4.658\cdot10^{-3}$	0.9	1.576
0.15	$-14.58\cdot10^{-3}$	1.0	1.686
0.2	$-12.47\cdot10^{-3}$	1.5	1.979
0.25	$27.82\cdot10^{-3}$	2.0	2.094
0.3	$117.9\cdot10^{-3}$	5.0	2.227
0.4	$407.6\cdot10^{-3}$	10.0	2.247
0.5	$735.0\cdot10^{-3}$	20.0	2.252
0.6	1.0236	∞	2.255 (Saffman)

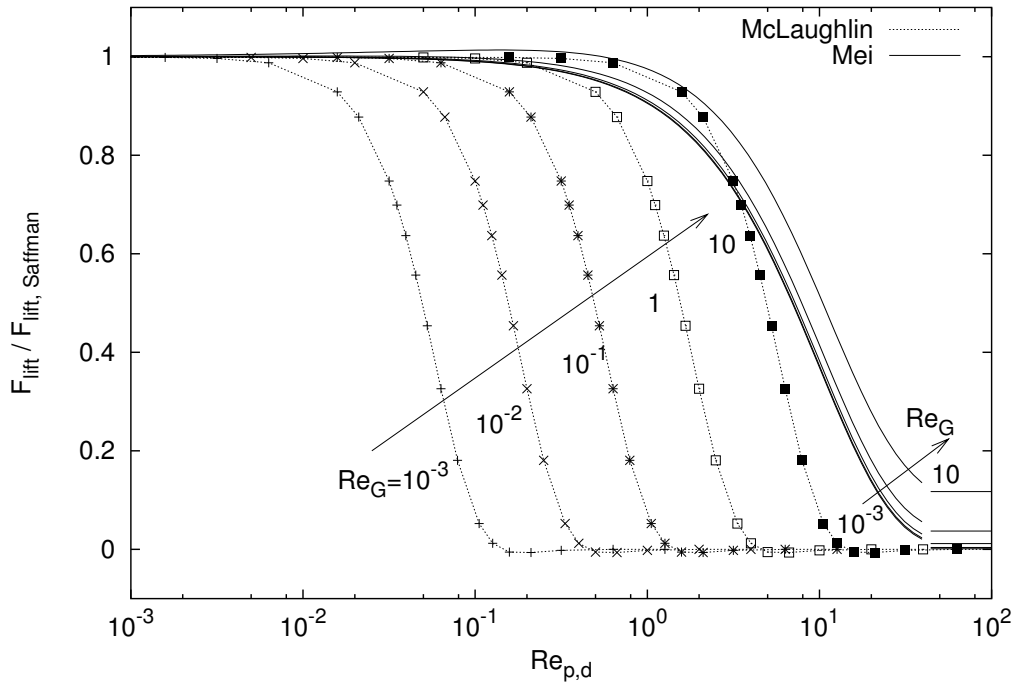

Figure 5.3: Comparison of correlation Mei (1992) and values of McLaughlin (1991).

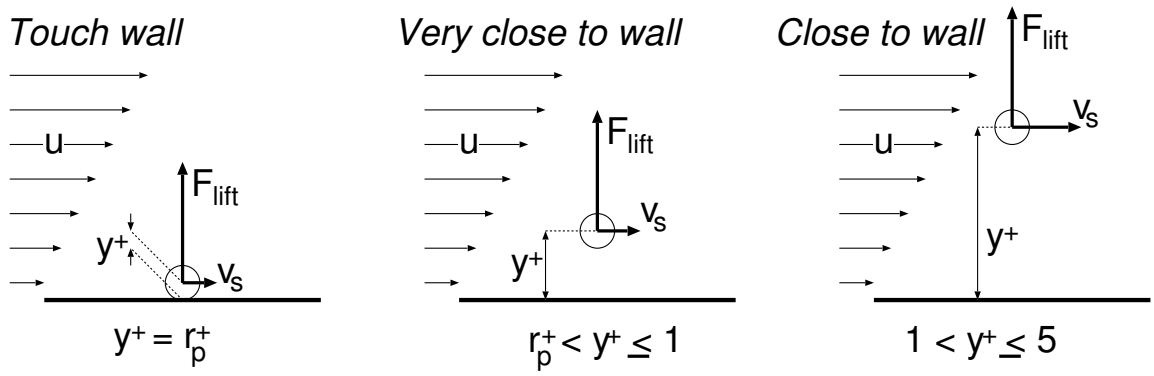

Figure 5.4: Lift force of a particle close to the wall.

Close to the wall ($y^+ \leq 1$), the correction factor of Cox and Hsu (1977), which modifies the Saffman lift force, is used:

$$\begin{aligned} \vec{F}_{\text{lift,Cox}} &= S_{\text{Cox}}\, \vec{F}_{\text{lift,Saffman}} \\ S_{\text{Cox}} &= \left(0.19635\frac{|\vec{v}_{\text{s}}|}{\sqrt{G}} + 1.8333y^+\right)\frac{1}{2.255} \end{aligned} \tag{5.22}$$

where y^+ is the dimensionless distance from the centre of the particle to the wall.

$$y^+ = \frac{l_{\text{p}}\sqrt{\frac{\tau_{\text{w}}}{\rho}}}{\nu} \tag{5.23}$$

where l_{p} is the distance of the particle to the wall and τ_{w} is the wall shear stress. When the particle is very close to the wall, Cox and Hsu (1977)'s expression is no longer valid. Cherukat and McLaughlin (1994) developed a lift force that removed the restriction $y^+ >> r_{\text{p}}^+$. Hence, their expression is also valid in the very near wall region. However, Chen and McLaughlin (1995) report that the expression of Cox and Hsu (1977) produces nearly the same results as the expression of Cherukat and McLaughlin (1994). Therefore, in the work presented here, Cox and Hsu (1977)'s expression is used.

When $1 < y^+ \leq 5$, the expression of McLaughlin (1993) is used, which is equal to

$$\begin{aligned} \vec{F}_{\text{lift,McL}} &= S_{\text{McL}}\, \vec{F}_{\text{lift,Saffman}} \\ S_{\text{McL}} &= \frac{J'}{2.255} \end{aligned} \tag{5.24}$$

where S_{McL} is the modification factor and the values of J' are listed in table 5.4. One should note that, in this table the two emphasised values of the 8$^{\text{th}}$ column (ϵ=2.0) do not follow the trend of the other values. Since the two values are the same as the next to values, it was assumed that this was a typo. Private communication with Prof. John B. McLaughlin confirmed this assumption and the correct values were obtained.

For convenience a power-law fit was made to data of McLaughlin. The fit has the following form:

$$J' = A\,(y^+)^B \tag{5.25}$$

where

$$\begin{aligned} A &= 0.35358 + 4.0415\epsilon - 6.2575\epsilon^2 + 3.7323\epsilon^3 - 0.76485\epsilon^4 \quad \text{and} \\ B &= -2.6442 + 7.3561\epsilon - 7.4827\epsilon^2 + 3.5232\epsilon^3 - 0.6228\epsilon^4 \quad \text{when} \quad 0.2 \leq \epsilon \leq 2.0 \\ A &= 0.92679 \quad \text{and} \quad B = 0.51105 \quad \text{when} \quad \epsilon > 2.0 \end{aligned}$$

Table 5.4: Power-law Fit compared to McLaughlin (1993) table, values represent J'.

y^+	$\epsilon = 0.2$	0.4	0.6	0.8	1.0	1.5	2.0	> 2.0
Original table from McLaughlin (1993), emphasised values suspected typos								
1.000	0.903	1.190	1.20	1.17	1.13	1.05	1.01	0.886
1.200	0.727	1.080	1.17	1.18	1.16	1.12	1.10	1.01
1.400	0.580	0.977	1.12	1.17	1.18	1.17	1.17	1.12
1.600	0.475	0.889	1.08	1.16	1.19	1.21	1.23	1.22
1.800	0.398	0.816	1.04	1.15	1.20	1.25	*1.52**	1.300
2.000	0.342	0.766	1.01	1.14	1.21	1.28	*1.69***	1.370
3.000	0.192	0.572	0.908	1.13	1.27	1.44	1.52	1.69
4.000	0.126	0.463	0.857	1.15	1.34	1.58	1.69	1.89
5.000	0.090	0.396	0.848	1.19	1.42	1.70	1.82	2.02
* correct value: 1.28, ** correct value: 1.32								
Power-law fit								
1.000	0.940	1.188	1.233	1.180	1.105	1.061	1.027	0.917
1.200	0.722	1.048	1.179	1.180	1.131	1.119	1.097	1.017
1.400	0.578	0.942	1.136	1.180	1.154	1.170	1.159	1.101
1.600	0.477	0.859	1.099	1.180	1.174	1.217	1.216	1.178
1.800	0.402	0.792	1.068	1.180	1.192	1.259	1.268	1.252
2.000	0.345	0.737	1.041	1.180	1.209	1.299	1.317	1.321
3.000	0.192	0.557	0.943	1.180	1.274	1.462	1.522	1.625
4.000	0.127	0.457	0.879	1.181	1.323	1.590	1.688	1.882
5.000	0.092	0.392	0.832	1.181	1.361	1.697	1.828	2.110

The error of the fit is below 5% for all points. One should note that for particles that are located at $y^+ > 5$ the wall effects on the lift force are neglected.

5.2.3 Assessment of importance of the different forces

The forces that act on particles of different size are investigated in a reactor with a diameter of 5 cm. Two Reynolds number (Re=200 and Re=500) and different settling rates for the particles (St/Fr=0.01 and St/Fr=0.05) were considered. Figure 5.5 shows the importance of the different forces that act on a spherical particle under these different conditions. The history, added mass, acceleration and lift force, respectively, are plotted relative to the drag force as a function of the particle radius. The forces are obtained by averaging 4 arbitrary particle trajectories. One should note that the history force was not included in the particle tracking code and was calculated afterwards.

It can be observed that the history force is of the same order as the acceleration force and added mass force, but it is small compared to the drag force for small particles. When the particles become larger than r_p=50μm, the history force becomes more important and can no longer be neglected. The same applies for the added mass force and acceleration force. However, they are included in the particle force balance, because it is rather straightforward to implement these forces at almost no additional computational costs.

Since the copper particles that are investigated for the project have a maximum size of r_p=30μm, the history force is neglected. It should be noted that, the lift force is very small compared to the drag force, but acts perpendicular to the drag force and, hence, can have some influence on the particles.

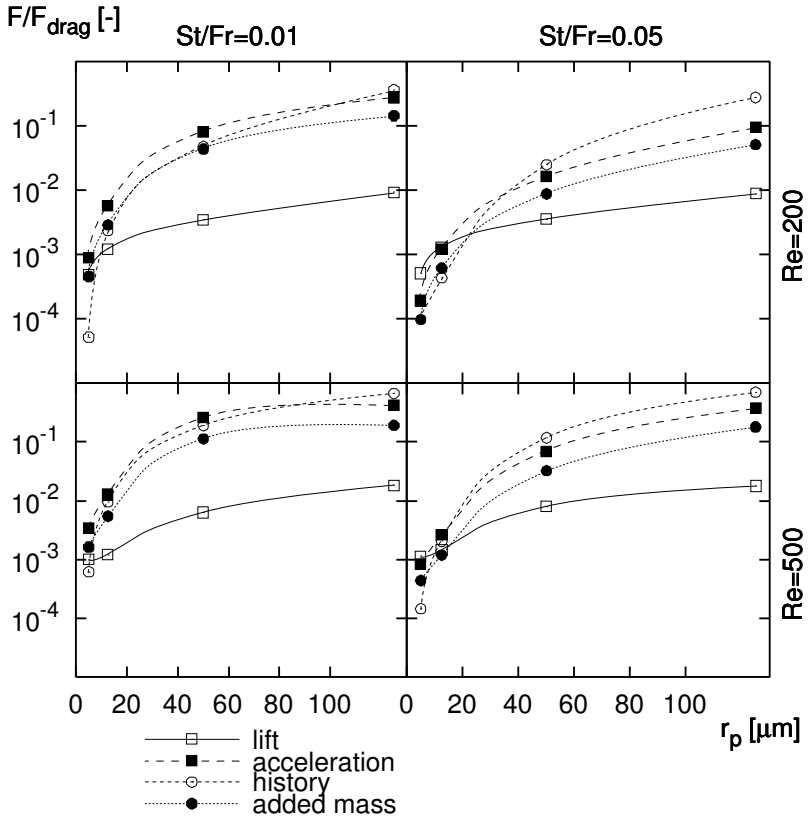

Figure 5.5: Magnitude of the lift, added mass, acceleration and history force relative to the drag force for different particle sizes, Reynolds numbers and St/Fr ratios.

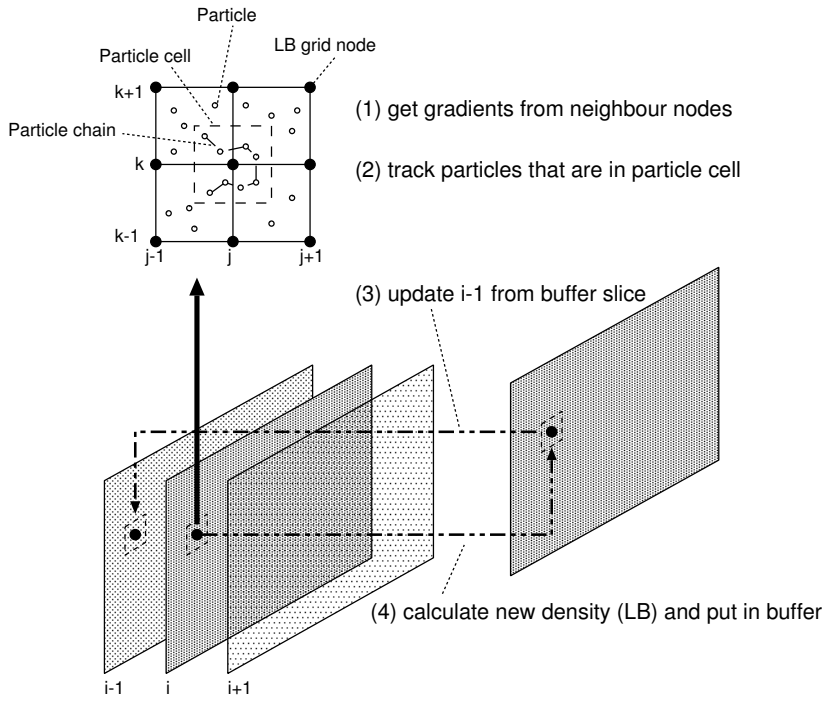

Figure 5.6: Overview of linking of particle tracking code to LB code in collision phase

5.3 Numerical techniques

The particle tracking code is embedded in the Lattice Boltzmann (LB) code, see also chapter 2. The particles are tracked within the collision phase of LB, which consist of a loop over all the LB grid nodes. In the collision phase the LB particle densities are updated for each node. Since the particles are tracked within the collision phase, all the particle that are located near the same grid node are linked together in a chain. In a chain a particle points to the next particle until the last particle which is in the vicinity of the cell is reached. This way the velocity gradients only need to be interpolated one time for each particle cell that is comprised around a LB grid node. If the chain is empty no velocity gradients are calculated. The particle chains are calculated right before the collision phase of LB. In the collision loop, the following approach is used at all grid nodes (figure 5.6).

First, the velocity gradients are calculated via linear interpolation with the neighbour grid nodes. It should be noted that, the velocities at the neighbour nodes are calculated from the (LB) particle densities, after which the upwind and downwind velocity gradients of the particle cell are obtained.

Second, the particles that are located in the particle cell are tracked by solving the force balance, equation 5.3. Because the old (LB) particle densities (at time = t) are necessary for the correct interpolation of the velocity gradients of the next cell, the new (LB) particle densities (at time = $t+1$) are temporarily stored in a buffer slice.

Third, the i-1th node is updated, since the velocity information at this node is no longer needed. Finally, the new particle densities (LB) are calculated and stored in the buffer slice.

5.3.1 Particle tracking

The velocities are known at the centre grid node of the particle cell and are interpolated linearly to the position of the particle using the velocity gradients. For the velocity gradient at the position of the particle the gradient of the cell is used, where the location of the particle determines which gradient (up or down wind) is used. The particle velocity is obtained by integrating equation 5.3 with a second order accurate Runge Kutta integration scheme. The particle position is obtained by integrating the following equation:

$$\frac{\mathrm{d}\vec{x}_\mathrm{p}}{\mathrm{d}t} = \vec{v}_\mathrm{p}(\vec{x}_\mathrm{p}) \tag{5.26}$$

where $\vec{v}_\mathrm{p}(\vec{x}_\mathrm{p})$ is the velocity vector of the particle at position $\vec{x_\mathrm{p}} = (x, y, z)$. x is the (horizontal) axial direction, y the (vertical) direction of gravity, z is the (horizontal) direction perpendicular to x. A trapezoid integration scheme was used to integrate this equation.

To ensure stability of the particle tracking code, the particle time step Δt_p is adapted and based on the particle relaxation time τ_p such that:

$$\Delta t_\mathrm{p} \leq 2\tau_\mathrm{p} \tag{5.27}$$

It should be noted that within one LB time step multiple particle time steps are possible. In practise only for small particles adaptation of the time step is necessary, because the LB time step is already small.

Tracer with gravity

When the particle relaxation time of the particles is extremely small, an extremely small time step is necessary to ensure stability of the integration scheme, which results in a very long computational time. Therefore, particles with an extremely small particle relaxation time are modelled as tracers. One should note that these particles are very small and have a dominant drag force, which justifies this approach. The effect of gravity on these particles is modelled by means of the stationary slip velocity ($v^*_{\mathrm{s}0} = \mathrm{St}/\mathrm{Fr}$). In this case the particle velocity in equation 5.26 is set to $\vec{v}_\mathrm{p} = \vec{u} + \vec{v}_{\mathrm{s}0}$.

5.3.2 Boundary conditions

In the LB simulations, the wall boundary is stair-cased, which causes problems for the particle boundary. Therefore, an analytical function is used to describe the exact location of the mixing elements, which is shown in figure 5.7. The analytical function $F(x, y, z)$ of the mixing elements and tube yield:

$$\begin{aligned}
F(x,y,z) \quad &= \quad -y\sin\left(\beta + \frac{\alpha(x-x_0)}{L}\right) + z\cos\left(\beta + \frac{\alpha(x-x_0)}{L}\right) \pm \frac{t}{2} = 0 \\
&\qquad\qquad 0 < \quad x \quad \leq 0.75D \quad : \quad \beta = 0 \qquad \alpha = \pi \qquad x_0 = 0 \\
&\qquad\qquad 0.75 < \quad x \quad \leq 2.25D \quad : \quad \beta = -\tfrac{1}{2}\pi \quad \alpha = -\pi \quad x_0 = 1.5D \\
&\qquad \text{with} \quad 2.25 < \quad x \quad \leq 3.75D \quad : \quad \beta = 0 \qquad \alpha = \pi \qquad x_0 = 3D \\
&\qquad\qquad 3.75 < \quad x \quad \leq 5.25D \quad : \quad \beta = -\tfrac{1}{2}\pi \quad \alpha = -\pi \quad x_0 = 4.5D \\
&\qquad\qquad 5.25 < \quad x \quad \leq 6D \qquad : \quad \beta = 0 \qquad \alpha = \pi \qquad x_0 = 6D \\
\text{tube} \quad : \quad & \quad y^2 + z^2 < \frac{1}{4}D^2
\end{aligned} \tag{5.28}$$

where L, D, t, are the element length, diameter and thickness, respectively. The offset in the axial direction is denoted by x_0 and the angle between two mixing elements and twist angle are

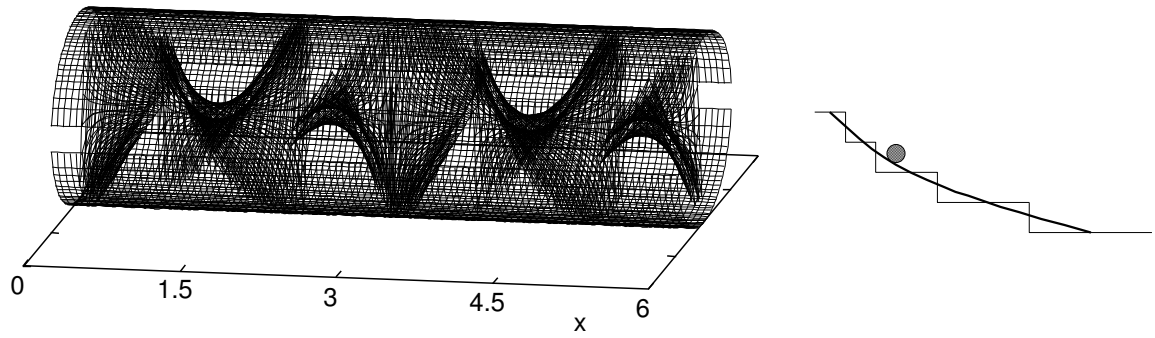

Figure 5.7: Analytical description of the static mixer.

represented by β and α, respectively. For the first mixing element ($x \in [0, 0.75D]$), $F(x, y, z)$ is equal to

$$F(x, y, z) = -y \sin(\frac{\alpha\, x}{L}) + z \cos(\frac{\alpha\, x}{L}) \pm \frac{t}{2} = 0 \tag{5.29}$$

With equation 5.28, it is rather difficult to calculate the distance of the particle to the wall. Therefore, the particle coordinates are transformed to the coordinate system of the element. The transformation consists of a rotation θ around the x-axis and is indicated with an apostrophe, see figure 5.8. The angle θ yields

$$\theta = \frac{\alpha\, x}{L} \tag{5.30}$$

and the rotation matrix $\mathbf{R}_\theta$ around the x-axis is given by

$$\mathbf{R}_\theta = \begin{pmatrix} 1 & 0 & 0 \\ 0 & \cos\theta & -\sin\theta \\ 0 & \sin\theta & \cos\theta \end{pmatrix} \tag{5.31}$$

Substituting equation 5.30 in equation 5.29 gives the equation of the mixing element in the new coordinate system.

$$-y \sin\theta + z \cos\theta = z' = \pm\frac{\mathrm{t}}{2} \tag{5.32}$$

In the element coordinate system the distance of the particle to the element wall, l_p can be easily obtained:

$$l_\mathrm{p} = |z'_\mathrm{p}| - \frac{\mathrm{t}}{2} \tag{5.33}$$

where z'_p is the z coordinate of the particle in the coordinate system of the mixing element. The distance of a particle to the tube wall is determined by the radial position of the particle. If the distance to the (tube or element) wall is negative, the particle is placed back at the surface of the tube or mixing element (touching) and its velocities are mirrored with respect to the normal vector of the wall. It should be noted that this approach introduces a small error in the slip velocity near the wall. Since the particles and the grid spacing both are small, it is not expected that this error will have a significant influence on the particle trajectories near the wall.

To ensure that no particles get trapped, when a particle collides with the front of a mixing element, a particle is placed either left or right from the element depending on the location of the collision. It

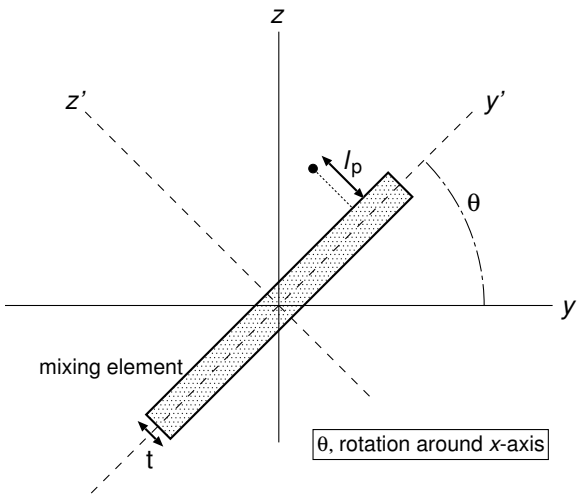

Figure 5.8: Determination of the distance to the wall via rotation around x axis

should be noted that in reality, the mixing element are sharpened to avoid accumulation of particles at the front of an element. Furthermore, the distance to the wall is only calculated in the near wall region, which consists of the 2 LB nodes near the wall. This is sufficient for the modifications of the lift and drag force near the wall, because the particle diameter is much smaller than the distance between two LB nodes. Moreover, the curvature of the element in the x direction is neglected as to calculate the distance to the wall and forces that are related to the wall. One should note that, this curvature is not neglected for the calculation of the normal vector.

Calculation of wall normal vector

If a particle is touching a wall, the normal force is taken into account, which allows the particle to slide along the wall (figure 5.9). The normal vector of the mixing element is needed for the normal force and for the modifications to the lift and drag force. The normal vector can be described by the gradient of equation 5.29 or via two rotations along the x axis and y' axis, respectively. The normal vector in Cartesian coordinates yields:

$$\vec{n} = \nabla F(x,y,z) = \begin{pmatrix} -\frac{\alpha}{L}(y\cos\theta + z\sin\theta) \\ -\sin\theta \\ \cos\theta \end{pmatrix} \quad \text{and} \quad \hat{\vec{n}} = \frac{\vec{n}}{|\vec{n}|} \tag{5.34}$$

where $\theta = \frac{\alpha\, x}{L}$ and $\hat{\vec{n}}$ is the unit normal vector.

The unit normal vector in the coordinate system of the mixing element is equal to

$$\hat{\vec{n}}'' = \begin{pmatrix} 0 \\ 0 \\ 1 \end{pmatrix} \tag{5.35}$$

This vector can be transformed to Cartesian coordinates via two rotations. First, the coordinate system of the mixing element is rotated around the y' axis with an angle ϕ in order to match the y-z plane. Second, it is rotated around the x axis with an angle θ as to obtain the Cartesian coordinates. The angle ϕ yields:

$$\tan\phi = \pm\frac{\alpha\, z'}{L} \tag{5.36}$$

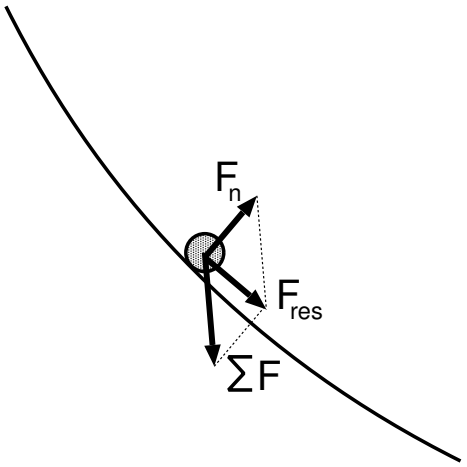

Figure 5.9: Normal force acting on a particle that touches the wall

and the rotation matrix of ϕ yields:

$$\mathbf{R}_\theta = \begin{pmatrix} \cos\phi & 0 & -\sin\phi \\ 0 & 1 & 0 \\ \sin\phi & 0 & \cos\phi \end{pmatrix} \tag{5.37}$$

After two rotations the unit normal vector in Cartesian coordinate is obtained:

$$\hat{\vec{n}} = \mathbf{R}_\theta \mathbf{R}_\phi \hat{\vec{n}}'' = \begin{pmatrix} -\sin\phi \\ -\sin\theta\cos\phi \\ \cos\theta\cos\phi \end{pmatrix} \tag{5.38}$$

Division of equation 5.38 by $\cos\phi$ shows that this vector has the same direction as the normal vector, which was obtained via the gradient of the analytical function of the mixing element $F(x, y, z)$ (equation 5.34):

$$\vec{n} = \begin{pmatrix} -\tan\phi \\ -\sin\theta \\ \cos\theta \end{pmatrix} \overset{(5.36)}{=} \begin{pmatrix} -\frac{\alpha\, z'}{\mathrm{L}} \\ -\sin\theta \\ \cos\theta \end{pmatrix} \overset{(5.32)}{=} \begin{pmatrix} -\frac{\alpha}{\mathrm{L}}(y\cos\theta + z\sin\theta) \\ -\sin\theta \\ \cos\theta \end{pmatrix} \tag{5.39}$$

5.4 Numerical setup

The numerical setup consists of a 4 element Kenics™ static mixer to which periodic boundary conditions are applied. This way an infinitely long mixer is simulated. The properties of the static mixer are L/D=1.5, t/D=0.08 and $\alpha = \pi$ rad. The reactor is placed either horizontal or vertical (upward or downward flow) and its diameter is D=5 cm. Furthermore, particles of different size (r_p=5, 12.5, 50 and 125μm) are tracked through the mixer under different flow condition. The Reynolds number ranged from Re=10$\cdots$500 and the St/Fr ratio varied from St/Fr=0.01$\cdots$10 and the density of the particles was equal to $9.0{\cdot}10^3$ kg/m^3.

Each tracked particle has the following properties: *id*, *position*, *velocity*, *diameter*, *density*, *body force*, *processor number*, *number of cycles* and *residence time*. Because each particle has his own body force, different cases can be solved at the same time. One should note that it is assumed that the particles do not influence each other nor the flow. In total 16 cases per Reynolds number (4 St/Fr ratios and 4 particle sizes) were investigated simultaneously. Furthermore, the combined

particle tracking and LB code is parallel and the program was run on 4 processors. To make sure all processors had roughly the same computational load, at each processor 4 cases were initialised. Each case consisted of 30k similar particles, which were distributed uniformly over the injection plane. The injection plane was the same for each case and was located at the beginning of a mixing element, see figure 5.10. Furthermore, the particles properties were recorded, when the particles passed the different planes along the mixer (at x/L=1,2,3,. . .).

5.5 Results

In this section, the results regarding the mixing and settling of particles under gravity and without gravity are presented. It was found that the St/Fr ratio is a good measure for the settling rate. In order to investigate how close the reactor resembles an ideal plug flow reactor under the different circumstances, the residence time of the particles is investigated as well.

5.5.1 Mixing

Mixing is investigated qualitatively by injecting 30k particle at the injection plane. The particles are tracked and recorded at the planes as indicated in figure 5.10. The particle *id* enables us to investigate the mixing of individual or certain groups of particles. In the cases presented here only the particles that were injected at the bottom half of the reactor are plotted. This way the mixing of the particles can be assessed.

The recorded particles are plotted in figure 5.11 for different Reynolds numbers and at different axial positions. The results (Re=10, Re=100) compare well to the numerical results with tracers, Hobbs and Muzzio (1998). Since the particles are small it is not surprising that they have a similar behaviour as the tracer particles, when no gravity is considered. It should be noted that Hobbs and Muzzio (1998) also present results for Re=1000. However, those results were calculated on a relatively coarse mesh and it is unlikely that all flow structures were resolved. Moreover, in Van Wageningen et al. (2004a), it was shown that for high Reynolds numbers the flow is unsteady and a dense computational mesh is required in order to resolve all structures. No such unsteady behaviour was mentioned by Hobbs and Muzzio (1998). More details on the grid size that is required for the high Reynolds numbers are presented in chapter 4 and can also be found in Van Wageningen et al. (2004a).

At a low Reynolds number (Re=10), mixing takes place solely via cutting and recombining at the intersection of two elements and via stretching of the cut areas along the mixing element. It can be observed that this kind of mixing is efficient. After 8 elements the particles are almost fully mixed. Hobbs and Muzzio (1998) mention that at higher Reynolds number the mixing efficiency of the Kenics™ static mixer decreases. A similar behaviour is observed in this work. At Re=$20\cdots100$ a single large vortical structure is present in the flow, which seems to have a negative effect on the mixing and as a result the particles are no longer fully mixed after 8 elements. One should note that the vortex is absent at lower Reynolds numbers. The vortex starts at the start of a mixing element and stretches out over the mixing element. If the Reynolds number is higher the vortex stretches out further along the mixing element (chapter 4, figure 4.18).

Starting from Re=200 the mixing efficiency improves again due to the fact that more vortical structures appear in the flow. In this case, the particles are fully mixed again after 8 elements. When the Reynolds number is further increased (Re=500), the vortices start to oscillate (unsteady flow), which improves the mixing efficiency. Now, the particles are already mixed after 2 elements.

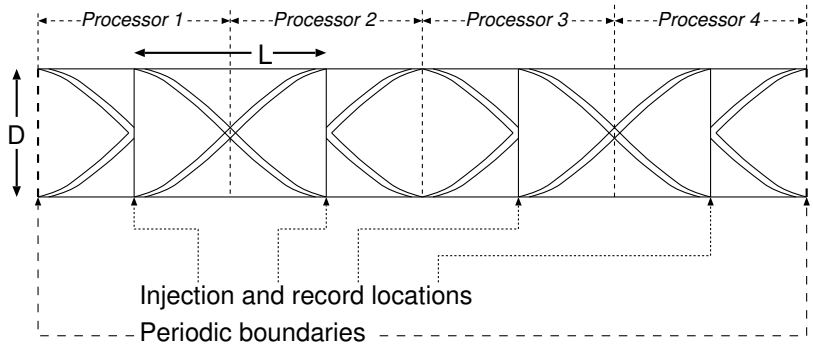

Figure 5.10: Numerical setup for the particle tracking

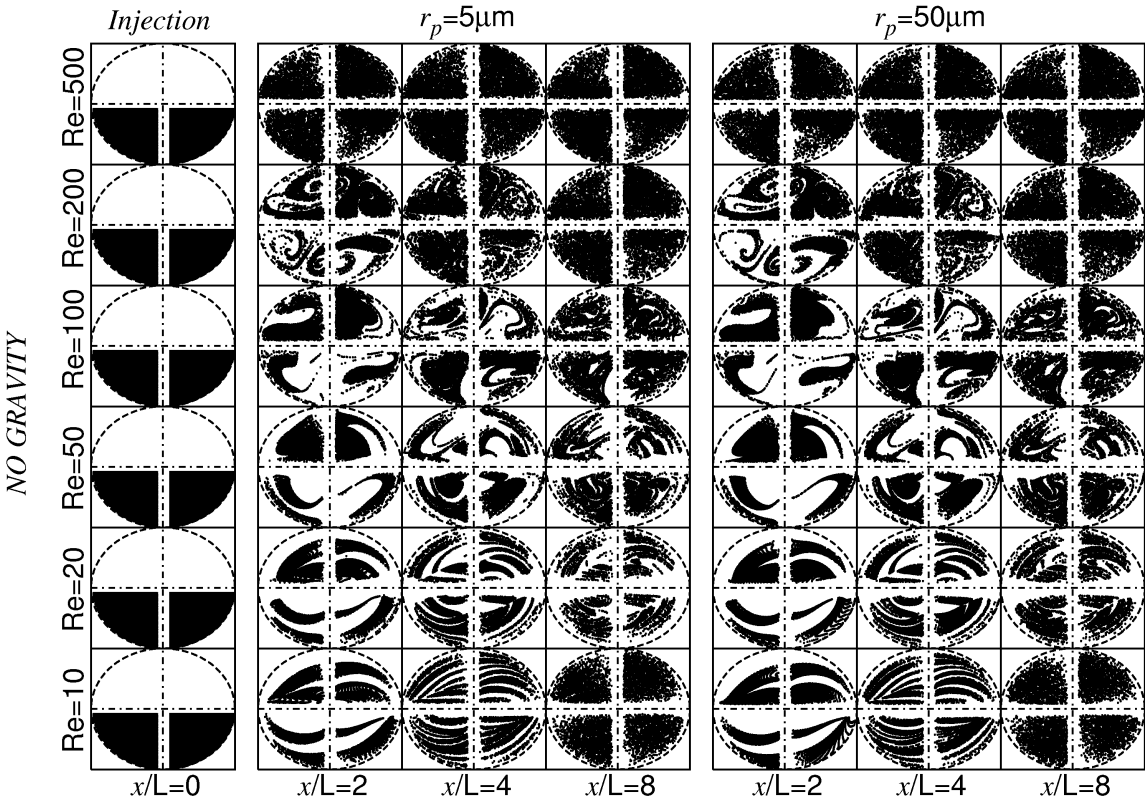

Figure 5.11: Mixing of particles in the Kenics™ static mixer at different Reynolds numbers (no gravity)

The influence of the particle size is investigated by variation of the particle diameter. It was found that the particle size does not play a role in the mixing process for the small particles that are investigated and when there is no gravity. Three cases with gravity are considered: a horizontal reactor in which gravity acts perpendicular to the flow direction and a vertical reactor in which gravity can act either in the flow direction or opposite to the flow direction.

First, the mixing of the particles without gravity is considered. The horizontal case is shown in figure 5.12 and the influence of gravity is investigated by looking at the St/Fr ratio. At low St/Fr ratio (0.01), the gravitational force is relatively weak and no settling of the particles is observed. The mixing looks quite similar to the cases without gravity (figure 5.11). When the influence of gravity increases (St/Fr=0.05, 0.1), the particles are still mixed. However, particles 'disappear', because they the get trapped at the bottom of the reactor. Furthermore, the particles seem to be better mixed at higher Reynolds numbers (Re=200,500). It seems that at Re=500 the mixer is able to better keep more particles in suspension. The entrapment as a function of the St/Fr ratio and Reynolds number is explored in more detail in section 5.5.2.

In practise, the entrapment of the particles is a problem, since the St/Fr ratio is relatively high for 'real' particles. Therefore, a vertical reactor was considered and investigated. Figure 5.13 shows the mixing of particles in a vertical Kenics™ static mixer as a function of the St/Fr ratio and Reynolds number. In this case, gravity can act in the flow direction (*down flow*) and opposite to the flow direction (*up flow*). Again at low St/Fr ratio (weak gravity), the cases look similar to the ones without gravity. In the *up flow* case the particle are no longer transported with the flow if gravity becomes to strong. One can observe that at St/Fr$\geq$1 no particles pass through the reactor, which is shown by the empty plots.

In the *down flow* case, mixing still takes place at St/Fr=1. However, it is less efficient, because the particles collide with the element due to their relatively high slip velocity. It can be observed that at a higher Reynolds number (Re=500) the particles are more evenly distributed over the reactor, while at lower Reynolds numbers (Re=100, 200), in contrast, the majority of the particles are located near the mixing element. The black lines near the center of the graph are the particles that are located at the mixing element.

At St/Fr=10 (*down flow*), all the particles slide down along the mixing elements and appear in the graph as black line in the center. Almost no mixing of the particles takes place, because the particles do not follow the flow and collide with the mixing element. Furthermore, the particles are pushed outward due to lift and acceleration forces. This effect seems to be stronger at low Reynolds numbers.

Figure 5.14 shows that the particle size does not play a mayor role as long as the St/Fr ratio remains constant, which implies that the gravitational force and drag force dominate the particle trajectories. The small differences that arise are due to the lift force, which pushes the particles outward. This effect is stronger for larger particles, since the drag and lift force per unit mass scale with $1/d_{\mathrm{p}}^2$ and $1/d_{\mathrm{p}}$, respectively. Furthermore, the lift force becomes more important, when the St/Fr ratio increases (a high St/Fr leads to a larger slip velocity).

5.5.2 Settling

Another important problem, which occurs when gravity acts on the particles, is the entrapment of particles, which can cause the reactor to get clogged. The entrapment of the particles is investigated by looking at the particle fraction ϵ, which is defined as the number of recorded particles divided by

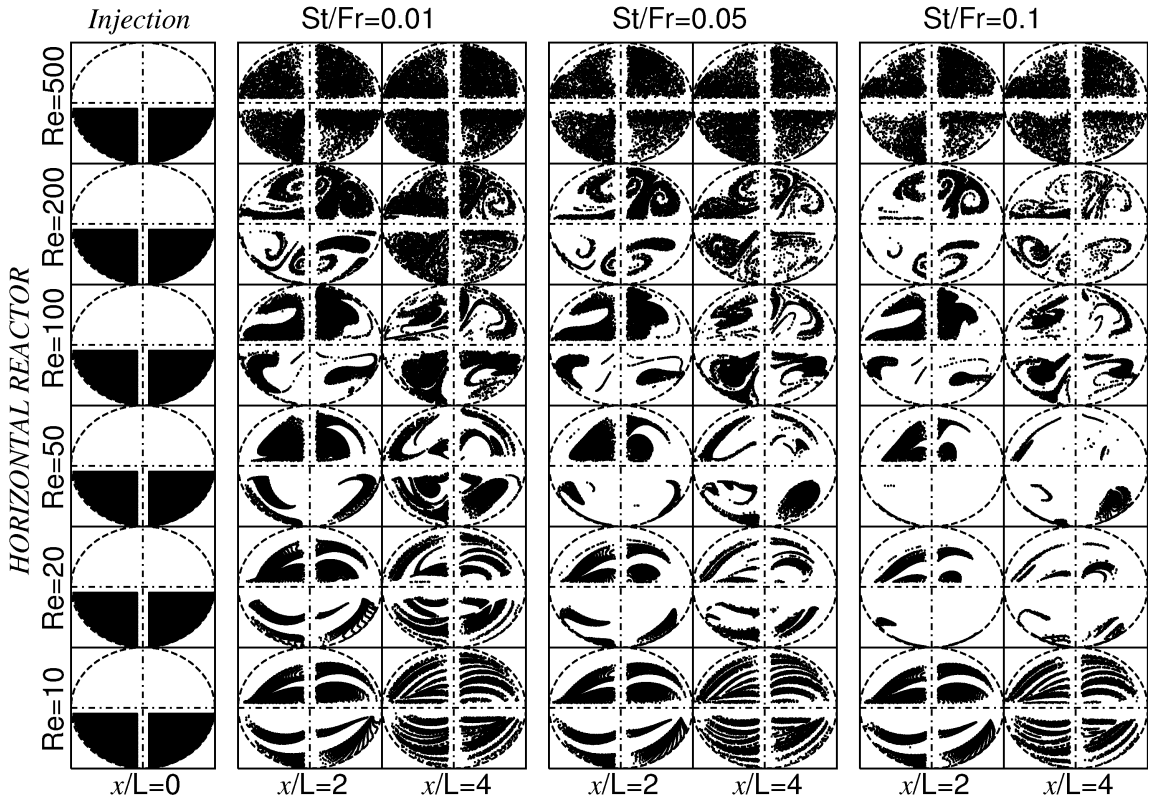

Figure 5.12: Mixing of particles in a horizontal Kenics™ static mixer at different Reynolds numbers (with gravity)

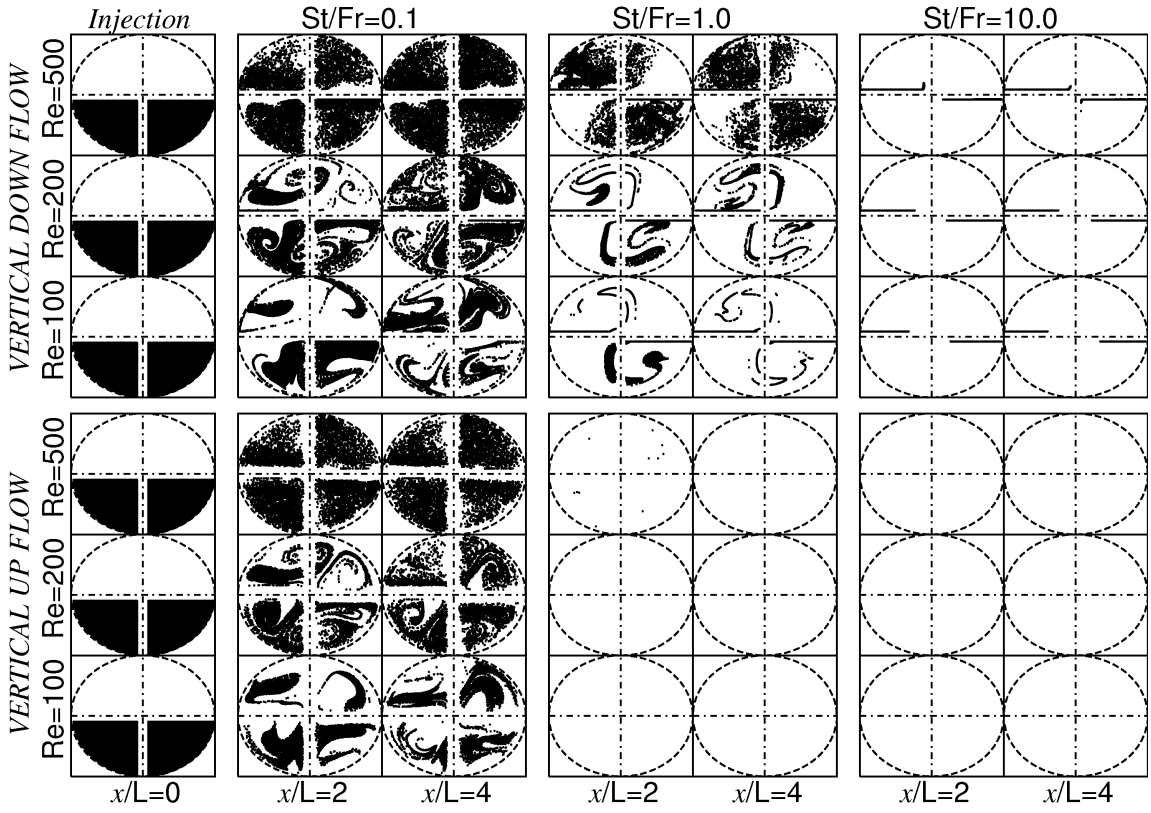

Figure 5.13: Mixing of particles in a vertical Kenics™ static mixer at different Reynolds numbers (with gravity)

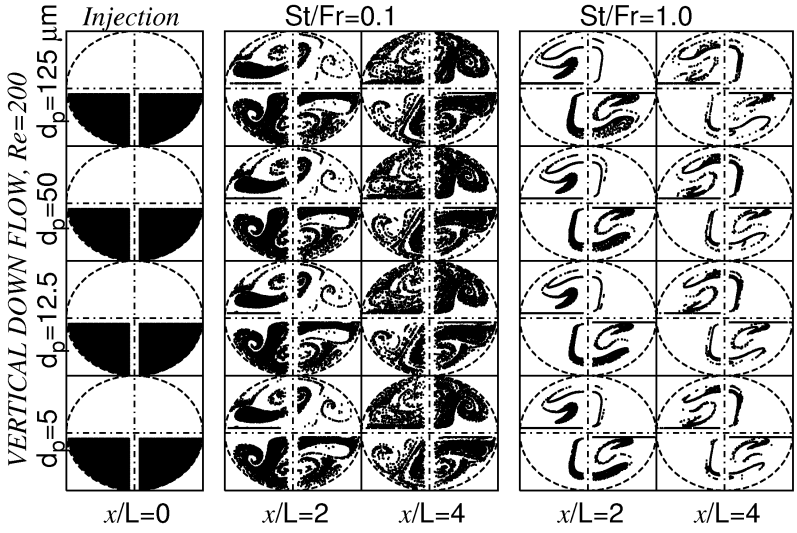

Figure 5.14: Different particle sizes and different St/Fr ratios at Re=200

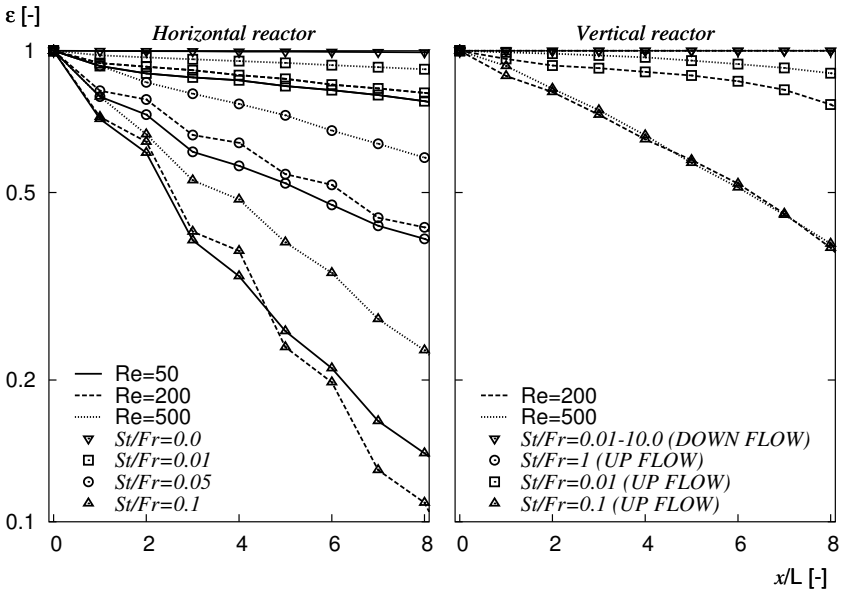

Figure 5.15: Particle fraction as a function of the axial position

the total number of injected particles.

The left side of figure 5.15 shows the entrapment of the particles at the bottom wall of the horizontal reactor. The entrapment results in a decrease of the particle fraction as a function of the reactor length. When there is no gravity (St/Fr=0), the particle fraction remains one, since no particles get trapped at the bottom wall. If gravity acts perpendicular to the axial direction, the particle fraction decreases exponentially and with increasing stationary St/Fr ratio the decrease is faster. Furthermore, increasing the Reynolds number helps to keep particles in suspension. The highest Reynolds number that is investigated is Re=500, which still doesn't keep all particles in suspension. Thus, a horizontal reactor does not seems to be feasible at the low Reynolds that are considered.

The right side of figure 5.15 shows the particle fraction for a vertical reactor (*up* and *down flow*). No particles get trapped, when gravity acts in the flow direction (*down flow*), because the particles slide down along the mixing elements in the same direction as the flow. When gravity acts opposite to the flow direction (*up flow*), some particles no longer can be dragged along with the flow. Especially, near the wall the liquid velocity is low, which results in particles that slide downward in that area. One can observe that at St/Fr=1 no particles are able to travel upward. Thus, a vertical reactor only is feasible, when the flow direction is downward.

5.5.3 Residence time

A plug flow behaviour of the particles is desired, because this ultimately determines the size distribution of the growing copper particles. To assess whether the particles show a plug flow behaviour, the residence time distribution of the particles is investigated. The distribution function of the cumulative residence time $F(\theta)$, in which the residence time θ is made dimensionless by the median residence time τ_{med}, is defined as follows:

$$F(\theta) = \frac{1}{N_{\mathrm{p}}} \sum_{i=1}^{\mathrm{N_{p,rec}}} H(\theta - \frac{\tau_{\mathrm{p,i}}}{\tau_{\mathrm{med}}}) \tag{5.40}$$

where τ_{p} and $H()$ are the residence time of a particle and Heaviside function or unit step function, respectively. The residence time of the flow is investigated by tracking tracer particles without gravity. Hobbs and Muzzio (1997b) showed that the residence time distribution function approaches plug flow as the number of elements is increased. In the work that is presented here, a similar result was found. Moreover, the influence of the Reynolds number on the residence time distribution was investigated as well. In figure 5.16, the cumulative residence time is plotted for Re=10 and Re=200. This figure shows that Re=200 approaches the plug flow profile faster than Re=10. It seems that the vortices, which arise at the higher Reynolds numbers, enhance the 'plug flow behaviour' of the static mixer. Higher Reynolds numbers were not investigated, because the flow is transient in those cases, which would lead to extremely long simulation times.

The question arises if 'real' particles show a similar behaviour as tracer particles and what the role of gravity is. Therefore, the residence time of 'real' particles is investigated at different Reynolds numbers and St/Fr ratios. The cumulative residence time distribution of the particles is plotted after the 2^{nd} and 4^{th} element, respectively. It was found that gravity does not seem to have much influence on the residence time of the particles that exit in a horizontal reactor (figure 5.17). The residence time distribution after 4 elements is closer to plug flow than the residence time distribution after 2 elements, which indicates that the mixer still promotes plug flow. One should note that not all particles were recorded at the higher St/Fr ratios, because some particles were trapped at the bottom wall. If these particles would be released due to collisions, this might influence the residence time

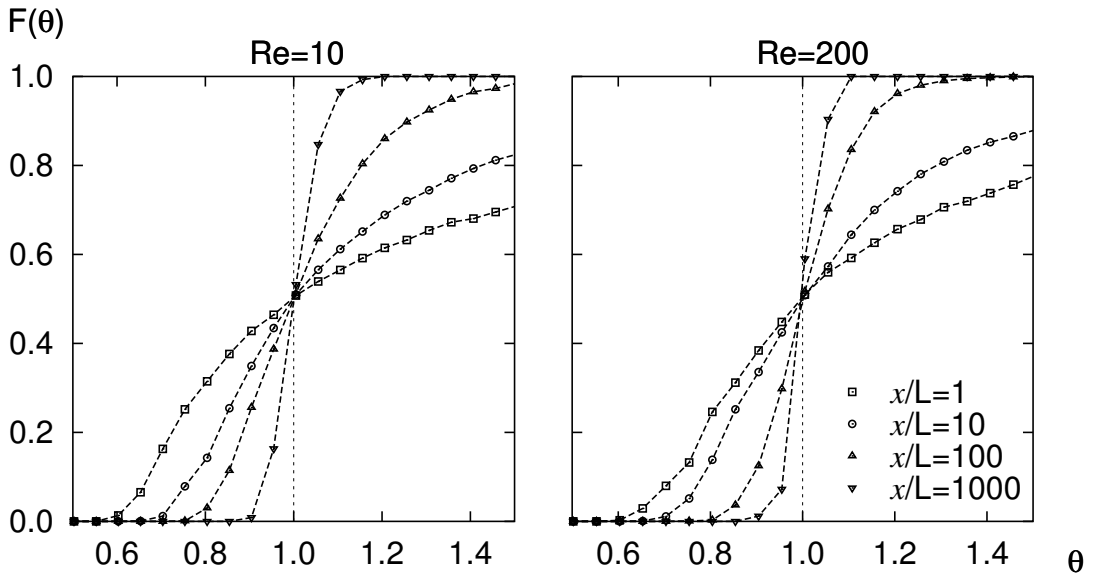

Figure 5.16: Cumulative residence time at Re=10 and Re=200 different number of elements

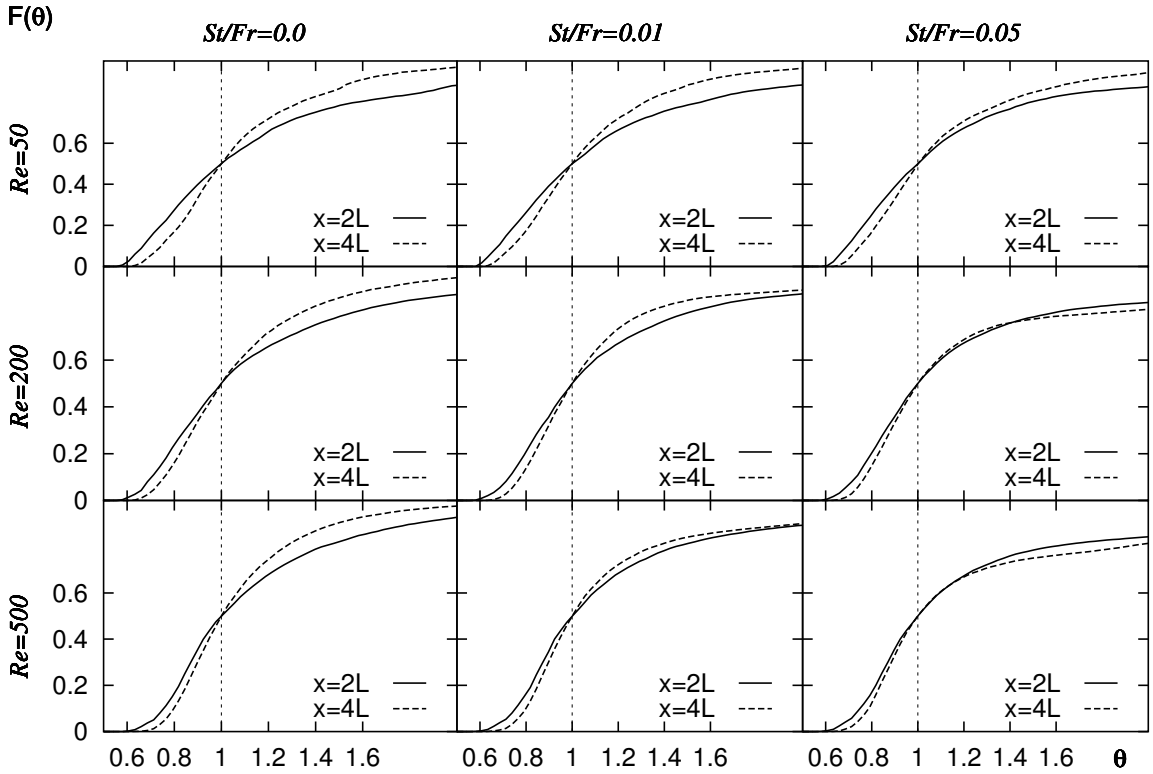

Figure 5.17: Cumulative residence time in horizontal reactor

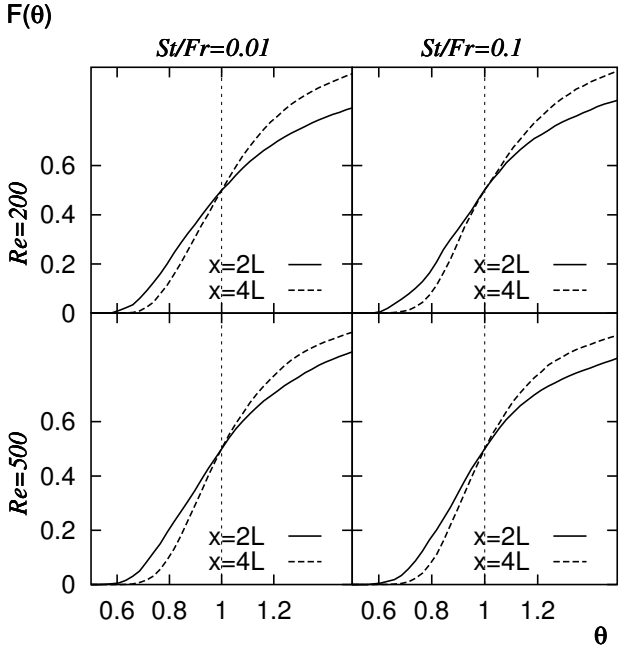

Figure 5.18: Cumulative residence time in vertical reactor (up flow)

distribution.

The figures 5.18 and 5.19 show the cumulative residence distribution in the vertical reactor. In the *up flow* case (figure 5.18), the results again look similar to the cases without gravity. In the *down flow* case (figure 5.19, the residence time distribution at a high St/Fr ratio is more close to plug flow than at a low St/Fr ratio. At a high St/Fr ratio the domination of gravity results in a more equal residence time of the particles. In this case, the flow has little influence on the particles.

5.6 Discussion and conclusion

A particle tracking code was developed and included into the LB code to assess the mixing of particles in the Kenics™ static mixer. Smooth boundaries were used at the wall and for that purpose the mixing elements were described analytically, which allowed the particles to move or slide along the wall. It should be noted that this approach introduces a small error in the slip velocity near the wall. It was found that the drag and gravitational forces were dominant. Furthermore, the lift force, although small, was found to have some influence on the particle trajectories and is most significant, when the particles and their slip velocity are large. When gravity was not considered the results compare well to results found in literature, which involved tracer particles, e.g. Hobbs and Muzzio (1997b).

The results indicate that two important design parameters for the Kenics™ static mixer reactor prove to be the Reynolds number, which is a measure for the flow regime, and the St/Fr ratio, which is a measure for the settling rate of the particles. The two numbers determine to a large extend the mixing, settling and residence time of the particles. Ideally, the particles are uniformly distributed and have an uniform residence time distribution (plug flow). It was found that these conditions were best matched at a low St/Fr ratio (St/Fr$<$1) and either a low or high Reynolds number (Re$<$20 or Re$>$200). Furthermore, this investigation showed that the oscillating vortices, which arise at the

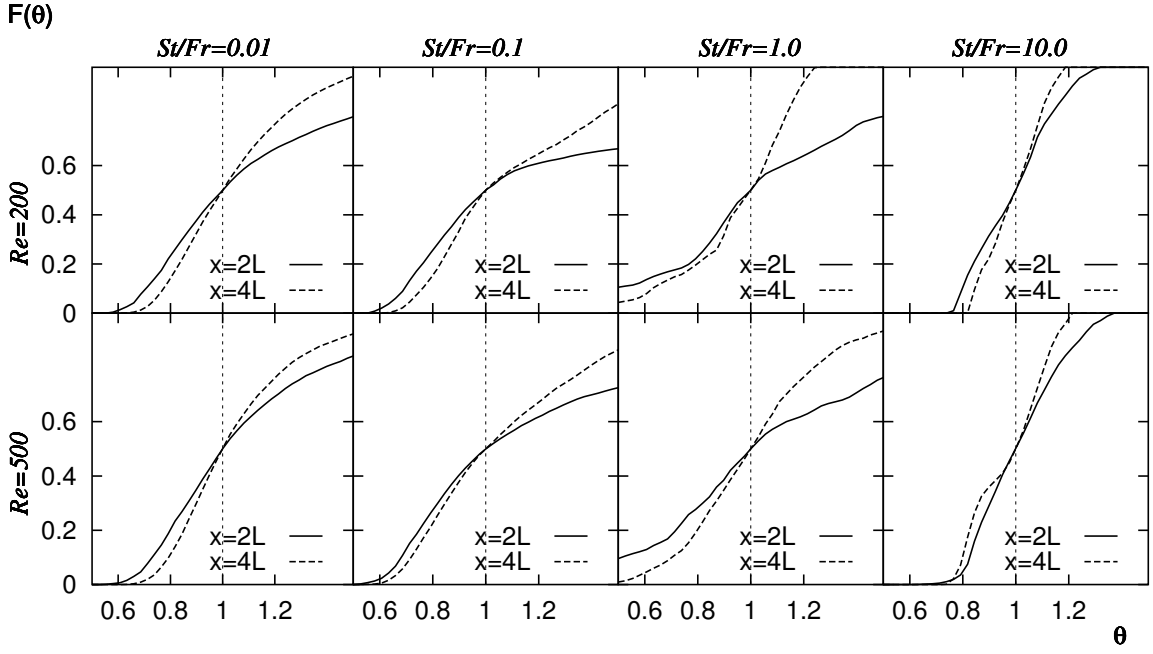

Figure 5.19: Cumulative residence time in vertical reactor (down flow)

higher Reynolds numbers (Re>200), promote the plug flow behaviour of the reactor.

In a horizontal reactor, settling of the particles is a serious problem and is directly related to the St/Fr ratio. It was found that in order to keep the majority of the particles in suspension the St/Fr ratio should be small and the Reynolds number high (St/Fr<0.01 and Re>500). One should note that particle-particle collisions are not included in the model. These collisions likely play a role in the settling process. Since particle-particle collisions help to keep particles in suspension, neglecting these collisions might lead to an over-prediction of the number of particles that settle down.

Because of this strict and impractical limit on the St/Fr, it was concluded that a vertical reactor is more suitable for the process. If the flow direction is downward, no problems regarding the entrapment of particles occur, which removes the limit on the St/Fr ratio considering the settling of the particles. However, the limits regarding the mixing of the particles remain the same, because particles collide with the mixing element, which leads to accumulation of the particles near the mixing elements, when the St/Fr ratio is high (>1). The residence time distribution improves at high St/Fr ratios. Apparently, all particles slide down along the mixing element with roughly the same velocity.

The insight, which is gained about the mixing of real particles in the Kenics™ static mixer, is relevant for other industrial processes that involve the translation of a continuous stirred tank reactor into a pipe reactor. In that case the control of the residence time and mixing is important for the efficiency of the process. A suggestion for future research into the performance of the Kenics™ static mixer reactor is to investigate different angles (between horizontal and vertical) and higher Reynolds numbers. An other interesting topic is the influence of the mixing on the growth process of the copper particles, which will be explored in more detail in the next chapter.

6

Numerical simulation of growing Cu particles in a Kenics™ static mixer reactor

Numerical simulations of the mixing of copper ions (Cu^{2+}) and growing particles have been performed in the range of Re=10-1000 in a vertical (down-flow) Kenics™ static mixer reactor. The growth of the particles is based upon the local Cu^{2+} concentration and determines the reduction rate of the Cu^{2+} concentration, which is solved with a finite volume code. The particles are tracked using a code that solves the BBO-equation and the flow is solved using a Lattice Boltzmann code.
It was found that the Kenics™ static mixer enhances the mixing of Cu^{2+}. However, at low Reynolds numbers (Re<500) the particles are not well mixed, which has a negative influence on the particle size distribution. Furthermore, in a pipe (without a mixer) the particle size distribution is more narrow than in a Kenics™ static mixer reactor, but the Cu^{2+} concentration is not well mixed in a pipe, which slows down the reduction process. Results indicate that a high Reynolds number is necessary to mix both the particles and Cu^{2+} concentration in the Kenics™ static mixer[1].

6.1 Introduction

Copper is one of the most important metals known to mankind. It is used in electronic devices, heat exchange devices, electric wires and so on. Unfortunately, copper is a heavy metal, which can be harmful to the environment. Therefore, waste-water, which contains copper ions needs to be treated. A conventional method to treat this waste-water and recover the copper is via electrolysis. Hage et al. (1999) showed that an alternative for electrolysis can be a (non-ionic type of) reduction process based on autoclave oxidation of carbohydrates. A drawback of this reduction method is that for a low copper concentration the hydraulic load increases dramatically. Therefore, a solvent extraction step, which is also needed for electrolysis, is necessary. This is an expensive step, which can be made redundant by the use of a (continuous) plug flow reactor (PFR), which is investigated in the work presented here.

This novel reduction process can be used to process two waste streams at the same time. A waste stream containing copper ions is combined with a waste stream containing carbohydrates in order to recover copper particles. This is an example of a waste-to-waste-to-product technology. The reduction process of copper(II)sulfate with xylose can be described by an elementary reaction equation, Van der Weijden et al. (2002a):

$$Cu^{2+} + C_5H_{10}O_5 + H_2O \rightarrow Cu(s) + C_5H_{10}O_6 + 2\,H^+ \tag{6.1}$$

The copper particles that are formed are the end product and they grow during their residence in the reactor. Their size distribution determines the economic value of the end product. A more uniform

[1] Accepted for publication in the ISCRE 18 Special Issue of Chemical Engineering Science

size distribution has a higher economic value. The particle size distribution (PSD) depends on the residence time of the particles and copper ion concentration ($[Cu^{2+}]$) that the particles encounter. Therefore, it is important to control the residence time of the particles in such a way that it becomes more uniform and to mix the copper ion concentration. In this work it is investigated, whether it is possible to achieve this is by placing Kenics™ static mixers along the PFR.

A CFD approach is used in order to develop the reactor and to determine the right reactor conditions. The key question is whether it is possible to get a close to uniform particle size distribution in the Kenics™ static mixer reactor. Therefore, the growth and transport of the copper particles is investigated together with the transport of Cu^{2+} concentration inside the static mixer. It is assumed that the rate limiting factor of the particle growth is the diffusion of Cu^{2+} to the particle surface. Experimental results in an autoclave Van der Weijden et al. (2002a), seem to confirm this assumption. Furthermore, the copper particles are recorded along various planes along the reactor, which can provide us with statistical information such as the particle size.

6.2 Growth and reaction model

There are different options to model the growth of particles. An often used approach is the population balance method, Van Leeuwen (1998). In this method, the particles are distributed over a certain number of size ranges, which can be modelled as the population density. If the moment transformation is used, this method is computational cheap. However, gravity is not included in the population balance method of Van Leeuwen (1998). Since the growth takes place at the surface of a particle, the location of the particles is important for the reduction process. The results, which are presented in the previous chapter, show that gravity has a profound influence on the location of the particles. Therefore, the population balance method will not be able to accurately predict the shape of the particle size distribution, because gravity is not included in the model. Despite its shortcomings, the population method could be interesting for engineering applications, when the exact details of the particle size distribution do not play a role. Therefore, the population balance method is explored in more detail in appendix A. In this chapter, however, another growth model is used. Here, the growth takes place at the surface of the particle that is tracked. A copper particle will grow based upon the concentration of copper ions that it encounters.

The precipitation process as described in equation 6.1 is a surface reaction. A surface reaction can be either diffusion controlled or reaction controlled (Sugimoto (1987)). In previous work (Van Wageningen et al. (2002); Van der Weijden et al. (2002a)), it was assumed that the precipitation process was reaction controlled and the reaction kinetics were modelled as a first order reaction (constant rate k_r=0.06 min^{-1}). This assumption was based on experiments that were performed in a titanium autoclave. However, it was found recently that in this setup the reaction takes place at the surface of the reactor instead of at the surface of the particles. Since the total surface of all particles is small compared to the surface of the reactor, diffusion to the surface of the particles plays a minor role in the titanium reactor.

New experiments, Van der Weijden et al. (2002b), were performed in a glass-lined/Teflon autoclave in order to prevent growth at the surface of the reactor. These experiments seem to indicate that the reaction is diffusion controlled, which means that the diffusion process is very slow with respect to the surface reaction. The diffusion of Cu^{2+} to the surface of the particle forms the basis for the growth model of the particles. In figure 6.1, the Cu^{2+} concentration as a function of time is plotted relative to the initial Cu^{2+} concentration. The crosses indicate the experimental results obtained in a titanium autoclave and the pluses indicate the experimental results obtained in the glass-lined autoclave. The two straight (dotted and dashed/dotted) lines indicate the reduction model based

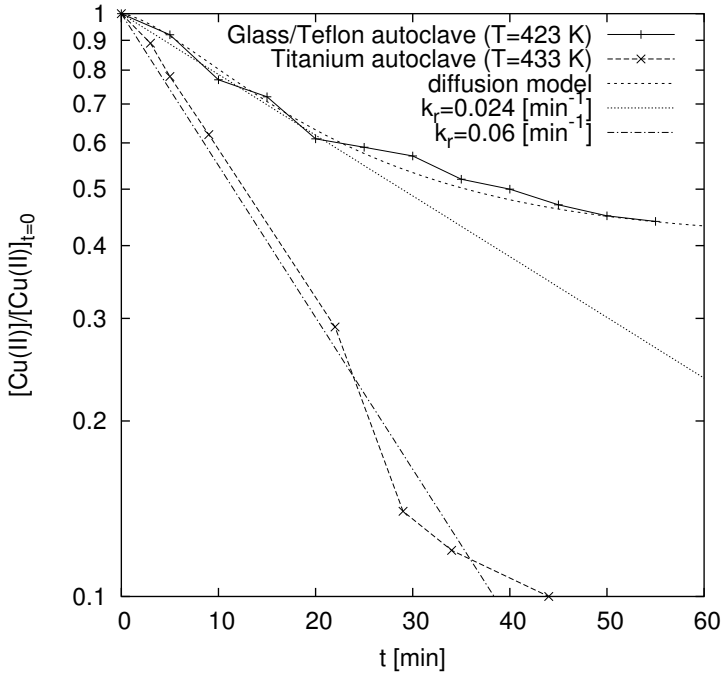

Figure 6.1: Autoclave experiments (titanium and glass-lined/Teflon) compared to first order reaction model (k_r=0.023 & 0.06 min^{-1}) and diffusion model respectively.

upon a constant reaction rate:

$$\frac{\mathrm{d}\mathrm{Cu}^{2+}}{\mathrm{d}t} = -k_\mathrm{r}\mathrm{Cu}^{2+} \tag{6.2}$$

The curved (dashed) line indicates the diffusion model, which is described in the next paragraphs. This model corresponds well to experimental results that are performed in the glass-lined/Teflon autoclave (figure 6.1). Therefore, the growth model of the particles and sink term of the Cu^{2+} concentration are both based upon the diffusion of Cu^{2+} to the particle surface.

The diffusive mass-flow of Cu^{2+} to the surface of a spherical particle, Φ_m is equal to

$$\Phi_\mathrm{m} = 4\pi r_\mathrm{p}\mathbb{D}(T)([\mathrm{Cu}^{2+}](t) - [\mathrm{Cu}^{2+}]_\mathrm{surface}) \tag{6.3}$$

where r_p is the radius of the particle, $\mathbb{D}(T)$ is the diffusion coefficient, which is a function of the temperature T, and $[\mathrm{Cu}^{2+}](t)$ and $[\mathrm{Cu}^{2+}]_\mathrm{surface}$ are the bulk Cu^{2+} concentration and Cu^{2+} concentration at the surface of the particle respectively. It is assumed that the Cu^{2+} concentration in a computational cell is equal to the bulk Cu^{2+} concentration and it is assumed that the surface concentration is equal to the final Cu^{2+} concentration at which the reaction stops. One should note that the final Cu^{2+} concentration depends on the pH, which is not included in the diffusion model.

Furthermore, the mass-flow determines the volumetric and radial growth of a single spherical particle, according to:

$$\frac{\mathrm{d}V_\mathrm{p}}{\mathrm{d}t} = \frac{\Phi_\mathrm{m}}{\rho_\mathrm{p}} \quad \text{and} \quad \frac{\mathrm{d}r_\mathrm{p}}{\mathrm{d}t} = \frac{\Phi_\mathrm{m}}{4\pi r_\mathrm{p}^2\rho_\mathrm{p}} = \frac{\mathbb{D}(T)([\mathrm{Cu}^{2+}](t) - [\mathrm{Cu}^{2+}]_\mathrm{surface})}{r_\mathrm{p}\rho_\mathrm{p}} \tag{6.4}$$

where V_p and ρ_p are the volume and density of the particle, respectively. The sink term of the Cu^{2+}

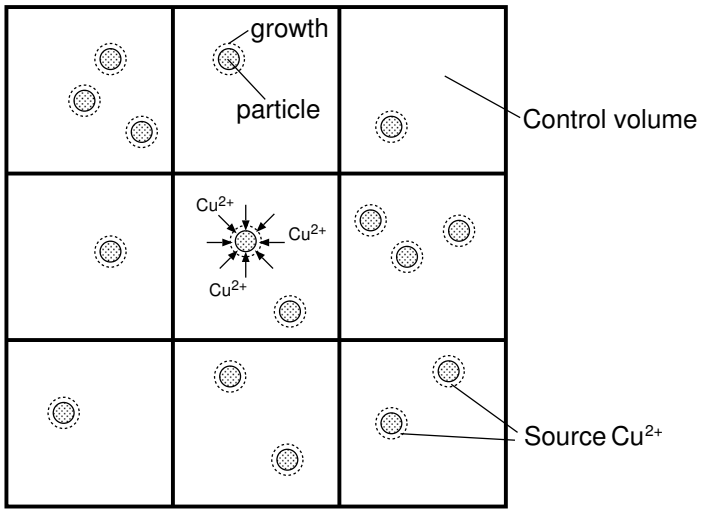

Figure 6.2: Diffusion of Cu^{2+} to the surface of particles.

concentration can be obtained from the mass transfer to all the particles in a given control volume:

$$\begin{aligned} \frac{\mathrm{d}}{\mathrm{d}t}[\mathrm{Cu}^{2+}](t) &= \frac{\sum_{\mathrm{i}=1}^{n_\mathrm{p}} \Phi_{\mathrm{m,i}}}{V_\mathrm{control}} = \overline{\Phi_\mathrm{m}}\,[c_\mathrm{p}] \\ \text{where} \qquad & \Phi_{\mathrm{m,i}} = 4\pi r_{\mathrm{p,i}} \mathbb{D}(T)([\mathrm{Cu}^{2+}] - [\mathrm{Cu}^{2+}]_\mathrm{surface}) \end{aligned} \tag{6.5}$$

where n_p is the total number of particles in the control volume V_control and $[c_\mathrm{p}]$ is the particle concentration. The average mass-flow and particle concentration are used to calculate the reduction of the Cu^{2+} concentration in a single reactor (control) volume in order to compare the diffusion model to the autoclave data (in figure 6.1), where it is assumed that all particles have the same growth characteristics. In the simulation, the source of the Cu^{2+} concentration is linked to the growth of the individual particles in a control volume, which is illustrated in figure 6.2.

One should note that for the diffusion model, which is used in figure 6.1, the particle concentration was estimated from the initial and final Cu^{2+} concentration:

$$[c_\mathrm{p}] = \frac{([\mathrm{Cu}^{2+}]_\mathrm{initial} - [\mathrm{Cu}^{2+}]_\mathrm{final})\, V_\mathrm{autoclave}}{< m_\mathrm{p} >} \tag{6.6}$$

where the average mass of the particles $< m_\mathrm{p} >$ is estimated from the particle size distribution (PSD) that was obtained at the end of the autoclave experiment with Malvern, Van der Weijden et al. (2002b). The particle concentration was equal to c_p=1.2·10^9 [particles/m^3]. Furthermore, the model was fit to the experimental results by modifying the diffusion coefficient of Cu^{2+} (at T=423 K). The diffusion coefficient was estimated from this fit ($\mathbb{D}$=3.2·10^{-9} m^2/s]) and used as an input parameter for the simulations in the Kenics™ static mixer reactor. Since the conditions in both reactors (autoclave and static mixer) are similar, it is assumed that the chemical and particle parameters are the same.

6.3 Numerical setup

The numerical setup is comprised of a 4 element static mixer and consists of 720*120*120=10.4M grid nodes (7.2M fluid and 3.2M wall) to which periodic boundaries are applied (figure 6.3). In this figure L and D are the element length and pipe diameter respectively and their ratio is equal to

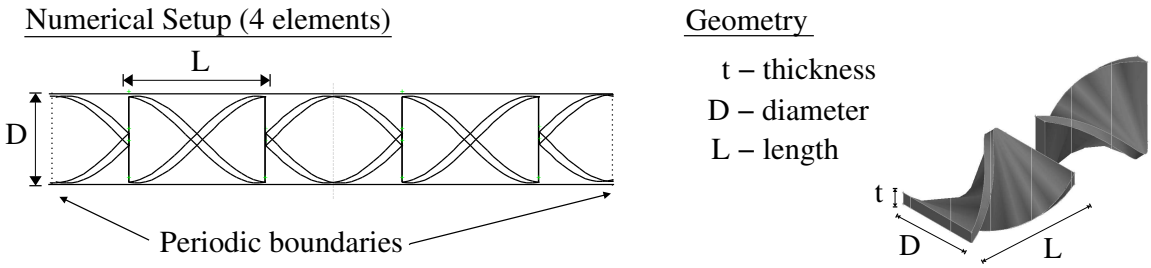

Figure 6.3: Numerical setup and geometry of Kenics™ static mixer.

L/D=1.5. Furthermore, the computational grid is distributed over 8 processors (each 2.1 GHz, 1GB). In this setup the following numerical approach was used.

First, the flow field was solved using a Lattice Boltzmann (LB) flow solver, which solves the Navier-Stokes equation. More details on this method and a thorough validation of the flow field can be found in chapter 4. Second, the Cu^{2+} concentration was solved using a finite volume solver, where the control volumes (CV), which are of uniform size, are formed around each LB grid node. This solver solves the convection diffusion equation with a sink-term $S([Cu^{2+}])$:

$$\frac{\partial}{\partial t}[\mathrm{Cu}^{2+}] + \vec{u} \cdot \nabla[\mathrm{Cu}^{2+}] = \mathbb{D}\, \nabla^2[\mathrm{Cu}^{2+}] - \mathrm{S}([\mathrm{Cu}^{2+}]) \tag{6.7}$$

where $\vec{u}$ is the velocity vector of the fluid. The boundary conditions (inflow/outflow, solid wall) for the Cu^{2+} concentration are a constant gradient in the axial direction at the outlet (end of 4^{th} element), a constant profile at the inlet (start 1^{st} element) and no diffusion at the walls.

Simultaneously with the Cu^{2+} concentration, particles are tracked using a tracking code that solves the Basset-Boussinesq-Oseen (BBO) equation, Maxey and Riley (1983):

$$\frac{\mathrm{d}\vec{v}_\mathrm{p}}{\mathrm{d}t} = \underbrace{\frac{9\mu\ \vec{v}_\mathrm{s}}{2r_\mathrm{p}^2\rho_\mathrm{a}}}_{\text{drag}} + \underbrace{\frac{\rho_\mathrm{p}-\rho}{\rho_\mathrm{a}}\vec{g}}_{\text{gravitation}} + \underbrace{\frac{3}{2}\frac{\rho}{\rho_\mathrm{a}}\frac{\mathrm{D}\vec{u}}{\mathrm{D}t}}_{\text{acceleration}} + \underbrace{\frac{\vec{F}_\mathrm{lift}}{m_\mathrm{p}+\frac{1}{2}m_\mathrm{l}}}_{\text{lift}} \tag{6.8}$$

where $\vec{v}_\mathrm{p}$ and $\vec{v}_\mathrm{s}$ are the particle and slip velocity respectively, μ and $\vec{g}$ are the dynamic viscosity and gravity vector respectively, $\vec{F}_\mathrm{lift}$ is Saffman's lift force, and ρ is the density of the fluid and $\rho_\mathrm{a} = \rho_\mathrm{p} + 0.5\rho$. One should note that the history force and Faxen correction terms are neglected, because they are small compared to the other forces. Moreover, the lift force is added to the equation, because it acts perpendicular to the other forces. When a particle is located close to the wall, modifications are made to both the lift and drag coefficient Chen and McLaughlin (1995); Cherukat and McLaughlin (1994); McLaughlin (1993); Cox and Hsu (1977); O'Neill (1964); Brenner (1961). In order to determine accurately the location of the wall, an analytical function is used to describe the exact location of the mixing elements. Furthermore, if a particle is touching a wall, the normal force of the wall is taken into account, which allows the particle to slide along the wall. One should note that since the mass loading of the particles is low, it is assumed that the particles do not influence the flow. More details about the particle tracking can be found in chapter 5.

Initially, all particles are distributed uniformly over the mixer, where the number of particles is based on the particle concentration found in the autoclave experiments (≈700k particles). The particles have an initial diameter of 10μm and they grow during their residence in the Kenics™ static mixer according to equation 6.4. Their growth is directly linked to the sink-term of the Cu^{2+} concentration,

which is equal to the amount of mass that is consumed by the particles within a control volume, see also equation 6.5. Furthermore, when a particle exits the mixer, it is placed back at the inlet plane at an arbitrary location with its initial diameter (10μm). The simulation is carried out until the average Cu^{2+} concentration does not change anymore. It should be noted that it is assumed that there is no secondary nucleation. Autoclave experiments, Van der Weijden et al. (2002b), seem to support this assumption.

6.4 Reactor design

One of the problems that arises in a horizontal plug flow reactor is the settling of copper particles under gravity, due the relatively large density difference between copper particles and solvent ($\rho_p/\rho \approx 9$). In chapter 5, it was shown that the ratio between the Stokes and the Froude number is an important parameter to describe the settling of the particles in the Kenics™ static mixer reactor. The Stokes and Froude number appear in the dimensionless form of equation 6.8, which yields:

$$\frac{\mathrm{d}\vec{v}_\mathrm{p}^*}{\mathrm{d}t^*} = \frac{\vec{v}_\mathrm{s}^*}{\mathrm{St}} + \frac{\vec{1}}{\mathrm{Fr}} + \frac{3}{2}\rho^* \frac{\mathrm{D}\vec{u}^*}{\mathrm{D}t^*} + \vec{F}_{\mathrm{lift,m}}^* \tag{6.9}$$

where

$$\mathrm{St} = \frac{\rho_\mathrm{a} d_\mathrm{p}^2}{18\mu}\frac{\overline{u}_\mathrm{ax}}{\mathrm{D}}, \qquad \mathrm{Fr} = \frac{\rho_\mathrm{a}}{\rho_\mathrm{p}-\rho}\frac{\overline{u}_\mathrm{ax}^2}{\mathrm{D}g}, \qquad \rho^* = \frac{\rho}{\rho_\mathrm{a}}$$

are the Stokes, Froude and density number respectively.

Furthermore, in chapter 5, it was found that in a horizontal reactor the St/Fr ratio should be smaller than 0.1 in order to prevent the settling of the particles. However, under the given process conditions the St/Fr ratio can range from 0.25-8.7 (Re=1000) to 25-870 (Re=10). Therefore, a horizontal reactor does not seem feasible and a vertical reactor is considered instead. In a vertical reactor there are no problems with sedimentation if the flow direction is downward. However, if the relative slip velocity of a particle is large, the particle may collide with a mixing element, which can lead to the accumulation of the particles near the mixing element and leads to a non-uniform distribution of the particles. This investigation tries to assess, what the influence is of the non-uniform distributed particles on the PSD and if the particle distribution can be improved. In this work the reactor has a diameter of 5 cm, the kinematic viscosity of the liquid is equal to ν=3.0·10^{-7} m^2/s, the initial particle diameter is 10 μm and the initial copper concentration is 2 g/L.

6.5 Results

In figure 6.4, a vertical pipe (downward flow without a mixer) is shown. Here, the sink of the Cu^{2+} concentration is located at the surface of the particles and the flow conditions are Re=200 and initial St/Fr=1.2. In this case the particles tend to move towards the wall of the pipe due to the lift force. The migration velocity of the particles towards the wall, v_m, is estimated from the balance between the Saffman lift and drag force in the radial direction, where the particle slip velocity in the axial direction is used to calculate the lift force. It was found that $v_\mathrm{m} \approx 0.001\ v_\mathrm{s}$, which leads to a particle concentration at the 'near wall' cells that is approximately 2-3 times larger than cells located next to these cells. Because there are more particles located in the near wall region, there is more surface available in that region. Furthermore, the particles have a longer residence time near the wall than in the centre of the pipe. Therefore, the reaction mainly takes place near the wall of the pipe (figure 6.4). Since there are no mixing elements, Cu^{2+} is transported to the particles solely by diffusion,

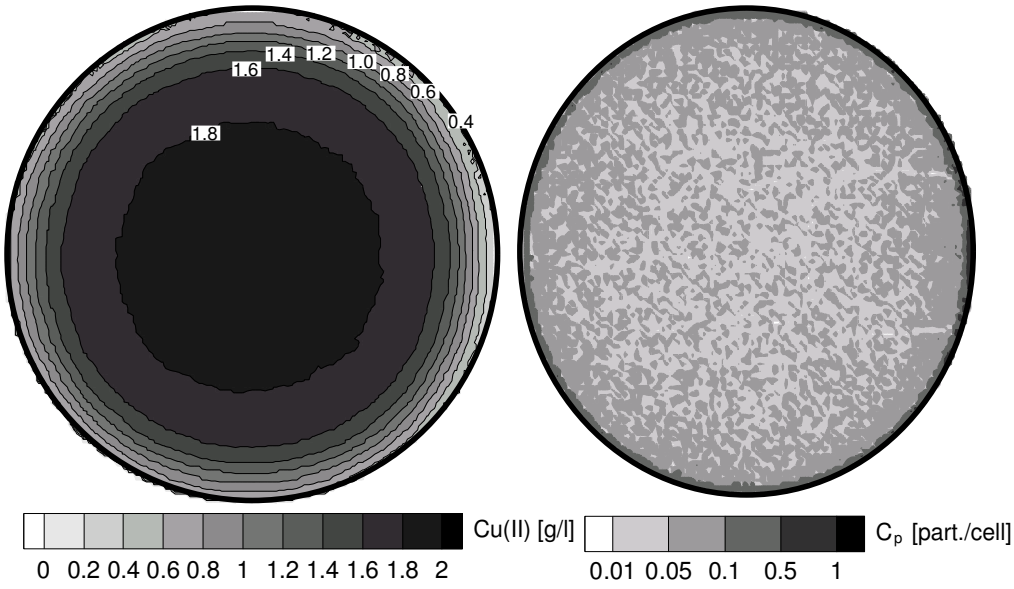

Figure 6.4: Re=200 (pipe), Cu^{2+} and particle concentration after 6 diameters, which corresponds to 4 elements

which slows down the reduction process.

Figure 6.5 shows the results of the simulation of the Kenics™ static mixer under similar conditions. The results indicate that the mixing of the Cu^{2+} improves, but now all the particles are located near the mixing element. The reason for this is the fact that due to their relatively high slip velocity the particles collide with the element and slide down along it. Since the particles are located near the mixing element, the reaction only takes place at that location. Furthermore, the lift and acceleration forces still tend to push the particle outward, which leads to a higher concentration of particles in the corners of the mixing element, and hence the reaction is strongest over there.

When the Reynolds number is increased, the mixing of the particles improves. At Re=500 (initial St/Fr=0.5) less particles are located near the wall, but the distribution is still far from uniform, (figure 6.6). A more uniform distribution is obtained at Re=1000 (initial St/Fr=0.25), but there is still a higher particle concentration near the wall of the mixing element, (figure 6.7). The reason for the improved mixing of the particles is the fact that the relative slip velocity of the particles is lower, which leads to less collisions with the mixing elements.

It should be noted that the initial particle size of 10 μm is somewhat arbitrary. Therefore a few remarks regarding the particle size are made. For smaller particles, the St/Fr ratio will be small, which will likely lead to a more uniform distribution as can also be observed at Re=1000, at which the St/Fr ratio is also small. For larger particles the opposite is true. The particles will have a larger St/Fr ratio and as a result they will more likely collide with the mixing element. Therefore, for larger particles a higher axial liquid velocity will be necessary to avoid collision with the mixing element. One should note that a higher axial liquid velocity will decrease the St/Fr ratio, but it will increase the Reynolds number.

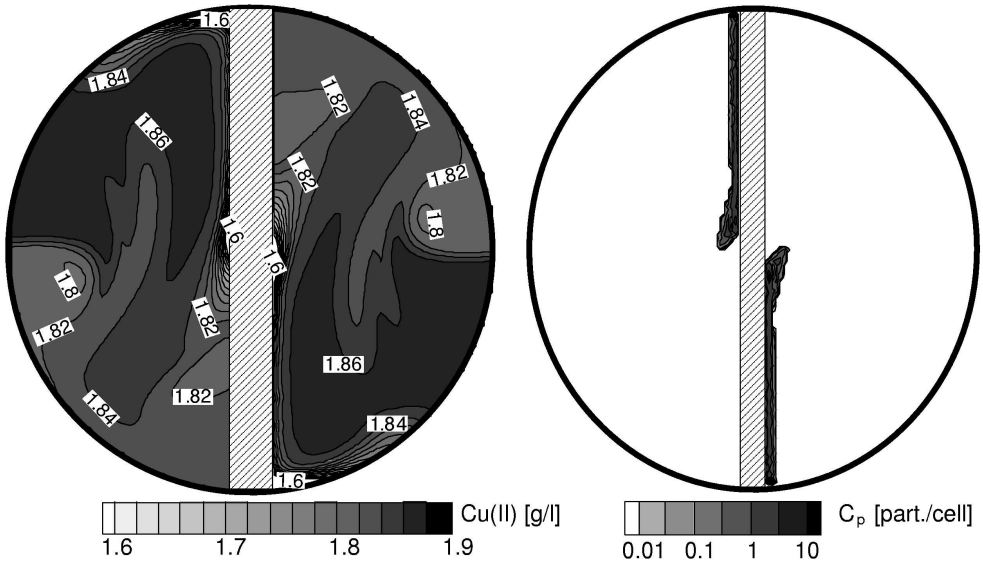

Figure 6.5: Re=200, Cu^{2+} and particle concentration after 4 elements

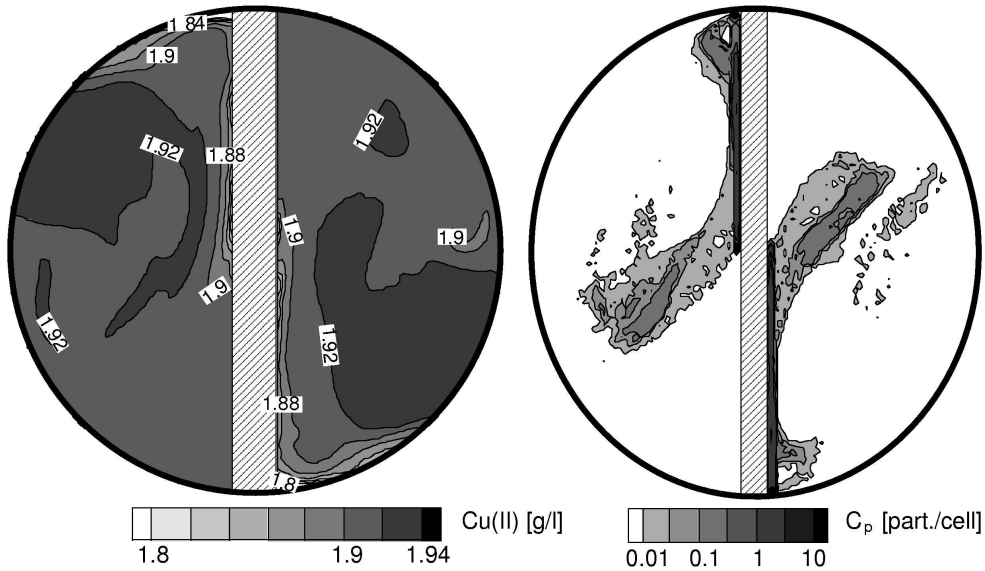

Figure 6.6: Re=500, Cu^{2+} and particle concentration after 4 elements

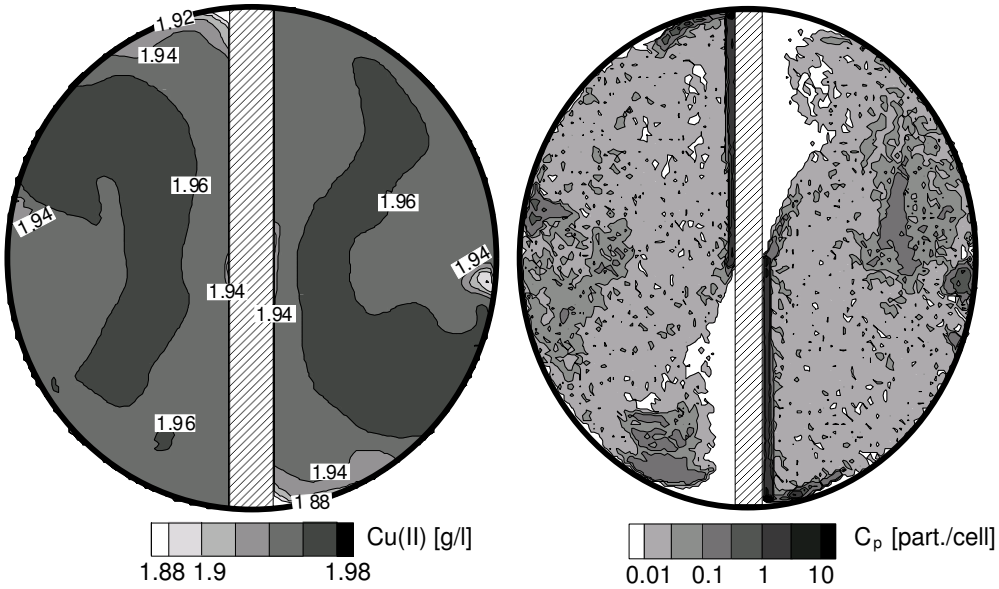

Figure 6.7: Re=1000, Cu^{2+} and particle concentration after 4 elements

6.6 Particle size distribution (PSD)

The key question that remains is how the particle size distributions are influenced by the non uniform distribution of the particles. Figure 6.8 shows the probability density functions (pdfs)of the particle radii of the cases that are discussed before. The pdf of the pipe at Re=200 is very narrow, which seems surprising. It can be explained, however, by the fact that nearly all particles reside in the same region (close to the wall). Hence, they 'see' the same Cu^{2+} concentration and liquid velocity, which leads to a more uniform growth of the particles.

The pdf of the mixer at Re=200 is not narrow and shows to peaks. The two peaks form at the intersection between the first and second mixing element (figure 6.9). structures in the flow. Here, one half of the particles collides with the 2^{nd} mixing element at a later stage than the other half. The particles that slide along the wall have a longer residence time and therefore will have more time to grow than particles that are in the free stream region, which explains the formation of the two peaks. When the Reynolds number is increased (Re=500 and Re=1000) the pdf of the particle size in the mixer is more narrow, but is still less narrow than the pdf found in the pipe. At Re=1000 the pdf improves, when the particles pass another 4 elements (i.e. the pdf at the 8^{th} element), while at Re=500 the pdf shows to peaks similar to the pdf at Re=200. One should note that for the '8^{th} element' simulations the output concentrations and pdf of the '4^{th} element' simulations were used as input parameters.

6.7 Concluding remarks

The new reaction model, which has the sink of the reaction at the surface of the particles, leads to new insight regarding the growth of the particles and behaviour of the particles in the Kenics™ static mixer. First it was assumed that the Kenics™ static mixer would improve both the mixing of the particles and Cu^{2+} concentration. Indeed, the mixing of the Cu^{2+} concentration improves significantly in the Kenics™ static mixer reactor. However, the mixing of particles fails at low Reynolds numbers. At higher Reynolds numbers the mixing of the particles improves, but the axial velocity

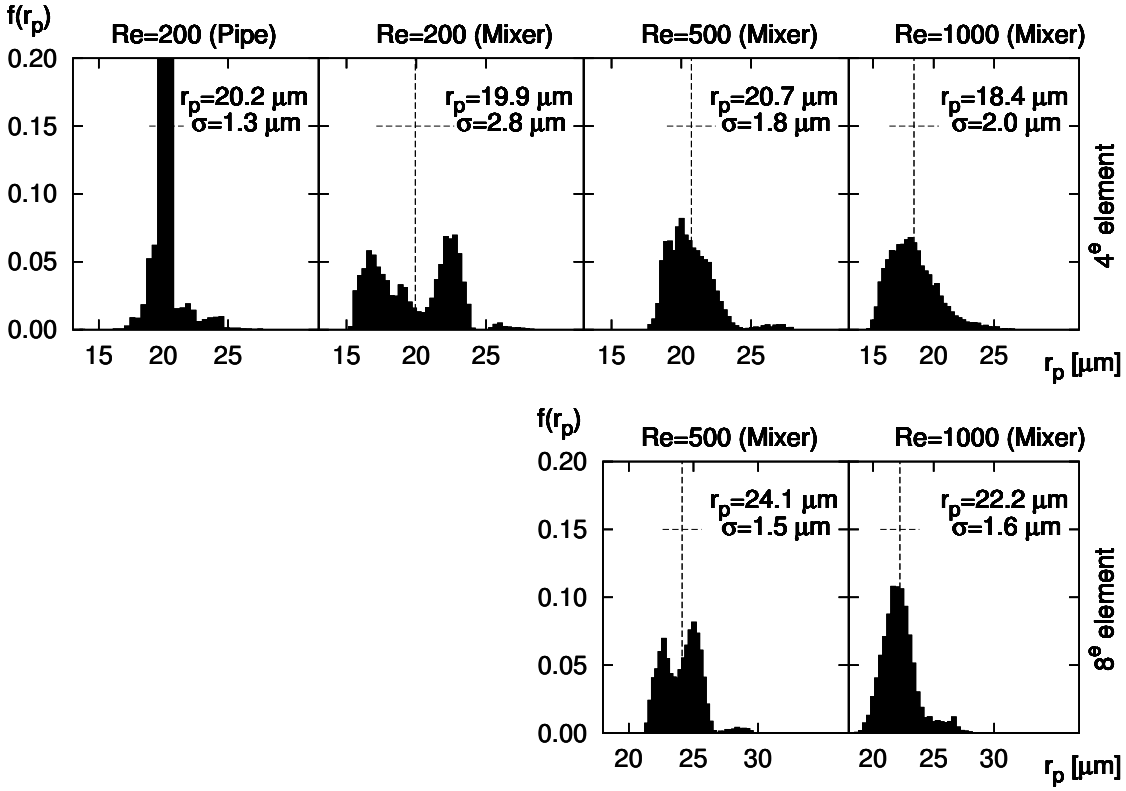

Figure 6.8: Particle size distribution of the particles

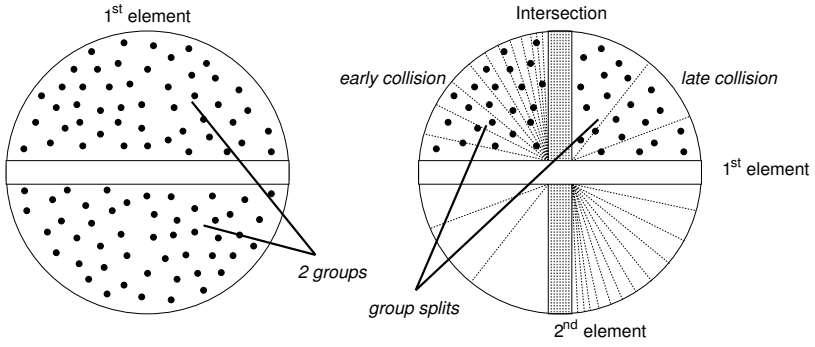

Figure 6.9: Collision of particles after first mixing element

of the liquid increases in that case, which will lead to a longer reactor.

It should be noted, that not merely a low Reynolds number causes the poor mixing of the particles in the Kenics™ static mixer, but the St/Fr ratio, which is high at a low Reynolds number, is the cause of the poor mixing of the particles. In chapter 5 it was shown if the St/Fr ratio is larger than one, particles start to collide with the mixing elements. In that case, a large number of particles are located near the mixing element (figure 6.5), which causes the particle size distribution to be wide (figure 6.8). In this context is should be remarked that the St/Fr ratio is low when (1) the flow-rate is high, which corresponds to a high Reynolds number, or (2) the particles are small.

Other methods such as the population balance method, Van Leeuwen (1998), do not take into account gravity and the exact location of the particles. However, it was found that the location of the particles, i.e. the source of the reaction, has a profound influence on the shape of the PSDs. Therefore, it can be concluded that the PSD can only be predicted correctly if also the location of the particles is taken into account. In other words, a model that includes both the particle growth and particle trajectories can more accurately predict the particle size distribution. However, it should be noted that the computational demand increases significantly, when compared to the population balance method as described by Van Leeuwen (1998).

Surprisingly, under the given conditions, a pipe without mixing elements performs better with respect to the PSD than a reactor equipped with a Kenics™ static mixer. However, in a pipe the reduction process is limited by the diffusion of Cu^{2+} towards the wall region, where more particles are located and the particles move slower. Therefore, adding mixing elements seems to be recommendable in order to mix the Cu^{2+} and speed up the reduction process. Furthermore, it would be both interesting and important to investigate whether the Kenics™ static mixer will be able to 'free' the particles from the wall, when it is added to a pipe reactor, and to check what the influence will be on the PSD. A combination of a pipe and a static mixer might have the best or worst of both worlds. The static mixer can be applied, when St/Fr is smaller than one and a pipe can be applied, when this value is exceeded. In a pipe, the particles eventually end up near the wall due to the lift force. The question arises, whether it is possible to 'free' the particles from the wall with a static mixer, which stresses the importance for further research.

7

Design of a reactor for the reduction of Cu^{2+} with soluble carbohydrates

This chapter combines all previous investigations into the reduction of Cu^{2+} with soluble carbohydrates to come up with a design proposal for a novel reactor. A one dimensional model is used to predict the reduction in three reactor configurations (batch, horizontal plug flow reactor and vertical plug flow reactor). Experiments in a glass-lined autoclave were used to test the model and to obtain the model parameters. The faster reduction at higher Cu^{2+} concentrations that was observed in the glass-lined autoclave could be predicted by the model. Based upon the model predictions, the aspect of process energy and feasibility of the different reactor types was evaluated and compared to the conventional method, i.e. electro-winning. It was found that the mechanical energy, which used for pumping and stirring, is much lower than the energy that is necessary for heating. Furthermore, the reduction process can compete with the conventional method (electro-winning), when concentrated streams are processed (40 g/l) or when the (waste) stream is contaminated with organic material. The ultimate choice of the reactor type depends on the (waste) stream size, equipment costs, quality of the end product and whether an integration into a continuous process is desired. [1]

7.1 Introduction

Copper is one of the most important metals used by mankind. It finds its application in electronic devices, heat exchange devices, electric wires and so on. Copper, however, is a heavy metal, which can be harmful to the environment. Therefore, wastewater that contains copper ions needs to be treated prior to discharge. Aqueous copper waste can originate from various industries such as the electronic, galvanic and mining industries. A conventional method to treat this wastewater or other (concentrated) copper containing streams is to recover the copper via electrolysis.

Hage et al. (1999) studied reduction of copper with cellulose in autoclave experiments. Total copper recoveries of 99% were reported. At least 20% of the recovery, however, resulted from cementation by the stainless steel stirrer used in their autoclave. Still, this process had the potential to be further developed into an alternative process for electro-winning. Van der Weijden et al. (2002a) continued these investigations by testing other reductants yielding carbohydrates such as, wood extracts, wood dust, bacteria, starch and various sugars. Almost a 100% recovery was achieved at temperatures as low as 140 °C using sugars as reductant and by controlling pH. Mambote et al. (2000) pointed out that such a waste-to-waste-to-product process is both commercially and environmentally attractive. It could find its application e.g. as an alternative reduction step in the processing of low-grade copper ores in the mining industry. Furthermore, tests with solutions that contain both silver and copper

[1] to be submitted to the Canadian Metallurgical Quarterly

showed that by controlling the temperature, silver could be reduced prior to copper and thus both metals could be retrieved separately (Van der Weijden et al. (2001)).

An important economic aspect for success is the reactor type. Initial tests were carried out in autoclaves, but for a continuous process and for a more optimal use of reactor volume, a plug flow reactor would be more suitable. To investigate this alternative reduction process, experiments were carried out using titanium autoclaves and a titanium plug flow reactor. A major problem, however, was the formation of copper platelets on the titanium reactor wall. Although the plug flow reactor had static mixers after each 50 m interval of pipe (diameter = 1 cm), the reactor would get clogged after a week of continuous operation at low Cu^{2+} concentrations (2 g/L) and after only hours at higher Cu^{2+} concentrations ($>$10 g/L).

Besides this problem of reduced throughput, an additional aspect for the economics and viability of this process is the quality of the end products, i.e. the quality of the copper powder and the composition of the remaining solution. Since the purpose of this process is also to reduce the environmental impact of the combined waste streams, the residual aqueous copper, acid and organic concentration as well as discharge costs are important aspects to consider (Van der Weijden et al. (2001)). Autoclave investigations in search of the optimal process parameters to achieve a good product as well as a clean solution have been carried out (Van der Weijden et al. (2002b)).

Considering the quality of the copper powder, the formation of fragile and porous copper platelets that adhere to the reactor wall is not ideal. The prevention of the growth of copper platelets on the reactor wall seemed to be one of the major challenges in order to render this process successful. For a high quality powder a uniform size distribution and a regular shape of the particles is preferred, because of the higher product price. Several studies were carried out to optimize the copper powder shape and size distribution (Van der Weijden et al. (2002b)). At the same time, the relationship between particle size distribution and flow properties was investigated through computer simulations (Van Wageningen et al. (2002); Van der Weijden et al. (2003); Van Wageningen et al. (2004b)).

The present study combines all mentioned investigations in order to propose a sustainable (plug flow) reactor design for the treatment of copper streams with soluble carbohydrates. Computer simulations of the growth of copper particles in various reactor configurations were compared. Additional laboratory experiments to verify the numerical results were carried out. Furthermore, the aspect of process energy consumption is evaluated. Considering the elevated temperature at which the process runs, this is an important aspect from both economic and environmental point of view. Therefore, in this study an estimate is made of the energy requirements (per kg recovered copper) for different reactor configurations and compared to electro-winning and EMEW (Treasure (2002)), which are a conventional method and a new method to recover copper, respectively.

7.2 Process chemistry

Van der Weijden et al. (2002a) describe in detail the hydrolysis and degradation reactions of several carbohydrates and their influence on the reduction of Cu^{2+}. The degradation of the carbohydrates occurs simultaneously with the oxidation reaction. Although several carbohydrates were studied and found to be successful reductants, xylose, a pentose sugar, was selected in previous studies and in the present study, because of its solubility and its effectiveness at lower temperatures in comparison to the hexose sugars. The redox reaction of copper with xylose equals:

$$\mathrm{Cu^{2+}} + \mathrm{C_5H_{10}O_5} + \mathrm{H_2O} \rightarrow \mathrm{Cu(s)} + \mathrm{C_5H_{10}O_6} + 2\mathrm{H^+} \tag{7.1}$$

In equation 7.1 only the oxidation reaction of xylose to xylonic acid in combination with Cu^{2+} reduction is considered. Because degradation of xylose is not considered, the molar ratio of Cu^{2+} to xylose of 1:1 is too optimistic and an excess dose of xylose is used to reduce all copper present. In order to prevent formation of cuprite, the initial pH of the solution should not be higher than 3.5.

From equation 7.1, it is obvious that the acidity increases during the process. This apparently causes the reduction reaction to stall, whereas the carbohydrate degradation reaction is accelerated. New observations indicate that not merely the acidity increase is responsible for the decrease in reaction rate, because the pH at which the reduction stalls differs for different copper concentrations (figure 7.1). It can also be observed that the reduction at 2 g/L in a glass or Teflon configuration stalls at different pH. Depletion of xylose as a factor for the recovery decrease was ruled out by adding more xylose. The time at which stalling of the reduction occurs, appears to be linked to the moment at which the solution turns yellow/brown and a caramel scent is developed both at high and low copper concentrations. This is typical for the degradation to furfural. Furthermore, it is demonstrated in figure 7.1, that indeed the reduction rate in a mixture of xylose and furfural (1.66 mL/L) is lower, while the pH is the same.

The formation of degradation products together with low pH appear to form a barrier for reduction. By addition of NaOH over 99% recovery of copper is possible. This positive effect of NaOH is not merely achieved by an increase in pH, but is also related to the reduced activity of the produced organic acids and degradation products and by formation of organic salts. This was shown in a study of Abbadi et al. (1998), in which the oxidation of D-glucose using Pd as catalyst is hindered by gluconic acid and complexation with Pd unless KOH is added.

7.3 Influence of process conditions

7.3.1 Reactor type: comparison of the reduction process in an autoclave and a plug flow reactor

Experiments have been carried out in a titanium autoclave and titanium plug flow reactor. In order to be able to use experimental data for computer simulations, it is important to know whether data generated by autoclave experiments can be used to simulate plug flow reactor phenomena. In this section, a short description is given of the two experimental setups that were used (autoclave and PFR). Next, the autoclave results (Van der Weijden et al. (2002a)) are compared to the results that were obtained in a pilot PFR (Van der Weijden et al. (1999)).

The autoclave is equipped with a double bladed Rushton turbine and can be filled upto 2/3 of the total volume (i.e. 7 L). An oscillation pump was connected to the autoclave to inject the xylose at set-point. The same pump was used to inject a 1M NaOH solution to adjust the pH after 10 minutes. Furthermore, the pressure in the autoclave could be increased by injecting nitrogen and the autoclave was kept at constant temperature (i.e. 185 °C). A dip tube was used to take samples at certain time intervals. The samples are cooled with a cooling unit before their release in order to stop the reaction and to avoid flash evaporation. A schematic overview of the autoclave can be found in figure 7.2.

The plug flow reactor was comprised of 10 titanium coils (5 pairs), which each have a length of 25m. Between the coils static mixers were placed and the diameter of the reactor tube was 1 cm. The coils are heated in separate compartments, which are comprised of temperature controlled oil vessels. The feed is prepared in a stirred tank, which had a volume of 200 L, and is pumped into the plug flow

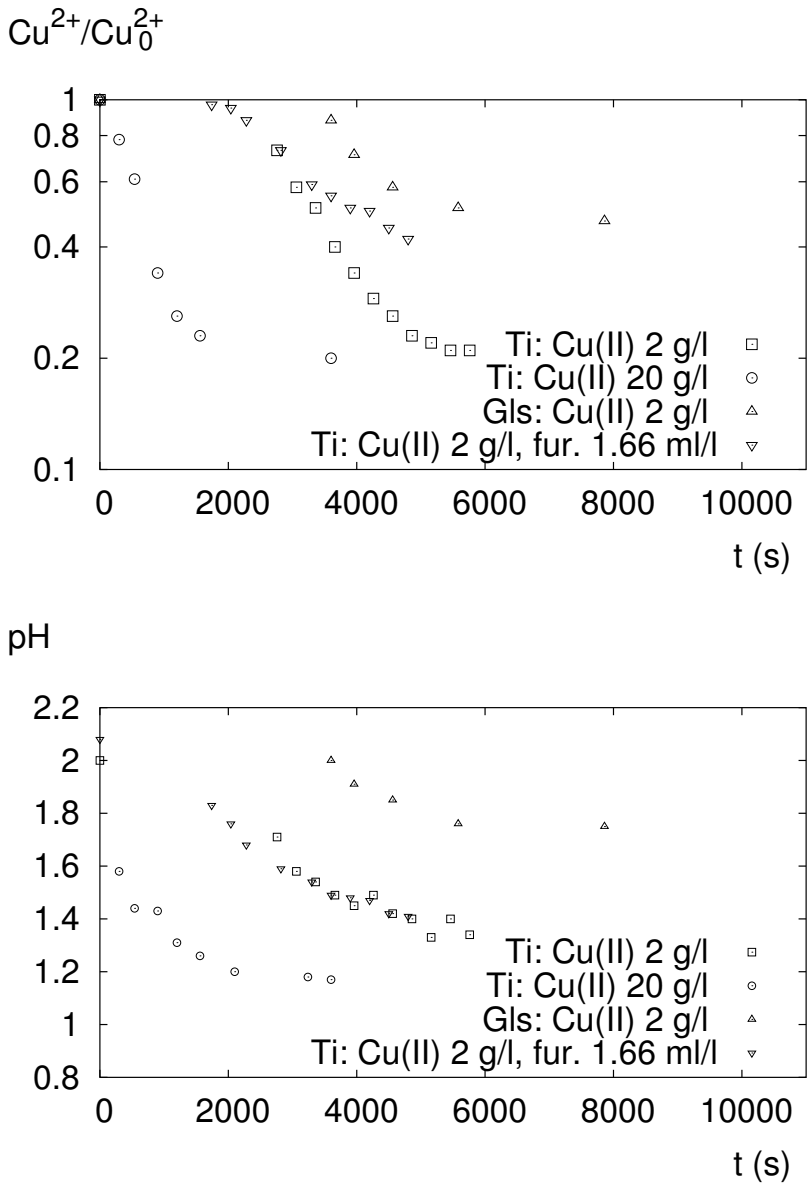

Figure 7.1: Comparison of Cu^{2+} reduction (top) and pH (bottom) of solution containing small amount of furfural and solutions containing only xylose (T=150 °C).

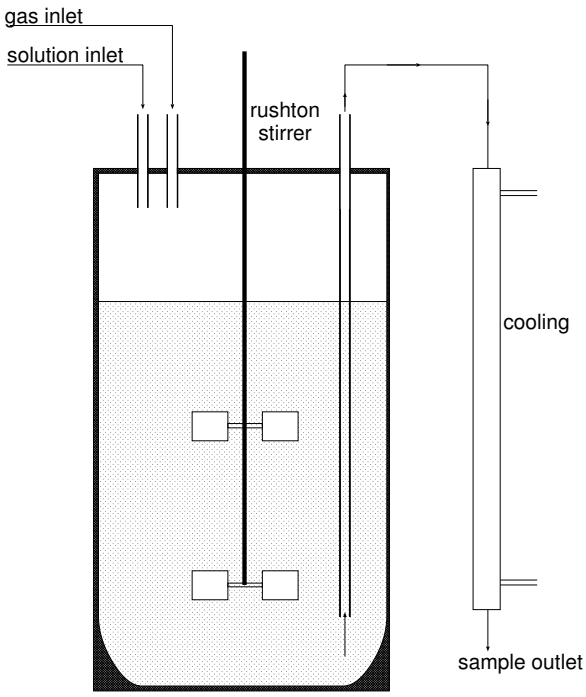

Figure 7.2: Titanium autoclave equipped with Rushton stirrer

reactor with a flow rate of 35-50 L/h. The pressure of the feed can be adjusted by injecting nitrogen to avoid that the feed exceeds the boiling point in the PFR. Samples are taken at three sample points, which are located at the exit of the 1st, 3rd and 5th coil pair after 50, 150 and 250 m, respectively. The pH could be adjusted via entry points, which are located at 100 and 200 m, respectively. A schematic overview of the original plug flow reactor can be found in figure 7.3 and more detailed information about this setup can be found in Van der Weijden et al. (1999).

During a typical run, the temperature in both reactors was set to 185 °C and the initial solution consisted of 5.7 g/L xylose and 2 g/L Cu^{2+}. The solution was acidified with sulphuric acid (pH$\leq$3.5). Furthermore, the pH in some experiments was increased after a certain time by adding 1M NaOH to achieve a higher reduction. To obtain a full reduction of Cu^{2+}, both the autoclave and PFR experiments were repeated with pH adjustment, which is indicated with the filled symbols (figure 7.4). In the case of the PFR, 1M NaOH was continuously added at a rate of 1.5 L/h. The injection point was located at 100 m, which roughly corresponds to a residence time of 10 minutes (at a reactor flow rate of 50 L/h). In the case of the autoclave experiments the pH was adjusted after 10 minutes with a continuous flow of NaOH (0.01 L/h). It should be noted that the pH adjustments of the autoclave and PFR are not fully comparable, since the NaOH was continuously added into the autoclave. To have a one to one comparison, a single (pulse) injection of 1M NaOH (0.15 L in 5 L solution) would be required. However, both experiments show that a full reduction is possible with pH correction.

The reduction of Cu^{2+} in the titanium autoclave and PFR can be compared with respect to the residence time (t_{res}). The residence time of the PFR is obtained from the position of the sample location (l_{sample}) and average axial velocity (u_{ax}):

$$t_{\mathrm{res}} = \frac{l_{\mathrm{sample}}}{u_{\mathrm{ax}}} \qquad \text{with} \qquad u_{\mathrm{ax}} = \frac{\Phi_{\mathrm{l}}}{0.25\pi D^2} \tag{7.2}$$

where Φ_{l} is the flow rate and D is the diameter of the reactor tube. Figure 7.4 shows the Cu^{2+}

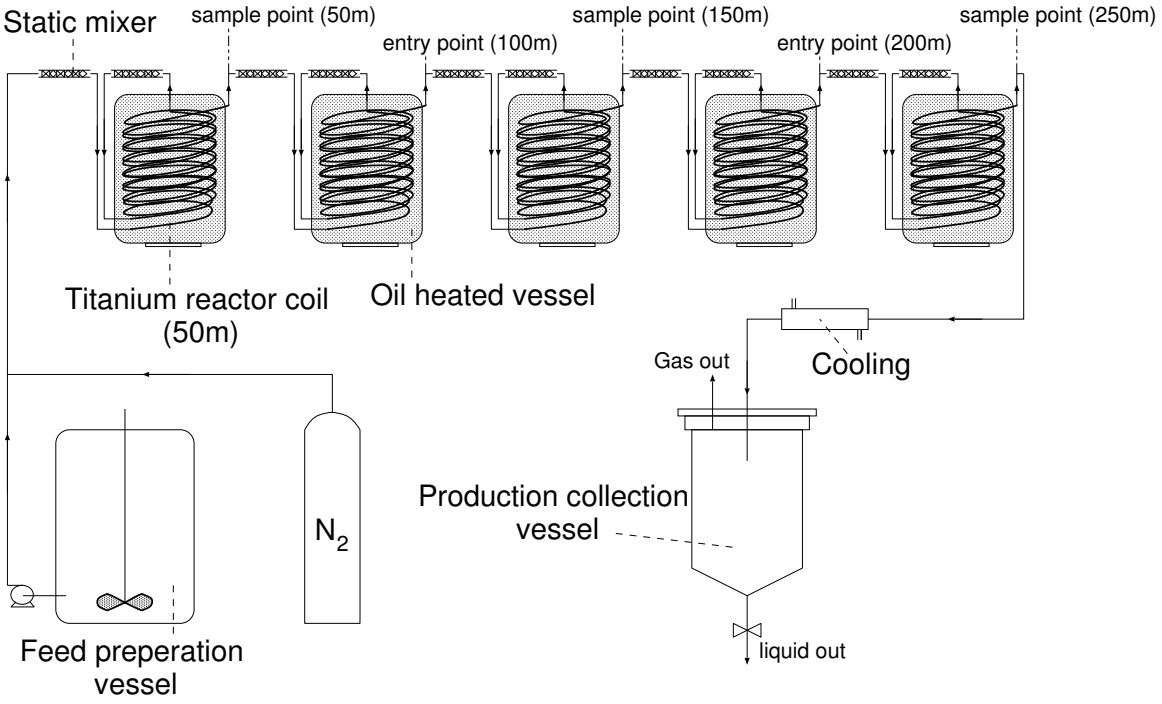

Figure 7.3: Titanium plug flow reactor

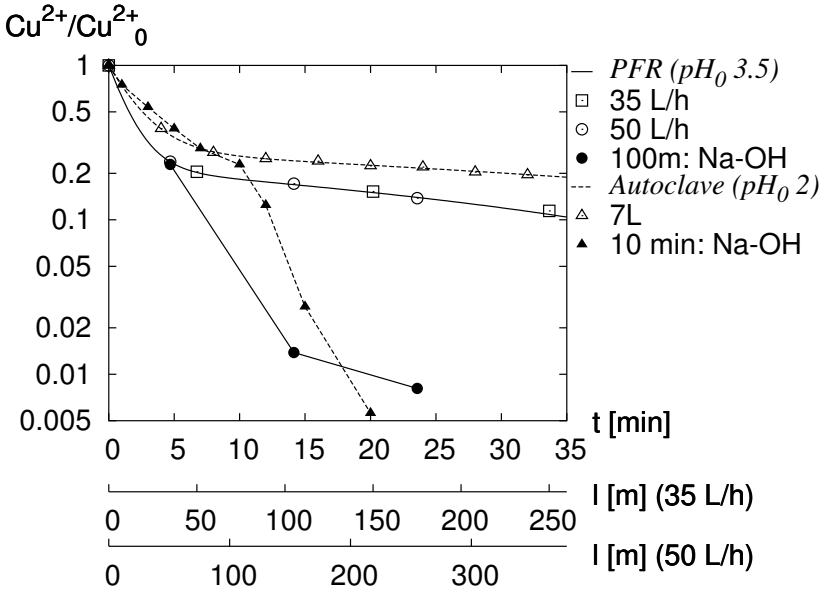

Figure 7.4: Cu^{2+} concentration as a function of residence time (and reactor length)

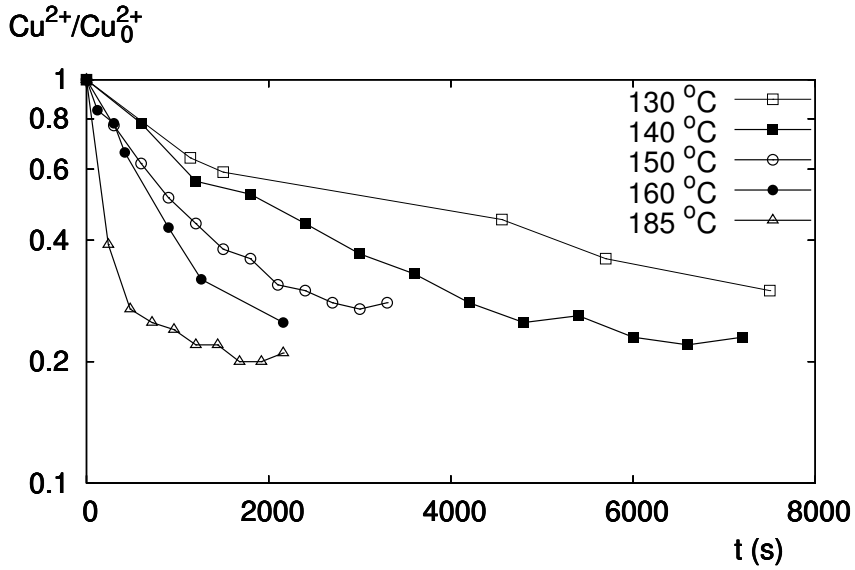

Figure 7.5: Cu^{2+} reduction as a function of the temperature in a titanium autoclave (T=130... 185 °C).

concentration relative to the initial concentration as a function of the residence time, which in the case of the PFR is proportional to the reactor length. The squares and circles indicate the residence time of the PFR and the triangles the residence time in the autoclave. One should note that different residence times of the PFR could be obtained by varying the flow rate in the PFR. A similar trend in Cu^{2+} reduction can be observed for both the PFR and autoclave. Since the surface of the reactor is much larger than the total surface of the metallic particles, the particle surface does not influence the reaction rate in a titanium reactor environment. For this reason, the reaction rates of the autoclave and plug flow reactor are comparable. In the next sections, the influence of the reactor material and temperature on the process will be discussed in more detail.

7.3.2 Reduction at different temperatures

The influence of process temperature was investigated in a titanium autoclave and plug flow reactor. The process temperature is important with respect to energy consumption and annual throughput. For the study presented here, additional autoclave experiments have been conducted in a titanium autoclave at low temperatures. In figure 7.5, the Cu^{2+} concentration relative to its initial concentration is plotted as a function of time for the different temperatures. It can be observed, that the reduction rate is faster, at higher temperatures. All experiments show that initially, the reduction rate is constant, after which the reduction rate stalls. This decrease in reduction can largely be attributed to the formation of furfural.

7.3.3 Influence of process conditions on the copper product

The copper product that is recovered from the titanium reactors shows a wide variety of shapes and sizes and size distributions. In figure 7.6(a), the large dendritic platelets formed in the titanium reactor ($[Cu_0^{2+}]$=2 g/L) are shown.

The reactor wall catalyses the reduction process by reducing the energy barrier for nucleation. From these nuclei platelets can develop by epitaxial growth as the misfit between the titanium substrate

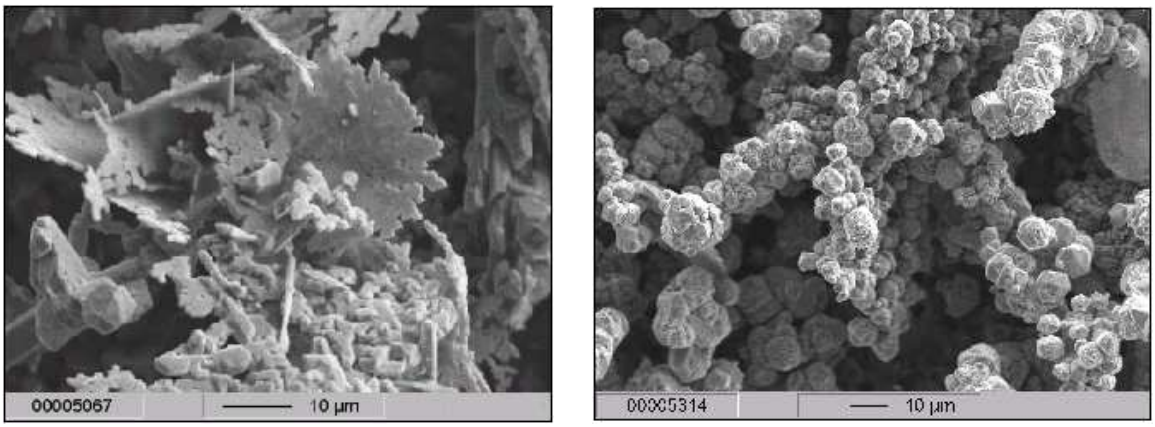

(a) (b)

Figure 7.6: Copper particles in a titanium reactor (a), with additive gelatin (b) (Cu_0^{2+}=2 g/L,Van der Weijden et al. (2003)).

and copper precipitate is small (Mutaftschiev (2001)). These porous and voluminous platelets have a lower economical value. The platelets detach after a certain time and tend to coagulate resulting in clogging of the PFR. Furthermore, a platelet has a larger surface than a spherical particle, which leads to a higher reaction rate, because there is more surface available for the reaction. The size of the platelets decreases with (1) increasing temperature (200 μm at 140 °C and 50 μm at 185 °C), (2) decreasing pH and (3) increasing copper concentration. It is hard to relate this finding to the degree of supersaturation, because the oxidants that form in time at the various temperatures cannot be properly quantified and qualified. In situ Raman spectrometry might provide more information regarding degrees of supersaturation.

When additives such as gelatine and EDTA are used, the formation of platelets on the reactor wall is prevented and a dense copper powder with an almost uniform size distribution ($<$10 μm, depending on the additive concentration) can be formed. Whereas the effectiveness of EDTA lies in its complexation capacity with copper ions, gelatine works as a glue and changes the surface characteristics. Figure 7.6(b) shows the shape and size of the particles, when these additives are used.

Additional experiments in a glass lined autoclave have been performed to determine whether growth at the reactor wall can be avoided and to gain a better insight in the growth process. In a glass-lined reactor the precipitate (Cu_0^{2+}=2. . . 20 g/L) consists of prisms, cubes and rhombododecahedrons with a more uniform size than in the titanium reactor ($<$30 μm (figure 7.7)). Glass is a wholly structureless substrate and hardly any nucleation occurs on the walls. Therefore, the reduction rate is slower and since the degradation of xylose continues, the reaction already stalls at a lower recovery percentage of copper.

Ideally, copper particles that are formed in the process have a spherical shape and uniform size distribution. It can be concluded that with additives and in a glass lined reactor a more regular shape and size is obtained than in a titanium reactor. The use of additives, however, has the drawback that it is either expensive (gelatin) or harmful to the environment (EDTA). Therefore, coating or glass-lining the reactor seems to be the best option to obtain regularly shaped particles. The application of a glass-lined reactor was therefore further examined in autoclave experiments.

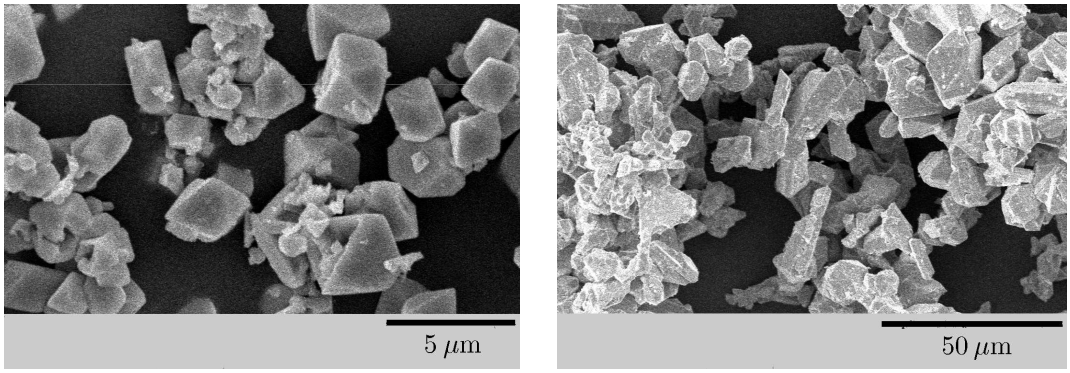

Figure 7.7: Copper particles in a glass-lined reactor: (a) Cu_0^{2+}=2 g/L and (b) Cu_0^{2+}=20 g/L.

In figure 7.8, the reduction rate for the different reactor types (glass-lined and titanium) are compared for different Cu^{2+} concentrations at T=150 °C. At [Cu^{2+}]=2 g/L, the reduction rate in the glass-lined autoclave is much lower than in the titanium autoclave (figure 7.8(a)). The reaction in the glass-lined reactor is slower, because there is less surface available. In a titanium reactor, the growth of the particles starts at the (large) titanium surface, which leads to formation of platelets. These platelets have a larger surface than the spherical particles, hence, the reaction is faster. At [Cu^{2+}]=20 g/L, there is no difference in reduction rate between the glass-lined and titanium configuration (figure 7.8(b)). Apparently, at these high concentrations, the available surface for the reaction in the titanium reaction is comparable to the available surface in the glass-lined reactor. The copper product that is retrieved, however, is significantly different. In the glass lined reactor at 20 g/L no platelet formation is observed. From these experiments, it can be concluded that a glass reactor (or a reactor made of another material that is not a good substrate for copper growth) is a good choice to prevent clogging of a pipe reactor. In view of reaction time, such a reactor would be especially suitable for waste streams with high copper concentrations.

7.4 Computer modelling

7.4.1 One dimensional modelling of the reduction process

The results of the autoclave experiments that have been conducted in the glass-lined autoclave (150 °C) are used as input parameters for a one dimensional model of the reduction process. In this model, the diffusion of Cu^{2+} towards the surface of the copper particles is assumed to be the rate limiting factor and the reduction of Cu^{2+} is modelled with the following equation:

$$\frac{\partial[\mathrm{Cu}^{2+}]}{\partial t} = -S_{\mathrm{Cu}} \tag{7.3}$$

where the sink S_{Cu} is linked to the growth of the copper particles via a mass balance, which over a control volume (for a discrete time step Δt) is equal to:

$$\left([\mathrm{Cu}^{2+}]\right)_{\mathrm{t}} - \left([\mathrm{Cu}^{2+}]\right)_{\mathrm{t}+\Delta\mathrm{t}} + \left(m_{\mathrm{p}}[c_{\mathrm{p}}]\right)_{\mathrm{t}} - \left(m_{\mathrm{p}}[c_{\mathrm{p}}]\right)_{\mathrm{t}+\Delta\mathrm{t}} = 0 \tag{7.4}$$

where m_{p} is the particle mass and $[c_{\mathrm{p}}]$ is the particle concentration.

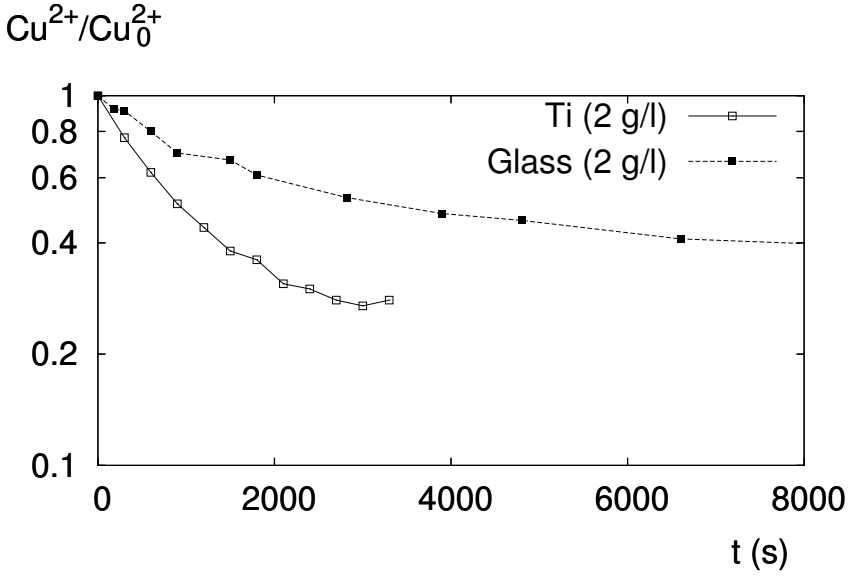

(a)

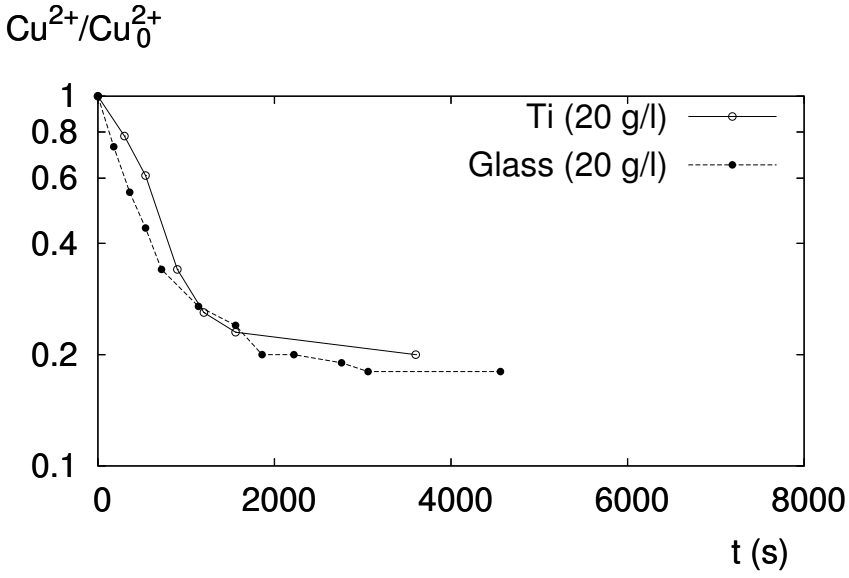

(b)

Figure 7.8: Cu^{2+} reduction at different initial concentrations (2 g/L (a) and 20 g/L (b)) in a glass and titanium reactor, respectively (T=150 °C).

The particle concentration in the reactor was estimated from the average size of the particles at the end of the (glass-lined) autoclave experiments and the amount of Cu^{2+} that was reduced. The final average particle size was 5 μm at an initial concentration of Cu_0^{2+}=2 g/L (Cu_{end}^{2+}=0.39 g/L), and 12 μm at an initial concentration of Cu_0^{2+}=20 g/L (Cu_{end}^{2+}=3.6 g/L). Both estimations result in a particle concentration that is roughly equal to c_p=2·10^{12} particles/m^3. Apparentely, the same number of particles was formed at high and low Cu^{2+} concentrations. This result is surprising, since it was expected that at higher concentrations more nuclei would be formed. It appears that the Cu^{2+} concentration is not the limiting factor for nucleation in the experiments that were conducted. It should be noted that the mean size of the particles formed in a glass-lined reactor is about 10 times smaller than the mean size of the particles formed in a titanium reactor.

Equation 7.4 shows that the reduction of Cu^{2+} is proportional to the increase in mass of the particles. To calculate the increase in mass, the growth of a single particle is considered. Here, it is assumes that all particles meet the same conditions and hence grow at the same rate. The growth rate of a single particle is obtained from the diffusion of Cu^{2+} to a sphere and is equal to:

$$\frac{\partial r_p}{\partial t} = \frac{\mathbb{D}[Cu^{2+}]}{r_p \rho_p} \tag{7.5}$$

where ρ_p is the density of the particle, r_p is the particle radius and $\mathbb{D}$ is the diffusion constant of the copper ions. The density of copper is equal to 9.0·10^3 kg/m^3 and the initial particle size was set to r_p=0.1 μm. The diffusion coefficient is dependent on the temperature and determines the reaction rate. Furthermore, $\mathbb{D}$ was used to fit the model to the experiment in the glass-lined reactor (2 g/l, T=150°C). The diffusion coefficient was set to 1.3 10^{-11} m^2/s, a value used in all the simulations.

For a batch reactor, one control volume is used to predict the copper reduction and the equations 7.4 and 7.5 are solved numerically. The same model is used to simulate the reduction process in a (horizontal and vertical) plug flow reactor, but now the convective transport of Cu^{2+} is included in equation 7.3. One should note that the diffusive transport is neglected, since the convective transport is dominant in the axial direction of the reactor. Equation 7.3 now becomes:

$$u\frac{\partial[Cu^{2+}]}{\partial x} = -S_{Cu} \tag{7.6}$$

where u is the axial velocity in the plug flow reactor. Again the sink S_{Cu} is linked to the growth of the particles via a mass balance, which now yields:

$$\left(u[Cu^{2+}]\right)_x - \left(u[Cu^{2+}]\right)_{x+\Delta x} + \left(m_p v_p [c_p]\right)_x - \left(m_p v_p [c_p]\right)_{x+\Delta x} = 0 \tag{7.7}$$

where v_p is the particle velocity. Figure 7.9 shows the (1D) control volume of the Cu^{2+} concentration. Here, the discrete size of the control volume Δx is determined by the particle velocity and discrete time step.

For the horizontal reactor, the particle velocity is assumed to be equal to the liquid velocity ($v_p = u$). While for a vertical reactor, the particle velocity is obtained from the equilibrium between the drag force and gravity, and is equal to:

$$v_p = \frac{(\rho_p - \rho) g d_p^2}{18\mu} + u \tag{7.8}$$

where d_p is the particle diameter and ρ and μ are the density and dynamic viscosity of the solution, respectively, which depend on the temperature, xylose and Cu^{2+} concentration. It should be noted that in this study, a constant dynamic viscosity and density are assumed (μ=3.0·10^{-4} Pa s

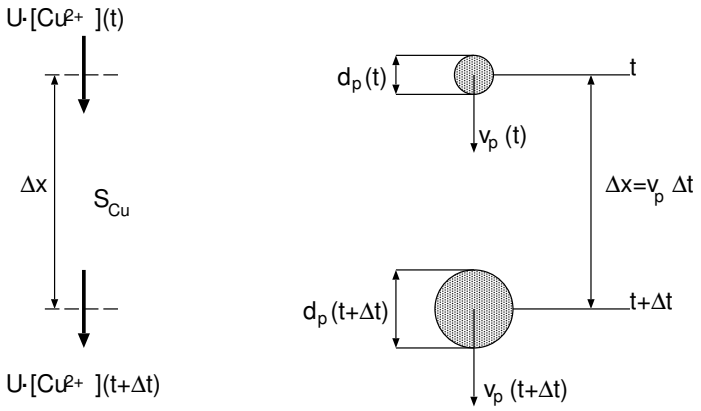

Figure 7.9: One dimensional model of growing particle and Cu^{2+} reduction.

and ρ=1000 kg/m^3). In a vertical reactor, the particle velocity changes, when the particle grows. Since the growth process is slow, there is a small change of the particle diameter in time. Therefore, it is assumed that the particle velocity adjusts instantaneously, when the diameter of the particle changes. Since the particle velocity changes, the particle concentration will change as well in a vertical reactor ($[c_{\mathrm{p},0}] \cdot v_{\mathrm{p},0} \cdot A = [c_{\mathrm{p}}](t) \cdot v_{\mathrm{p}}(t) \cdot A$).

The position in the plug flow reactor l is related to the particle velocity:

$$\frac{\partial l}{\partial t} = v_{\mathrm{p}} \tag{7.9}$$

To predict the Cu^{2+} concentration as a function of the length of the plug flow reactor, the equations 7.5, 7.7 and 7.9 are solved numerically. The results are used to predict the minimal length of the plug flow reactor, which is necessary to reach the desired end Cu^{2+} concentration (0.01 g/L).

The 1D model of the batch reactor is compared to the experiments that were performed in the glass-lined autoclave at T=150°C and Cu_0^{2+}=2. . . 20 g/L (figure 7.10). The 1D simulations show a reasonable agreement with the autoclave experiments. The deviation at longer times can be explained by the fact that the stalling of the reaction due to the formation of furfural is not included into the 1D model. The 1D model predicts that the reduction rate is faster at high Cu^{2+} concentrations, which is confirmed by the experiments in the glass-lined autoclave at Cu_0^{2+}=20 g/L. The faster reduction that is obtained with a higher initial Cu^{2+} concentration can be attributed to the availabilty of more surface. At an initial Cu^{2+} concentration of 20 g/L, the particles initially grow faster due to the high concentration. As a result the particles are larger and more surface will be available for the reaction, which leads to a faster reduction. It can therefore be concluded that high concentrations are more favourable for the process.

7.5 Reactor configuration and efficiency

In this section, three different reactor types (batch, horizontal pipe and vertical pipe) are compared with respect to their energy consumption. For electro-winning (EW) the 'electric' energy consumption per kg is 12.2 MJ/kg (3.4 kWh/kg), where the energy loss in producing the electricity is not taken into account (Maldonado et al. (2001)). For EMEW the energy consumption to reach levels of 10 ppm is 5.1 kWh/kg (Treasure (2002)). In order for the novel process to be competitive on an industrial scale, the energy consumption should be smaller than the convential EW and the newer

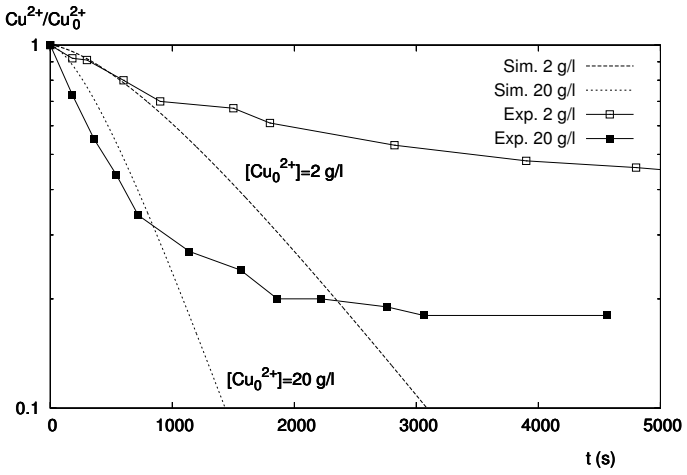

Figure 7.10: Cu^{2+} concentration in batch reactor as a function of t based upon 1D model.

Table 7.1: Heating energy requirement per kg recovered copper as a function of T and Cu_0^{2+}

	E_{heat} [MJ/kg]		
T	$[Cu_0^{2+}]$ =2 g/l	$[Cu_0^{2+}]$ =20 g/l	$[Cu_0^{2+}]$ =40 g/l
130	231	23.1	11.6
150	273	27.3	13.7
185	346	34.6	17.3

EMEW process. To assess whether the reactor can be energy efficient, two parameters are evaluated, the heating power and mechanical energy (due to stirring or pressure drop). Three waste streams of different initial Cu^{2+} concentrations are compared (2, 20 and 40 g/l).

The process takes place at elevated temperature (T_{proc}=130°C up to 185°C) so the waste stream needs to be heated to this temperature. In table 7.1, the amount of heating energy that is necessary to recover 1 kg of copper is evaluated for the different streams (2, 20 and 40 g/l). Here, the specific heat of water (4.2 kJ/(kg °C) is used to calculate the amount of energy. It is obvious that the processing of more concentrated streams is more energy efficient, because less liquid needs to be heated per kg recovered copper. Since heating the solution requires a lot of energy, a low temperature is desirable. However, one should note that a low temperature will yield a slow reduction. Furthermore, it should be noted that the heat used for the process is not lost, it can partly be recovered and used to pre-heat the waste stream, which can reduce the energy consumption (50%).

In the next sections, the mechanical energy consumption for different reactor types (batch reactor, horizontal pipe reactor and vertical pipe reactor) is evaluated for the different initial concentrations at T=150°C. The 1D model is used to predict the time and reduction rate for the different reactor configurations and results of the experiments conducted in the glass-lined autoclave were used as input parameters.

(Mechanical) energy dissipation in a batch reactor

To keep the particles suspended in a batch reactor, a certain impeller speed is necessary. The critical impeller speed (rev/s) at which the particles are just suspended can be calculated with the Zwietering

Table 7.2: Mechanical energy consumption of batch reactor per kg recovered copper (Po=5, T=150°C)

Cu_0^{2+}	**2 g/L**		**20 g/L**		**40 g/L**	
$d_{\mathrm{p,max}}$	6.0 μm		12.8 μm		16.2 μm	
t_{res} ($[Cu^{2+}] < 0.01$ g/l)	6200 s		3980 s		3420 s	
E_{heat} ($T = 150°C$)	273 MJ/kg		27.3 MJ/kg		13.7 MJ/kg	
V [m^3]	N [rev/s]	E_{dis} [MJ/kg]	N [rev/s]	E_{dis} [MJ/kg]	N [rev/s]	E_{dis} [MJ/kg]
0.001	15.6	3.64	24.5	0.905	28.1	0.587
0.01	8.14	2.39	12.8	0.593	14.7	0.385
0.1	4.24	1.57	6.67	0.389	7.63	0.252
1	2.21	1.03	3.47	0.255	3.98	0.165

(1958) correlation, which is equal to

$$N_c = 8\,\frac{d_p^{0.2}\,\nu^{0.1}\,(|g|(\rho_{\mathrm{p}}-\rho))^{0.45}\,c_m^{0.13}}{\rho^{0.45}\,D^{0.85}} \tag{7.10}$$

where ν is the kinematic viscosity, c_m is the mass fraction in % and D is the diameter of the impeller. The energy consumption can be calculated with the Power number:

$$\mathrm{Po} = \frac{P}{\rho N^3 D^5} \tag{7.11}$$

where P is the stirring power.

A prediction is made of the mechanical energy that is needed to reduce different Cu^{2+} concentrations (2 g/L, 20 g/L and 40 g/L) towards an end concentration of Cu^{2+}_{end} <0.01 g/L. Table 7.2 lists the energy dissipation per kg recovered copper for the different concentrations and reactor volumes. Here, the one dimension model is used to predict the Cu^{2+} concentration over time and the final particle diameter $d_{\mathrm{p,max}}$, which is the particle size at the end of the reaction, is used to calculate the critical stirrer speed. The critical stirrer speed, the diameter of the stirrer and Power number are used to determine the power input of the stirrer. Subsequently, the total energy per kg recovered copper is obtained from the stirring power and residence time. It can be observed that a large batch and high Cu^{2+} concentration is most efficient. Furthermore, the mechanical energy is significantly less than the heating energy necessary for the process. Therefore, from an energy perspective a batch reactor is a feasible reactor for the process. A batch reactor, however, has the disadvantage that integration of a batch process into a continuous process generally leads to higher operating costs and that the reactor volume is not optimally used.

(Mechanical) energy dissipation in a horizontal pipe reactor

An alternative for a batch reactor is a continuous pipe reactor. To minimize the pressure drop and length of such a reactor, a low axial velocity is preferred. In a horizontal reactor, the copper particles that are formed in the process will not remain in suspension, if the axial velocity is too low. The critical velocity, which is the minimum velocity necessary to keep solid particles in suspension in horizontal pipes, can be obtained by the correlation of Davies (1987), which is based upon the

empirical Durand and Condolios (1952) relation, and is equal to

$$v_c = 1.08 f(c)\ \nu^{-0.09}\ d_p^{0.18}\ (\frac{2g\Delta\rho}{\rho})^{0.54}\ D^{0.46}$$
$$\text{with} \quad f(c) = (1 + 3.64c)^{1.09}\ (1 - c)^{2.2} \tag{7.12}$$

where ν is the kinematic viscosity, d_p is the diameter of the particles, g is the gravitational acceleration, $\Delta\rho$ is the density difference between the particles and liquid, ρ is the density of the liquid, D is the pipe diameter and c is the mean concentration of particles in the pipe (volume fraction).

The length of the reactor is predicted with the 1D model, where it is assumed that the velocity of the particles and the flow are close to plug flow and that the slip velocity of the particles is zero ($v_p = u$). The diameter and length of the reactor together with the critical velocity determine the pressure drop, which is a measure for the mechanical energy that is needed. The length of the reactor is determined by the axial velocity in the reactor and the residence time, which is defined as the time that the process needs to reach the end concentration of Cu^{2+}_{end} <0.01 g/L. In table 7.3, the energy consumption per kg recovered copper is given for an initial Cu^{2+} concentrations of 2, 20 and 40 g/L, respectively. It can be observed that the energy requirement increases, when the tube diameter increases. This can be explained by the fact that the critical velocity increases and as a results a longer reactor is necessary. Both aspects will yield a larger pressure drop and hence more energy is required. Furthermore, when a higher initial Cu^{2+} concentration is considered, the energy per kg recovered copper decreases. Despite the fact that the critical velocity is larger in that case (due to the larger particles that are formed), still less energy is required, because (1) the reaction is faster so a shorter reactor is necessary and (2) more copper is recovered.

It is clear that the reactor is most suitable for large Cu^{2+} concentrations. A large pipe diameter (high throughput) is feasible from an energy perspective, since the mechanical energy that is required is a lot less than the energy needed for heating. Furthermore, the troughput (flow rate) scales with a factor of D^2, while the length of the reactor scales roughly with a factor $\sqrt{D}$ (equation 7.12 shows that the critical velocity also scales roughly with $\sqrt{D}$). Therefore, a reactor with a large diameter will require less tubing than a series of parallel reactors with a small diameter. However, the length of the reactor is an important issue to consider. Since a long reactor length is required for a small throughput or pipe diameter (L=3.6 km when D=1 cm, Φ_v=0.07 L/s and Cu^{2+}=40 g/L). For small streams, a long reactor is not economical, because it will require a lot of space and equipment for a small amount of product.

(Mechanical) energy dissipation in a vertical pipe reactor

An attractive alternative for a horizontal pipe reactor can be a vertical reactor. In that case the particles do not settle down at the bottom of the reactor and as a result the axial velocity is no longer limited by the critical velocity, which allows a shorter reactor. To efficiently mix particles and reacting species in a vertical reactor, static mixers need to be added to the reactor. In Van Wageningen et al. (2003, 2004b) and in chapter 5 and 6 of this thesis, the mixing efficiency of the Kenics static mixer was assessed for the novel reduction process. It was found that for efficient mixing of the particles in a vertical reactor equipped with a Kenics static mixer, there are constraints on the ratio between the settling velocity of the particles and the axial velocity in the reactor. This ratio can be expressed by the dimensionless group St/Fr, where St is the Stokes number and Fr is the Froude number. For efficient mixing of the particles, the St/Fr ratio should be below one. At higher numbers, the particles collide with the mixing elements and are no longer mixed, which results in a non uniform particle distribution.

Table 7.3: Energy usage of horizontal pipe reactor.

$[Cu_0^{2+}] = 2$ g/L	$d_{p,max} = 6.0$ μm	$t_{res} = 6200$ s	E_{heat} (150°C)=273 MJ/kg	
D [cm]	v_c [m/s]	Φ_l [L/s]	L [m]	E_{dis} [MJ/kg]
1	0.883	0.07	5470	0.853
2	1.21	0.38	7530	1.10
5	1.85	3.6	11500	1.57
10	2.55	20	15800	2.06
20	3.50	110	21700	2.66
$[Cu_0^{2+}] = 20$ g/L	$d_p = 12.8$ μm	$t_{res} = 3980$ s	E_{heat} (150°C)=27.3 MJ/kg	
D [cm]	v_c [m/s]	Φ_l [L/s]	L [m]	E_{dis} [MJ/kg]
1	1.01	0.08	4030	0.082
2	1.39	0.44	5540	0.107
5	2.12	4.2	8450	0.152
10	2.92	23	11600	0.198
20	4.02	126	16000	0.259
$[Cu_0^{2+}] = 40$ g/L	$d_p = 16.2$ μm	$t_{res} = 3420$ s	E_{heat} (150°C)=13.7 MJ/kg	
D [cm]	v_c [m/s]	Φ_l [L/s]	L [m]	E_{dis} [MJ/kg]
1	1.06	0.08	3610	0.041
2	1.45	0.46	4970	0.052
5	2.22	4.4	7570	0.075
10	3.05	24	10400	0.097
20	4.19	132	14300	0.126

Table 7.4: Energy usage of vertical pipe reactor

Vertical pipe reactor (PFR)						
$[Cu_0^{2+}]$ [g/L]	d_p [μm]	v_p [mm/s]	u [mm/s]	St/Fr [-]	E_{dis} [MJ/kg]	E_{heat} [MJ/kg]
2	6.0	3.23	3.1	0.042	0.1	273
20	12.8	5.10	4.5	0.13	0.01	27.3
40	16.2	5.95	5.0	0.19	0.005	13.7

Table 7.5: Reynolds number and flow rate as a function of the tube diameter for the different concentrations

	$Cu_0^{2+} = 2$ g/L		$Cu_0^{2+} = 20$ g/L		$Cu_0^{2+} = 40$ g/L	
D[cm]	Re	Φ_l [L/s]	Re	Φ_l [L/s]	Re	Φ_l [L/s]
1	103	$2.43\ 10^{-4}$	150	$3.53\ 10^{-4}$	167	$3.93\ 10^{-4}$
2	207	$9.74\ 10^{-4}$	300	$1.41\ 10^{-3}$	333	$1.57\ 10^{-3}$
5	517	$6.09\ 10^{-3}$	750	$8.84\ 10^{-3}$	833	$9.82\ 10^{-3}$
10	1033	$2.43\ 10^{-2}$	1500	$3.53\ 10^{-2}$	1667	$3.93\ 10^{-2}$
20	2067	$9.74\ 10^{-2}$	3000	$1.41\ 10^{-1}$	3333	$1.57\ 10^{-1}$

For a vertical reactor, the length of the reactor becomes the limiting factor ($L \leq$20 m). To achieve a full reduction, the downward axial velocity has to be low. Initially, the downward liquid velocity was estimated from the reactor length (20 m) and the residence time in the batch reactor ($u_{\text{est.}} = L/t_{\text{res}}$). This estimated velocity proved to be too large, because the reduction in a vertical tube is a little bit slower. The slower reduction is caused by the fact that the particles move faster than the flow, which implies that the available surface for the reaction is somewhat smaller than in an ideal plug flow reactor. The correct downward velocity was obtained via iteration, where an end Cu^{2+} concentration <0.01 g/L was demanded. In table 7.4, the energy usage for the different concentrations (2, 20 and 40 g/L) is compared for a 20 m long vertical reactor. In all cases, the energy usage is low compared to the energy necessary for heating. The energy usage is directly related to the energy that is required to lift the liquid towards a height of 20 m. Since the downward liquid velocity is low, the flow can be gravity driven. Furthermore, mixing of the particles is feasible with the Kenics static mixer, since the St/Fr condition is satisfied for all concentrations (St/Fr<1).

It should be noted that the tube diameter is not taken into account in the 1D model. The tube diameter will determine the Reynolds number ($\text{Re} = \frac{Du}{\nu}$) at a certain flow rate. The efficiency of the Kenics static mixer is also determined by the Reynolds number (chapter 5 and 6). The optimal mixing conditions are matched, when Re<20 or Re>200. In table 7.5, the Reynolds number and corresponding flow rate are listed as a function of the tube diameter for the different concentrations. It can be observed that, when the pipe diameter is larger than 2 cm, the Reynolds number is larger than 200. Under these conditions, the Kenics static mixer can be used effectively. One should note that if the reactor diameter becomes to large, the mixing efficiency per unit length will decrease, because the number of mixing elements decreases. A reactor diameter of 20 cm has a mixing element length of 30 cm and the total number of mixing elements in the reactor is equal to 67. If the tube diameter increases, the number of mixing elements will decrease.

A vertical reactor has the advantage that it is uses less space than a horizontal reactor. Especially, for small streams (Φ_v <1 L/s) a vertical reactor forms an attractive alternative for a horizontal plug flow reactor. For large streams (Φ_v >10 L/s), different reactors need to be placed parallel and as a results more tubing is required. In that case the advantage, which a vertical reactor has over a horizontal reactor (short length), will disappear.

7.6 Environmental aspects

From an environmental point of view the process is attractive, when energy consumption compared to other removal or winning techniques is low and when aqueous copper and organic material in streams are reduced to environmentally acceptable levels. According to Treasure (2002),

electro-winning power is the largest component in the operating costs. Conventional EW is more energy-consuming than reduction with carbohydrates for concentrated copper streams. Also, potential noxious fumes can be generated in the open EW baths. EMEW is especially suitable for low concentrations < 1 g/L, yet is flexible to treat concentrations of up to 5 g/L. Energy consumption of EMEW is higher than for EW, but the current efficiency is higher. Furthermore, stripping of the cathodes is automated and acid mist or fumes are not released. For highly concentrated copper streams (> 30 g/L) carbohydrate reduction would thus be favorable regarding the use of resources.

Regarding copper removal from solution, end concentrations of 1-3 ppm were obtained from solutions with initial concentrations of 27 g/kg within an hour at 160 °C (Van der Weijden et al. (2001)). With increasing process time, levels can be reduced even more. For drinking water the levels of copper should not exceed the 10 μm/L level. EMEW, a cell technology, especially fit for treating low concentrated streams (< 1 g/L), can reach levels of 0.1 ppm (100 μm/L) from streams containing 3 g/L after numerous treatment cycles and long processing times (> 10 hours) and levels of 2 ppm after a processing time of 9 hours. Carbohydrate reduction is therefore more economic and faster than EMEW to achieve reduction to ppm levels. The copper remaining in solution after reduction with carbohydrates also depends on the presence of complexing agents that are not destructed at the processing temperatures and pH. The use of EDTA for improving copper powder quality is therefore less suitable.

In contrast to EW, the presence of organic material in solution (dissolved or particulate) is not a problem for copper reduction with carbohydrates. This technology is therefore especially suitable (and maybe the only suitable one) for treatment of streams that contain organics as well as copper. Tests with etching solutions containing organic components that could not be treated with EW could be treated by reduction of copper in an autoclave (Van der Weijden et al. (2001)).

This waste-to-waste-to-product technology was also meant for degradation of organics to reduce the Carbon Oxygen Demand (COD). In Figure 7.11, it can be seen that COD, as well as Total Organic Carbon (TOC) and dissolved organic carbon (DOC) decrease by 15, 55 and 40% during the reduction of carbohydrate with copper. COD is the oxidative degradation potential that is generally higher than the TOC. Chemical degradation of the organics that are present can enhance the biodegradability of these organics. The formation of ketones, aldehydes and acids results in an increase of the Biological Oxygen Demand (BOD), which is usually less than the TOC (Alvares et al. (2001)). Chemical oxidation processes in the treatment of waste streams, such as the oxidation of the carbohydrates in the copper reduction process, can thus inactivate inhibitory compounds and improve biodegradability. Since the COD after reduction of copper is still high, further treatment with bacteria, oxygen or ozone may be required. Alternatively, the reaction time may be extended to achieve lower COD.

7.7 Concluding remarks

New data on the reduction of Cu^{2+} with soluble carbohydrates was used to design an energy efficient and sustainable reactor as an alternative for technologies such as electro-winning. Experimental results show that a reactor that is glass-lined, Teflon coated or is lined with an otherwise structureless material is favourable over a titanium reactor, because the copper powder has a higher quality and growth on reactor walls is prevented.

The reduction of Cu^{2+} in different reactor configurations could successfully be simulated with a 1D reduction model that takes the diffusion towards a spherical particle as the rate limiting step. The energy usage per kg recovered copper was evaluated for the different reactor configurations

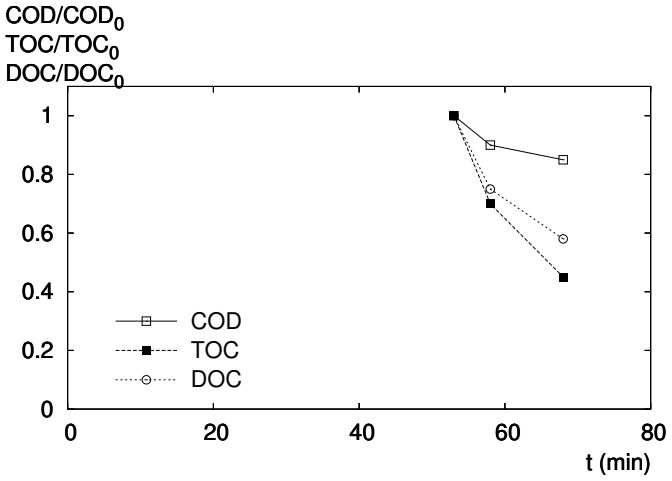

Figure 7.11: Xylose degradation as a function of the process time.

and compared to electro-winning i.e. the conventional method. Heating the liquid towards the set temperature proved to be the main energy consumer compared to the mechanical energy. Therefore, a lower temperature is recommendable although the reduction rate will then be slower.

The ultimate choice of the reactor type depends on the (waste) stream size, composition, equipment costs, available space, quality of the end product and whether an integration into a continuous process desired. It can be concluded that the novel reduction process is an energy efficient alternative for electro-winning in the following cases: (1) when streams with high Cu^{2+} concentrations are processed ($>$ 40 g/L) or (2) when the generated heat can be re-used (Aurich and Koene (2001)) or is available from an other process (e.g. other heat sources can be used to pre-heat the waste stream). Furthermore, the novel process can be applied in situations where electrolysis is not possible, for example when the copper containing waste stream is also contaminated with organics or other metals (such as silver, Aurich and Koene (2001)). For example, if bioleach is used to dissolve copper ore, the copper containing stream is contaminated with bacteria, (Van der Weijden et al. (2001)). In contrast to electro-winning, the bacteria pose no problem for the novel reduction process, since their organic parts (together with additional carbohydrates) can be used to reduce the copper to its solid state.

8

Discussion & Conclusions

Heavy metals that can be found in waste water streams can be reduced to their metallic form via the reduction with carbohydrates. The carbohydrates may originate from organic waste sources. With this techniques two different waste streams are combined to clean both streams and to obtain a valuable end product, which are the metallic particles. This study has focused on copper in particular. However, the process is also feasible for other valuable heavy metals such as gold and silver. The aim of this project was to develop a suitable continuous pipe reactor for the novel reduction process. Such a reactor is equipped with static mixers to enhance mixing, to improve the heat exchange and to promote plug flow. Ideally, a static mixer distributes all species and particles uniformly over the reactor and it changes the flow conditions in such a way that the residence time of the particles is uniform. The main focus of this thesis is the working principle of the Kenics™ static mixer at different flow regimes, which includes the hydrodynamics of the flow inside the mixer and the mixing of 'real' particles. Furthermore, its feasibility for the reduction process is assessed. This chapter will summarise findings and conclusions from this work. First, the hydrodynamics of the flow inside the Kenics™ static mixer is discussed. Second, the behaviour of particles in a Kenics™ static mixer and the consequences it has for the reactor design are explained. Third, the conclusions regarding the 'direct' numerical simulation of the growing particles inside the Kenics™ static are given, where 'direct' refers to the direct coupling between the particle growth and the reaction sink term. Finally, this thesis is concluded with an outlook on the applicability of the process in and outside The Netherlands.

8.1 Hydrodynamics of a Kenics™ static mixer

The flow inside the Kenics™ static mixer was investigated both experimentally and numerically in the range of Re=10. . . 1000. Two experimental methods were used, *viz.* Particle Image Velocimetry in combination with Refractive Index Matching (RIM) and Laser Doppler Anemometry (LDA). The results of the experiments were used to validate the numerical results, which were obtained with two different flow solvers, *viz.* the commercial package FLUENT and an in-house lattice Boltzmann (LB) D3Q19 BGK solver (Qian et al. (1992)).

PIV measurements were made in a 2 element glass static mixer at Re=80 and Re=430. Despite the geometrical inconsistencies of the glass static mixer, a qualitative agreement was found at Re=430 between the numerical results and PIV. However, the PIV experiments were not accurate enough for a quantitative comparison between the numerical and experimental results. Therefore, it was decided to abandon the PIV technique and to continue with LDA. Point measurements in a steel static mixer were performed with LDA. A good agreement between the CFD results and LDA measurements was found. Furthermore, the measurements demonstrated that an early transition to unsteady flow takes place in the Kenics™ static mixer at Re=300.

This transient behaviour was studied in more detail with CFD. The simulations were performed with both FLUENT and LB, which were compared to one another. Good agreement was found between FLUENT and LB, but the in-house LB code was considerably faster than the commercial code FLUENT for the transient problems. An other disadvantage of FLUENT is that large problems, which need to be solved on parallel processors, are expensive to solve, because each processor requires a separate license. Therefore, when it comes to transient flow problems, the limitations of a commercial code like FLUENT make the use of an in-house code attractive.

In this study, an overview of the different flow regimes in the Kenics™ static mixer was given. The existing knowledge about the flow in Kenics™ static mixer (Hobbs and Muzzio (1998); Bakker and LaRoche (1995)) was extended. It was discovered that the flow becomes transient at an early stage (Re=300). In this transitional flow regime, oscillating vortical structures dominate the flow and render the flow time dependent. The onset of the transient behaviour in the Kenics™ static mixer is explained by the length of the elongated vortices that appear in the flow. When the vortices stretch out along the full length of a mixing element, the vortical structures create a disturbance at the start of the next mixing element, which triggers the transient behaviour of the flow at Re=300. If the Reynolds number is increased further, the flow gets more chaotic and more small vortical structures appear and at Re=1000 the flow seems to have become turbulent. The most important conclusions of the study into the hydrodynamics of the Kenics™ static mixer are summarised below:

- A commercial CFD code like FLUENT is not the best tool to simulate a complex transient flow in a complex geometry.
- It was discovered that the transition to time dependent flow inside the Kenics™ static mixer takes place at an earlier stage than reported thus far in literature. This early transition to unsteady flow was demonstrated with both LDA and CFD.
- The time dependent flow can be divided in a transitional regime, in which there are oscillating vortices in a regular pattern (Re=300. . . 500), and a pre-turbulent regime in which the motion of the vortices becomes irregular (Re=500. . . 1000).
- The onset of the transient behaviour is linked to the appearance of vortical structures: when a vortical structures reaches the next mixing element, it creates a disturbance that triggers the transition to unsteady flow.

8.2 Suspending particles in a Kenics™ static mixer

The suspension of small particles was investigated numerically in the Kenics™ static mixer to determine under which conditions the particles can be kept in suspension and are well mixed, i.e. have a uniform distribution. For this purpose, a (parallel) particle tracking code was developed and added to the in-house LB code. The tracking code solves the BBO equation (Maxey and Riley (1983)) to which the lift force has been added. Because the Kenics™ static mixer has a complex curved geometry and the LB code uses a staircase boundary, particles can get trapped inside the ”stairs” of the wall. Therefore, a smooth boundary for the particles was applied to the staircase (LB) wall in the form of an analytical function, which describes the mixing elements. This way, it was avoided that particles got trapped at the wall and the normal force could be applied, when a particle touches the wall.

The Kenics™ static mixer can help keeping the particles in suspension in the following way. A particle can be transported upwards before it settles down due to the twist of the mixing elements,

where the driving force is provided by the liquid velocity in the reactor. It was assumed that the ratio between the settling velocity of a particle and the average (axial) liquid velocity is a good measure to describe the settling behaviour of the particles in the Kenics™ static mixer. This ratio can be expressed by the dimensionless group St/Fr, which is the ratio between the Stokes and the Froude number. In order to test this assumption, simulations were carried out in the Kenics™ static mixer under different flow conditions and for different particle sizes, where the St/Fr ratio was kept constant. The results of the simulation indicated that the St/Fr ratio can be used indeed as a scaling parameter for the settling of particles in the Kenics™ static mixer. The Reynolds number determines the flow conditions. The two dimensionless groups (Re and St/Fr) can be used to describe the mixing of particles inside the Kenics™ static mixer.

The Re number and St/Fr ratio were varied to select the right process conditions (Re=10. . . 500 and St/Fr=0.01. . . 10). Simulations without gravity (St/Fr=0) gave results that compare well to results found in literature, which involved tracer particles, e.g. Hobbs and Muzzio (1997b). Furthermore, the results showed that the optimal mixing conditions for particles were best matched at a low St/Fr ratio (St/Fr$<$1) and either a low or high Reynolds number (Re$<$20 or Re$>$200). In the intermediate range (20$<$Re$<$200), the vortical structures that appear in the reactor have a negative influence on the mixing process. At higher Reynolds numbers the mixing improves again, because the vortices start to move and interact with each other.

The settling of particles was investigated by tracking the particle fraction along the Kenics™ static mixer. It was found that in a horizontal reactor, to keep the majority of the particles in suspension the St/Fr ratio should be small and the Reynolds number high (St/Fr$<$0.01 and Re$>$500). This implied that in practise a horizontal reactor is not feasible, because it can only operate either for extremely small particle sizes ($\sim \mu$m) or at extremely large flow rates, which makes the reactor long ($\sim$km). Therefore, a vertical reactor is more suitable for the process. If the flow direction is downward, no settling problems occur, which removes the limit on the St/Fr ratio based upon the settling of the particles. However, there remains a limit on the St/Fr ratio due to the mixing efficiency of the particles. It was found that particles collide with the mixing element, which lead to accumulation of the particles near the mixing elements, when the St/Fr ratio is too high ($>$1). Therefore, in a vertical reactor equipped with a Kenics™ static mixer, there are limitations on the particle size and/or flow rate as well, if a uniform distribution of the particles is desired. A different geometry of the mixer might remove these limitations.

The main conclusions about the mixing of small particles in the Kenics™ static mixer are:

- There are two important design parameters that describe the mixing and settling of particles in a Kenics™ static mixer at different flow conditions: the Reynolds number and the ratio between the Stokes and the Froude number.
- The transient motion of the vortices improves the mixing of species inside the Kenics™ static mixer.
- A horizontal reactor equipped with a Kenics™ static mixer is not suitable for the reduction process, because the settling of the particles cannot be prevented.
- In a vertical reactor equipped with a Kenics™ static mixer, a high settling velocity of the particles results into collisions of the particles with the mixing elements, which leads to poor mixing and an accumulation of the particles in the centre of the reactor (near the mixing element).

8.3 'Direct' numerical simulation of growing particles

To assess the efficiency of the Kenics™ static mixer for the copper reduction process in a tubular reactor, simulations were carried out for copper particles growing in a vertical Kenics™ static mixer reactor. A uniform size distribution of the particles is desired, because it improves the value of the end product. Furthermore, an efficient mass transfer of the copper ions towards the particles (i.e. the reaction location) leads to a faster reduction process, which reduces the length of the reactor. To meet both conditions, the Kenics™ static mixer should efficiently mix both the particles and copper ions. In order to carry out the simulations, a particle growth model and finite volume code, which was used to calculate the local copper ion concentration, were developed and added to LB-particle code. The particle growth depends on the local copper ion concentration and a simple diffusion model is used for the growth rate of a particle. The total growth of all particles in a finite volume cell directly makes up the sink term of the copper ions. This way, the presence of the particles is the source of the reduction reaction.

The results showed that the Kenics™ static mixer improves the mixing of the copper ion concentration. However, the constraints for the mixing of particles remain. If the particles become too big, their settling velocity increases and they no longer satisfy the St/Fr condition, which results in an accumulation of the particles near the mixing element. It was investigated what the influence of this ill-mixing of the particles was on the particle size distribution. It was found that the particle size distribution is broader, when the particles are not mixed effectively. Furthermore, the results of the vertical reactor equipped with the Kenics™ static mixer were compared to the results of a vertical pipe reactor without a mixer. At high flow rates, the particle size distribution improves in the Kenics™ static mixer reactor, when more mixing elements are used. Surprisingly, a pipe without mixing elements performed better, when it comes down to the particle size distribution than a reactor equipped with a Kenics™ static mixer. However, it is obvious that in a laminar pipe flow there is no mixing of the copper ions. Therefore, adding mixing elements is recommendable in order to mix the copper ions and speed up the reduction process.

Based upon these finding a design for a vertical reactor can be made. At the start of the reactor a Kenics™ static mixer can be used to mix the reacting species and small particles that are formed. Since the particles are small, there is not much surface available for the reaction so mixing is important to speed up the reduction process. When the particles grow beyond a certain size and no longer satisfy the St/Fr condition (which depends on the conditions inside the reactor such as viscosity and flow rate), the reactor continues with a pipe without a mixer. The length of the reactor will be determined by the reduction of the copper ions in the centre of the reactor. There, the particles will travel fastest so more length is needed for a complete reduction. The new insight that was gained by means of the simulations of the growing particles in the Kenics™ static mixer is listed below:

- The location of the reaction source is important and should be included in the simulation of the reduction process. Because the reaction takes place at the surface of the particles, it is necessary to link the reduction of the copper ions to the growth of the particles that reside in the reactor directly.
- The particle size distribution is not narrow, when the particles do not satisfy the St/Fr condition and slide down along a mixing element. Apparently, the particles do not meet the same conditions (they have a different residence time and/or encounter a different copper ion concentration).
- A combination of mixer and pipe can be a good option for a vertical reactor, when the final particle size is large and no longer satisfies St/Fr$<$1.

8.4 Feasibility of the process

In The Netherlands, the novel reduction process can be applied to waste treatment in the IC and galvanic industry. In chapter 7, the energy usage per kg recovered copper was evaluated for the different reactor types (batch, horizontal plug flow reactor (PFR) and vertical PFR) and compared to the conventional electro-winning method. Heating the liquid towards the set temperature proved to be the main energy consumer, since the mechanical energy necessary for pumping or stirring was small compared to the heating energy for all investigated reactor configurations. One should note that the heat generated is not lost at the end of the process, it can partly be re-used, e.g. to pre-heat the waste-stream. Moreover, heat available from an other process may be used to pre-heat the waste-stream. Both aspects will lower the energy demand of the process.

The ultimate choice of the reactor type depends on the (waste) stream size, equipment costs, quality of the end product and whether an integration into a continuous process is desired. For a typical waste stream (Φ_v <1 L/s) in the IC-industry, a vertical PFR is the most optimal reactor, because it uses less space and equipment than a comparable horizontal PFR and can be integrated into the continuous process. Furthermore, it was demonstrated in chapter 7, that the novel reduction process can be an energy efficient alternative for electro-winning, when streams that have high Cu^{2+} concentrations are processed (>40 g/L). Such concentrated streams exist in the IC industry, but there are also stream that have a low Cu^{2+} concentration (1.2 g/L). For these small streams, the novel reduction process requires a relatively large amount of energy per kg recovered copper. The waste streams found in the IC industry, however, are often contaminated with organics. These organics limit the application of electro-winning. The novel reduction process, on the other hand, can use these organics to reduce the copper. This way, the copper is recovered in the form of particles and above that the organic content of the stream is partly consumed. Therefore, despite its larger energy requirement for dilute streams, the process can still be attractive, when the (dilute) waste streams are contaminated with organics.

Outside The Netherlands, the reduction process is applicable in the mining industry. Especially, when bioleaching is used to dissolve the copper ore, the process can be an attractive alternative for the conventional electro-winning method. In bioleaching, bacteria are used to dissolve the copper ore, which causes contamination of the Cu^{2+} stream with organic material (the cells of the bacteria). In contrast to electro-winning, these bacteria don't pose a problem to the novel reduction process, since their organic parts (together with additional carbohydrates) can be used to reduce the copper to its solid state. It should be noted that in the mining energy large streams are processed ($\sim$1 m^3/s). The present design of vertical reactor was explicitly developed for small waste stream sizes and is limited to a relatively low throughput (Φ_v <1 L/s). This limitation can be overcome by placing different vertical reactors in parallel to accommodate a large throughput. However, the use of another type of static mixer might extend the feasibility of the vertical reactor towards a higher throughput. The design of such a 'large' vertical reactor can form an interesting topic for future investigations. Finally, the conclusions about the applicability of the novel reduction process are summarised below:

- The novel reduction process is an energy efficient alternative for electro-winning, when streams with high Cu^{2+} concentrations are processed (> 40 g/L) and/or when the generated heat can be re-used or is available from an other process (e.g. other heat sources can be used to pre-heat the waste stream).
- The novel reduction process can be applied in situations where the application of electrolysis is limited, for example when the copper containing waste stream is also contaminated with organics or other metals (such as silver).

- The proposed vertical plug flow reactor is applicable for waste treatment in the IC-industry. It is especially suitable for the processing of relatively small waste streams with high Cu^{2+} concentration and contaminated with organics.
- The reduction process can be applied in the (copper) mining industry, when the ores are processed by means of bioleaching. Then, because of the large throughput of the reactor, a different type of static mixer needs to be applied to the vertical plug flow reactor. Such a 'large' reactor can be an interesting topic for future research.

A

Population balance method

Population balance

The copper particles that are formed in the precipitation process can be distributed over a certain size ranges. These different size ranges can be modeled as the population density $n(l, \vec{x}, t)$, which is the concentration of a particle class with certain size l at a given position ($\vec{x}$) and time t. The particle conservation equation or population balance can be described in terms of the population density:

$$\frac{\partial n}{\partial t} + \nabla \cdot \vec{u}\, n + \frac{\partial}{\partial l}(G\, n) = 0 \tag{A.1}$$

where G is the growth rate. If a control volume is considered, the time rate of change of the population density is equal to the flow in or out the control volume plus the amount of particles that grow in or outside the size class of the population density. To equation A.1 the following boundary condition is applied:

$$n(0, \vec{x}, t) = \frac{J(\vec{x}, t)}{G(0, \vec{x}, t)} \tag{A.2}$$

where J is the nucleation.

It should be noted that nucleation is not considered in this study and it is assumed that there is no secondary nucleation. When the growth rate is diffusion controled, the growth rate G is reciprocal to the length scale, $G = G_0\, l^{-1}$ with $G_0 = \frac{4\mathbb{D}[\mathrm{Cu}^{2+}]}{\rho_{\mathrm{Cu}}}$. More details on the diffusion model are explained in chapter 6. Here, it is assumed that the reaction at the surface is much faster than the diffusion process and that the particle radius is much smaller than the diffusion layer. Other growth models for particles are constant growth $G = A_0$ and linear growth $G = B_0\, l$.

In order to evaluate the statistical properties of the particle-size distribution (PSD), the average properties of the population balance can be solved by using the moment transformation as described by Randolph and Larson (1998) and Van Leeuwen (1998). The moments of the particle size distribution are defined as

$$m_{\mathrm{j}} = \int_0^\infty n\, l^{\mathrm{j}}\, \mathrm{d}l \tag{A.3}$$

When the growth rate G is reciprocal ($G = G_0 l^{-1}$), the population balance in terms of the moments of the distribution becomes

$$\frac{\partial m_{\mathrm{j}}}{\partial t} + \nabla \cdot u_{\mathrm{i}}\, m_{\mathrm{j}} - 0^{\mathrm{j}}\, J = j\, G_0\, m_{\mathrm{j}-2} \tag{A.4}$$

where the moments m_0, m_1, m_2, m_3 are the number, length, area and volume concentration of the particles, respectively. When the growth rate G is first order ($G = A_0 + B_0 l$), the following equation for the moments is obtained:

$$\frac{\partial m_{\mathrm{j}}}{\partial t} + \nabla \cdot \vec{u}\, m_{\mathrm{j}} - 0^{\mathrm{j}}\ J = j\ (A_0\ m_{\mathrm{j}-1} + B_0\ m_{\mathrm{j}}) \tag{A.5}$$

It can be observed that equation A.5 gives a closed system for the different moments, which can be solved numerically. All moments depend on known other moments. For reciprocal growth, however, there is a dependency on unknown moments. Equation A.4 requires closure for the first moment m_1, since it depends on the moment m_{-1}. Closure can be achieved by looking at physical meaning of the different moments and the source terms of the moments. The physical meaning of the moments can easily be understood, if a control volume V_{c} is considered. The moment m_0, which is the particle concentration, is linked to the total number of particles n_{p} in a control volume:

$$m_0 = \frac{1}{V_{\mathrm{c}} n_{\mathrm{p}}} \tag{A.6}$$

The moment m_1, which is the concentration of the specific length, is linked to the total length of the particles, l_{s}, in a control volume:

$$m_1 = [l_{\mathrm{s}}] = \frac{1}{V_{\mathrm{c}}} \sum_{i=1}^{n_{\mathrm{p}}} d_{\mathrm{p,i}} \tag{A.7}$$

where $d_{\mathrm{p,i}}$ is the particle diameter. The moment m_2, which is the concentration of the specific surface, is linked to the total area of the particles, A_{s} in a control volume:

$$k_{\mathrm{a}}\, m_2 = \frac{k_{\mathrm{a}}}{V_{\mathrm{c}}} \sum_{i=1}^{n_{\mathrm{p}}} d_{\mathrm{p,i}}^2 = [A_{\mathrm{s}}] = \frac{1}{V_{\mathrm{c}}} \sum_{i=1}^{n_{\mathrm{p}}} A_{\mathrm{p,i}} \tag{A.8}$$

where k_{a} is the area shape factor and $A_{\mathrm{p,i}}$ is the area of a single particle. The moment m_3, which is the specific volume concentration, is linked to the total volume of the particles, V_{s} in a control volume:

$$k_{\mathrm{v}}\, m_3 = \frac{k_{\mathrm{v}}}{V_{\mathrm{c}}} \sum_{i=1}^{n_{\mathrm{p}}} d_{\mathrm{p,i}}^3 = [V_{\mathrm{s}}] = \frac{1}{V_{\mathrm{c}}} \sum_{i=1}^{n_{\mathrm{p}}} V_{\mathrm{p,i}} \tag{A.9}$$

where k_{v} is the volume shape factor and $V_{\mathrm{p,i}}$ is the volume of a single particle. Along these lines, the moment m_{-1} is equal to

$$m_{-1} = \frac{1}{V_{\mathrm{c}}} \sum_{i=1}^{n_{\mathrm{p}}} \frac{1}{d_{\mathrm{p,i}}} \tag{A.10}$$

The source terms of the moments can be obtained from equation A.4 and are equal to:

$$S_0 = 0 \tag{A.11}$$
$$S_1 = G_0\, m_{-1} \tag{A.12}$$
$$S_2 = 2\, G_0\, m_0 \tag{A.13}$$
$$S_3 = 3\, G_0\, m_1 \tag{A.14}$$

If a single particle is considered, the growth rates or source terms of the moments can be derived from a physical model. If the growth rate is based upon a diffusion model, the following equations

describe the growth of a single particle:

$$\frac{\mathrm{d}}{\mathrm{d}t}d_\mathrm{p} = \frac{4\mathbb{D}[\mathrm{Cu}^{2+}]}{d_\mathrm{p}\,\rho_\mathrm{Cu}} = G_0\,d_\mathrm{p}^{-1} \tag{A.15}$$

$$\frac{\mathrm{d}}{\mathrm{d}t}A_\mathrm{p} = \frac{8\pi\mathbb{D}[\mathrm{Cu}^{2+}]}{\rho_\mathrm{Cu}} == \frac{8k_\mathrm{a}\mathbb{D}[\mathrm{Cu}^{2+}]}{\rho_\mathrm{Cu}} = k_\mathrm{a}\,2G_0 \tag{A.16}$$

$$\frac{\mathrm{d}}{\mathrm{d}t}V_\mathrm{p} = \frac{2\pi\mathbb{D}d_\mathrm{p}[\mathrm{Cu}^{2+}]}{\rho_\mathrm{Cu}} = \frac{12k_\mathrm{v}\mathbb{D}d_\mathrm{p}[\mathrm{Cu}^{2+}]}{\rho_\mathrm{Cu}} = k_\mathrm{v}\,3G_0\,d_\mathrm{p} \tag{A.17}$$

where $A_\mathrm{p} = \pi d_\mathrm{p}^2$ and $V_\mathrm{p} = \frac{\pi}{6}d_\mathrm{p}^3$ are the area and volume of a particle, respectively, and $k_\mathrm{a} = \pi$ and $k_\mathrm{v} = \frac{\pi}{6}$ are the area and volume shape constants, respectively. It can be observed that there is a similarity between the equations that describe the growth of a single particle and the equations of the source terms of the moments. From the moments the average particle properties can be obtained, which are equal to

$$< d_\mathrm{p} >= \frac{m_1}{m_0} \tag{A.18}$$

$$< A_\mathrm{p} >= \frac{k_\mathrm{a}m_2}{m_0} \tag{A.19}$$

$$< V_\mathrm{p} >= \frac{k_\mathrm{v}m_3}{m_0} \tag{A.20}$$

where $< d_\mathrm{p} >$, $< A_\mathrm{p} >$ and $< V_\mathrm{p} >$ are the average diameter, area and volume of the particles, respectively. The moment m_{-1} can be approximated by considering only average properties.

$$< d_\mathrm{p}^{-1} >= \frac{m_{-1}}{m_0} \qquad \rightarrow \qquad m_{-1} \approx \frac{m_0}{< d_\mathrm{p} >} = \frac{m_0^2}{m_1} \tag{A.21}$$

where the assumption is made that $< d_\mathrm{p}^{-1} >= 1/ < d_\mathrm{p} >$, which is only valid if the size differences between the particles within one control volume are small.

The volumetric growth of the particles is equal to the depletion of Cu^{2+}, which implies that the source term of the moment m_3 is linked to source term of the Cu^{2+} concentration.

$$S_{\mathrm{Cu}^{2+}} = k_\mathrm{v}\,S_3\,\rho_\mathrm{Cu} = k_\mathrm{v}\,3\,G_0\,m_1\,\rho_\mathrm{Cu} \tag{A.22}$$

Since the source term of the Cu^{2+} concentration depends on the moment m_1 and the moments m_0 and m_1 do not depend on the higher order moments, it is not necessary to solve the higher order moments m_2 and m_3 in order to predict the Cu^{2+} concentration.

Concluding remarks

The population balance method has the advantage that it is computationally cheap. Hovever, for reciprocal growth, a closure model is necessary. This closure relation is not very accurate, when the particles differ much in size. Furthermore, gravity is not included into the population balance. Since it is possible to 'directly' simulate the trajectory and growth of particles with the present computational power and since the closure model is not very accurate, it was decided not to use the population balance method. Instead, a 'direct' numerical simulation of the particle trajectories and growth was conducted.

Bibliography

Abbadi, A., K. F. Gotlieb, and H. Van Bekkum, "Study on solid acid catalyzed hydrolysis of maltose and related polysaccharides." *Starch/Staerke*, **50(1)**, 23 (1998).

Absil, L. H. J., *Analysis of the laser Doppler measurement technique for application in turbulent flows*, Ph.D. thesis, Delft University of Technology, Delft (1995).

Alvares, A. B. C., C. Diaper, and S. A. Parsons, "Partial oxidation by ozone to remove recalcitrance from wastewaters- a review," *Environmental Technology*, **22**, 409 (2001).

Arimond, J., and L. Erwin, "A simulation of a motionless mixer," *Chem. Eng. Comm.*, **37**, 105 (1985).

Aurich, V. G., and J. I. Koene, "Silver removal and recovery from effluent streams," *Chemical Innovation*, **1**, 49 (2001).

Bakker, A., *Hydrodynamics of stirred gas-liquid dispersions*, Ph.D. thesis, Delft University of Technology, Delft (1992).

Bakker, A., and R. LaRoche, "Flow and mixing with kenics static mixers," *Chem. Eng. Comm.*, **136**, 119 (1995).

Bakker, A., and E. M. Marshall, "Laminar mixing with kenics in-line mixers," in *Fluent Inc.'s 1992 Users Group Meeting*, Burlington, Vermont (USA) (1992).

Bergsma, H. L. T., "Eerste verkenning van de industriële toepassings-mogelijkheden van koperreductie met organische afvalstromen." Technical report, Senter (2003).

Bernaschi, M., and S. Succi, "Accelerated lattice boltzmann scheme for steady-state flows," *Int. J. Mod. Phys B*, **17**, 1 (2003).

Bouzidi, M., M. Firdaouss, and P. Lallemand, "Momentum transfer of a boltzmann-lattice fluid with boundaries," *Phys Fluids*, **13(11)**, 3452 (2001).

Brenner, H., "The slow motion of a sphere through a viscous fluid towards a plane surface," *Chem. Eng. Sci.*, **16**, 242 (1961).

Chen, H. D., C. Teixeira, and K. Molvig, "Realization of fluid boundary conditions via discrete boltzmann dynamics," *Int. J. Mod. Phys. C*, **9(8)**, 1281 (1998).

Chen, M., and J. B. McLaughlin, "A new correlation for the aerosol deposition rate in vertical ducts," *J. Colloid Interface Sci.*, **169**, 437 (1995).

Chen, S., and G. D. Doolen, "Lattice boltzmann method for fluid flows," *Annu. Rev. Fluid Mech.*, **30**, 329 (1998).

Chen, S. J., and A. R. MacDonald, "Motionless mixers for viscous polymers," *Chem. Eng.*, 105–110 (1973).

Cherukat, P., and J. B. McLaughlin, "The inertial lift on a rigid sphere in a linear shear flow field near a wall," *J. Fluid Mech.*, **263**, 1 (1994).

Cox, R. G., and S. K. Hsu, "The lateral migration of solid particles in a laminar flow near a plane," *Int. J. Multiphase Flow*, **3**, 201 (1977).

Cui, M. M., and R. J. Adrian, "Refractive index matching and marking methods for highly concentrated solid-liquid flows," *Experiments in fluids*, **22**, 261 (1997).

Cybulski, A., and K. Werner, "Static mixers criteria for applications and selection," *Int. Chem. Eng.*, **26**, 171 (1986)).

Dandy, D. S., and H. A. Dwyer, "A sphere in shear flow at finite reynolds number: effect of shear on particle lift, drag and heat transfer," *J. Fluid Mech.*, **216**, 381 (1990).

Davies, J. T., "Calculation of critical velocities to maintain solids in suspension in horizontal pipes," *Chem. Eng. Sc.*, **42**, 1667 (1987).

De Vahl Davis, G., and G. D. Mallinson, "False diffusion in numerical fluid mechanics," Report 1972/FMT/1, School of Mechanical and Industrial Engineering, University of New South Wales (1972).

Dean, W. R., "The streamline motion of a fluid in a curved pipe," *Phil. Mag.*, **7**, 208 (1927).

Derksen, J. J., "Numerical simulation of solids suspension in a stirred tank," *AIChE J.*, **49(11)**, 2700 (2003).

Derksen, J. J., and H. E. A. Van den Akker, "Large eddy simulations on the flow driven by a rushton turbine," *AIChE J.*, **45(2)**, 209 (1999).

Dorsman, R., *PIV measurements and numerical simulations of laminar flows in a Kenics static mixer*, Master's thesis, Delft University of Technology, Applied Physics (2001).

Drain, L. E., *The Laser Doppler Technique*, John Wiley and Sons (1980).

Durand, R., and E. Condolios, "Transport hydraulique et décantation des matériaux solides," *Deuxième Journée de lHydraulique*, 27–55 (1952).

Fluent Inc., "Computerized flow modeling for industry," (2003a).

Fluent Inc., "Fluent 6.1 documentation (online manual url http://www.fluentusers.com)," (2003b).

Fourcade, E., R. Wadley, H. C. J. Hoefsloot, A. Green, and P. D. Iedema, "Cfd calculation of laminar striation thinning in static mixer reactors," *Chem. Eng. Sc.*, **56**, 6729 (2001).

Frisch, U., D. d'Humiéres, B. Hasslacher, P. Lallemand, Y. Pomeau, and J. P. Rivet, "Lattice-gas hydrodynamics in two and three dimensions," *Complex Syst.*, **1**, 649 (1987).

Frisch, U., B. Hasslacher, and Y. Pomeau, "Lattice-gas automata for the navier-stokes equations," *Phys. Rev. Lett.*, **56**, 1505 (1986).

Genetti, W. E., "Laminar flow heat transfer with inline mixers," *Chem. Eng. Comm.*, **16**, 325 (1982).

Gerdemann, S. J., and L. R. Penner, "Design, construction and operation of a high pressure flow loop reactor for carbon sequestration," in *AIChE - Experimental Verification of Multiphase Reaction Engineering Models I*, volume [509] (2003).

Goldman, A. J., R. G. Cox, and H. Brenner, "Slow viscous motion of a sphere parallel to a plane walli motion through a quiescent fluid," *Chem. Eng. Sci.*, **22**, 637 (1967).

Grace, C. D., "Static mixing and heat transfer," *Chem. Proc. Eng.*, **52**, 57 (1971).

Hage, J. L. T., M. A. Reuter, R. D. Schuiling, and I. S. Ramtahalsing, "Reduction of copper with cellulose in an autoclave; an alternative to electrolysis," *Minerals Eng.*, **12**, 393 (1999).

Harnby, N., M. F. Edwards, and A. W. Nienow, *Mixing in the process industries, 2nd ed.*, Butterworth-Heinemann, Oxford (1992).

Harteveld, W. K., R. F. Mudde, and H. E. A. Van den Akker, "Dual burst wavelet lda processor implemented and tested on real flows," in *12th international symposium on application of Laser Techniques to Fluid Mechanics*, Lisbon (2004).

Hartmann, H., J. J. Derksen, C. Montavon, J. Pearson, I. S. Hamill, and H. E. A. Van den Akker, "Assessment of large eddy and rans stirred tank simulations by means of lda," *Chem. Eng. Sc.*, **59(12)**, 2419 (2004).

Heywood, N. I., L. J. Viney, and I. W. Stewart, "Mixing efficiencies and energy requirements of various motionless mixer designs for laminar mixing applications," in *Fluid Mixing II Symposium*, 147–176, Bradford (UK) (1984).

Hobbs, D. M., and F. J. Muzzio, "Effects of injection location, flow ratio and geometry on kenics mixer performance," *AiChE J.*, **43(12)**, 3121 (1997a).

Hobbs, D. M., and F. J. Muzzio, "The kenics static mixer: a three-dimensional chaotic flow," *Chem. Eng. J.*, **67**, 153 (1997b).

Hobbs, D. M., and F. J. Muzzio, "Reynolds number effects on laminar mixing in the kenics static mixer," *Chem. Eng. J.*, **70**, 93 (1998).

Hobbs, D. M., P. D. Swanson, and F. J. Muzzio, "Numerical characterization of low reynolds number flow in the kenics static mixer," *Chem. Eng. Sc.*, **53**, 1565 (1998).

Hoekstra, A. J., *Gas flow field and collection efficiency of cyclone separators*, Ph.D. thesis, Delft University of Technology, Delft (2000).

Hollander, E., *Shear induced agglomeration and mixing*, Ph.D. thesis, Delft University of Technology, Delft (2002).

Hollander, E. D., J. J. Derksen, G. M. Kramer, G. M. Van Rosmalen, and H. E. A. Van den Akker, "orthokinetic agglomeoration in stirred tanks," *Powder Technology*, **130**, 169 (2003).

Jaffer, S. A., and P. E. Wood, "Quantification of laminar mixing in the kenics static mixer: an experimental study," *Can. J. Chem. Eng.*, **76**, 516 (1998).

Joshi, P., K. D. P. Nigam, and E. B. Nauman, "The kenics static mixer: new data and propesed correlations," *Chem. Eng. J.*, **59**, 265 (1995).

Kandhai, D., D. J. E. Vidal, A. G. Hoekstra, H. Hoefsloot, P. Iedema, and P. M. A. Sloot, "Lattice-boltzmann and finite element simulations of fluid flow in a smrx static mixer reactor," *Int. J. Numer. Meth. Fluids*, **31**, 1019 (1999).

Keane, R. D., and R. J. Adrian, "Optimization of particle image velocimeters. part i: Double pulsed systems," *Measurement Science and Technology*, **1**, 1202 (1990).

Kemblowski, Z., and P. Pustelnik, "Residence time distribution of a power-law fluid in kenics static mixers," *Chem. Eng. Sci.*, **43**, 473 (1988).

Kritzinger, H. P., J. J. Derksen, and H. E. A. Van den Akker, "Simulation and measurement of the turbulent flow in a monolithic stirred tank," in *ASME-PVP "3rd International Symposium on Computational Technologies for Fluid/Thermal/Chemical Systems with Industrial Applications"*, volume 424(2), 27, New York, USA (2001).

Lathouwers, D., *Modelling and Simulation of Turbulent Bubbly Flow*, Ph.D. thesis, Delft University of Technology, Delft (1999).

Lecjacks, Z., I. Machac, and J. Sir, "Heat transfer to a newtonian liquid flowing through a tube with an internal helical element," *Int. Chem. Eng.*, **27**, 205 (1987).

Leighton, D., and A. Acrivos, "The lift on a small sphere touching a plane in the presence of a simple shear flow," *J. Appl. Math. Phys.*, **36**, 174 (1985).

Maldonado, P., S. Alvarado, and I. Jaques, "The chilean copper industry and energy-related greenhouse gases emissions," (2001).

Mambote, R. C. M., M. A. Reuter, P. Krijgsman, and R. D. Schuiling, "Hydrothermal metallurgy: an overview of basic concepts and applications," *Miner. Eng.*, **13**, 803 (2000).

Maxey, M. R., and J. J. Riley, "Equation of motion for small rigid sphere in a non-uniform flow," *Phys. of Fluids*, **26**, 883 (1983).

McLaughlin, J. B., "Inertial migration of a small sphere in linear shear flows," *J. Fluid Mechanics*, **224**, 261 (1991).

McLaughlin, J. B., "The lift on a small sphere in wall-bounded linear shear flows," *J. Fluid Mechanics*, **246**, 249 (1993).

Mei, R., "An approximate expression for the shear lift force on a spherical particle at finite reynolds number," *Int. J. Multiphase Flow*, **18**, 145 (1992).

Morsi, S. A., and A. J. Alexander, "An investigation of particle trajectories in two-phase flow systems," *J. Fluid Mech*, **55(2)**, 193 (1972).

Mudde, R. F., R. Van der Kleij, and R. Beugels, "Simulation of the heat transfer to a laminar flow in a primix static," in *Proceedings of ASME-PVP*, volume 491(1), 171–178, San Diego, CA, USA (2004).

Mudde, R. F., C. Van Pijpen, and R. Beugels, "Simulation of the laminar flow in a primix static mixer," in *Proceedings of ASME-PVP*, volume 448(2), 67–73, Vancouver (CAN) (2002).

Muguercia, I., E. Largaespada, and M. A. Ebadian, "Fluid flow behaviour in a circular helicoidal pipe using a laser doppler anemometry/velocimetry (lda/ldv) system," in *Third World Conference on Experimental Heat Transfer, Fluid Mechanics and Thermodynamics*, 958–963, Honolulu (USA) (1993).

Mutaftschiev, B., *The atomistic nature of crystal growth*, Springer (2001).

Nigam, K. D. P., , and K. Vasudeva, "Residence time distribution in static mixer," *Can. J. Chem. Eng.*, **58**, 543 (1980).

O'Neill, M. E., "A slow motion of viscous liquid caused by a slowly moving solid sphere," *Mathematika*, **11**, 67 (1964).

Ottino, J. M., *The kinematics of stretching, chaos and transport*, Cambridge University Press, Cambridge (UK) (1989).

Pahl, M. H., and E. Muschelknautz, "Static mixers and their applications," *Int. Chem. Eng.*, **22**, 197 (1982).

Qian, Y. H., D. d'Humieres, and P. Lallemand, "Lattice bgk models for navier-stokes equation," *Europhys. Lett.*, **17**, 479 (1992).

Qian, Y. H., and S. A. Orszag, "Lattice bgk models for the navier-stokes equation: nonlinear deviation in compressible regimes," *Europhys. Lett.*, **21**, 225 (1993).

Raffel, M., C. Willert, and J. Kompenhans, *Particle Image Velocimetry, A practical Guide*, Springer (1998).

Randolph, A. D., and M. A. Larson, *Theory of particulate processes; analysis and techniques of continuous crystallization*, Academic Press Inc., London, second edition (1998).

Rauline, D., J. M. Le Blevec, J. Bousquet, , and P. A. Tanguy, "A comparative assessment of the performance of the kenics and smx static mixers," *Trans IChemE*, **78**, 389 (2000).

Rauline, D., P. A. Tanguy, J. M. Le Blevec, and J. Bousquet, "A numerical study on mixing in the kenics static mixer," *Chem. Eng. Comm.*, **136**, 119 (1995).

Rohde, M., J. J. Derksen, and H. E. A. Van den Akker, "Volumetric method for calculating the flow around moving objects in lattice-boltzmann schemes," *Phys. rev. E*, **65(5)**, 056701 (2002).

Rohde, M., D. Kandhai, J. J. Derksen, and H. E. A. Van den Akker, "A mass conservative local grid refinement technique for inhomogeneous flow," *submitted to Int. J. Num. Meth. Fluids* (2004).

Saffman, P. G., "The lift on a small sphere in a slow shear flow," *J. Fluid Mechanics*, **22**, 385 (1965).

Saffman, P. G., "Corrigendum to "the lift on a small sphere in a slow shear flow"," *J. Fluid Mechanics*, **31**, 624 (1968).

Schlichting, H., *Boundary-Layer Theory*, McGraw-Hill, 6th edition (1968).

Shah, N. F., and D. D. Kale, "Pressure drop of laminar flow of non-newtonian fluids in static mixers," *Chem. Eng. Sci.*, **46**, 2159 (1991).

Sir, J., and Z. Lecjacks, "Pressure drop and homogenization efficiency of a motionless static mixer," *Chem. Eng. Comm.*, **16**, 325 (1982).

Sobera, M. P., C. R. Kleijn, H. E. A. Van den Akker, and P. Brasser, "Convective heat and mass transfer to a cylinder sheathed by a porous layer," *AIChE J.*, **49**, 3018 (2003).

Sugimoto, T., "Preparation of monodispered colloidal particles," *AdVances in Colloid and Interface Science*, **28**, 65 (1987).

Tchen, C. M., *Mean value and correlation problems connected with the motion of small particles suspended in a turbulent fluid*, Ph.D. thesis, Delft University of Technology, Den Haag (1947).

Ten Cate, A., *Turbulence and particle dynamics in dense crystal slurries*, Ph.D. thesis, Delft University of Technology, Delft (2002).

Ten Cate, A., C. H. Nieuwstad, J. J. Derksen, and H. E. A. Van den Akker, "Piv experiments and lattice boltzmann simulations on a single sphere settling under gravity," *Phys. Fluids.*, **14**, 4012 (2002).

Treasure, T., "Emew - a new contributor to process effluent control and management." *Electrometals Technologies Limited, (URL http://electrometals.com.au/EMEWTechPaper)*, **13** (2002).

Van der Kleij, R., *Measurement and simulations of heat transfer in a Primix static mixer*, Master's thesis, Delft University of Technology, Applied Physics (2004).

Van der Weijden, R., A. Mahabir, A. Abbadi, and M. A. Reuter, "Copper recovery from copper(ii) sulfate solutions by reduction with carbohydrates," *Hydrometallurgy*, **64(2)**, 131 (2002a).

Van der Weijden, R., M. Reuter, J. Voncken, and J. L. Sepulveda, "Characteristics of copper powder precipitated by reduction with carbohydrates," in *Proceedings of 9th International Workshop on Industrial Crystallization*, 220–225, Germany (2002b).

Van der Weijden, R. D., R. A. Penners, and M. A. Reuter, "Combined processing of various metal and organic (waste) streams," in *Conference of Metallurgists, COM2001, Productivity Through Technological Innovation*, 339–357, Toronto, Canada (2001).

Van der Weijden, R. D., M. A. Reuter, V. G. Aurich, and J. A. P. Bottema, "Pilot results of the recovery of copper from copper sulfate solutions via reduction in a plug flow reactor," in *ALTA Copper*, 1–10, Gold Coast, Australia (1999).

Van der Weijden, R. D., W. F. C. Van Wageningen, and M. A. Reuter, "Conditions for production of copper powder in a pipe reactor," in *XXII International Mineral Processing Congress* (2003).

Van Leeuwen, M., *Precipitation and mixing*, Ph.D. thesis, Delft University of Technology, Delft (1998).

Van Maanen, H. R. E., *Retrieval of Turbulence and Turbulence Properties from Randomly Sampled LDA Data with Noise*, Ph.D. thesis, Delft University of Technology, Delft (1999).

Van Pijpen, C., *Laminar flow in a Primix static mixer. Simulation and experiments*, Master's thesis, Delft University of Technology, Applied Physics (2002).

Van Wageningen, W. F. C., D. Kandhai, R. F. Mudde, and H. E. A. Van den Akker, "Dynamic flow in a kenics static mixer: An assessment of various cfd methods," *AIChE J.*, **8**, 1684 (2004a).

Van Wageningen, W. F. C., R. F. Mudde, and H. E. A. Van den Akker, "Cfd approach of growing cu-particles in a kenics static mixer reactor," in *ASME PVP2002 - 4th International Conference on Computational Technologies for Fluid/Thermal/Chemical Systems with Industrial Applications*, Vancouver, Canada (2002).

Van Wageningen, W. F. C., R. F. Mudde, and H. E. A. Van den Akker, "Numerical investigation into mixing of particle-laden flows in a kenics static mixer," in *11th European Mixing Conference*, 137–144, Bamberg, (Germany) (2003).

Van Wageningen, W. F. C., R. F. Mudde, and H. E. A. Van den Akker, "Numerical simulation of growing cu-particles in a kenics static mixer reactor in which cu^{2+} is reduced by carbohydrates," *Chem. Eng. Sc.*, **59**, 5193 (2004b), Special issue ISCRE18.

Venneker, B. C. H., *Turbulent flow and gas dispersion in stirred vessels with pseudoplastic liquids*, Ph.D. thesis, Delft University of Technology, Delft (1999).

Verberg, R., and A. J. C. Ladd, "Accuracy and stability of a lattice-boltzmann model with subgrid scale boundary conditions," *Phys. Rev. E*, **65(1)**, 016701 (2002).

Wilkinson, W. L., and M. J. Cliff, "An investigation into the performance of a static in-line mixer," in *2nd European conf. On mixing*, Cambridge (1977).

Zwietering, T. N., "Suspending of solid particles in liquid by agitators," *Chem. Eng. Sc.*, **8**, 244 (1958).

Dankwoord

Na 4 jaar met veel plezier op het Kramers laboratorium gewerkt te hebben, ligt hier dan eindelijk het resultaat in de vorm van mijn proefschrift. Ook al is een promotie-onderzoek een individuele aangelegenheid, ik had het niet kunnen volbrengen zonder de steun en hulp van mijn collega's, vrienden en familie. De noodzakelijke sponsoring kwam van het IOP Zware Metalen (Senter). Verder wil ik PRIMIX BV noemen en de begeleidingscommissie van het IOP als belanghebbenden van het onderzoek. De interesse die zij toonden in mijn onderzoek, was een belangrijke motivatiebron voor mij. Een paar mensen wil ik in het bijzonder bedanken:

Allereerst Harrie en Rob voor het vertrouwen dat zij mij schonken om 4 jaar onderzoek te doen op het KLFT. De vrijheid die ik heb gekregen om me zowel als onderzoeker als ook persoonlijk te ontwikkelen zijn van grote waarde geweest en hebben me uiteindelijk een geweldige baan opgeleverd. Natuurlijk ook niet te vergeten, Thea en Karin, zij stonden altijd klaar om dingetjes op tijd geregeld te krijgen.

Tijdens je promotie breng je eigenlijk het grootste gedeelte van je tijd achter de computer door. Een stabiel systeem is dan ook onmisbaar. Peter zorgde niet alleen voor een uitermate stabiel computer systeem, maar was ook elke keer weer bereid mijn lastige linux-probleempjes op te lossen en voor helpdesk te spelen.

Ik heb ook het genoegen gehad te mogen spelen met water en andere stofjes in de labhal. Het geavanceerde speelgoed dat daar voor nodig is, is op papier vrij aardig te schetsen. Het omzetten van mijn ideeën naar de praktijk had ik echter niet kunnen doen zonder de expertise van Ab, Wouter, Jan, Jaap, Jaap en Jaap. Als dan de meetopstelling af is en je eindelijk gaat meten, kom je er achter dat je toch nog iets toe wil voegen. Gelukkig waren zij dan bereid mijn opstelling te modificeren.

Het ontrafelen van de stroming in de statische mengers was een leuke uitdaging, waarbij ik de hulp gehad heb van de afstudeerstudenten Casper, Remi en Ruurd. In het bijzonder wil ik Ruurd bedanken voor de goede samenwerking en de uitstekende PIV metingen. Een belangrijk onderdeel van het project was het toepassen van de kennis voor de terugwinning van zware metalen uit afvalstromen. Tijdens het modelleren van het chemisch proces en de studie naar het gedrag van de groeiende deeltjes in de statische menger heb ik met veel plezier samengewerkt met Renata. Haar inbreng op chemisch vlak en meer op de praktijk gerichte blik, heeft mij de nodige realiteitszin bijgebracht.

De numerieke simulaties had ik nooit kunnen uitvoeren als Drona mij zijn LB code niet beschikbaar had gesteld. Zijn zeer goed gestructureerde code stelde mij in staat zelf modellen toe te voegen. De beperkingen die ik had met de commerciële code FLUENT vielen ineens weg, waardoor ik eindelijk mijn ideeën uit kon voeren. Hetgeen mij mooie publicaties heeft opgeleverd in AIChE Journal en Chemical Engineering Science.

Humor is belangrijk om 4 jaar denkwerk te relativeren. Gelukkig was daar altijd Wouter met zijn

cynische grappen en foto's. Discussie is een ander belangrijk element. Met iedereen heb ik goede discussies gehad, maar Luis wil ik in het bijzonder noemen. Altijd had hij tijd om mijn vragen te beantwoorden en lastige vraagstellingen te bediscussiëren. Hetgeen mij geholpen heeft bij het vormen van mijn gedachten.

Een leuke tijd heb ik gehad met mijn oude kamergenoten Ridwan, HP, Michal en Phillip. Het was altijd heel gezellig, misschien zelfs iets te gezellig. Op een gegeven moment was het zelfs zo gezellig dat het nodig was om kamerschermen te plaatsen. Ik ben toen maar een andere kamer gezellig gaan maken. Ik hoop dat de promotie van Joost daardoor niet nog langer geduurd heeft.

Sporten was een belangrijke uitlaatklep voor mij. Zwemmen bij Wave gaf de nodige balans en de biertjes na de training smaakten altijd ook goed. De fitness-sessies tijdens de lunch met Cas, Wouter en Roel gaven mij weer energie voor de rest van de dag. Roel (of Bob) wil ik verder bedanken voor de talloze liften naar sportcentrum en andere meer interessante plekken.

Een promotie is een belangrijke stap in je leven. Toch wil ik hen die mij mijn eerste stapjes geleerd hebben en mij altijd door dik en dun gesteund hebben bij alle daaropvolgende stappen, in het bijzonder vermelden. Papa, mama, heel erg bedankt voor alles wat mij gemaakt heeft tot wie ik nu ben.

Als laatste wil ik Femke noemen, die nog veel belangrijker voor mij is dan dit proefschrift.

About the Author

Niels van Wageningen was born on June 23, 1976 in Westkapelle, The Netherlands. After having obtained his 'Gymnasium Beta' certificate in 1994 at the 'Stedelijke Scholengemeenschap Middelburg', he started studying Applied Physics at Delft University of Technology. In February 2000, Niels obtained his MSc degree in Applied Physics. The research was conducted at the 'Kramers Laboratorium voor Fysische Technologie', and the topic of his thesis was 'The determination of the dynamic flow in a bubble column by means of Laser Doppler Anemometry'. In May 2000, he continued his career at the Kramers Laboratory and started his PhD research under the supervision of Professor Mudde and Professor Van den Akker, which resulted in this dissertation. Sports play an important role in the life of Niels. After having played tennis for 18 years at the tennis-club 'LTC de Westkaap' in his hometown Westkapelle, he started swimming at the Delft student swimming club, 'Wave' in 2000. From December 2004, Niels has been working as a Reservoir Engineer at Shell International Exploration and Production B.V. (SIEP) in Rijswijk.